UNIVERSITE CATHOLIQUE DE LOUVAIN

INSTITUTE OF EXPERIMENTAL AND CLINICAL RESEARCH

POLE OF PHARMACOLOGY AND THERAPEUTICS

ULTRA HIGH FIELD MRI FOR THE CHARACTERIZATION OF MURINE MODELS OF CARDIOVASCULAR DISEASES

DOCTEUR LAETITIA VANHOUTTE

PROMOTEURS:

PROFESSEUR STÉPHANE MONIOTTE

PROFESSEUR OLIVIER FERON

THÈSE PRÉSENTÉE EN VUE DE L'OBTENTION DU GRADE DE

DOCTEUR EN SCIENCES MÉDICALES

A ma maman

A Pierre et Hadrien

REMERCIEMENTS

Merci à toutes les personnes qui ont contribué à cette grande aventure…

Merci à mes promoteurs, les Professeurs Stéphane Moniotte et Olivier Feron, qui m'ont guidée tout au long de ce parcours doctoral. Je remercie particulièrement le Professeur Moniotte de m'avoir initiée à la Cardiologie pédiatrique et aux techniques d'IRM cardiaque.

Merci aux membres du Jury, les Professeurs Jean-Luc Balligand, Luc Bertrand, Christophe Chantrain, Bernard Gallez et Alexandre Persu, qui ont suivi le déroulement de ce projet et ont évalué ce manuscrit. Merci aux membres extérieurs, le Professeur Giovanni Aquaro et le Docteur Julie Magat, d'avoir accepté d'y apporter leur lecture critique.

Merci aux Professeurs Jean-Luc Balligand et Chantal Dessy pour les riches discussions qui ont nourri ce travail.

Un énorme merci aux nombreux collègues qui ont partagé mon quotidien durant ces 4 années, et qui pour la plupart sont devenus des amis. En particulier, merci à Céline Guilbaud et Hrag Esfahani, qui, au-delà de leur aide technique, m'ont énormément appris.

Merci à Caroline Bouzin et Chantal Fregimilicka, de la plateforme d'imagerie, pour leur grande aide dans les manipulations d'immunohistochimie.

Merci à Madame Sabrina El Bachiri et au Professeur William d'Hoore pour leur aide concernant les statistiques de ce travail.

Un grand merci à toute l'équipe de REMA, qui m'a toujours accueillie dans la bonne humeur. Merci en particulier à Julie Magat, Hassan Jassar, Chrystelle Pô et Nicolas Joudiou pour leur aide technique.

Merci à mes collègues cliniciens qui m'ont relayée quand c'était nécessaire. Merci à Maëlle de Ville de Goyet, ma « grande sœur de thèse », pour son soutien. Merci aux membres de l'équipe de Cardiologie pédiatrique pour leur aide ponctuelle. Merci aux technologues du service d'IRM clinique qui m'ont souvent aidée lors des acquisitions. Merci à toutes les personnes cotoyées pendant ma formation clinique qui ont eu une oreille attentive, un mot encourageant envers ce projet.

Merci à ma famille, qui m'a toujours accompagnée et soutenue. Je remercie sincèrement ma maman, ma sœur Mercédès et mon mari Pierre, sans qui je n'aurais pas été au bout de ce projet. Sans oublier Hadrien, qui m'a souvent aidée à remettre les choses en perspective et m'a transmis son énergie débordante quand il le fallait.

Cette thèse a obtenu le soutien du Fonds National de la Recherche Scientifique, de la Fondation Saint Luc et de la Fondation Nationale de Recherche en Cardiologie Pédiatrique.

ABBREVIATIONS

ASL Arterial Spin Labeling
CEST Chemical Exchange Saturation Transfer
CHD Congenital Heart Diseases
CMR Cardiac Magnetic Resonance
CS Compressed Sensing
CT Computed Tomography
DENSE Displacement Encoding with Stimulated Echoes
EDA End-diastolic Area
EDV End-diastolic Volume
EF Ejection Fraction
ESA End-systolic Area
ESV End-systolic Volume
FISP Fast Imaging with Steady State Precession
FLASH Fast low angle shot
FPP First pass perfusion
IR Inversion recovery
LV Left Ventricle
LGE Late gadolinium enhancement
MBF Myocardial blood flow
MEMRI Manganese-enhance magnetic resonance imaging
MRA Magnetic resonance angiography
MRS Magnetic resonance spectroscopy
MRSI Magnetic resonance spectroscopic imaging
PET Positron Emission Tomography
PC Phase Contrast
RF Radiofrequency
SNR Signal-to-noise Ratio
SPIONs Superparamagnetic Iron Oxide Nanoparticles
SV Stroke Volume
TG Transgenic
TOF Time of flight
UHF Ultra High field
Venc Velocity encoding
WT Wild-type

TABLE OF CONTENTS

Chapter I – INTRODUCTION

1. Global burden of cardiomyopathies

With more than 4 million deaths per year, cardiovascular diseases remain the leading cause of mortality in Europe (Nichols, Townsend et al. 2014) and, alone, they are responsible for about one third of all deaths worldwide (Mortality and Causes of Death 2015). Ischaemic cardiomyopathy, when considered separately, accounts for almost half of deaths (Nichols, Townsend et al. 2014). In the paediatric population, cardiovascular conditions rank sixth in causes of death in 1- to 19-year-olds (Vetter, Covington et al. 2015). Among them cardiomyopathies are the second prior condition present (23%) just after congenital heart diseases (48.5%), and the third common cardiovascular cause of death (11.8%) after CHD (40.8%) and arrhythmias (27.1%). Therefore, comprehensive assessment of pathophysiological processes leading to myocardial disorders is of prime importance.

Stricto sensu, cardiomyopathy is defined as a heart muscle disease sufficient to cause structural and functional myocardial abnormality in the absence of coronary artery disease, hypertension, valvular disease, and congenital heart disease (Arbustini, Narula et al. 2014). A classification, primarily based on the phenotype, has progressively evolved over the last two decades (Table 1). The American Heart Association (AHA) has proposed to group cardiomyopathies into genetic, mixed, and acquired forms (Maron, Towbin et al. 2006) whereas the European Society of Cardiology proposed subgrouping of cardiomyopathies into familial or genetic, and nonfamilial or nongenetic forms (Elliott, Andersson et al. 2008). Of note, the term of ischaemic cardiomyopathy, previously described in the World Health Organization classification of 1996 (Richardson, McKenna et al. 1996), has been abandoned in these last updates. However, cardiomyopathies are clinically heterogeneous diseases, and within each subtype there are differences in sex, age of onset, rate of progression, risk of development of heart failure, and likelihood of sudden death. The MOGE(S) nosology system was recently proposed in order to take into account all of these characteristics,

by describing the morphofunctional- phenotype (M), organ(s) involvement (O), genetic inheritance pattern (G), etiological annotation (E) including genetic defect or underlying disease/substrate, and the functional status (S) of the disease using both the American College of Cardiology/American Heart Association stage and New York Heart Association functional class. Nevertheless, the morphofunctional phenotype-based classification of cardiomyopathies remains the usual reference for clinicians, as it offers the possibility of using a simple and clinically useful diagnostic language, and because treatment protocols are currently based on it. Hence, in order to stay close to the routine clinical vocabulary, we will use in this work the terms of hypertrophic, ischaemic and dilated cardiomyopathy.

2. Ultra high field magnetic resonance imaging of rodent models of cardiovascular diseases

The advent of transgenic and knockout mice has brought new perspectives in cardiovascular research, allowing novel specific investigations and new therapeutic interventions. Non-invasive, accurate *in vivo* characterization of the cardiovascular phenotype of small animals has then become essential despite the challenge of their small heart size (<200mg weight) and rapid heart rate (400-600 bpm). In recent years, Ultra high field (UHF) cardiac magnetic resonance (CMR) has evolved to become an essential tool for experimental imaging, with an increase in reported studies characterizing these small animal models with MR systems operating at 7 Tesla or higher. The following work, published in Basic Research in Cardiology, provides a review of the various sequences and techniques already available to image mice on 7-11.7T magnets and summarizes the main issues related to the increase of the magnetic field when studying small animals (Vanhoutte, Gerber et al. 2016).

Basic Res Cardiol (2016)111:46
DOI 10.1007/s00395-016-0565-2

REVIEW

High field magnetic resonance imaging of rodents in cardiovascular research

Laetitia Vanhoutte[1,2] · Bernhard L. Gerber[3,4] · Bernard Gallez[5] · Chrystelle Po[6] · Julie Magat[7] · Balligand Jean-Luc[2] · Olivier Feron[2] · Stéphane Moniotte[1]

Received: 27 July 2015 / Accepted: 1 June 2016

Abstract Transgenic and gene knockout rodent models are primordial to study pathophysiological processes in cardiovascular research. Over time, cardiac MRI has become a gold standard for in vivo evaluation of such models. Technical advances have led to the development of magnets with increasingly high field strength, allowing specific investigation of cardiac anatomy, global and regional function, viability, perfusion or vascular parameters. The aim of this report is to provide a review of the various sequences and techniques available to image mice on 7–11.7 T magnets and relevant to the clinical setting in humans. Specific technical aspects due to the rise of the magnetic field are also discussed.

✉ Laetitia Vanhoutte
laetitia.vanhoutte@uclouvain.be

1 Department of Paediatric Cardiology, Cliniques universitaires Saint Luc, Université Catholique de Louvain (UCL), Brussels, Belgium

2 Pole of Pharmacology and Therapeutics (FATH), Institute of Experimental and Clinical Research (IREC), Université Catholique de Louvain (UCL), Brussels, Belgium

3 Division of Cardiology, Cliniques universitaires Saint Luc, Université Catholique de Louvain (UCL), Brussels, Belgium

4 Pole of Cardiovascular Research (CARD), Institute of Experimental and Clinical Research (IREC), Université Catholique de Louvain (UCL), Brussels, Belgium

5 Biomedical Magnetic Resonance Unit (REMA), Louvain Drug Research Institute (LDRI), Université Catholique de Louvain (UCL), Brussels, Belgium

6 CNRS, ICube, FMTS, Institut de Physique Biologique, Faculté de Médecine, Université de Strasbourg, Strasbourg, France

7 L'Institut de RYthmologie et de Modélisation Cardiaque (LIRYC), Inserm U1045, Bordeaux, France

Keywords High field · MRI · Cardiovascular diseases · Mouse

Abbreviations

ASL	Arterial spin labeling
CEST	Chemical exchange saturation transfer
CS	Compressed sensing
CT	Computed tomography
DENSE	Displacement encoding with stimulated echoes
FLASH	Fast low angle shot
FPP	First pass perfusion
IR	Inversion recovery
LGE	Late gadolinium enhancement
MBF	Myocardial blood flow
MEMRI	Manganese-enhance magnetic resonance imaging
MRA	Magnetic resonance angiography
MRS	Magnetic resonance spectroscopy
MRSI	Magnetic resonance spectroscopic imaging
PET	Positron emission tomography
PC	Phase contrast
RF	Radiofrequency
SNR	Signal-to-noise ratio
SPIONs	Superparamagnetic iron oxide nanoparticles
TOF	Time of flight
HF	High field
Venc	Velocity encoding

Introduction

Transgenic and knockout mice models are currently fundamental tools to study pathophysiological processes and therapeutic interventions in cardiovascular research. In recent years, high field (HF) MRI has evolved to become

Published online: 10 June 2016

an essential tool for experimental imaging, with an increase in reported studies characterizing these small animal models with MR systems operating at 7 T or higher. Indeed, since its introduction in the 1970s by Paul C. Lauterbur and Sir Peter Mansfield, improvements have led to spectacular development of MRI technology, allowing now to image hearts of rodents (<200 mg weight) in vivo at heart rates up to 600 bpm. The specific advantages of HF cardiac MR over other techniques such as echocardiography are its high accuracy and reproducibility [7, 137] and large versatility with the ability to provide insight into many physiological processes. Similar to human low-field CMR, HF CMR in rodents allows comprehensive evaluation of various parameters by different pulse sequences, not only allowing assessment of systolic and diastolic function but also of myocardial perfusion, viability, flow and molecular imaging [4, 44, 98, 116, 148, 159]. This work is primarily addressed to nonspecialist readers who have basic knowledge in (clinical) MRI and cardiology and are likely to perform cardiac HF MRI on small experimental animals. Basic principles of MRI [151] and thorough technical aspects [14] have been reviewed elsewhere. Here, we seek to provide a general overview of current imaging techniques and sequences available for HF imaging in mice and to define their interest in connection with clinical applications in humans.

Technical considerations

Hardware

HF MR Systems are dedicated small bore magnets allowing animal imaging at very high field strengths (>7 T). The main advantage of increasing field strength for MR imaging is the increased signal-to-noise ratio (SNR) allowing higher resolution. The downtrades are greater field inhomogeneity and susceptibility to artifacts and higher radiofrequency (RF) power deposition in tissue—measured by the specific absorption rate (SAR) [101]. Overall, although some authors report nice image acquisitions at clinical field strength (1.5–3 T) with optimized coils [29, 53, 62], or at the very high field of 17.6 T [60, 61], it is generally admitted that the range of 7–11.7 T offers the best trade off for most applications in small animals [48]. Systems can be either horizontally or vertically mounted. Vertical position of the magnet (as encountered in some biochemistry-based core facilities) although unphysiological and less practical for monitoring and customizing the probes, does not seem to interfere with cardiac hemodynamics [123, 173].

Various RF coil designs have been proposed to maximize SNR: surface coils, linear volume coils or birdcages [46, 98]. CMR in mice using a cryogenic quadrature RF coil has also been reported, offering significant gain in SNR compared to conventional coils operating at room temperature (see "Improving imaging speed: parallel imaging, compressed sensing (CS) and cryoprobes") [167]. In small animals applications, mid-range coils are usually used, which means that the product (fd) of the frequency f and the coil diameter d is in the range 2–30 MHz-m.

Animal handling and gating strategies

Small animal CMR is particularly demanding in terms of experimental setup installation and recording of vital parameters, in particular because of the small body size of the animals and their high cardiac and respiratory frequency, which increases the magnitude of motion artifacts.

To perform CMR procedures in living animals, general anesthesia is required throughout the acquisition. Currently, the preferred approach is isoflurane inhalation, because it causes minimal hemodynamic depression, allows short induction and fast awakening times, together with and easy regulation of anesthesia depth [74, 85]. In general, anesthesia is induced by placing the animal in a closed container using 3–5 % isoflurane for 2–3 min. Then the animal is installed in the scanner and anesthesia is maintained by continuous inhalation of 0.5–1.5 % isoflurane through a nose cone. Because anesthesia leads to rapid heat loss, the core body temperature must be carefully followed with a rectal probe and regulated by external heating with a heating blanket. ECG signal and other vital parameters can be recorded with specific monitoring systems. ECG electrodes are wrapped around the paws. During anesthesia, the rodents remain under spontaneous breathing, and respiratory rate is monitored by pneumatic sensor placed under the animal. The depth of anesthesia is modulated during the examination to remain within physiological heart rates (around 400–600 heartbeats/min) and respiration rates (around 50–100 cycles/min). This is allowed to remain within the physiological loading and pressure states, and ensures a proper reproducibility of the data [34, 163]. ECG and respiration gating signals can be integrated in the MR systems to allow prospective or retrospective trigger of the MRI acquisition, and minimize motion artifacts as breath holding is impossible in small animals.

Because at HF ECG signal is often degraded by the magnetohydrodynamic effects, RF pulses, and gradient switching during scanning [53], alternative techniques to the classical gating have been reported for rodents, using optimized gating strategies with cardiorespiratory monitoring [6, 33] or complete monitoring-free approaches [63–65, 103]. Optimized approaches developed to speed up image acquisitions are developed in "Improving imaging

speed: parallel imaging, compressed sensing (CS) and cryoprobes".

Evaluation of cardiac volumes, mass and function

The assessment of left ventricular function and volumes is fundamental in the comprehensive evaluation of animal models mimicking human diseases. Because of its high availability and ease, 2D-echocardiography remains the most commonly used noninvasive method for in vivo evaluation of rodent ventricular function. Yet it suffers from well-documented limitations, such as restricted acoustic windows, the need for an experienced operator and geometrical assumptions used to extrapolate data, as generally only 2- and 4-chambers long-axis slices or parasternal M-mode images can be acquired. CMR, being a true three-dimensional imaging technique, with an unrestricted access to the heart from all directions allows acquisitions in various directions (i.e., 4-, 3-, 2-chambers long axis and continuous stacks of serial short-axis images), and therefore, provides a better reproducibility [7, 137, 150] of measurements of the biventricular volumes and masses.

CMR assessment of biventricular function is typically acquired using segmented k-space fast gradient echo sequence (fast low angle shot—FLASH) with short TE, either with prospective gating or self-gated navigator sequences with retrospective reordering of images, applied to obtain short-axis views covering the entire left and right ventricular volumes. Temporal resolution of 10–20 phases per heartbeat (i.e., 5–10 ms) can be obtained, while spatial resolution typically approximates 0.1–0.2 mm. Generally, a stack of 6–8 serial 1 mm-thick short-axis slices is prescribed to cover the entire left and right ventricles. Ventricular volumes and masses are usually derived using Simpson's method where endocardial and epicardial borders are drawn on serial short-axis slices and volumes are derived by summing compartment area multiplied by slice thickness (Fig. 1). Masses can be extrapolated as the myocardial volume (difference between epicardial and endocardial volumes) multiplied by the myocardial specific density (1.05 g/cm^3).

Serial assessments of systolic function in various mouse models have already been described in the literature, even in neonatal mice [175], and have proved high accuracy in comparison to phantom measurements [120], ex vivo data [120, 123, 163] and invasive flow measurements [104]. The

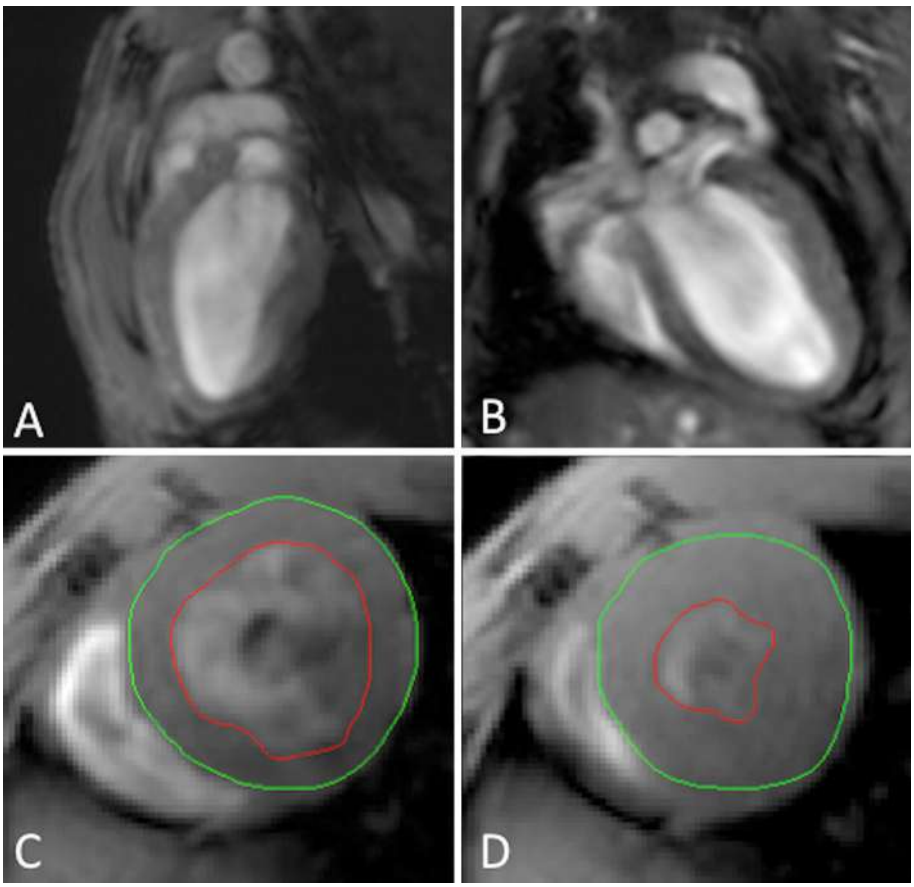

Fig. 1 Long axis two-chamber (**a**), long axis four-chamber (**b**) and short-axis (**c**, **d**) views of mouse hearts obtained with a FLASH sequence, at 11.7 T (Biospec, Bruker, Ettlingen, Germany). Endocardial (*red*) and epicardial (*green*) outlines were drawn in end-diastolic (**c**) and end-systolic (**d**) phases. Imaging parameters: TE/TR 1.5 ms/4.1 ms; FOV 30.0 × 30.0 mm; slice thickness 1.25 mm

high reproducibility of the method has also been assessed in several publications [59, 120, 123, 150, 163]. Therefore, the technique is ideally applied to study genetic, pharmacological or surgical interventions in mouse models of cardiovascular diseases.

By contrast, diastolic function assessment by CMR in rodents remains challenging. Drelicharz and colleagues reported filling rates (FR) derived from time-area curves obtained in the mid ventricular short-axis plane, as slope of the beginning part of diastolic limbs. They demonstrated that this approach allowed a reliable assessment of diastolic function in a mouse model of dilated cardiomyopathy at 4.7 T [47, 147] and the technique was further successfully used by other teams at higher field [1, 17, 174]. More recently, Buonincontri et al. used a similar (simplified) approach derived from echocardiographic color kinesis (Echo-CK), to measure diastolic index in a mouse model of diabetes ([30], at 4.7 T), a concept previously described and validated in humans [113]. Ideally, these measurements require acquisitions with high temporal resolution ($\geq$20 phases), to improve their reliability. If their use remains limited so far, they could still be easily transposed to other experimental models in the near future.

Intramyocardial function and strain

In models of cardiovascular diseases characterized by inhomogeneous dyskinetic regions in the myocardium, detailed quantification of the regional contractile performance of the heart may bring additional information to functional and volumetric indices. Several approaches are currently available for this purpose.

Tagging

Tagging is a technique in which selective spatial presaturation pulse are noninvasively applied on the image using delays alternating with nutations for tailored excitation (DANTE) [102] or spatial modulation of magnetization (SPAMM) [11] prepulse techniques prior to the acquisition of cine FLASH sequences. This results in stamping the myocardium with orthogonal lines or grid patterns (tags) which can then be followed during the cardiac cycle. Strain and torsion can be quantified with specific methods, such as the harmonic phase (HARP) based analysis [114] (Fig. 2).

The use of this sequence in small rodents at high field remains challenging because of the high heart rate requiring very short echo times to achieve sufficient temporal resolution during the cardiac cycle. Also, these images must be acquired using prospective gating with quality ECG to adequately deposit the tagging pattern in early systole and avoid subsequent taggrid deformation [90]. Furthermore, as a consequence of the small anatomy, very high spatial resolution and small tag spacing are required to characterize the strain. Finally, the post-processing and image analysis need to be adapted to lower SNR.

Some authors described successful applications of tagging sequences to rodents at field strengths $\geq$7 T [90, 132], showing that it can provide more sensitive measures of functional alterations than global functional indexes, helping to better understand the pathophysiology of various cardiovascular diseases, such as dilated cardiomyopathy [37, 57, 58, 141], restrictive cardiomyopathy [69] or cardiac dysfunction accompanying neurodegenerative diseases ([89], at 4.7 T).

Besides conventional tagging, other approaches have also successfully been used for deformation imaging at HF,

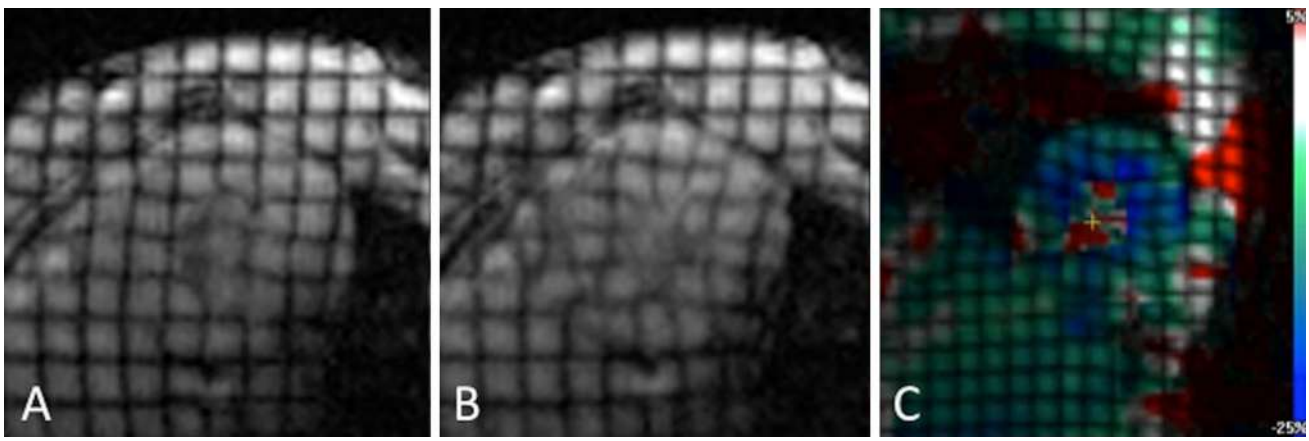

Fig. 2 SPAMM tagged images in mice. Compared to the reference image in end-diastole (**a**), the tag lines show clear contraction and twist of myocardium in end-systole (**b**). Imaging parameters: TE/TR 1.8 ms/12 ms; tag distance 0.3 mm, tag thickness 1 mm. **c** Representative short-axis strain map obtained with HARP software (Diagnosoft, Inc., Baltimore, MD, USA). *Blue zones* correspond to the highest deformation

tissue phase mapping (TPM) and displacement encoding with stimulated echoes (DENSE). Vector-based feature tracking software for strain measurement on classical cine images has also been shown feasible [75, 119].

To our best knowledge, only one study has compared echocardiographic and HF MRI strain measurements in mice. In their work, Azam et al. demonstrated that although echocardiographic vector velocity imaging seemed to be feasible and accurate, strains measured with DENSE method were more variable than those measured with MRI with similar variability for radial and circumferential strains [12].

Displacement encoding with stimulated echoes (DENSE)

DENSE is based on a stimulated echo sequence, in which the displacement of the myocardium is directly encoded into the phase of the MR signal, allowing strain quantification with high spatial resolution [5]. If its preclinical application has been more limited than tagging so far, technical adjustments allowing multiphase application [177], 3D acquisitions [178] and simplified post-processing [52, 140], could allow wider use of DENSE MRI in mice in the future.

Tissue phase mapping (TPM)

Dubbed phase contrast imaging or tissue phase mapping (TPM) provides pixel-wise encoding of the velocity—rather than displacement—in its phase images (see "Phase contrast angiography"). Different studies have successfully determined myocardial velocities in mice at different time point of cardiac cycles using this technique. If first studies were using bright blood contrast [60, 105, 134], blood suppression has been shown to improve accuracy of measurements in further developments [43, 79]. Baseline values of normal transmural wall motion pattern have been carefully established with TPM, allowing further comparison with genetically and surgically manipulated mouse models [43].

Perfusion, stress imaging and tissue characterization

Evaluation of myocardial perfusion and stress response is fundamental for the comprehension of pathophysiology of various models of cardiac disease. Tissue characterization (myocardial viability) and infarct visualization allows the comprehensive understanding of models of ischemic heart disease and subsequent myocardial remodeling.

Perfusion

Myocardial perfusion (i.e., myocardial blood flow per gram of tissue expressed as ml/g/min) is a key parameter in the investigation of cardiac diseases, as it allows characterizing the relationship between blood flow (oxygen delivery) and cardiac contraction in cardiac diseases. Currently, there are two different approaches to evaluate myocardial perfusion using HF CMR: (1) gadolinium-enhanced first pass perfusion (FPP) after the bolus injection of exogen contrast agent through a vein, and (2) arterial spin labeling (ASL) which makes use of intrinsic properties of the protons, and does not require contrast injections.

FPP sequences make use of the intravenous injection of gadolinium chelated contrast agents, which present paramagnetic effects. At moderate doses these agents shorten T1 times of the surrounding tissues in direct proportion to their concentration. At high doses the relation may become non-linear because of additional T2 and T2* susceptibility effects. In the literature, contrast doses between 0.1 and 0.9 mmol/kg have been used in rodents. Because of the fast systemic blood circulation time (4–5 s) [40] added to the general limitations of cardiac imaging in rodents, HF contrast-enhanced FPP CMR requires very fast acquisitions. At the same time, adequate spatial resolution has to be preserved, to visualize the regional myocardial inflow of the gadolinium. These challenges explain the very recent emergence of studies on FPP CMR in the experimental field. They all rely on rapid acquisition of saturation recovery sequences during the passage of a contrast bolus through the heart. Parameters like myocardial blood flow (MBF), myocardial tissue function (TF) and arterial input function (AIF) could be precisely quantified using dual-bolus [9, 154, 155] or dual-contrast [106] strategies either by tracer kinetic modeling or Fermi function deconvolution [76]. FPP MRI has successfully been applied at HF in mouse models of myocardial infarction [9, 40], cardiac hypertrophy [154] and obesity [106], with a good reproducibility of the regional quantitative perfusion estimates [155].

ASL has been described for more than 10 years to investigate myocardial perfusion in small animals. This approach, described by Bauer et al. [21], and further validated by comparison to the well-established microsphere technique in the isolated heart [20] and in the intact animal [170], does not require injection of external contrast agent, but makes use of modification of the magnetic properties of hydrogen protons circulating in the blood entering the imaging slice. As a consequence, image intensity changes occur depending on blood supply to the tissue. Circulating spins are labeled through an RF impulsion, and the myocardial blood flow (MBF) is detected by comparing the resulting tissue T1 relaxation time change between an

acquisition with labeled and unlabeled protons from adjacent slice. Practically, a gradient echo sequence is used to obtain a stack of images at an array of delay times following slice-selective (SS) and non selective (NS) inversions. Then myocardial perfusion can be measured in ml/g/min through the following formula: $P = (1/T1_{ss} - 1/T1_{ns})T1_{ns}/T1_{blood}\lambda$, where λ is the blood/tissue partition coefficient [48]. At HF, the ASL sequence benefits from a better difference between $T1_{ns}$ and $T1_{SS}$, this increases with the magnetic field strength for a given level of perfusion [159]. Over time, the ASL sequence has been properly applied to measure MBF in different mouse models of cardiovascular diseases, after some methodological adjustments to improve the resolution and scan time [2, 32, 55, 80, 135, 144, 162], with a proven reproducibility [32].

Another technique, the blood oxygen dependent imaging (BOLD), has also been considered an alternative perfusion sequence because of its wide use in functional neuroimaging [19]. It makes use of the modification of T2 times of deoxygenated blood. However, many technical considerations have limited its transfer for cardiac imaging [128]. In particular, at high field, many parameters beside deoxyHb/oxyHb may contribute to susceptibility differences [84], and so far, no cardiac study was published in rodents at HF.

Stress-CMR and cardiac reserve

The acquisition of functional data during inotropic stimulation is useful for the detection of ventricular filling abnormalities and to unmask early dysfunction, not detectable in the resting state. In humans, cardiac reserve is also an effective predictor for survival [72]. Stress imaging can be performed in rodents before and after β1-adrenergic stimulation induced by injection of dobutamine at doses ranging from 4 to 16μg/kg/min intravenously or from 20 to 40μg/kg/min intraperitoneally [147].

Inherent challenges to the use of stress-CMR in rodents are the increase in their already high heart rate, complicating ECG-triggered data acquisition, and the need for reproducible measurements. These difficulties have been overcome by optimization of classic functional sequences for higher temporal resolution. Wiesmann et al. were the first to describe the technique at HF in normal and chronically failing mouse hearts [174]. Other studies have then followed on various models of cardiovascular diseases [131, 136, 143], bringing additional interesting data, inter alia the role played by high-capacity creatine kinase system CK/PCr [143] and the neuronal nitric oxide synthase nNOS ([160], at 4.7 T) in inotropic and lusitropic responses to dobutamine but not in the cardiac function at rest.

Late gadolinium enhancement and myocardial viability

In clinical imaging, late gadolinium enhancement (LGE) CMR is a gold standard for the investigation of myocardial viability, because of its superiority for the detection of small myocardial lesions undetectable with nuclear imaging [126]. Viability is also a key prognostic factor in human cardiovascular diseases.

LGE images are acquired late (at least 10 min) after the intravenous or intraperitoneal injection of gadolinium-based contrast agents. The technique is based on the principle that Gd-chelates have an extravascular distribution volume. Infarcted or fibrotic tissues present reduced cellular and increased extravascular volume, with therefore higher contrast concentrations at equilibrium, translating into shorter T1 times. To obtain optimal T1 weighing contrast between normal and abnormal myocardium, an inversion recovery (IR) technique is applied, nulling the signal intensity for normal myocardium (Fig. 3). Optimal inversion time to null viable tissue is previously defined with a look-locker sequence. This approach—well-established in clinical practice—has been successfully described at HF, validated by the great correlation with ex vivo data, and became soon an accepted modality for the study of preclinical models [24, 35, 54, 112, 117].

Nevertheless, applying this technique at HF to rodents remains quite challenging, as their rapid heart rate often results in suboptimal ECG triggering. This may impact the effectiveness of IR sequences, as they rely on a constant time delay between successive IR pre-pulses. Hence, some authors argue that a classical cine FLASH sequence could be used for LGE in place of IR MRI for infarct size assessment, because of its high spatial and temporal resolution. Indeed, unlike at clinical field strength, it seems to provide similar accuracy at high field while being more robust, faster and easier to use [118]. Whatever the type of acquisition used, LGE brings precious information on the pathophysiology of diseases impairing the viability of the myocardium.

Manganese-enhanced MRI (MEMRI)

Similar to gadolinium, manganese (Mn^{2+}) is paramagnetic and decreases T1 in surrounding tissues. In addition, it is actively pumped through the voltage-gated L-type Ca^{2+} channels in cardiomyocytes. Exploiting these specific properties, manganese-enhanced MRI (MEMRI) has been applied at HF in mice for two main applications. First, dynamic MEMRI allows specific measurement of Ca^{2+} channels activity, using T1-imaging at baseline and after infusion of dobutamine. Signal enhancement relates then to calcium influx and inotropic response [8, 23, 68, 168].

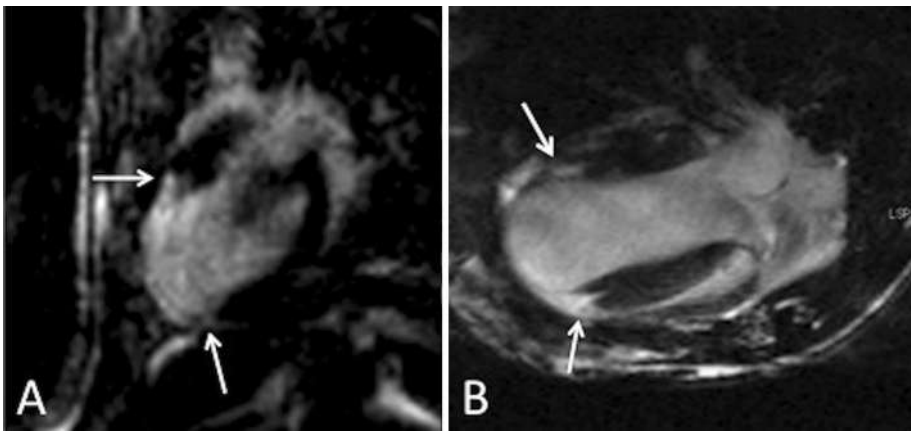

Fig. 3 Long-axis inversion recovery T1-weighted MR image in a mouse with LAD ligation, 20 min after peritoneal injection of a 0.5 mmol/kg bolus of gadolinium DTPA. Limits between the nonviable infarcted myocardium (*hyperenhanced zone*), and the healthy myocardium (*dark zone*) are well visible (*arrows*). Imaging parameters: TE/TR 2.2 ms/4.5 ms, inversion time 350 ms

Second, infarct zone can be accurately delineated after injection of $MnCl_2$, as the uptake of Mn^{2+} is greater in functional regions [67].

Compared to histology, MEMRI is more accurate to determine infarct size than LGE, as the latter tends to overestimate nonviable zone at acute stage. However, unlike MEMRI, LGE has the advantage of showing a decrease in signal when myocardial infarction changes from the acute to the chronic stage [129].

Although MEMRI represents a powerful preclinical tool for the study of ischemic disease, its transfer to the clinical field is hampered by the potential toxicity of free Mn^{2+}.

Relaxometry

The strength of MRI remains its powerful soft tissue contrast, based on the intrinsic relaxation properties T1 and T2. Quantitative measurement of these parameters, also referred to as quantitative relaxometry, can be informative in various pathophysiological processes, and has the advantage of objectively measuring biological changes whereas classical techniques based on qualitative or semiquantitative evaluation may under- or overestimate disease processes. Hence, these last years, T1-, T2- and T2*-weighted imaging already used for clinical applications has emerged in the field of HF CMR in rodents, with or without the use of contrast agents.

T1 mapping

T1 is the longitudinal (or spin–lattice) relaxation time of a tissue. It is known to be prolonged in some conditions like fibrosis, edema and amyloid deposition, and reduced in lipid accumulation, siderosis, hemorrhage and in acute infarction [27]. Parametric maps for T1 are obtained by applying different T1 weighting to a series of images so that each voxel can be assigned a T1 value. They can be displayed using color or threshold scales to enable visual interpretation.

Since the description of the modified look-locker inversion recovery method (MOLLI) by Messroghli et al. [99], which has simplified the acquisition in comparison to the classical look-locker sequence [92], the clinical use of T1 mapping has never stopped to spread. Even if more standardized protocols are needed in this rapidly evolving field, myocardial T1 mapping is already used in numerous hospital centers and has proven its diagnostic and prognostic value in both cardiac diseases (acute coronary syndromes, myocarditis, hypertrophic and dilated cardiomyopathy, congenital heart diseases, heart failure) and cardiac involvement in systemic diseases (amyloidosis, Anderson-Fabry disease, siderosis, diffuse fibrosis of various origins) [49, 100, 121]. In the specific case of diffuse myocardial fibrosis, T1 mapping is considered as superior to the highly invasive and partial endomyocardial biopsies and the indirect technique of LGE. Indeed, it provides a quantitative T1 relaxation time per voxel, instead of a qualitative T1 contrast, allowing discrimination of remaining healthy areas [156].

T1-contrast is also the most used for parametric mapping in mice at HF. T1-mapping is commonly acquired with a sequence based on the look-locker method although some authors described SNAPSHOT-FLASH Inversion Recovery (SNAP-IR) [24, 124] or variable flip angle [39] strategies for the acquisition. In mouse, the acquisition is mainly made in combination with a contrast agent, gadolinium [24, 39, 138] or manganese [8, 77, 87, 88, 168, 169]. Up to now, the technique has been successfully applied to murine models of myocardial infarction [24, 39, 168], cardiac hypertrophy [8, 138] and dystrophinopathy [77]. Various applications have been studied: quantification of infarct size [24, 39, 168], identification of potentially salvageable myocardium [168] and evaluation of monocyte and macrophage spatiotemporal kinetics [107] in the vicinity of a myocardial infarction site,

quantification of focal and diffuse fibrosis [138], or detection of changes in Ca^{2+} channels activity in combination with MEMRI [8, 77, 168, 169]. T1 mapping can also provide valuable information on the pharmacology of contrast agents, and as mentioned earlier, quantitative T1 measurements are essential for perfusion studies based on the ASL technique.

T2 and T2* mapping

Other parametric mappings have not received as much attention as T1-mapping in mice. Nevertheless, they can provide valuable information in the field of cardiovascular research.

T2 is the transversal (or spin–spin) relaxation time. Since T2-weighted imaging is sensitive to liquids, parametric maps for T2 have been described in mouse models of MI to identify edema and area at risk [22, 25, 41, 123], with different strategies of acquisition. It has also been successfully applied to a mouse model of diabetes, with an adequate quantification of fibrosis [28].

Of note, Aguor et al. have also developed a T2* mapping in a mouse model of myocardial infarction, using a multi gradient echo sequence. They showed that T2*-weighted images could be used to discriminate between acute and chronic phase of MI, as a reduction of T2* was observed with infarct age, probably because of the presence of iron [3]. Potential interest of such sequence in mouse models of chronic iron overload has also been assessed at field <7 T [110], but still need further validation at HF, as T2* is very sensitive to large scale magnetic field homogeneities, and may be difficult to measure in case of high iron concentration, as signal decay may become rapid [130].

MR angiography

The increasing number of transgenic murine models mimicking vascular pathophysiological processes, and the growing awareness of the importance of some hemodynamic parameters as independent prognostic factors for morbidity and mortality in cardiovascular diseases [164] has led to an interest in developing reliable MRI techniques for the study of vascular parameters in rodents. If gadolinium-enhanced angiography is often used in the clinical field, the very fast washout of conventional low-molecular weight contrast agents such as Gd-DTPA after injection renders it difficult to apply to rodents [66]. Together with the high cost of contrast agents, these limitations have led to a wider use of non-contrast MR angiography (MRA) sequences in preclinical studies, i.e., time of flight (TOF) and phase contrast (PC) angiography.

Time of flight angiography

The TOF angiography technique is based on inherent vessel contrast resulting from the inflow effect. A flow-compensated gradient echo sequence is applied to a volume with a very short repetition time, saturating the stationary tissue, whereas longitudinal magnetization remains maximal in moving spins. Images obtained are combined using a technique of reconstruction such as maximum intensity projection (MIP) resulting in a 3D angiogram.

Classical limitations of TOF angiography are the signal loss due to spin dephasing when flows are turbulent or too slow and the progressive saturation of the blood signal in the imaging volume leading to a loss of contrast in the distal regions. However, at HF, the angiogram quality clearly benefits from the higher SNR and longer T1 relaxation times of background tissues [166]. In addition, preparation techniques have been developed to enhance the vessel-to-background contrast and its uniformity [122, 145].

If in preclinical studies TOF-MRA is widely used for the characterization of cerebral vasculature, it has also been applied with success to various murine models of cardiovascular disease, including mice with carotid artery ligation [71, 145, 149], hindlimb ischemia [71], aortic aneurysms [82, 83] and/or mice with a hyperlipidemic pattern [149]. A TOF 3D angiogram of the aortic root obtained in a mouse model of aortic banding on an 11.7 T MRI machine is shown in Fig. 4. In such models, the sequence allows longitudinal study of regional neovascularization processes and vessel stenosis or dilation. Moreover, Lefrançois et al. were able to generate a murine whole-body angiogram [86], while Cochet et al. have characterized mice coronary arteries with a high spatial resolution (80μm) TOF-MRA. They further assessed left coronary artery velocity measurements and coronary flow velocity reserve through dynamic MR angiography at seven successive phases throughout the cardiac cycle [38]. The same method of in vivo quantification of blood velocity based on a series of TOF acquisitions was already reported in 2009 by Parzy et al. in mouse carotids and pulmonary arteries [115], bringing evidence that the TOF technique can be more than an anatomical sequence.

Phase contrast angiography

PC-MRA is a functional sequence allowing flow and velocity measurements. This is performed by applying a bipolar gradient that causes moving spins to receive magnetization dephasing, proportional to their velocity. The principle may be applied in all three directions (in- and through-plane) and requires the repetition of sequences with and without flow encoding to generate, respectively, magnitude (anatomical) and phase (quantitative) images (Fig. 5). The encoding gradients are set by the user to

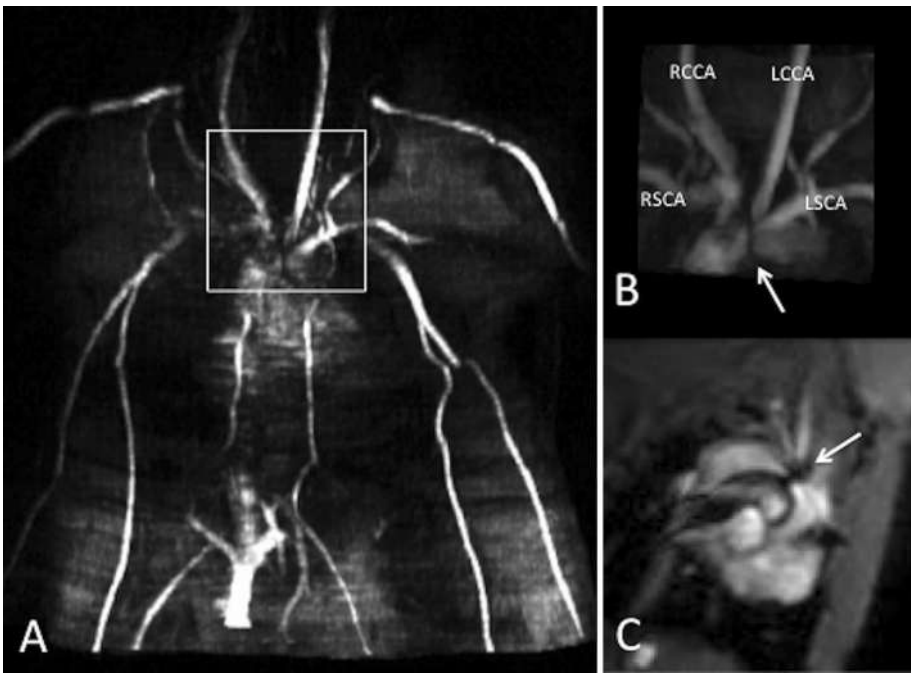

Fig. 4 **a** 3D maximum intensity projection (MIP) of a TOF angiography of the trunk in a mouse (anterior view). *Blurring* corresponds to artifacts due to heart motion. Imaging parameters: TE/TR 2.4/12 ms; matrix 256 × 256 × 120, slice thickness 0.4 mm, flip angle 80°. **b** Details of the aortic arch and the supra-aortic vasculature, showing the transverse aortic stenosis due to surgical banding (*arrow*). *LCCA* left common carotid artery, *RCCA* right common carotid artery, *LSCA* left subclavian artery, *RSCA* right subclavian artery. **c** Sagittal view of the aorta with FLASH sequence, in the same animal. The *arrow* indicates the transverse aortic constriction

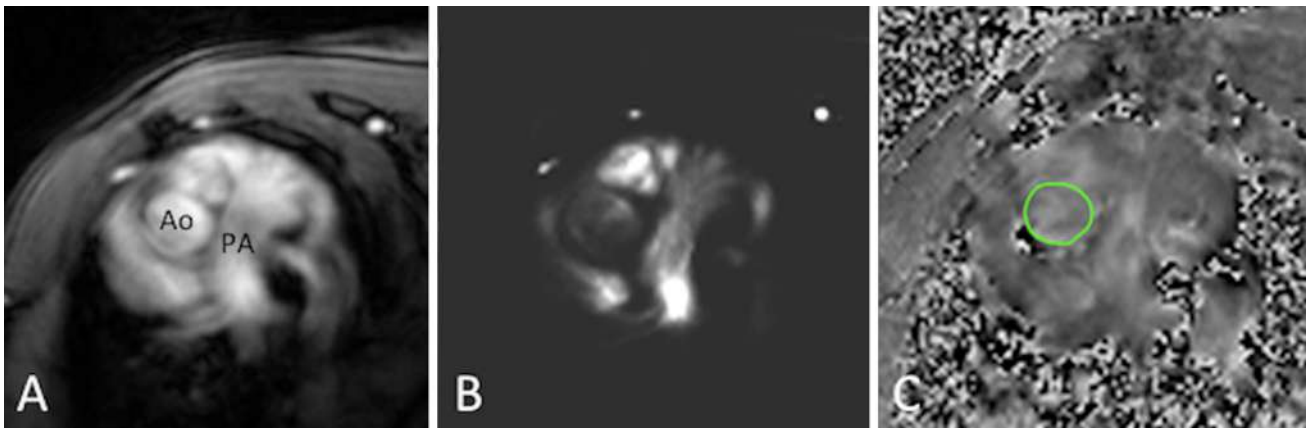

Fig. 5 Transverse FLASH view of the mouse ascending aorta (**a**) and corresponding phase contrast magnitude (**b**) and phase images (**c**). The region of interest where aortic flow measurement can be performed is indicated in *green* on the phase image. *Ao* aorta, *PA* pulmonary artery. Imaging parameters: TE/TR 2.3/8.7 ms, spatial resolution 0.138 mm/pixel, slice thickness 1 mm, VENC 250 cm/s

encode flows within a certain velocity range from −Venc (velocity encoding) to +Venc. These Venc values must be chosen adequately as flow outside this range of values will present velocity aliasing (or wraparound).

Measuring blood flow velocities (BFV) in rodents is challenging, as velocities in the mouse aortic arch are similar to those found in human (about 100 cm/s) [73] while the anatomy is extremely small with aortic cross-sections of a few millimeters square. For years, Doppler ultrasound has been largely used to obtain vascular parameters in small animals' models of vascular diseases [139]. Unlike this approach, which is constrained to measuring velocities along transducer orientation, MRI offers the possibility to study vector component of velocity in any spatial orientation. This makes it more accurate in the determination and follow-up of parameters like BFV, wall shear stress (WSS), pulse wave velocity (PWV) or oscillatory shear index (OSI), even in curved vasculature. These valuables indexes are known to be early markers of dysfunction in mice with atherosclerotic patterns [61, 73, 176].

Cellular and molecular imaging

Although MRI has become one of the preferred imaging modalities used in cardiology, its resolution remains insufficient at a cellular or molecular scale, unless detectable probes or spectroscopic measurements are employed.

Superparamagnetic iron oxide nanoparticles (SPIONs)

Over years, different in vivo MRI detectable probes have been considered for molecular or cellular imaging in small animal studies, as conventional methods (LGE, T2-weighted imaging, T2-mapping) remain not specific for a particular type of tissue process or injury. Among them, superparamagnetic iron oxide nanoparticles (SPIONs) represent a powerful tool for cellular MR imaging. After labeling of stem cells with these small biocompatible crystalline magnetite structures, cell engraftment, differentiation and viability can be noninvasively monitored thanks to the high sensitivity of SPIONs for MRI [26]. If so far, cardiovascular applications in mice at HF remain scarce [36, 96, 111, 133, 165], it represents a promising approach for the study and follow-up of stem cell therapy in the field of cardiology.

Magnetic resonance spectroscopy (MRS) and X-nuclei MRI

Magnetic resonance spectroscopy (MRS) has made possible investigation at a molecular level, allowing comprehensive assessment of metabolic changes in vivo, by producing a collection of peaks at various radiofrequencies—the spectrum—representing a considered nucleus in different chemical environments. The peak position is determined by chemical bonds and the area under the peak is related to the amount of the specific nucleus in the region of interest.

Theoretically, all nuclei with nonzero spin can be employed for magnetic resonance imaging and spectroscopy, with adjustment of scanner hardware and sequences to select the nucleus-specific frequency and to enable imaging with sufficient signal-to-noise ratio. Hence, besides conventional proton resonance spectroscopy (^{1}H MRS) that represents a powerful technique to study myocardial content of metabolites, such as lipids and creatine in vivo [1, 13, 17, 18, 56, 125], MRS has also been successfully developed in rodent models of cardiovascular diseases for the study of various other nuclei, including ^{13}C, ^{19}F, ^{31}P and ^{23}Na. These nuclei are mostly investigated to noninvasively map regional metabolic processes in vivo, through combination with ^{1}H MRI acquisitions

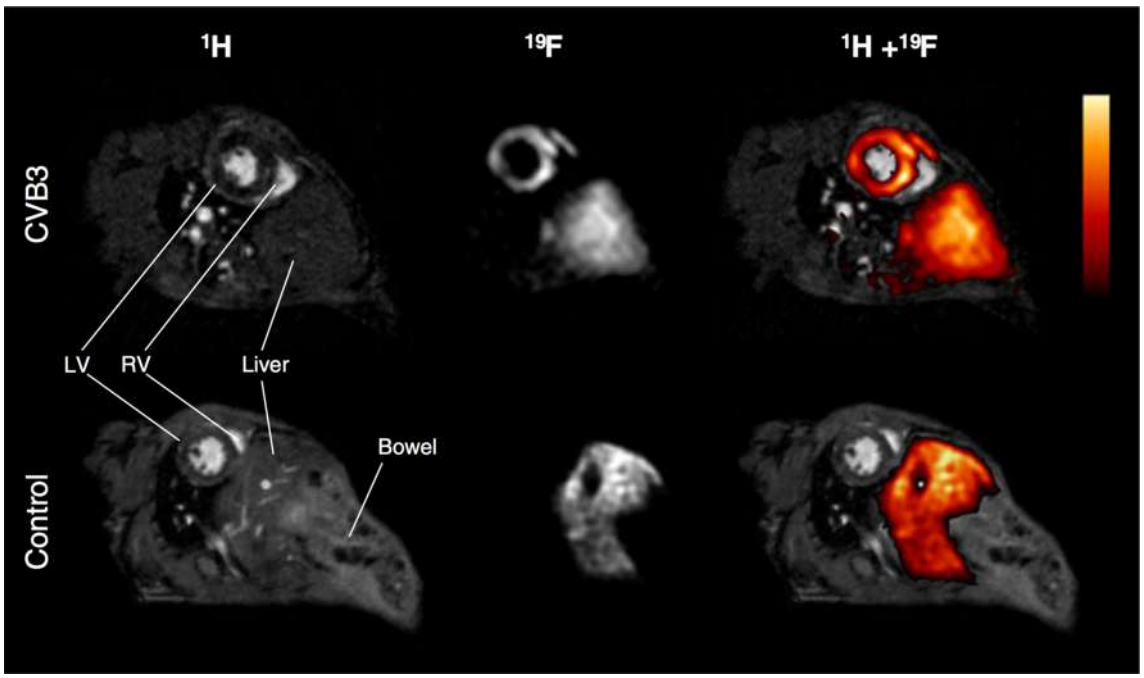

Fig. 6 Short-axis ^{1}H and ^{19}F MR images from a mouse thorax 14 days after inducing myocarditis by injection of coxsackievirus B3 and two days after application of PFCs (*top row*). Merged images (*right*) clearly show a homogenous accumulation of PFCs within the left ventricular wall of treated animals, whereas no ^{19}F signal was observed within the heart of control animals (*bottom*). Reproduced with permission from Jacoby et al. [70]

providing anatomic information. The combination of both techniques has brought the term of magnetic resonance spectroscopic imaging (MRSI).

^{13}C MRS of infused hyperpolarized 1-^{13}C-pyruvate, allows to monitor activity of the pyruvate dehydrogenase complex, as is reflects myocardial use of carbohydrates and their contribution to energetic homeostasis [16, 45]. Low intrinsic sensitivity of ^{13}C requires combined use of hyperpolarization techniques such as dynamic nuclear polarization (DNP) [10].

^{19}F MRI combined with injection of perfluorocarbon (PFC) allows study of inflammatory processes in the context of cardiac ischemia [50], myocarditis (Fig. 6) [70, 153], atherosclerotic [152] or thromboembolic processes [142]. PFCs are inert, nontoxic carbohydrates with fluorine that are phagocytized by circulating cells. As ^{19}F is virtually absent in tissue from animals and humans, fluorine can be detected without any background and with direct proportionality to the amount of ^{19}F nuclei present in the tissue, allowing quantitative measurement, whereas use

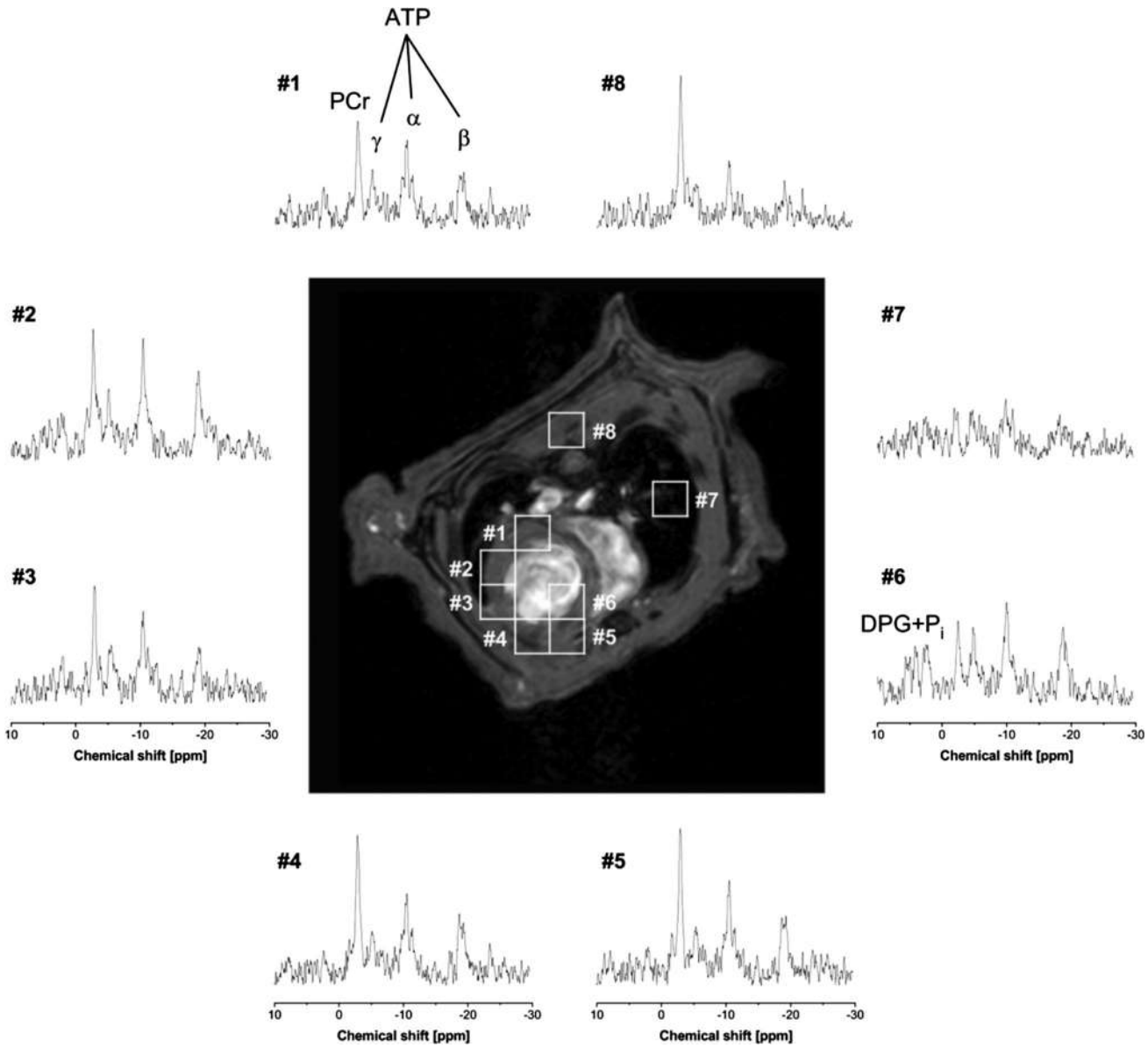

Fig. 7 Representative ^{31}P MR spectra from selected voxels of the mouse thorax superimposed with the anatomical ^{1}H MR image acquired in the same examination. Spatially localized spectra of the posterior (*#1*), lateral (*#2* and *#3*), and anterior (*#4* and *#5*) walls, and the septum (*#6*) of the heart are displayed. Additionally, spectra from the lungs (*#7*) and the skeletal muscle of the animal's back (*#8*) are shown. Reproduced with permission from Flögel et al. [51]

of gadolinium and oxide-based contrast agents relies on relaxation time alterations and nonlinear dose–signal response are often seen at high concentration. Furthermore, transition into clinical applications is likely feasible for ^{19}F MRSI, as PFC exhibit a high safety profile according to preliminary experiments, while concerns related to toxicity and safety could limit the use of other contrast agents to humans.

The analysis of ATP and phosphocreatine in tissue samples is problematic because of the instability of these molecules. Therefore, the principal method for measuring components of cardiac energy metabolism remains phosphorus-31 magnetic resonance spectroscopy ^{31}P MRS [108]. This well-established method has already been applied to various mouse models to study in vivo cardiac energetic metabolism, as assessed by the PCr/ATP ratio [1, 15, 16, 42, 51]. Representative ^{31}P MR spectra from selected regions of the mouse thorax superimposed with the anatomical ^{1}H MR image are shown in Fig. 7.

^{23}Na MRS reflects the activity of the sodium–potassium pump (Na^+/K^+-ATPase). As disruption of normal electrochemical gradients indicates cellular injury or dysfunction, following regional concentration of Na could provide precocious information regarding myocardial viability. Precise localization of infarction could be performed by observing the changes in the magnitude of sodium signal, since Na concentration is increased by >200 % in infarcted area [81]. Up to now, only technical studies have been reported on mice [94, 109], but recent methodological improvements suggest that further studies on models of myocardial infarction could soon be available.

Of note, MRS using other nuclei have been subject to preliminary development in small animals, inter alia oxygen-17 (^{17}O) [93] and rubidium-87 (^{87}Rb) MRS [78]. Detailed description of these techniques is beyond the scope of this review.

Chemical exchange saturation transfer (CEST) MRI

Besides spectroscopy, current development of chemical exchange saturation transfer (CEST) MRI techniques in cardiovascular research could allow multiplexed molecular imaging in a single session [158]. CEST-MRI takes advantage of the transfer of magnetization from endogenous macromolecules, chemical contrast agents or engineered reporter genes with nearby water molecules to generate contrast on MRI, with a higher sensitivity compared to MRS [91].

Perspectives: fast acquisitions and multimodal imaging

Improving imaging speed: parallel imaging, compressed sensing (CS) and cryoprobes

An important issue when considering MRI imaging of small animals is the need to simplify the manipulations, especially by shortening acquisition time of sequences. Various approaches have been studied for that purpose. Here, we describe those that are currently the most successful in mice.

Parallel imaging exploits the multiple elements of a phased array coil. Each element is associated with an independent radiofrequency pathway whose signals can be processed and combined together. A combination of such overlapping multiple receiver coil elements can be utilized to improve the signal-to-noise ratio and allows to speed up acquisitions as the number of spatial encoding steps can be decreased and conventional Fourier encoding reduced [40, 124].

Other techniques aim to specifically reduce the amount of acquired data without degrading the image quality. Indeed, compressed sensing (CS) allows to reconstruct images from significantly fewer measurements than were traditionally thought necessary, by exploiting the redundancy of the image in space or time. Signals and images are reconstructed with good accuracy from these measurements through a nonlinear procedure. The increasing and successful use of this method to improve cardiovascular MRI characterization of small animal models suggests that it will continue to expand in the near future.

Cryoprobe is a technology where the RF coil and/or preamplifier are cooled with a stream of Helium gas. As a consequence, the coil performance is improved and the level of thermal noise generated by the associated electronics is reduced. This allows significantly shorter measurement times and improvement of in vivo resolution compared to room temperature conventional probes. If its use may reduce the available space within the magnet, studies have shown that cardiovascular studies on small animals with a cryoprobe were feasible at HF [167].

Multimodal imaging

Now that several HF MRI sequences are routinely used for the characterization of murine models, their combination to get fundamental energetics, functional and anatomic cardiac information for the same animal promises to be an important in vivo tool for assessing the physiological relevance of structural and functional modifications and the

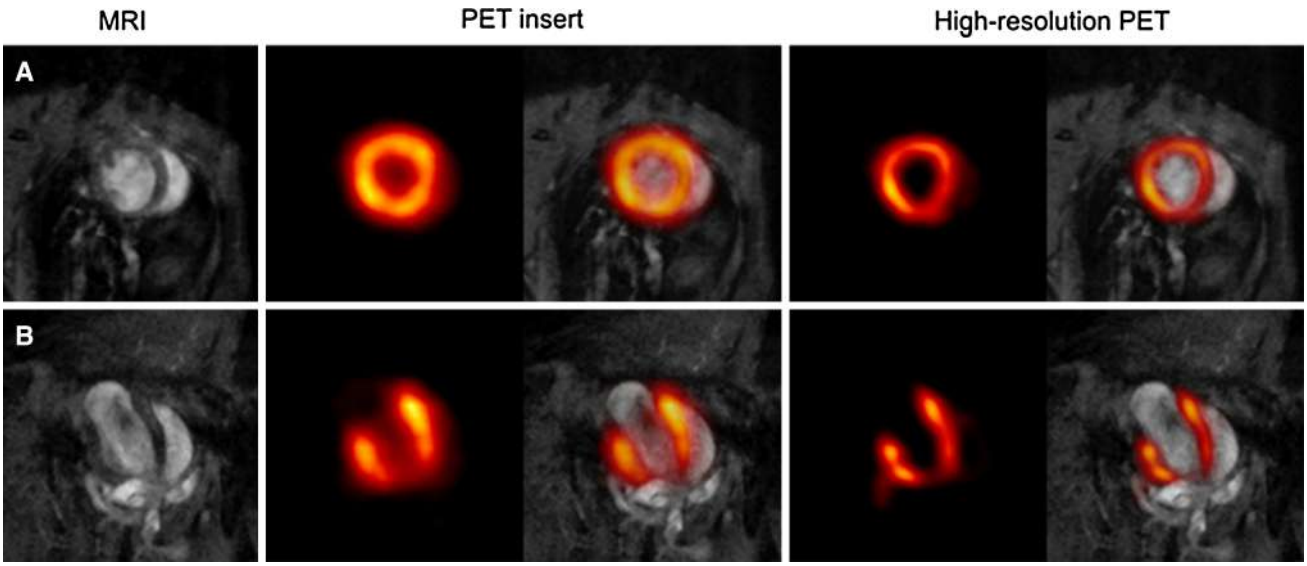

Fig. 8 Sample coregistered ^{18}F FDG PET and ^{1}H MR images at 7 T in a mouse model of myocardial infarction. **a** Short-axis view. **b** Long-axis view. Reproduced with permission from Büscher et al. [31]

usefulness of therapeutic interventions. Besides the classical coupling of ^{1}H-MRI with MRS of other nuclei to get spatially encoded metabolic information, several other studies combining different imaging modalities on the same animal models have recently exemplified the power multimodal imaging [25, 105, 160, 161].

Beyond the use of multimodality MRI examination, the combination of MRI with another imaging technology such as positron emission tomography (PET) results in a promising hybrid molecular imaging tool, taking advantage of both the high-resolution cardiovascular imaging of MRI and the high sensitivity of PET for sparse molecular or cellular targets. Compared to computed tomography (CT) imaging, classically combined with PET, MRI is more flexible due to its plurality of sequences and offers improved contrast [157, 171]. PET/MRI also enables dual target molecular imaging by simultaneous use of MRI agents [146]. While PET and MR imaging can be done sequentially with offline fusion of data, newer scanners allow for synchronous data acquisitions in mice (Fig. 8).

Integrating PET and MRI technologies is more complex than the evolution towards multimodality PET-CT due to the presence of the magnetic field, explaining the slow progress to efficient systems. Historically, the first approach for simultaneous PET/MR used optical fibers guiding the scintillation light to the photomultiplier tubes—important elements of standard PET detectors—outside the MRI [127]. Further improvements, mainly initiated by the advent of avalanche photodiodes allowed the operation of magnetic field insensitive PET detectors inside the MRI bore [172].

Sequential [95, 146] or combined use of PET and MRI [31, 97] has been reported to study various issues on the mouse models of cardiovascular diseases at HF. In light of this success, manufacturers will probably propose more automated tools for combined PET/MRI imaging in the near future.

Conclusions

We provided a comprehensive overview of HF MRI sequences available for cardiovascular investigation in mice, with practical information and reference literature for researchers wishing to implement this tool in their practice.

Despite the many challenges encountered when moving to higher field strength and small animal imaging, HF MRI has undoubtedly become an essential technique in cardiovascular research, as evidenced by the extensive literature on the subject in recent years. Because of the huge ongoing development in the field, further refinement of the technique will allow even wider opportunities in basic animal research.

Acknowledgments The authors thank Hassan Jassar and Nicolas Joudiou for assistance during MRI manipulations. This work was supported by Grants from the Fonds de la Recherche Scientifique FRS-FNRS, the Foundation Saint-Luc and the Belgian National Foundation for Research in Pediatric Cardiology.

Compliance with ethical standards

Conflict of interest No potential conflicts of interest were disclosed.

Animal studies All institutional and national guidelines for the care and use of laboratory animals were followed and approved by the appropriate institutional committees. No human studies were carried out by the authors for this article.

References

1. Abdurrachim D, Ciapaite J, Wessels B, Nabben M, Luiken JJ, Nicolay K, Prompers JJ (2014) Cardiac diastolic dysfunction in high-fat diet fed mice is associated with lipotoxicity without impairment of cardiac energetics in vivo. Biochim Biophys Acta 1842:1525–1537. doi:10.1016/j.bbalip.2014.07.016
2. Abeykoon S, Sargent M, Wansapura JP (2012) Quantitative myocardial perfusion in mice based on the signal intensity of flow sensitized CMR. J Cardiovasc Magn Reson 14:73. doi:10.1186/1532-429X-14-73
3. Aguor EN, Arslan F, van de Kolk CW, Nederhoff MG, Doevendans PA, van Echteld CJ, Pasterkamp G, Strijkers GJ (2012) Quantitative T2* assessment of acute and chronic myocardial ischemia/reperfusion injury in mice. MAGMA 25:369–379. doi:10.1007/s10334-012-0304-0
4. Akki A, Gupta A, Weiss RG (2013) Magnetic resonance imaging and spectroscopy of the murine cardiovascular system. Am J Physiol Heart Circ Physiol 304:H633–H648. doi:10.1152/ajpheart.00771.2011
5. Aletras AH, Ding S, Balaban RS, Wen H (1999) DENSE: displacement encoding with stimulated echoes in cardiac functional MRI. J Magn Reson 137:247–252. doi:10.1006/jmre.1998.1676
6. Alsaid H, Sabbah M, Bendahmane Z, Fokapu O, Felblinger J, Desbleds-Mansard C, Corot C, Briguet A, Cremillieux Y, Canet-Soulas E (2007) High-resolution contrast-enhanced MRI of atherosclerosis with digital cardiac and respiratory gating in mice. Magn Reson Med 58:1157–1163. doi:10.1002/mrm.21308
7. Amundsen BH, Ericsson M, Seland JG, Pavlin T, Ellingsen O, Brekken C (2011) A comparison of retrospectively self-gated magnetic resonance imaging and high-frequency echocardiography for characterization of left ventricular function in mice. Lab Anim 45:31–37. doi:10.1258/la.2010.010094
8. Andrews M, Giger ML, Roman BB (2015) Manganese-enhanced MRI detection of impaired calcium regulation in a mouse model of cardiac hypertrophy. NMR Biomed 28:255–263. doi:10.1002/nbm.3249
9. Antkowiak P, Janiczek R, Gibberman L, Xu C, Kramer C, Meyer C, French B, Epstein F (2010) Quantitative first-pass perfusion MRI of the mouse heart. J Cardiovasc Magn Reson 12:M10
10. Ardenkjaer-Larsen JH, Fridlund B, Gram A, Hansson G, Hansson L, Lerche MH, Servin R, Thaning M, Golman K (2003) Increase in signal-to-noise ratio of >10,000 times in liquid-state NMR. Proc Natl Acad Sci USA 100:10158–10163. doi:10.1073/pnas.1733835100
11. Axel L, Dougherty L (1989) MR imaging of motion with spatial modulation of magnetization. Radiology 171:841–845. doi:10.1148/radiology.171.3.2717762
12. Azam S, Desjardins CL, Schluchter M, Liner A, Stelzer JE, Yu X, Hoit BD (2012) Comparison of velocity vector imaging echocardiography with magnetic resonance imaging in mouse models of cardiomyopathy. Circ Cardiovasc Imaging 5:776–781. doi:10.1161/CIRCIMAGING.111.972406
13. Bakermans AJ, Abdurrachim D, Geraedts TR, Houten SM, Nicolay K, Prompers JJ (2015) In vivo proton T1 relaxation times of mouse myocardial metabolites at 9.4 T. Magn Reson Med 73:2069–2074. doi:10.1002/mrm.25340
14. Bakermans AJ, Abdurrachim D, Moonen RP, Motaal AG, Prompers JJ, Strijkers GJ, Vandoorne K, Nicolay K (2015) Small animal cardiovascular MR imaging and spectroscopy. Prog Nucl Magn Reson Spectrosc 88–89:1–47. doi:10.1016/j.pnmrs.2015.03.001
15. Bakermans AJ, Abdurrachim D, van Nierop BJ, Koeman A, van der Kroon I, Baartscheer A, Schumacher CA, Strijkers GJ, Houten SM, Zuurbier CJ, Nicolay K, Prompers JJ (2015) In vivo mouse myocardial P MRS using three-dimensional image-selected in vivo spectroscopy (3D ISIS): technical considerations and biochemical validations. NMR Biomed. doi:10.1002/nbm.3371
16. Bakermans AJ, Dodd MS, Nicolay K, Prompers JJ, Tyler DJ, Houten SM (2013) Myocardial energy shortage and unmet anaplerotic needs in the fasted long-chain acyl-CoA dehydrogenase knockout mouse. Cardiovasc Res 100:441–449. doi:10.1093/cvr/cvt212
17. Bakermans AJ, Geraedts TR, van Weeghel M, Denis S, Joao Ferraz M, Aerts JM, Aten J, Nicolay K, Houten SM, Prompers JJ (2011) Fasting-induced myocardial lipid accumulation in long-chain acyl-CoA dehydrogenase knockout mice is accompanied by impaired left ventricular function. Circ Cardiovasc Imaging 4:558–565. doi:10.1161/CIRCIMAGING.111.963751
18. Bakermans AJ, van Weeghel M, Denis S, Nicolay K, Prompers JJ, Houten SM (2013) Carnitine supplementation attenuates myocardial lipid accumulation in long-chain acyl-CoA dehydrogenase knockout mice. J Inherit Metab Dis 36:973–981. doi:10.1007/s10545-013-9604-4
19. Baltes C, Bosshard S, Mueggler T, Ratering D, Rudin M (2011) Increased blood oxygen level-dependent (BOLD) sensitivity in the mouse somatosensory cortex during electrical forepaw stimulation using a cryogenic radiofrequency probe. NMR Biomed 24:439–446. doi:10.1002/nbm.1613
20. Bauer WR, Hiller KH, Galuppo P, Neubauer S, Kopke J, Haase A, Waller C, Ertl G (2001) Fast high-resolution magnetic resonance imaging demonstrates fractality of myocardial perfusion in microscopic dimensions. Circ Res 88:340–346
21. Bauer WR, Roder F, Hiller KH, Han H, Frohlich S, Rommel E, Haase A, Ertl G (1997) The effect of perfusion on T1 after slice-selective spin inversion in the isolated cardioplegic rat heart: measurement of a lower bound of intracapillary-extravascular water proton exchange rate. Magn Reson Med 38:917–923
22. Beyers RJ, Smith RS, Xu Y, Piras BA, Salerno M, Berr SS, Meyer CH, Kramer CM, French BA, Epstein FH (2012) T(2)-weighted MRI of post-infarct myocardial edema in mice. Magn Reson Med 67:201–209. doi:10.1002/mrm.22975
23. Blain A, Greally E, Laval S, Blamire A, Straub V, MacGowan GA (2013) Beta-blockers, left and right ventricular function, and in vivo calcium influx in muscular dystrophy cardiomyopathy. PLoS One 8:e57260. doi:10.1371/journal.pone.0057260
24. Bohl S, Lygate CA, Barnes H, Medway D, Stork LA, Schulz-Menger J, Neubauer S, Schneider JE (2009) Advanced methods for quantification of infarct size in mice using three-dimensional high-field late gadolinium enhancement MRI. Am J Physiol Heart Circ Physiol 296:H1200–H1208. doi:10.1152/ajpheart.01294.2008
25. Bonner F, Jacoby C, Temme S, Borg N, Ding Z, Schrader J, Flogel U (2014) Multifunctional MR monitoring of the healing process after myocardial infarction. Basic Res Cardiol 109:430. doi:10.1007/s00395-014-0430-0
26. Bull E, Madani SY, Sheth R, Seifalian A, Green M, Seifalian AM (2014) Stem cell tracking using iron oxide nanoparticles. Int J Nanomedicine 9:1641–1653. doi:10.2147/IJN.S48979
27. Bulluck H, Maestrini V, Rosmini S, Abdel-Gadir A, Treibel TA, Castelletti S, Bucciarelli-Ducci C, Manisty C, Moon JC (2015) Myocardial T1 mapping. Circ J 79:487–494. doi:10.1253/circj.CJ-15-0054
28. Bun SS, Kober F, Jacquier A, Espinosa L, Kalifa J, Bonzi MF, Kopp F, Lalevee N, Zaffran S, Deharo JC, Cozzone PJ, Bernard M (2012) Value of in vivo T2 measurement for myocardial

fibrosis assessment in diabetic mice at 11.75 T. Invest Radiol 47:319–323. doi:10.1097/RLI.0b013e318243e062
29. Bunck AC, Engelen MA, Schnackenburg B, Furkert J, Bremer C, Heindel W, Stypmann J, Maintz D (2009) Feasibility of functional cardiac MR imaging in mice using a clinical 3 Tesla whole body scanner. Invest Radiol 44:749–756. doi:10.1097/RLI.0b013e3181b2c135
30. Buonincontri G, Hu C-H, Sawiak S, Krieg T (2014) P516Diastolic dysfunction in diabetic mice revealed by MRI. Cardiovasc Res 103 (Suppl 1):S94–S95
31. Buscher K, Judenhofer MS, Kuhlmann MT, Hermann S, Wehrl HF, Schafers KP, Schafers M, Pichler BJ, Stegger L (2010) Isochronous assessment of cardiac metabolism and function in mice using hybrid PET/MRI. J Nucl Med 51:1277–1284. doi:10.2967/jnumed.110.076448
32. Campbell-Washburn AE, Price AN, Wells JA, Thomas DL, Ordidge RJ, Lythgoe MF (2013) Cardiac arterial spin labeling using segmented ECG-gated look-locker FAIR: variability and repeatability in preclinical studies. Magn Reson Med 69:238–247. doi:10.1002/mrm.24243
33. Cassidy PJ, Schneider JE, Grieve SM, Lygate C, Neubauer S, Clarke K (2004) Assessment of motion gating strategies for mouse magnetic resonance at high magnetic fields. J Magn Reson Imaging 19:229–237. doi:10.1002/jmri.10454
34. Chacko VP, Aresta F, Chacko SM, Weiss RG (2000) MRI/MRS assessment of in vivo murine cardiac metabolism, morphology, and function at physiological heart rates. Am J Physiol Heart Circ Physiol 279:H2218–H2224
35. Chapon C, Herlihy AH, Bhakoo KK (2008) Assessment of myocardial infarction in mice by late gadolinium enhancement MR imaging using an inversion recovery pulse sequence at 9.4 T. J Cardiovasc Magn Reson 10:6. doi:10.1186/1532-429X-10-6
36. Chen J, Jia ZY, Ma ZL, Wang YY, Teng GJ (2011) In vivo serial MR imaging of magnetically labeled endothelial progenitor cells homing to the endothelium injured artery in mice. PLoS One 6:e20790. doi:10.1371/journal.pone.0020790
37. Chuang JS, Zemljic-Harpf A, Ross RS, Frank LR, McCulloch AD, Omens JH (2010) Determination of three-dimensional ventricular strain distributions in gene-targeted mice using tagged MRI. Magn Reson Med 64:1281–1288. doi:10.1002/mrm.22547
38. Cochet H, Montaudon M, Laurent F, Calmettes G, Franconi JM, Miraux S, Thiaudiere E, Parzy E (2010) In vivo MR angiography and velocity measurement in mice coronary arteries at 9.4 T: assessment of coronary flow velocity reserve. Radiology 254:441–448. doi:10.1148/radiol.2542090735
39. Coolen BF, Geelen T, Paulis LE, Nauerth A, Nicolay K, Strijkers GJ (2011) Three-dimensional T1 mapping of the mouse heart using variable flip angle steady-state MR imaging. NMR Biomed 24:154–162. doi:10.1002/nbm.1566
40. Coolen BF, Moonen RP, Paulis LE, Geelen T, Nicolay K, Strijkers GJ (2010) Mouse myocardial first-pass perfusion MR imaging. Magn Reson Med 64:1658–1663. doi:10.1002/mrm.22588
41. Coolen BF, Simonis FF, Geelen T, Moonen RP, Arslan F, Paulis LE, Nicolay K, Strijkers GJ (2014) Quantitative T2 mapping of the mouse heart by segmented MLEV phase-cycled T2 preparation. Magn Reson Med 72:409–417. doi:10.1002/mrm.24952
42. Cui W, Jang A, Zhang P, Thompson B, Townsend D, Metzger JM, Zhang J (2015) Early detection of myocardial bioenergetic deficits: a 9.4 Tesla complete non invasive 31P MR spectroscopy study in mice with muscular dystrophy. PLoS One 10:e0135000. doi:10.1371/journal.pone.0135000
43. Dall'Armellina E, Jung BA, Lygate CA, Neubauer S, Markl M, Schneider JE (2012) Improved method for quantification of regional cardiac function in mice using phase-contrast MRI. Magn Reson Med 67:541–551. doi:10.1002/mrm.23022
44. de Kemp RA, Epstein FH, Catana C, Tsui BM, Ritman EL (2010) Small-animal molecular imaging methods. J Nucl Med 51(Suppl 1):18S–32S. doi:10.2967/jnumed.109.068148
45. Dodd MS, Ball V, Bray R, Ashrafian H, Watkins H, Clarke K, Tyler DJ (2013) In vivo mouse cardiac hyperpolarized magnetic resonance spectroscopy. J Cardiovasc Magn Reson 15:19. doi:10.1186/1532-429X-15-19
46. Doty FD, Entzminger G, Kulkarni J, Pamarthy K, Staab JP (2007) Radio frequency coil technology for small-animal MRI. NMR Biomed 20:304–325. doi:10.1002/nbm.1149
47. Drelicharz L, Wozniak M, Skorka T, Tyrankiewicz U, Heinze-Paluchowska S, Jablonska M, Gebska A, Chlopicki S (2009) Application of magnetic resonance imaging in vivo for the assessment of the progression of systolic and diastolic dysfunction in a mouse model of dilated cardiomyopathy. Kardiol Pol 67:386–395
48. Epstein FH (2007) MR in mouse models of cardiac disease. NMR Biomed 20:238–255. doi:10.1002/nbm.1152
49. Ferreira VM, Piechnik SK, Robson MD, Neubauer S, Karamitsos TD (2014) Myocardial tissue characterization by magnetic resonance imaging: novel applications of T1 and T2 mapping. J Thorac Imaging 29:147–154. doi:10.1097/RTI.0000000000000077
50. Flogel U, Ding Z, Hardung H, Jander S, Reichmann G, Jacoby C, Schubert R, Schrader J (2008) In vivo monitoring of inflammation after cardiac and cerebral ischemia by fluorine magnetic resonance imaging. Circulation 118:140–148. doi:10.1161/CIRCULATIONAHA.107.737890
51. Flogel U, Jacoby C, Godecke A, Schrader J (2007) In vivo 2D mapping of impaired murine cardiac energetics in NO-induced heart failure. Magn Reson Med 57:50–58. doi:10.1002/mrm.21101
52. Gilliam AD, Epstein FH, Acton ST (2009) Cardiac motion recovery via active trajectory field models. IEEE Trans Inf Technol Biomed 13:226–235. doi:10.1109/TITB.2008.2009221
53. Gilson WD, Kraitchman DL (2007) Cardiac magnetic resonance imaging in small rodents using clinical 1.5 T and 3.0 T scanners. Methods 43:35–45. doi:10.1016/j.ymeth.2007.03.012
54. Gnyawali SC, Roy S, McCoy M, Biswas S, Sen CK (2009) Remodeling of the ischemia-reperfused murine heart: 11.7-T cardiac magnetic resonance imaging of contrast-enhanced infarct patches and transmurality. Antioxid Redox Signal 11:1829–1839. doi:10.1089/ARS.2009.2635
55. Gutjahr FT, Kampf T, Winter P, Meyer CB, Williams T, Jakob PM, Bauer WR, Ziener CH, Helluy X (2014) Quantification of perfusion in murine myocardium: a retrospectively triggered T-based ASL method using model-based reconstruction. Magn Reson Med. doi:10.1002/mrm.25526
56. Hankiewicz JH, Banke NH, Farjah M, Lewandowski ED (2010) Early impairment of transmural principal strains in the left ventricular wall after short-term, high-fat feeding of mice predisposed to cardiac steatosis. Circ Cardiovasc Imaging 3:710–717. doi:10.1161/CIRCIMAGING.110.959098
57. Hankiewicz JH, Goldspink PH, Buttrick PM, Lewandowski ED (2008) Principal strain changes precede ventricular wall thinning during transition to heart failure in a mouse model of dilated cardiomyopathy. Am J Physiol Heart Circ Physiol 294:H330–H336. doi:10.1152/ajpheart.01109.2007
58. Hankiewicz JH, Lewandowski ED (2007) Improved cardiac tagging resolution at ultra-high magnetic field elucidates transmural differences in principal strain in the mouse heart and reduced stretch in dilated cardiomyopathy. J Cardiovasc Magn Reson 9:883–890. doi:10.1080/10976640701693683
59. Heijman E, Aben JP, Penners C, Niessen P, Guillaume R, van Eys G, Nicolay K, Strijkers GJ (2008) Evaluation of manual and

automatic segmentation of the mouse heart from CINE MR images. J Magn Reson Imaging 27:86–93. doi:10.1002/jmri.21236
60. Herold V, Morchel P, Faber C, Rommel E, Haase A, Jakob PM (2006) In vivo quantitative three-dimensional motion mapping of the murine myocardium with PC-MRI at 17.6 T. Magn Reson Med 55:1058–1064. doi:10.1002/mrm.20866
61. Herold V, Parczyk M, Morchel P, Ziener CH, Klug G, Bauer WR, Rommel E, Jakob PM (2009) In vivo measurement of local aortic pulse-wave velocity in mice with MR microscopy at 17.6 Tesla. Magn Reson Med 61:1293–1299. doi:10.1002/mrm.21957
62. Herrmann KH, Schmidt S, Kretz A, Haenold R, Krumbein I, Metzler M, Gaser C, Witte OW, Reichenbach JR (2012) Possibilities and limitations for high resolution small animal MRI on a clinical whole-body 3 T scanner. MAGMA 25:233–244. doi:10.1007/s10334-011-0284-5
63. Hiba B, Richard N, Janier M, Croisille P (2006) Cardiac and respiratory double self-gated cine MRI in the mouse at 7 T. Magn Reson Med 55:506–513. doi:10.1002/mrm.20815
64. Hiba B, Richard N, Thibault H, Janier M (2007) Cardiac and respiratory self-gated cine MRI in the mouse: comparison between radial and rectilinear techniques at 7 T. Magn Reson Med 58:745–753. doi:10.1002/mrm.21355
65. Hoerr V, Nagelmann N, Nauerth A, Kuhlmann MT, Stypmann J, Faber C (2013) Cardiac-respiratory self-gated cine ultra-short echo time (UTE) cardiovascular magnetic resonance for assessment of functional cardiac parameters at high magnetic fields. J Cardiovasc Magn Reson 15:59. doi:10.1186/1532-429X-15-59
66. Howles GP, Ghaghada KB, Qi Y, Mukundan S Jr, Johnson GA (2009) High-resolution magnetic resonance angiography in the mouse using a nanoparticle blood-pool contrast agent. Magn Reson Med 62:1447–1456. doi:10.1002/mrm.22154
67. Hu TC, Bao W, Lenhard SC, Schaeffer TR, Yue TL, Willette RN, Jucker BM (2004) Simultaneous assessment of left-ventricular infarction size, function and tissue viability in a murine model of myocardial infarction by cardiac manganese-enhanced magnetic resonance imaging (MEMRI). NMR Biomed 17:620–626. doi:10.1002/nbm.933
68. Hu TC, Pautler RG, MacGowan GA, Koretsky AP (2001) Manganese-enhanced MRI of mouse heart during changes in inotropy. Magn Reson Med 46:884–890
69. Huby AC, Mendsaikhan U, Takagi K, Martherus R, Wansapura J, Gong N, Osinska H, James JF, Kramer K, Saito K, Robbins J, Khuchua Z, Towbin JA, Purevjav E (2014) Disturbance in Z-disk mechanosensitive proteins induced by a persistent mutant myopalladin causes familial restrictive cardiomyopathy. J Am Coll Cardiol 64:2765–2776. doi:10.1016/j.jacc.2014.09.071
70. Jacoby C, Borg N, Heusch P, Sauter M, Bonner F, Kandolf R, Klingel K, Schrader J, Flogel U (2014) Visualization of immune cell infiltration in experimental viral myocarditis by (19)F MRI in vivo. MAGMA 27:101–106. doi:10.1007/s10334-013-0391-6
71. Jacoby C, Boring YC, Beck A, Zernecke A, Aurich V, Weber C, Schrader J, Flogel U (2008) Dynamic changes in murine vessel geometry assessed by high-resolution magnetic resonance angiography: a 9.4 T study. J Magn Reson Imaging 28:637–645. doi:10.1002/jmri.21482
72. Jahnke C, Nagel E, Gebker R, Kokocinski T, Kelle S, Manka R, Fleck E, Paetsch I (2007) Prognostic value of cardiac magnetic resonance stress tests: adenosine stress perfusion and dobutamine stress wall motion imaging. Circulation 115:1769–1776. doi:10.1161/CIRCULATIONAHA.106.652016
73. Janiczek RL, Blackman BR, Roy RJ, Meyer CH, Acton ST, Epstein FH (2011) Three-dimensional phase contrast angiography of the mouse aortic arch using spiral MRI. Magn Reson Med 66:1382–1390. doi:10.1002/mrm.22937
74. Janssen BJ, De Celle T, Debets JJ, Brouns AE, Callahan MF, Smith TL (2004) Effects of anesthetics on systemic hemodynamics in mice. Am J Physiol Heart Circ Physiol 287:H1618–H1624. doi:10.1152/ajpheart.01192.2003
75. Janssen PM, Murray JD, Schill KE, Rastogi N, Schultz EJ, Tran T, Raman SV, Rafael-Fortney JA (2014) Prednisolone attenuates improvement of cardiac and skeletal contractile function and histopathology by lisinopril and spironolactone in the mdx mouse model of Duchenne muscular dystrophy. PLoS One 9:e88360. doi:10.1371/journal.pone.0088360
76. Jerosch-Herold M, Wilke N, Stillman AE (1998) Magnetic resonance quantification of the myocardial perfusion reserve with a Fermi function model for constrained deconvolution. Med Phys 25:73–84
77. Jiang K, Li W, Li W, Jiao S, Castel L, Van Wagoner DR, Yu X (2014) Rapid multislice T mapping of mouse myocardium: application to quantification of manganese uptake in alpha-Dystrobrevin knockout mice. Magn Reson Med. doi:10.1002/mrm.25533
78. Jilkina O, Xiang B, Kuzio B, Rendell J, Kupriyanov VV (2005) Potassium transport in Langendorff-perfused mouse hearts assessed by 87Rb NMR spectroscopy. Magn Reson Med 53:1172–1176. doi:10.1002/mrm.20450
79. Jung B, Odening KE, Dall'Armellina E, Foll D, Menza M, Markl M, Schneider JE (2012) A quantitative comparison of regional myocardial motion in mice, rabbits and humans using in vivo phase contrast CMR. J Cardiovasc Magn Reson 14:87. doi:10.1186/1532-429X-14-87
80. Kampf T, Helluy X, Gutjahr FT, Winter P, Meyer CB, Jakob PM, Bauer WR, Ziener CH (2014) Myocardial perfusion quantification using the T1 -based FAIR-ASL method: the influence of heart anatomy, cardiopulmonary blood flow and look-locker readout. Magn Reson Med 71:1784–1797. doi:10.1002/mrm.24843
81. Kim RJ, Lima JA, Chen EL, Reeder SB, Klocke FJ, Zerhouni EA, Judd RM (1997) Fast 23Na magnetic resonance imaging of acute reperfused myocardial infarction. Potential to assess myocardial viability. Circulation 95:1877–1885
82. Klink A, Heynens J, Herranz B, Lobatto ME, Arias T, Sanders HM, Strijkers GJ, Merkx M, Nicolay K, Fuster V, Tedgui A, Mallat Z, Mulder WJ, Fayad ZA (2011) In vivo characterization of a new abdominal aortic aneurysm mouse model with conventional and molecular magnetic resonance imaging. J Am Coll Cardiol 58:2522–2530. doi:10.1016/j.jacc.2011.09.017
83. Klink A, Hyafil F, Rudd J, Faries P, Fuster V, Mallat Z, Meilhac O, Mulder WJ, Michel JB, Ramirez F, Storm G, Thompson R, Turnbull IC, Egido J, Martin-Ventura JL, Zaragoza C, Letourneur D, Fayad ZA (2011) Diagnostic and therapeutic strategies for small abdominal aortic aneurysms. Nat Rev Cardiol 8:338–347. doi:10.1038/nrcardio.2011.1
84. Kohler S, Hiller KH, Griswold M, Bauer WR, Haase A, Jakob PM (2003) NMR-microscopy with TrueFISP at 11.75 T. J Magn Reson 161:252–257
85. Lairez O, Lonjaret L, Ruiz S, Marchal P, Franchitto N, Calise D, Fourcade O, Mialet-Perez J, Parini A, Minville V (2013) Anesthetic regimen for cardiac function evaluation by echocardiography in mice: comparison between ketamine, etomidate and isoflurane versus conscious state. Lab Anim 47:284–290. doi:10.1177/0023677213496236
86. Lefrancois W, Thiaudiere E, Ben Hassen W, Sanchez S, Franconi JM, Miraux S (2011) Fast whole-body magnetic resonance angiography in mice. Magn Reson Med 66:32–39. doi:10.1002/mrm.22985

87. Li W, Griswold M, Yu X (2012) Fast cardiac T1 mapping in mice using a model-based compressed sensing method. Magn Reson Med 68:1127–1134. doi:10.1002/mrm.23323
88. Li W, Griswold M, Yu X (2010) Rapid T1 mapping of mouse myocardium with saturation recovery look-locker method. Magn Reson Med 64:1296–1303. doi:10.1002/mrm.22544
89. Li W, Liu W, Zhong J, Yu X (2009) Early manifestation of alteration in cardiac function in dystrophin deficient mdx mouse using 3D CMR tagging. J Cardiovasc Magn Reson 11:40. doi:10.1186/1532-429X-11-40
90. Li W, Yu X (2010) Quantification of myocardial strain at early systole in mouse heart: restoration of undeformed tagging grid with single-point HARP. J Magn Reson Imaging 32:608–614. doi:10.1002/jmri.22256
91. Liu G, Song X, Chan KW, McMahon MT (2013) Nuts and bolts of chemical exchange saturation transfer MRI. NMR Biomed 26:810–828. doi:10.1002/nbm.2899
92. Look DC, Locker DR (1970) Time saving in measurement of NMR and EPR relaxation times. Rev Sci Instrum 41:250–251. doi:10.1063/1.1684482
93. Lu M, Atthe B, Mateescu GD, Flask CA, Yu X (2012) Assessing mitochondrial respiration in isolated hearts using (17)O MRS. NMR Biomed 25:883–889. doi:10.1002/nbm.1807
94. Maguire ML, Geethanath S, Lygate CA, Kodibagkar VD, Schneider JE (2015) Compressed sensing to accelerate magnetic resonance spectroscopic imaging: evaluation and application to 23Na-imaging of mouse hearts. J Cardiovasc Magn Reson 17:45. doi:10.1186/s12968-015-0149-6
95. Majmudar MD, Yoo J, Keliher EJ, Truelove JJ, Iwamoto Y, Sena B, Dutta P, Borodovsky A, Fitzgerald K, Di Carli MF, Libby P, Anderson DG, Swirski FK, Weissleder R, Nahrendorf M (2013) Polymeric nanoparticle PET/MR imaging allows macrophage detection in atherosclerotic plaques. Circ Res 112:755–761. doi:10.1161/CIRCRESAHA.111.300576
96. Mani V, Adler E, Briley-Saebo KC, Bystrup A, Fuster V, Keller G, Fayad ZA (2008) Serial in vivo positive contrast MRI of iron oxide-labeled embryonic stem cell-derived cardiac precursor cells in a mouse model of myocardial infarction. Magn Reson Med 60:73–81. doi:10.1002/mrm.21642
97. Maramraju SH, Smith SD, Junnarkar SS, Schulz D, Stoll S, Ravindranath B, Purschke ML, Rescia S, Southekal S, Pratte JF, Vaska P, Woody CL, Schlyer DJ (2011) Small animal simultaneous PET/MRI: initial experiences in a 9.4 T microMRI. Phys Med Biol 56:2459–2480. doi:10.1088/0031-9155/56/8/009
98. Messner NM, Zollner FG, Kalayciyan R, Schad LR (2014) Pre-clinical functional magnetic resonance imaging. Part II: the heart. Z Med Phys 24:307–322. doi:10.1016/j.zemedi.2014.06.008
99. Messroghli DR, Radjenovic A, Kozerke S, Higgins DM, Sivananthan MU, Ridgway JP (2004) Modified look-locker inversion recovery (MOLLI) for high-resolution T1 mapping of the heart. Magn Reson Med 52:141–146. doi:10.1002/mrm.20110
100. Moon JC, Messroghli DR, Kellman P, Piechnik SK, Robson MD, Ugander M, Gatehouse PD, Arai AE, Friedrich MG, Neubauer S, Schulz-Menger J, Schelbert EB, Society for Cardiovascular Magnetic Resonance I, Cardiovascular Magnetic Resonance Working Group of the European Society of C (2013) Myocardial T1 mapping and extracellular volume quantification: a Society for Cardiovascular Magnetic Resonance (SCMR) and CMR Working Group of the European Society of Cardiology consensus statement. J Cardiovasc Magn Reson 15:92. doi:10.1186/1532-429X-15-92
101. Moser E, Stahlberg F, Ladd ME, Trattnig S (2012) 7-T MR-from research to clinical applications? NMR Biomed 25:695–716. doi:10.1002/nbm.1794
102. Mosher TJ, Smith MB (1990) A DANTE tagging sequence for the evaluation of translational sample motion. Magn Reson Med 15:334–339
103. Motaal AG, Coolen BF, Abdurrachim D, Castro RM, Prompers JJ, Florack LM, Nicolay K, Strijkers GJ (2013) Accelerated high-frame-rate mouse heart cine-MRI using compressed sensing reconstruction. NMR Biomed 26:451–457. doi:10.1002/nbm.2883
104. Nahrendorf M, Hiller KH, Hu K, Ertl G, Haase A, Bauer WR (2003) Cardiac magnetic resonance imaging in small animal models of human heart failure. Med Image Anal 7:369–375
105. Nahrendorf M, Streif JU, Hiller KH, Hu K, Nordbeck P, Ritter O, Sosnovik D, Bauer L, Neubauer S, Jakob PM, Ertl G, Spindler M, Bauer WR (2006) Multimodal functional cardiac MRI in creatine kinase-deficient mice reveals subtle abnormalities in myocardial perfusion and mechanics. Am J Physiol Heart Circ Physiol 290:H2516–H2521. doi:10.1152/ajpheart.01038.2005
106. Naresh NK, Chen X, Roy RJ, Antkowiak PF, Annex BH, Epstein FH (2015) Accelerated dual-contrast first-pass perfusion MRI of the mouse heart: development and application to diet-induced obese mice. Magn Reson Med 73:1237–1245. doi:10.1002/mrm.25238
107. Naresh NK, Xu Y, Klibanov AL, Vandsburger MH, Meyer CH, Leor J, Kramer CM, French BA, Epstein FH (2012) Monocyte and/or macrophage infiltration of heart after myocardial infarction: MR imaging using T1-shortening liposomes. Radiology 264:428–435. doi:10.1148/radiol.12111863
108. Neubauer S (2007) The failing heart—an engine out of fuel. N Engl J Med 356:1140–1151. doi:10.1056/NEJMra063052
109. Neuberger T, Greiser A, Nahrendorf M, Jakob PM, Faber C, Webb AG (2004) 23Na microscopy of the mouse heart in vivo using density-weighted chemical shift imaging. MAGMA 17:196–200. doi:10.1007/s10334-004-0048-6
110. Nick H, Allegrini PR, Fozard L, Junker U, Rojkjaer L, Salie R, Niederkofler V, O'Reilly T (2009) Deferasirox reduces iron overload in a murine model of juvenile hemochromatosis. Exp Biol Med (Maywood) 234:492–503. doi:10.3181/0811-RM-337
111. Odintsov B, Chun JL, Mulligan JA, Berry SE (2011) 14.1 T whole body MRI for detection of mesoangioblast stem cells in a murine model of Duchenne muscular dystrophy. Magn Reson Med 66:1704–1714. doi:10.1002/mrm.22942
112. Ojha N, Roy S, Radtke J, Simonetti O, Gnyawali S, Zweier JL, Kuppusamy P, Sen CK (2008) Characterization of the structural and functional changes in the myocardium following focal ischemia-reperfusion injury. Am J Physiol Heart Circ Physiol 294:H2435–H2443. doi:10.1152/ajpheart.01190.2007
113. Okayama S, Nakano T, Uemura S, Fujimoto S, Somekawa S, Watanabe M, Nakajima T, Saito Y (2013) Evaluation of left ventricular diastolic function by fractional area change using cine cardiovascular magnetic resonance: a feasibility study. J Cardiovasc Magn Reson 15:87. doi:10.1186/1532-429X-15-87
114. Osman NF, Kerwin WS, McVeigh ER, Prince JL (1999) Cardiac motion tracking using CINE harmonic phase (HARP) magnetic resonance imaging. Magn Reson Med 42:1048–1060
115. Parzy E, Miraux S, Franconi JM, Thiaudiere E (2009) In vivo quantification of blood velocity in mouse carotid and pulmonary arteries by ECG-triggered 3D time-resolved magnetic resonance angiography. NMR Biomed 22:532–537. doi:10.1002/nbm.1365
116. Price AN, Cheung KK, Cleary JO, Campbell AE, Riegler J, Lythgoe MF (2010) Cardiovascular magnetic resonance imaging in experimental models. Open Cardiovasc Med J 4:278–292. doi:10.2174/1874192401004010278
117. Price AN, Cheung KK, Lim SY, Yellon DM, Hausenloy DJ, Lythgoe MF (2011) Rapid assessment of myocardial infarct size in rodents using multi-slice inversion recovery late gadolinium

enhancement CMR at 9.4 T. J Cardiovasc Magn Reson 13:44. doi:10.1186/1532-429X-13-44
118. Protti A, Sirker A, Shah AM, Botnar R (2010) Late gadolinium enhancement of acute myocardial infarction in mice at 7 T: cine-FLASH versus inversion recovery. J Magn Reson Imaging 32:878–886. doi:10.1002/jmri.22325
119. Rafael-Fortney JA, Chimanji NS, Schill KE, Martin CD, Murray JD, Ganguly R, Stangland JE, Tran T, Xu Y, Canan BD, Mays TA, Delfin DA, Janssen PM, Raman SV (2011) Early treatment with lisinopril and spironolactone preserves cardiac and skeletal muscle in Duchenne muscular dystrophy mice. Circulation 124:582–588. doi:10.1161/CIRCULATIONAHA.111.031716
120. Ruff J, Wiesmann F, Hiller KH, Voll S, von Kienlin M, Bauer WR, Rommel E, Neubauer S, Haase A (1998) Magnetic resonance microimaging for noninvasive quantification of myocardial function and mass in the mouse. Magn Reson Med 40:43–48
121. Salerno M, Kramer CM (2013) Advances in parametric mapping with CMR imaging. JACC Cardiovasc Imaging 6:806–822. doi:10.1016/j.jcmg.2013.05.005
122. Schmitter S, Wu X, Adriany G, Auerbach EJ, Ugurbil K, Moortele PF (2014) Cerebral TOF angiography at 7 T: impact of B1 (+) shimming with a 16-channel transceiver array. Magn Reson Med 71:966–977. doi:10.1002/mrm.24749
123. Schneider JE, Cassidy PJ, Lygate C, Tyler DJ, Wiesmann F, Grieve SM, Hulbert K, Clarke K, Neubauer S (2003) Fast, high-resolution in vivo cine magnetic resonance imaging in normal and failing mouse hearts on a vertical 11.7 T system. J Magn Reson Imaging 18:691–701. doi:10.1002/jmri.10411
124. Schneider JE, Lanz T, Barnes H, Stork LA, Bohl S, Lygate CA, Ordidge RJ, Neubauer S (2011) Accelerated cardiac magnetic resonance imaging in the mouse using an eight-channel array at 9.4 Tesla. Magn Reson Med 65:60–70. doi:10.1002/mrm.22605
125. Schneider JE, Tyler DJ, ten Hove M, Sang AE, Cassidy PJ, Fischer A, Wallis J, Sebag-Montefiore LM, Watkins H, Isbrandt D, Clarke K, Neubauer S (2004) In vivo cardiac 1H-MRS in the mouse. Magn Reson Med 52:1029–1035. doi:10.1002/mrm.20257
126. Shan K, Constantine G, Sivananthan M, Flamm SD (2004) Role of cardiac magnetic resonance imaging in the assessment of myocardial viability. Circulation 109:1328–1334. doi:10.1161/01.CIR.0000120294.67948.E3
127. Shao Y, Cherry SR, Farahani K, Meadors K, Siegel S, Silverman RW, Marsden PK (1997) Simultaneous PET and MR imaging. Phys Med Biol 42:1965–1970
128. Shea SM, Fieno DS, Schirf BE, Bi X, Huang J, Omary RA, Li D (2005) T2-prepared steady-state free precession blood oxygen level-dependent MR imaging of myocardial perfusion in a dog stenosis model. Radiology 236:503–509. doi:10.1148/radiol.2362040149
129. Skardal K, Rolim NP, Haraldseth O, Goa PE, Thuen M (2013) Late gadolinium enhancement in the assessment of the infarcted mouse heart: a longitudinal comparison with manganese-enhanced MRI. J Magn Reson Imaging 38:1388–1394. doi:10.1002/jmri.24127
130. Song R, Lin W, Chen Q, Asakura T, Wehrli FW, Song HK (2008) Relationships between MR transverse relaxation parameters R*(2), R(2) and R'(2) and hepatic iron content in thalassemic mice at 1.5 T and 3 T. NMR Biomed 21:574–580. doi:10.1002/nbm.1227
131. Song W, Dyer E, Stuckey D, Leung MC, Memo M, Mansfield C, Ferenczi M, Liu K, Redwood C, Nowak K, Harding S, Clarke K, Wells D, Marston S (2010) Investigation of a transgenic mouse model of familial dilated cardiomyopathy. J Mol Cell Cardiol 49:380–389. doi:10.1016/j.yjmcc.2010.05.009
132. Sosnovik DE, Dai G, Nahrendorf M, Rosen BR, Seethamraju R (2007) Cardiac MRI in mice at 9.4 Tesla with a transmit-receive surface coil and a cardiac-tailored intensity-correction algorithm. J Magn Reson Imaging 26:279–287. doi:10.1002/jmri.20966
133. Sosnovik DE, Nahrendorf M, Deliolanis N, Novikov M, Aikawa E, Josephson L, Rosenzweig A, Weissleder R, Ntziachristos V (2007) Fluorescence tomography and magnetic resonance imaging of myocardial macrophage infiltration in infarcted myocardium in vivo. Circulation 115:1384–1391. doi:10.1161/CIRCULATIONAHA.106.663351
134. Streif JU, Herold V, Szimtenings M, Lanz TE, Nahrendorf M, Wiesmann F, Rommel E, Haase A (2003) In vivo time-resolved quantitative motion mapping of the murine myocardium with phase contrast MRI. Magn Reson Med 49:315–321. doi:10.1002/mrm.10342
135. Streif JU, Nahrendorf M, Hiller KH, Waller C, Wiesmann F, Rommel E, Haase A, Bauer WR (2005) In vivo assessment of absolute perfusion and intracapillary blood volume in the murine myocardium by spin labeling magnetic resonance imaging. Magn Reson Med 53:584–592. doi:10.1002/mrm.20327
136. Stuckey DJ, Carr CA, Camelliti P, Tyler DJ, Davies KE, Clarke K (2012) In vivo MRI characterization of progressive cardiac dysfunction in the mdx mouse model of muscular dystrophy. PLoS One 7:e28569. doi:10.1371/journal.pone.0028569
137. Stuckey DJ, Carr CA, Tyler DJ, Clarke K (2008) Cine-MRI versus two-dimensional echocardiography to measure in vivo left ventricular function in rat heart. NMR Biomed 21:765–772. doi:10.1002/nbm.1268
138. Stuckey DJ, McSweeney SJ, Thin MZ, Habib J, Price AN, Fiedler LR, Gsell W, Prasad SK, Schneider MD (2014) T(1) mapping detects pharmacological retardation of diffuse cardiac fibrosis in mouse pressure-overload hypertrophy. Circ Cardiovasc Imaging 7:240–249. doi:10.1161/CIRCIMAGING.113.000993
139. Stypmann J (2007) Doppler ultrasound in mice. Echocardiography 24:97–112. doi:10.1111/j.1540-8175.2006.00358.x
140. Suever JD, Wehner GJ, Haggerty CM, Jing L, Hamlet SM, Binkley CM, Kramer SP, Mattingly AC, Powell DK, Bilchick KC, Epstein FH, Fornwalt BK (2014) Simplified post processing of cine DENSE cardiovascular magnetic resonance for quantification of cardiac mechanics. J Cardiovasc Magn Reson 16:94. doi:10.1186/s12968-014-0094-9
141. Tangney JR, Chuang JS, Janssen MS, Krishnamurthy A, Liao P, Hoshijima M, Wu X, Meininger GA, Muthuchamy M, Zemljic-Harpf A, Ross RS, Frank LR, McCulloch AD, Omens JH (2013) Novel role for vinculin in ventricular myocyte mechanics and dysfunction. Biophys J 104:1623–1633. doi:10.1016/j.bpj.2013.02.021
142. Temme S, Grapentin C, Quast C, Jacoby C, Grandoch M, Ding Z, Owenier C, Mayenfels F, Fischer JW, Schubert R, Schrader J, Flogel U (2015) Noninvasive imaging of early venous thrombosis by 19F magnetic resonance imaging with targeted perfluorocarbon nanoemulsions. Circulation 131:1405–1414. doi:10.1161/CIRCULATIONAHA.114.010962
143. ten Hove M, Lygate CA, Fischer A, Schneider JE, Sang AE, Hulbert K, Sebag-Montefiore L, Watkins H, Clarke K, Isbrandt D, Wallis J, Neubauer S (2005) Reduced inotropic reserve and increased susceptibility to cardiac ischemia/reperfusion injury in phosphocreatine-deficient guanidinoacetate-*N*-methyltransferase-knockout mice. Circulation 111:2477–2485. doi:10.1161/01.CIR.0000165147.99592.01
144. Troalen T, Capron T, Cozzone PJ, Bernard M, Kober F (2013) Cine-ASL: a steady-pulsed arterial spin labeling method for myocardial perfusion mapping in mice. Part I. Experimental study. Magn Reson Med 70:1389–1398. doi:10.1002/mrm.24565

145. Trotier AJ, Lefrancois W, Ribot EJ, Thiaudiere E, Franconi JM, Miraux S (2015) Time-resolved TOF MR angiography in mice using a prospective 3D radial double golden angle approach. Magn Reson Med 73:984–994. doi:10.1002/mrm.25201
146. Tucci S, Flogel U, Hermann S, Sturm M, Schafers M, Spiekerkoetter U (2014) Development and pathomechanisms of cardiomyopathy in very long-chain acyl-CoA dehydrogenase deficient (VLCAD(−/−)) mice. Biochim Biophys Acta 1842:677–685. doi:10.1016/j.bbadis.2014.02.001
147. Tyrankiewicz U, Skorka T, Jablonska M, Petkow-Dimitrow P, Chlopicki S (2013) Characterization of the cardiac response to a low and high dose of dobutamine in the mouse model of dilated cardiomyopathy by MRI in vivo. J Magn Reson Imaging 37:669–677. doi:10.1002/jmri.23854
148. Vallee JP, Ivancevic MK, Nguyen D, Morel DR, Jaconi M (2004) Current status of cardiac MRI in small animals. MAGMA 17:149–156. doi:10.1007/s10334-004-0066-4
149. van Bochove GS, Straathof R, Krams R, Nicolay K, Strijkers GJ (2010) MRI-determined carotid artery flow velocities and wall shear stress in a mouse model of vulnerable and stable atherosclerotic plaque. MAGMA 23:77–84. doi:10.1007/s10334-010-0200-4
150. van de Weijer T, van Ewijk PA, Zandbergen HR, Slenter JM, Kessels AG, Wildberger JE, Hesselink MK, Schrauwen P, Schrauwen-Hinderling VB, Kooi ME (2012) Geometrical models for cardiac MRI in rodents: comparison of quantification of left ventricular volumes and function by various geometrical models with a full-volume MRI data set in rodents. Am J Physiol Heart Circ Physiol 302:H709–H715. doi:10.1152/ajpheart.00710.2011
151. van Geuns RJ, Wielopolski PA, de Bruin HG, Rensing BJ, van Ooijen PM, Hulshoff M, Oudkerk M, de Feyter PJ (1999) Basic principles of magnetic resonance imaging. Prog Cardiovasc Dis 42:149–156
152. van Heeswijk RB, De Blois J, Kania G, Gonzales C, Blyszczuk P, Stuber M, Eriksson U, Schwitter J (2013) Selective in vivo visualization of immune-cell infiltration in a mouse model of autoimmune myocarditis by fluorine-19 cardiac magnetic resonance. Circ Cardiovasc Imaging 6:277–284. doi:10.1161/CIRCIMAGING.112.000125
153. van Heeswijk RB, Pellegrin M, Flogel U, Gonzales C, Aubert JF, Mazzolai L, Schwitter J, Stuber M (2015) Fluorine MR imaging of inflammation in atherosclerotic plaque in vivo. Radiology 275:421–429. doi:10.1148/radiol.14141371
154. van Nierop BJ, Coolen BF, Bax NA, Dijk WJ, van Deel ED, Duncker DJ, Nicolay K, Strijkers GJ (2014) Myocardial perfusion MRI shows impaired perfusion of the mouse hypertrophic left ventricle. Int J Cardiovasc Imaging 30:619–628. doi:10.1007/s10554-014-0369-0
155. van Nierop BJ, Coolen BF, Dijk WJ, Hendriks AD, de Graaf L, Nicolay K, Strijkers GJ (2013) Quantitative first-pass perfusion MRI of the mouse myocardium. Magn Reson Med 69:1735–1744. doi:10.1002/mrm.24424
156. van Oorschot JW, Gho JM, van Hout GP, Froeling M, Jansen Of Lorkeers SJ, Hoefer IE, Doevendans PA, Luijten PR, Chamuleau SA, Zwanenburg JJ (2015) Endogenous contrast MRI of cardiac fibrosis: beyond late gadolinium enhancement. J Magn Reson Imaging 41:1181–1189. doi:10.1002/jmri.24715
157. Vandenberghe S, Marsden PK (2015) PET-MRI: a review of challenges and solutions in the development of integrated multimodality imaging. Phys Med Biol 60:R115–R154. doi:10.1088/0031-9155/60/4/R115
158. Vandsburger M, Vandoorne K, Oren R, Leftin A, Mpofu S, Delli Castelli D, Aime S, Neeman M (2015) Cardio-chemical exchange saturation transfer magnetic resonance imaging reveals molecular signatures of endogenous fibrosis and exogenous contrast media. Circ Cardiovasc Imaging. doi:10.1161/CIRCIMAGING.114.002180
159. Vandsburger MH, Epstein FH (2011) Emerging MRI methods in translational cardiovascular research. J Cardiovasc Transl Res 4:477–492. doi:10.1007/s12265-011-9275-1
160. Vandsburger MH, French BA, Helm PA, Roy RJ, Kramer CM, Young AA, Epstein FH (2007) Multi-parameter in vivo cardiac magnetic resonance imaging demonstrates normal perfusion reserve despite severely attenuated beta-adrenergic functional response in neuronal nitric oxide synthase knockout mice. Eur Heart J 28:2792–2798. doi:10.1093/eurheartj/ehm241
161. Vandsburger MH, French BA, Kramer CM, Zhong X, Epstein FH (2012) Displacement-encoded and manganese-enhanced cardiac MRI reveal that nNOS, not eNOS, plays a dominant role in modulating contraction and calcium influx in the mammalian heart. Am J Physiol Heart Circ Physiol 302:H412–H419. doi:10.1152/ajpheart.00705.2011
162. Vandsburger MH, Janiczek RL, Xu Y, French BA, Meyer CH, Kramer CM, Epstein FH (2010) Improved arterial spin labeling after myocardial infarction in mice using cardiac and respiratory gated look-locker imaging with fuzzy C-means clustering. Magn Reson Med 63:648–657. doi:10.1002/mrm.22280
163. Vanhoutte L, Gallez B, Feron O, Balligand JL, Esfahani H, d'Hoore W, Moniotte S (2015) Variability of mouse left ventricular function assessment by 11.7 Tesla MRI. J Cardiovasc Transl Res. doi:10.1007/s12265-015-9638-0
164. Vlachopoulos C, Aznaouridis K, Stefanadis C (2010) Prediction of cardiovascular events and all-cause mortality with arterial stiffness: a systematic review and meta-analysis. J Am Coll Cardiol 55:1318–1327. doi:10.1016/j.jacc.2009.10.061
165. von Elverfeldt D, Maier A, Duerschmied D, Braig M, Witsch T, Wang X, Mauler M, Neudorfer I, Menza M, Idzko M, Zirlik A, Heidt T, Bronsert P, Bode C, Peter K, von Zur Muhlen C (2014) Dual-contrast molecular imaging allows noninvasive characterization of myocardial ischemia/reperfusion injury after coronary vessel occlusion in mice by magnetic resonance imaging. Circulation 130:676–687. doi:10.1161/CIRCULATIONAHA.113.008157
166. von Morze C, Xu D, Purcell DD, Hess CP, Mukherjee P, Saloner D, Kelley DA, Vigneron DB (2007) Intracranial time-of-flight MR angiography at 7 T with comparison to 3 T. J Magn Reson Imaging 26:900–904. doi:10.1002/jmri.21097
167. Wagenhaus B, Pohlmann A, Dieringer MA, Els A, Waiczies H, Waiczies S, Schulz-Menger J, Niendorf T (2012) Functional and morphological cardiac magnetic resonance imaging of mice using a cryogenic quadrature radiofrequency coil. PLoS One 7:e42383. doi:10.1371/journal.pone.0042383
168. Waghorn B, Edwards T, Yang Y, Chuang KH, Yanasak N, Hu TC (2008) Monitoring dynamic alterations in calcium homeostasis by T (1)-weighted and T (1)-mapping cardiac manganese-enhanced MRI in a murine myocardial infarction model. NMR Biomed 21:1102–1111. doi:10.1002/nbm.1287
169. Waghorn B, Yang Y, Baba A, Matsuda T, Schumacher A, Yanasak N, Hu TC (2009) Assessing manganese efflux using SEA0400 and cardiac T1-mapping manganese-enhanced MRI in a murine model. NMR Biomed 22:874–881. doi:10.1002/nbm.1414
170. Waller C, Kahler E, Hiller KH, Hu K, Nahrendorf M, Voll S, Haase A, Ertl G, Bauer WR (2000) Myocardial perfusion and intracapillary blood volume in rats at rest and with coronary dilatation: MR imaging in vivo with use of a spin-labeling technique. Radiology 215:189–197. doi:10.1148/radiology.215.1.r00ap07189
171. Wehrl HF, Judenhofer MS, Wiehr S, Pichler BJ (2009) Preclinical PET/MR: technological advances and new perspectives in biomedical research. Eur J Nucl Med Mol Imaging 36(Suppl 1):S56–S68. doi:10.1007/s00259-009-1078-0

172. Weissler B, Gebhardt P, Duppenbecker P, Wehner J, Schug D, Lerche C, Goldschmidt B, Salomon A, Verel I, Heijman E, Perkuhn M, Heberling D, Botnar R, Kiessling F, Schulz V (2015) A digital preclinical PET/MRI insert and initial results. IEEE Trans Med Imaging. doi:10.1109/TMI.2015.2427993
173. Wiesmann F, Neubauer S, Haase A, Hein L (2001) Can we use vertical bore magnetic resonance scanners for murine cardiovascular phenotype characterization? Influence of upright body position on left ventricular hemodynamics in mice. J Cardiovasc Magn Reson 3:311–315
174. Wiesmann F, Ruff J, Engelhardt S, Hein L, Dienesch C, Leupold A, Illinger R, Frydrychowicz A, Hiller KH, Rommel E, Haase A, Lohse MJ, Neubauer S (2001) Dobutamine-stress magnetic resonance microimaging in mice: acute changes of cardiac geometry and function in normal and failing murine hearts. Circ Res 88:563–569
175. Wiesmann F, Ruff J, Hiller KH, Rommel E, Haase A, Neubauer S (2000) Developmental changes of cardiac function and mass assessed with MRI in neonatal, juvenile, and adult mice. Am J Physiol Heart Circ Physiol 278:H652–H657
176. Zhao X, Pratt R, Wansapura J (2009) Quantification of aortic compliance in mice using radial phase contrast MRI. J Magn Reson Imaging 30:286–291. doi:10.1002/jmri.21846
177. Zhong J, Yu X (2010) Strain and torsion quantification in mouse hearts under dobutamine stimulation using 2D multiphase MR DENSE. Magn Reson Med 64:1315–1322. doi:10.1002/mrm.22530
178. Zhong X, Gibberman LB, Spottiswoode BS, Gilliam AD, Meyer CH, French BA, Epstein FH (2011) Comprehensive cardiovascular magnetic resonance of myocardial mechanics in mice using three-dimensional cine DENSE. J Cardiovasc Magn Reson 13:83. doi:10.1186/1532-429X-13-83

Chapter II – AIM OF THE THESIS

In this work, in light of available MR imaging technologies allowing novel investigations in experimental models, and knowing the remaining lack of knowledge in some pathophysiological processes involved in cardiovascular diseases, we examined the feasibility and accuracy of UHF MRI techniques for the characterization of murine models of cardiomyopathy.

After a preliminary – but essential – validation of basic MRI sequences in a well-known model of surgically-induced hypertrophic cardiomyopathy, we aimed to develop specific investigations on a model of ischaemic cardiomyopathy in a collaborative study.

Besides the work on these more conventional models, we also wanted to investigate an original model of cardiomyopathy induced by active immunization against the β1-adrenoreceptor, in wild-type mice and in transgenic mice overexpressing the β3-adrenoreceptor. Indeed, it is common knowledge that the adrenergic system may become maladaptative in the course of development of cardiac diseases, and the understanding of the underlying mechanisms is crucial for the development and refinement of heart failure therapies. Furthermore, description of autoimmunity processes involving beta-adrenergic receptors have recently led to new perspectives of screening and treatment.

Overall, our main goal throughout this Thesis was to refine the characterization of murine models of cardiomyopathies in order to better understand underlying pathophysiological processes and to identify potential new therapeutic targets.

Chapter III - MATERIALS AND METHODS

1. Ultra high field Cardiac MRI

1.1. Hardware

All MRI experiments were performed on an 11.7 T MRI system dedicated to small animal applications (Biospec, Bruker, Ettlingen, Germany). A quadrature 1H resonator was used for radiofrequency transmission (inner diameter=72 mm, length=6.6 cm) in conjunction with a surface receive-only coil array (length=10.7cm) (Figure 1).

The animals were anaesthetized in an induction chamber by exposure to isoflurane 3%. The isoflurane was then maintained between 0.5 to 3% during the entire procedure, in order to get a steady cardiac frequency around 500 beats/min. Mice were placed in prone position and monitored for electrocardiogram and respiration with neonatal electrodes wrapped around the paws and a pneumatic sensor placed under the animal. Examinations were performed in a temperature-controlled setting, with a rectal probe and a dedicated heating blanket.

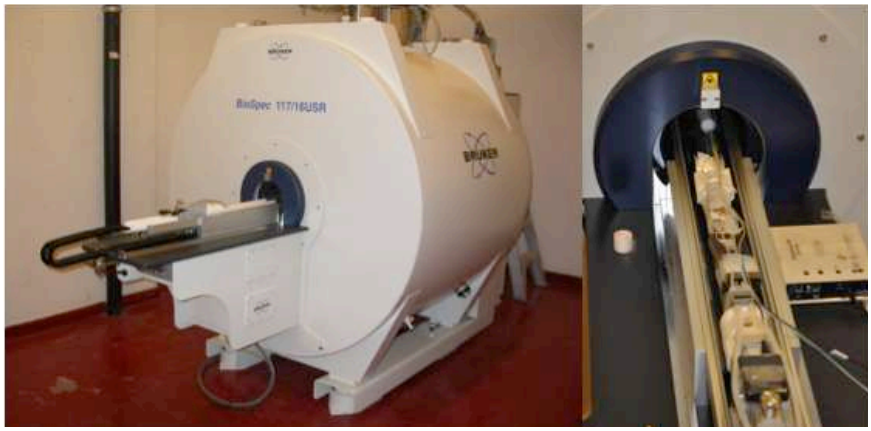

Figure 1. The 11.7T MRI machine dedicated to small animal applications (Biospec, Bruker, Ettlingen, Germany) and representative picture showing the small animal setup.

1.2. Imaging parameters

All sequences were acquired after preliminary tuning and matching of the quadrature transceiver coil.

1.2.1. Intragate FLASH cine sequence

First, a three-plane Intragate Fast Low Angle Shot sequence (TriPilot, Bruker) was performed for the definition of slice orientation, using the following parameters: repetition time/echo time = 6.2/1.55 ms, flip angle = 15°, field of view = 4.5x4.5 cm, matrix size=256×256, slice thickness = 1.0mm, number of repetitions = 10, acquisition time = 3 minutes per scan.

Then 7-8 contiguous short axis slices covering the entire mouse heart were obtained with Fast Low Angle Shots with navigator echo sequence (IntraGate, Bruker) using the following parameters: repetition time/echo time = 4.1/1.5 ms; flip angle= 25°; field of view= 3.0×3.0 cm; matrix size= 256×256; slice thickness = 1.25 mm; number of repetitions = 100; acquisition time around 9 minutes. Reconstruction with 10 phases per cardiac cycle was found to be the best trade-off for the acquisition of sufficient data while avoiding excessive postprocessing time, although more phases could have been preferred for the determination of systolic and diastolic indexes (see further). The total anesthesia time for the entire procedure was around 20 minutes.

1.2.2. Time of Flight imaging

For Time of Flight imaging, we used the Bruker FLASH-TOF-2D protocol with the following parameters: repetition time/echo time = 12/2.4 ms; flip angle= 80°; field of view = 3.0×3.0 cm; matrix size= 256x256x120; slice thickness= 0.4mm, number of averages =2, acquisition time around 7 minutes. We selected non-contiguous slices and a negative slice gap of -0.15mm in order to avoid a “beading” effect in the appearance of the angiogram. Signal originating from veins was suppressed by activating a flow saturation slice. Bruker “Duty Cycle” Macro was runned before sequence acquisition.

1.2.3. Phase contrast imaging

Datasets were acquired using Bruker "PhaseContrastAngiography" measuring method at the level of the ascending aorta with the following parameters: repetition time/echo time = 8.7/2.3ms; flip angle= 30°; field of view= 2.2cmx2.2cm; matrix size= 160x160; slice thickness= 1.0mm; spatial resolution= 0.138mm/pixel; Velocity encoding= 250cm/s, flow encoding: all directions; number of movie cycles= 20; acquisition time around 9 minutes. Magnitude images were integrated to acquired Phase images through RECO tool "output mapping: per object mapping".

1.2.4. Tagging

Tagged images were acquired in mid-ventricular short-axis view with the SPAMM tagging sequence applied immediately after the detection of the R-wave, followed by the acquisition of cine images that covered the whole cardiac cycle. Imaging parameters were: repetition time/echo time = 12/1.8 ms, field of view = 3.0×3.0 cm; matrix size= 192x192; slice thickness= 1.0 mm; tag distance= 0.3mm, tag thickness= 1.0mm. Acquisition time was about 8 minutes, depending mainly on the quality of ECG-gating.

1.2.5. Late Gadolinium Enhancement

10 minutes following intraperitoneal administration of 0.5mmol/kg of Gadolinium-DTPA, a Look-Locker inversion recovery sequence was used to acquire multiple inversion time images. Then a Fast Imaging with Steady State Precession (FISP) sequence was positioned in order to cover the area of infarction, using the following parameters: repetition time/echo time = 5.0/1.5 ms, flip angle = 30°, field of view = 3.0×3.0 cm, matrix size=192×192; slice thickness = 1.0 mm, number of averages= 6, acquisition time around 8 minutes. Inversion time was set 300 and 600ms according to previous Look-locker sequence and delay since IP injection.

1.3. Image analysis

Postprocessing of Intragate FLASH and Phase Contrast sequences was performed using the Paravision Software (v5.0 and 5.1, Bruker Biospin, Billerica, MA). We used the Segment software (Medviso®v1.8, Lund, Sweden) for classical ventricular systolic function assessment and semi-automated measurement of LV free wall and septum thickness, including measurements of the thickness of myocardial infarction zone. Osirix imaging Software (v4.0; Pixmeo; Geneva, Switzerland) was used for measurements of LV areas in the context of systolic and diastolic indexes assessment and for 3D reconstruction of time-of-flight angiograms.

1.3.1. Function

The LV systolic function was assessed from the stack of short-axis images by tracing epicardial and endocardial borders, including papillary muscles, on the Segment software (Medviso®v1.8, Lund, Sweden) (Figure 2). End-diastolic (EDV), end-systolic (ESV) and stroke volume (SV) were determined (µl) using modified Simpson rule as it has proven to be one of the most valuable method for calculating LV parameters (van de Weijer, van Ewijk et al. 2012). LV ejection fraction (EF, in %) and LV mass (mg) were subsequently deduced, knowing the specific density of myocardial tissue ($1.05 g/cm^3$)

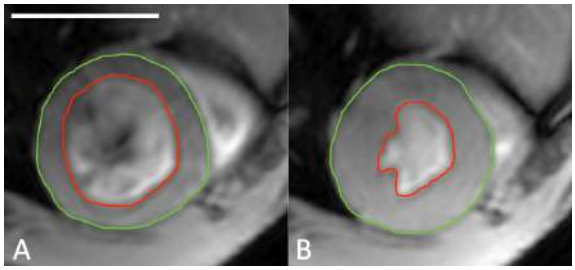

Figure 2. Representative end-diastolic (A) and end-systolic (B) short-axis images in mice, with left ventricular endocardial (red) and epicardial (green) outlines. Scale bar represents 500 µm.

1.3.2. Systolic and diastolic indexes

Systolic and diastolic indexes were determined as described previously (Okayama, Nakano et al. 2013, Buonincontri, Hu et al. 2014). Briefly, we visually determined the end-diastolic phase, end-systolic phase and the phase at 30% of diastole, and traced the endocardial contours at the mid-ventricular level on the Osirix imaging software (v4.0; Pixmeo; Geneva, Switzerland). Then we calculated the systolic fractional area change (systolic index, in %) through the following formula: EDA-ESA/EDA, where EDA= end-diastolic area and ESA= end-sytolic area. The fractional area change during the first 30% of diastole (diastolic index, in %) was also calculated through the following formula: dA-ESA/EDA-ESA, where dA= area at 30% of diastole (Figure 3).

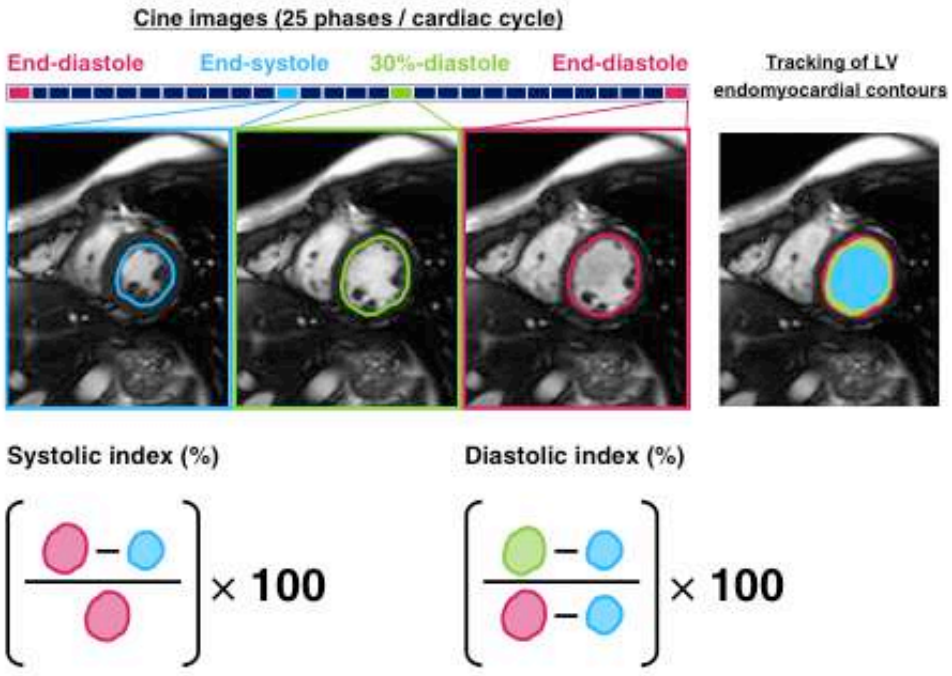

Figure 3. Evaluation of left ventricular systolic and diastolic function by fractional area change in cine CMR. End-diastolic and end-systolic phases are visually determined in datasets from short-axis cine images at mid-papillary muscle, and phase number during 30% of diastole is calculated by multiplying total phase number

during diastole by 0.3 and rounding up values. Left ventricular (LV) endocardial contours are then manually traced only on cine images of end-diastolic phase, end-systolic phase, and phase at 30% of diastole. The LV systolic fractional area change (systolic-index, in %) and fractional area change during the first 30% of diastole (diastolic-index, in %) are calculated. Reproduced from Okayama et al. (Okayama, Nakano et al. 2013).

1.3.3. LV wall measurements

A semi-automated technique was used for the determination of the ventricular thickness at the level of the free wall, the septum or in a zone of myocardial infarction. A zone covering the region of interest was determined using the "report per slice" tool from Segment Software (Medviso®v1.8, Lund, Sweden), and corresponding end-diastolic and end-systolic values obtained were exported in excel file.

1.3.4. Number of LV dyskinetic segments

All analyses were performed on a blinded basis using Segment imaging software (Medviso®v1.8, Lund, Sweden). The number of dyskinetic segments was visually evaluated on short axis cine sections, according to previously published standardized segmentation distinguishing 6 basal segments, 6 mid-cavity segments and 4 apical segments (Figure 4) (Cerqueira, Weissman et al. 2002). The 17th segment, corresponding to the apex, was not evaluated, as no cine images were acquired in 2- or 4-chamber view.

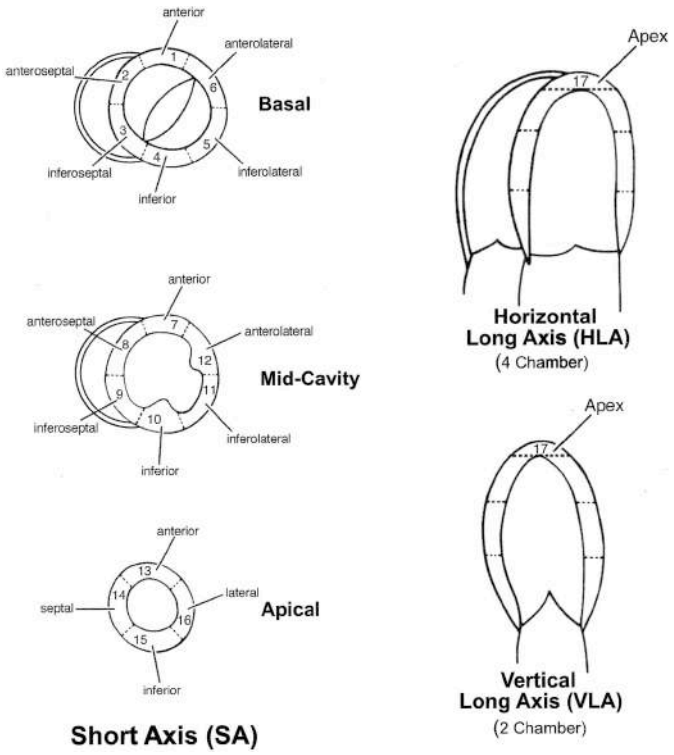

Figure 4. Diagram of vertical long-axis (VLA, approximating the 2-chamber view), horizontal long-axis (HLA, approximating the 4-chamber view), and short-axis (SA) planes showing the name, location, and anatomic landmarks for selection of the basal (tips of the mitral valve leaflets), mid-cavity (papillary muscles), and apical (beyond papillary muscles but before cavity ends) short-axis slices for the recommended 17-segment system. Reproduced from Cerqueira et al. (Cerqueira, Weissman et al. 2002).

2. Surgical procedure for transverse aortic constriction

Mice were anesthetized with an intraperitoneal- injection of a mixture of ketamine (150mg/kg) and xylazine (10mg/kg) and placed in supine position. Under stereoscope an incision was performed on the right side of the sternum, in order to avoid injury to the mammary artery. The thymus was pushed aside and a constrictive band was placed and tightened around the aorta and a 27-G blunted needle, which was then removed (Figure 5). The ligature was not tightened in sham-operated mice. Chest was closed with a polypropylene suture.

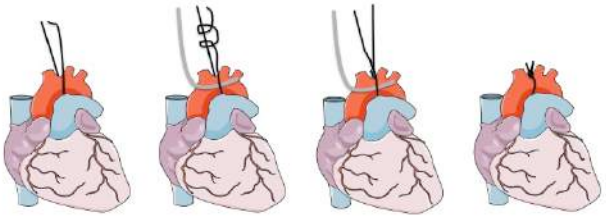

Figure 5. Transverse aortic constriction procedure.

3. Surgical procedure for myocardial infarction

Animal were anaesthetized with isoflurane inhalation through endotracheal intubation. Body temperature was controlled during the entire procedure. After left-sided thoracotomy at the fourth intercostal space, the left anterior descending coronary artery (LAD) was ligated with 6-0 silk thread. Infarction was confirmed by visual ventricular blanching. Sham mice were submitted to the same procedure except that no ligation was undertaken.

4. Treatment protocol for the mouse model of dilated cardiomyopathy

All animal experimental procedures were approved by the Animal Research Committee (Approval ID: 2012/UCL/MD/004) and performed in agreement with institutional guidelines. Mice were housed under standard conditions with ad libitum access to water and chow.

4.1. β1-immunization in C57BL/6J mice

8-weeks C57BL/6J male mice (Janvier, Paris, France) were monthly immunized with 200µg of a synthetic peptide (Eurogentec, Seraing, Belgium) corresponding to the human and mouse β1AR-ECII (residues 197-222: H-W-W-R-A-E-S-D-E-A-R-R-C-Y-N-D-P-K-C-C-D-F-V-T-N-R) administered through subcutaneous injection. The peptide was dissolved in 0.1M Na2CO3/1% β-mercaptoethanol and emulsified in

complete Freund's adjuvant for the first injection and incomplete adjuvant for the following ones in order to avoid excessive inflammatory response. Another group of 10 C57BL/6J male mice were vehicle-treated in the same manner. Mice were anaesthetized (150mg/kg ketamine, 10mg/kg xylazine, i.p.) prior each injection, allowing simultaneous collection of retro-orbital blood samples.

4.2. β1-immunization in β3TG mice

Male mice harboring β-myosin heavy chain-driven human β3-AR transgene (β3TG), generated as described previously (Tavernier, Toumaniantz et al. 2003), were included in the study, at the age of 8 weeks. A mouse line with moderate overexpression of the transgene was selected based on the pharmacological response to β3-AR agonists ex vivo that matched the response observed in human myocardium: 19 heterozygote male β3TG and 21 wild-type littermate controls (β3WT) of identical age and sex were used. 12 mice of each group were immunized according to the protocol described above, except that subcutaneous injections were performed under light anaesthesia with isoflurane 2-3% in oxygen for 3 minutes, and that no retroorbital- blood sample was taken at the same time. The other 16 mice were control mice, receiving only the vehicle.

5. Tissue specimens

After deep anaesthesia of animals, blood samples were taken through intracardiac puncture. Sera for ELISA analyses were collected by centrifugation (10000 rpm for 10 minutes), aliquoted and kept at -80°C.

Then hearts were excised and rinsed with saline. After cleaning and removal of large vessels, the heart weight was determined. Then LV was carefully isolated and its mass was also measured. LV was kept at -80°C for further processing.

6. ELISA experiments

To detect β1AR autoantibodies in mouse sera, the β1AR-ECII synthetic peptide was used in an enzyme-linked immunosorbent assay (ELISA). Plates (Reacti-Bind; Thermo scientific, Rockford, IL) were coated overnight at room temperature with 1μg/ml peptide (Eurogentec, Seraing, Belgium). Coating and blocking procedures were carried out using Ultrablock and Neptune buffers form AbD serotec (Oxford, UK) according to the manufacturer instructions. The sera diluted 1/2500 were then incubated overnight at 4°C. After washing, specific hybridization was measured with a peroxidase-conjugated antimouse IgG antibody (dilution 1/10 000) and addition of 3,3',5,5'-tetramethylbenzidine from Calbiochem (Merck Chemicals, Nottingham, UK). The absorbance was determined at 450nm in a microplate reader (Victor X4; Perkin Elmer, Waltham, MA).

7. qPCR experiments

Total RNA was isolated from heart tissue using TRI-reagent (Fermentas, Alost, Belgium) according to the manufacturer's instructions. 1 μg total RNA was reverse transcribed with RevertAidTM M-MuLV Reverse Transcriptase (Thermofischer Scientific, Alost, Belgium) using hexamer primers. The resulting cDNA served as template for quantitative real-time PCR analysis using the primers listed in Table 1 below. All samples were processed in triplicate reactions using Takyon for SYBR low Rox (Eurogentec, Seraing, Belgium) on the ViiA7 Real-Time PCR System (Applied Biosystems), using a fast cycling protocol. GAPDH was used as reference endogenous gene for normalization. Results are shown as fold expression relative to untreated samples according to the $\Delta\Delta C_T$method.

Table 1. Sequences of primers used in qPCR experiments.

Gene	Forward Primer Sequence	Reverse Primer Sequence
Adrb1	5'-GCTGATCTGGTCATGGGATT-3'	5'-AAGTCCAGAGCTCGCAGAAG-3'
Adrb2	5'-TTCGAAAACCTATGGGAACG-3'	5'-GGGATCCTCACACAGCAGTT-3'
Adrb3	5'-ACCAGAAGCCCTCAGCATCCCA-3'	5'-CACCCGCTTGTTTCAGGAGTCAC-3'
Myh6	5'- GGGACATTGGTGCCAAGAAGA-3'	5'-ATTGTGGATTGGCCACAGCG-3'
Myh7	5'-ACCAACCTGTCCAAGTTCCG-3'	5'-ACTCCTCATTCAGGCCCTTG-3'
Nppa	5'TGATAGATGAAGGCAGGAAGCCGC-3'	5'-AGGATTGGAGCCCAGAGTGGACTAGG-3'
Nppb	5'-GCCAGTCTCCAGAGCAATTC-3'	5'-AGCTGTCTCTGGGCCATTT-3'
Gapdh	5'-TGCACCACCAACTGCTTAGC-3'	5'-GGATGCAGGGATGATGTTCT-3'

8. Cardiac immunohistochemistry

At the end of the study, hearts were excised and representative pieces of left ventricles were fixed in 4% formaldehyde after rinsing with saline. For analysis of cardiac fibrosis, 5 µm sections of paraffin embedded hearts were stained with picrosirius red. Stained sections were digitalized with a SCN400 slide scanner (Leica Biosystems, Wetzlar, Germany). Quantification was made with Tissue IA software (Leica Biosystems, Dublin, Ireland). Area occupied by interstitial fibrosis was expressed as a percentage of total myocardial area.

To quantify transverse cardiomyocyte area and capillary density, cryosections were stained with Wheat germ agglutinin (WGA) as a membrane marker, and with biotinylated-Isolectine B4 as an endothelial marker. Mounted slides were observed with an Axioimager Z1/Apotome microscope equipped with a MRm camera (Zeiss, Germany). The data analysis was performed with Axiovision software (Zeiss, Germany). A minimum of 40 to 100 cells from 9 sections per heart were measured.

Other heart cryosections were incubated with antibodies raised against the monocyte marker CD11b and the lymphocytic marker CD45 (rat anti-CD11b and rat anti-CD45, both from BD Bioscience, San Jose, CA). Slides were scanned with a MIRAX Scanner

(Zeiss, Germany) and analysed with FRIDA software (Johns Hopkins University, Baltimore, MD). All analyses were performed on a blinded basis.

9. Statistical analysis

Statistical analyses were performed with GraphPad Prism 5.04 (San Diego, CA) and JMP 11.2.0 (SAS Institute, Cary, NC).

Data are all expressed as mean ± SEM. Raw data were analysed for normal distribution using the Shapiro-Wilk test. When normally distributed, unpaired Student t test was used to compare differences between two groups and one-way analysis of variance followed by Bonferroni post-hoc test was used to compare 3 or more groups. In absence of normal distribution, the statistical significance of differences was tested with non-parametric tests (Mann-Whitney or Kruskall-Wallis followed by Dunn's test).

For the reproducibility study, since most data were treated retrospectively, the 29 animals studied have not all been included in the different analysis groups. For intra- and interobserver variability, the same 24 mice were studied, including 13 sham and 11 TAC animals. For interexperiment variability 12 animals were studied, including 3 sham and 4 TAC (also included in the intra- and interobserver analysis), and the 5 control animals.

For intraobserver variability, the same stack of images was read twice by the same observer (datasets number 1 and number 2), for interobserver variability the same stack of images was read blindly by two independent observers (datasets number 1 and number 3), for interexperiment variability two different stacks of images acquired in the same animal were read by the first observer (datasets number 1' and number 4).

The mean and standard deviation of each parameter were computed in each group. Agreement between intraobserver, interobserver and interexperiment measurements was assessed by means of the Bland and Altman test (Bland and Altman 1986) that plots the difference between the two measurements against the average of the two methods. The bias corresponds to the mean difference. The limits of agreement were estimated using the mean bias between the 2 readings plus or minus twice the standard

deviation of the differences (SDD). The difference between the two measurements will be within these limits for 95% of observations. The coefficient of variability (CoV) corresponds to the SDD divided by the mean of the measurements, and mutiplied by 100%. It represents the percentage of dispersion of the measurements.

Unpaired student t test was used for intergroup comparison, including a comparative analysis of morphological and functional data (MRI dataset number 1) obtained for sham (n=13) and banded mice (n=11). Paired t test was used to compare intraobserver, interobserver and interexperiment results for each parameter.

A Pearson correlation was calculated in order to compare *in vivo* MRI data (dataset number 2) and ex vivo morphometric measurements of the LV mass and LV/TL ratio for the 13 sham and 11 TAC animals. $P<0.05$ was considered statistically significant.

Chapter IV – RESULTS

1. Study of a murine model of pressure overload hypertrophy induced by surgical transverse aortic constriction

Part of this work was published in Journal of Cardiovascular Translational Research (Vanhoutte, Gallez et al. 2015).

1.1. Description of the experimental transverse aortic constriction model

Hypertrophic cardiomyopathies are defined by the presence of increased ventricular wall thickness or mass in the absence of loading conditions sufficient to cause the observed abnormality (Elliott, Andersson et al. 2008). In humans, the disease is often of genetic origin and occur mostly in the paediatric age. However, hypertrophy of cardiac muscle cells may also occur as a maladaptive response to stimuli such as hypertensive disease, valvular disease or endocrine disorders.
To better understand the molecular/cellular determinants of cardiac hypertrophy and identify adequate therapeutic strategies, mouse models were developed. In particular, Rockman and colleagues pioneered an *in vivo* murine model of pressure overload hypertrophy, through surgical transverse aortic constriction (Rockman, Ross et al. 1991). The use of this model, later simplified by minimally invasive approaches (Hu, Zhang et al. 2003), has provided significant insights into the signalling pathways responsible for the development of hypertrophic cardiomyopathy.

1.2. Application of UHF MRI techniques

1.2.1. Assessment of left ventricular systolic function and study of accuracy and reproducibility data

a) Study of the accuracy and reproducibility of left ventricular systolic function data

In cardiovascular imaging, variations within and between observers, and between different acquisitions remain an important issue when evaluating *in vivo* data. This is particularly relevant when experimental groups are studied longitudinally to test a new hypothesis.

Even if regularly used to study experimental models of cardiovascular diseases, data related to the reproducibility of left ventricular systolic function assessment in mouse with UHF magnets where scarce when we started the current work. To our best knowledge, studies existing either used very small groups of animals (n<10) (Ruff, Wiesmann et al. 1998, Schneider, Cassidy et al. 2003, Tyler, Lygate et al. 2006), only rats (Tyler, Lygate et al. 2006, Stuckey, Carr et al. 2008), field strength under 7 Tesla (Heijman, Aben et al. 2008) or vertical bores (Schneider, Cassidy et al. 2003, Tyler, Lygate et al. 2006, Stuckey, Carr et al. 2008). They further only focused on the intra- and interobserver reproducibility, or compared segmentation techniques (Heijman, Aben et al. 2008, van de Weijer, van Ewijk et al. 2012), only one study by Stuckey et al. reported interexperimental- reproducibility data, on a group of 12 rats (Stuckey, Carr et al. 2008). However, such data are crucial to establish whether this technique is routinely applicable to mouse models, especially in dynamic studies using repeated acquisitions (Wiesmann, Ruff et al. 2001) – and to determine how it compares to high-frequency echocardiographic analysis.

Therefore, we first evaluated the intraobserver, interobserver and interexperiment variability of left ventricular mass and volumes in mice with the 11.7 Tesla horizontal bore MR system, and compared these MRI data with ex vivo morphometric measurements before using a similar approach in our various murine models of cardiomyopathy.

Methodology

We studied intraobserver- (n=24), interobserver- (n=24) and interexperiment- (n=12) reproducibility of left ventricular (LV) mass and volumes measurements in mice using an 11.7T MRI system. The LV systolic function was assessed with a short-axis FLASH-cine sequence in 29 mice, including animals having undergone minimally

invasive transverse aortic constriction, in order to study the experimental variability of the technique in a wider range of physiopathological conditions. Bland-Altman and regression analysis were used to compare the different datasets.

Intraobserver, interobserver and interexperiment variability of MRI data

The mean ± SD values of all morphometric data as well as the Bland-Altman analysis were obtained for the 29 animals studied. Detailed results are displayed in Table 2 and Figure 6.

We did not find statistically significant differences in the mean values of LV mass, LV/TL ratio, LV EDV, LV ESV, LV SV and LV EF when comparing the various sets of data ($p>0.05$).

As expected, the SDD, and hence the limits of agreement, were smaller for all parameters in the intraobserver- study, whereas the least clustered data were found in the interexperiment- study, with similar to larger confidence interval compared to the interobserver- study.

Using the Bland and Altman analysis, high reproducibility was found for LV mass, LV/TL and EDV, with a notably low intraobserver- CoV of 5.4% for all these data, and CoV <12% in the interexperiment- study, suggesting that these parameters can be effectively used in longitudinal studies. Good agreement was found for EF, with a CoV between 14.7% in the interobserver- study and 15.5% in the interexperiment- study. The small volumes suffered the most variability, with intermodality- CoV between 15.2 and 20.9% for ESV and SV, which implies that it is more difficult to compare these two last parameters during repeated acquisitions.

Table 2. Intraobserver, interexperiment and interobserver variability for LV mass (mg), LV/TL ratio (mg/mm), EDV (µl), ESV (µl), SV (µl), and EF (%). The table lists the mean ± SD values and the Bland-Altman analysis results. "n" represents the number of animals studied. Numbering of the data is organized as follows : 1 and 1' correspond to the first reading, 2 is the second reading of the same stack of images by the same observer (intraobserver), 3 is the third reading of the same stack of images by an independent observer (interobserver), and 4 corresponds to the reading of a second stack of images acquired on the same animal by the first observer (interexperiment).

Intraobserver variability (n=24)	**LV mass**	**LV/TL**	**EDV**	**ESV**	**SV**	**EF**
Mean ± SD dataset #1	87.3 ± 4.2	4.6 ± 0.2	67.4 ± 3.2	33.6 ± 3.5	33.7 ± 1.4	52.2 ±2.8
Mean ± SD dataset #2	86.2 ± 4.1	4.5 ± 0.2	68.2 ± 3.3	34.7 ± 3.7	33.4 ± 1.8	50.9 ± 3.2
Bias	1.1	0.1	0.8	1.1	0.3	1.3
Limits of agreement	-10.4 to 8.1	-0.6 to 0.4	-6.4 to 7.9	-9.1 to 11.3	-10.4 to 9.7	-16.8 to 14.1
SDD	4.7	0.2	3.6	5.2	5.1	7.9
Coefficient of variability	5.4%	5.4%	5.4%	15.2%	15.3%	15.3%
Interobserver variability n=24)	**LV mass**	**LV/TL**	**EDV**	**ESV**	**SV**	**EF**
Mean ± SD dataset #1	87.3 ± 4.2	4.6 ± 0.2	67.4 ± 3.2	33.6 ± 3.5	33.7 ± 1.4	52.2 ±2.8
Mean ± SD dataset #3	91.5 ± 4.4	4.8 ± 0.2	61.8 ± 3.0	29.1 ± 2.9	32.8 ± 1.0	55.0 ± 2.4
Bias	4.1	0.2	5.6	4.5	0.9	2.8
Limits of agreement	-6.0 to 14.2	-0.3 to 0.8	-17.3 to 6.1	-16.4 to 7.4	-12.7 to 10.9	-12.7 to 18.3
SDD	5.1	0.3	6.0	6.1	6.0	7.9
Coefficient of variability	5.8%	5.9%	9.2%	19.4%	18.1%	14.7%
Interexperiment variability (n=12)	**LV mass**	**LV/TL**	**EDV**	**ESV**	**SV**	**EF**
Mean ± SD dataset #1'	83.5 ± 5.8	4.3 ± 0.4	72.6 ± 4.2	35.4 ± 5.5	37.1 ± 2.3	53.4 ± 4.53
Mean ± SD dataset #4	87.3 ± 5.7	4.5 ± 0.4	70.2 ± 4.6	34.2 ± 6.0	35.8 ± 2.7	53.9 ± 5.0
Bias	3.8	0.2	2.4	1.3	1.3	0.5
Limits of agreement	-9.3 to 16.8	-0.5 to 0.9	-18.9 to 14.1	-12.7 to 10.2	-16.2 to 13.7	-13.9 to 14.9
SDD	6.6	0.4	8.4	5.8	7.6	7.4
Coefficient of variability	7.8%	8.3%	11.8%	16.8%	20.9%	15.5%

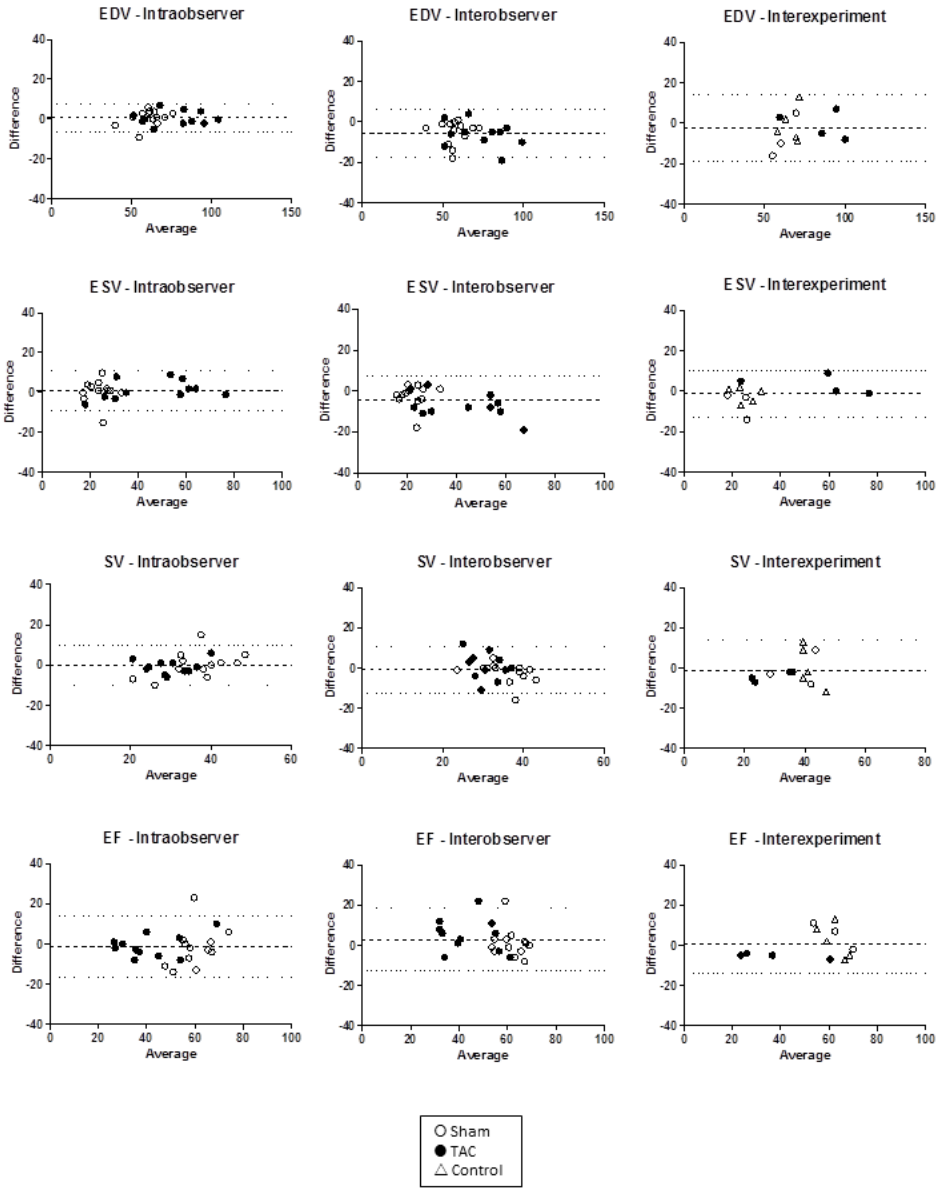

Figure 6. Bland-Altman plots for EDV, ESV, SV and EF, assessing the agreement between the readings (interobserver, intraobserver, interexperiment). The relative variability is defined as the difference between observations divided by their mean. The dashed line indicates the mean difference, while dotted lines indicate 95% limits of agreement. All measurements showed a rather similar agreement of these main 4 parameters, not only in intra- or interobserver- experiments (left and central column), but also in interexperiment- analyses (right column).

Linear regression analysis

Linear regression analysis for all mice revealed an adequate intraobserver, interobserver and interexperiment correlation for LV/TL, EDV, ESV and EF with R-square ranging between 0.67 and 0.95. Correlation for SV was the weakest of all parameters, with R-square between 0.30 (interobserver- study) and 0.67 (intraobserver-study). The line of best fit intercepted the origin for most measurements, and when not, the correlation remained significant, with a b0 significantly different from zero. The scatter plots with individual regression line, 95% confidence interval, R-squares and corresponding p-values are provided in Figure 7.

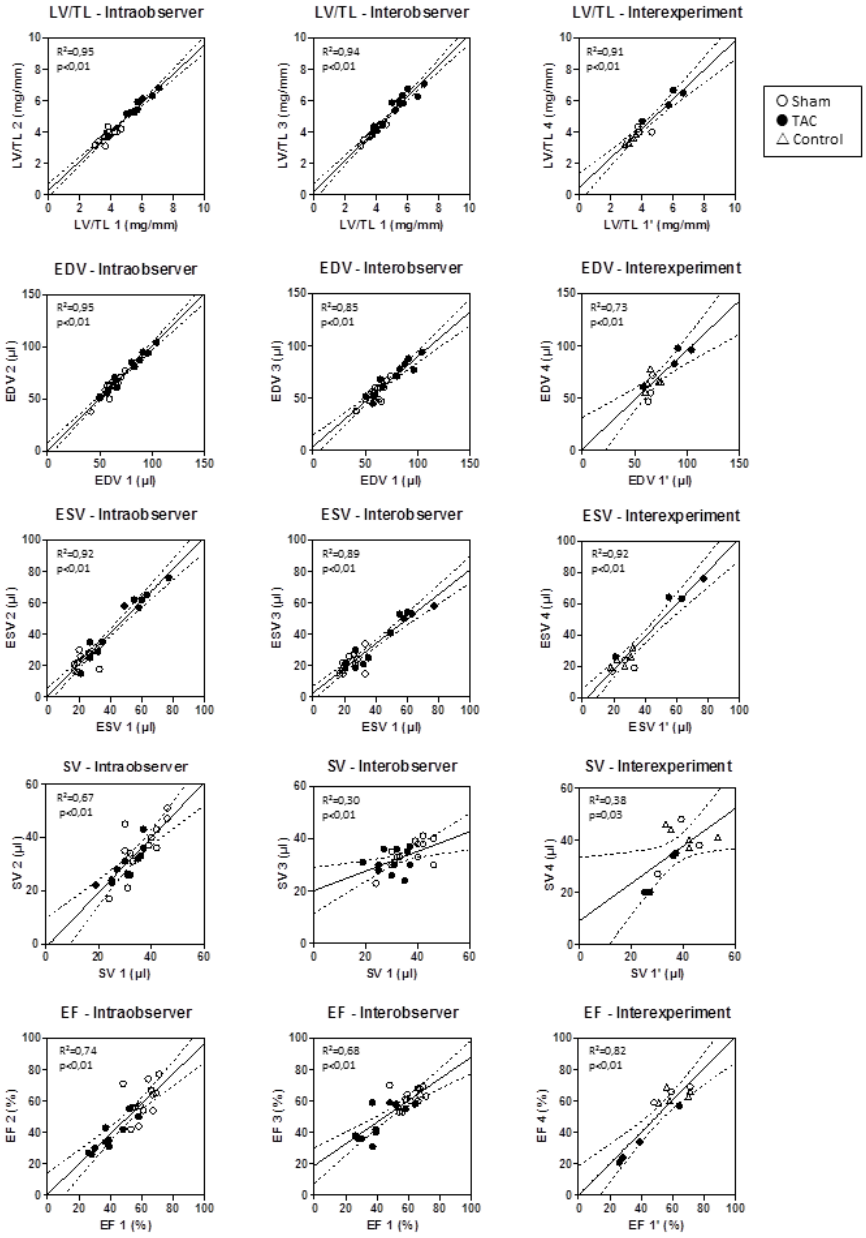

Figure 7. Scatterplots showing the intraobserver, interobserver-- and interexperiment-correlation between two readings, for LV/TL, EDV, ESV, SV and EF. Our linear regression analysis shows an excellent correlation for all data in intraobserver-, but moderate correlation in SV and EF for interobserver- data and in SV for interexperiment- data. The regression line is given with a 95% confidence interval (dotted lines). R-squares and p values can be found in the graph for each fit.

Correlation between in vivo MRI and ex vivo morphometric LV mass measurements

We demonstrated a strong correlation between LV mass measurements by LV mass weighing or high-field CMR imaging (dataset number 2), with a Pearson correlation (r) of 0.92 for both LV mass and LV/TL ratio ($p<0.05$, Fig 8). Of note, MRI data in absolute values were always smaller than morphometric data.

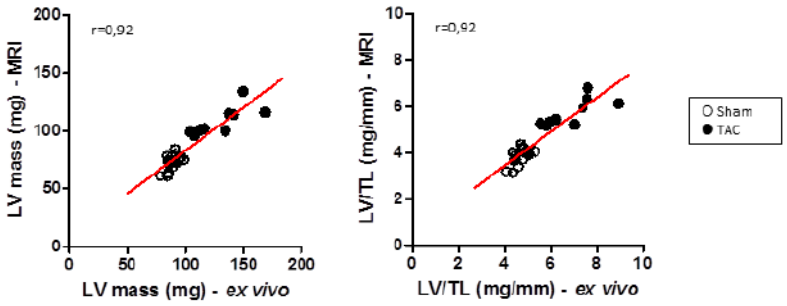

Figure 8. Correlation between *in vivo* MRI data and ex vivo morphometric data, in terms of LV mass and LV/TL ratio. MRI data are issued from the second reading (dataset #2).

In conclusion, this part of our work showed that the mouse LV systolic function can be assessed on an 11.7T MRI scanner, with an excellent reproducibility of LV mass and end-diastolic volumes analysis, allowing longitudinal phenotypic evaluation of animals with healthy or hypertrophic myocardium. Furthermore, *in vivo* LV mass MRI measurements were constantly in line with ex vivo morphometric data, bringing evidence that high-field CMR imaging is not only reproducible but also accurate. However, data should be interpreted taking into account the moderate reproducibility of very small volumes.

b) Assessment of left ventricular systolic function

We were able to detect myocardial remodelling in a C57BL/6J mouse model of LV hypertrophy due to pressure overload, with excellent correlation with ex vivo measurement, as shown above. Quantitative data were in line with previously published results (Ruff, Wiesmann et al. 1998, Wiesmann, Ruff J Fau - Engelhardt et al. 2001, Schneider, Cassidy et al. 2003, Kober, Iltis et al. 2004, Heijman, Aben et al. 2008, van de Weijer, van Ewijk et al. 2012). As expected, LV mass was significantly higher in the 11 animals with transverse aortic banding and hypertrophic cardiomyopathy, compared to the 13 sham animals. When using the LV mass/tibial length ratio (LV/TL), which normalizes the LV mass to the body size, sham mice showed a ratio of 4.7±0.1mg/mm and 3.8±0.1mg/mm for morphometric and MRI measurements respectively, and TAC mice showed a ratio of 6.5±0.4 and 5.4±0.3 respectively, demonstrating a clearly different cardiac phenotype between both groups ($p<0.05$, Fig. 9 and 10). Detailed cardiac functional parameters and LV mass measurements for the sham and banded groups are summarized in Table 3.

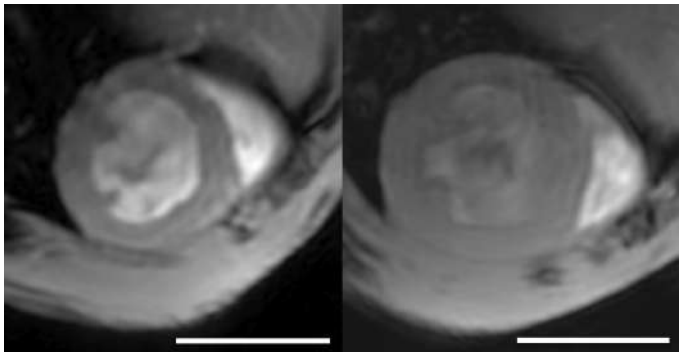

Figure 9. Representative end-diastolic short-axis views of mouse hearts, 8 weeks after a sham (left) or transverse aortic constriction surgical procedure (right), showing obvious LV wall thickening in the latter animal. Scale bars represent 500μm.

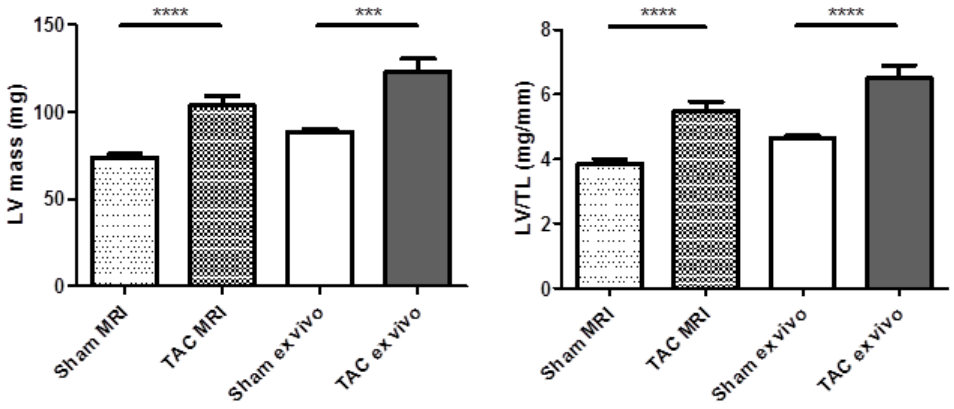

Figure 10. LV mass (mg) and LV/TL ratio (mg/mm) in sham and TAC mice, assessed by MRI or ex vivo morphometric measurements. MRI data are issued from the first reading (dataset #1).
*****P≤.0.001; ****P≤0.0001 vs sham.**

Table 3. Cardiac function and LV mass of sham and TAC mice. MRI data are issued from the first reading (dataset #1). n represents the number of animals in each group.

	Sham	TAC
n	13	11
Body weight (g)	28.2 ± 0.3	27.8 ± 0.5
LV mass *ex vivo* (mg)	88.7 ± 1.6	122.8 ± 7.7***
LV/TL *ex vivo* (mg/mm)	4.7 ± 0.1	6.5 ± 0.4****
LV mass MRI (mg)	73.5 ± 2.4	103.6 ± 5.7****
LV/TL MRI (mg/mm)	3.9 ± 0.1	5.5 ± 0.3****
Heart rate (bpm)	496.6 ± 11.1	509.5 ± 11.3
EDV (µl)	60.1 ± 2.4	76.1 ± 5.4**
ESV (µl)	23.2 ± 1.6	45.8 ± 5.5***
SV (µl)	36.5 ± 1.9	30.4 ± 1.8*
EF (%)	61.2 ± 2.0	41.6 ± 3.7****
CO (ml/minute)	18.1 ± 0.9	15.4 ± 0.8*

EDV = end-diastolic volume, ESV = end-systolic volume, SV = stroke volume, EF = ejection fraction, CO = cardiac output. *P≤.0.05; ***P≤.0.01; ***P≤.0.001; ****P≤0.0001 vs sham.

1.2.2. Time of Flight angiography

As previously mentionned, the TOF technique allows the creation of angiogram thanks to inherent vessel contrast resulting from the inflow effect. As a proof of concept, we applied the method to our model of transverse aortic ligation in order to characterize vessel remodelling. Such TOF 3D angiogram is shown in Figure 11.

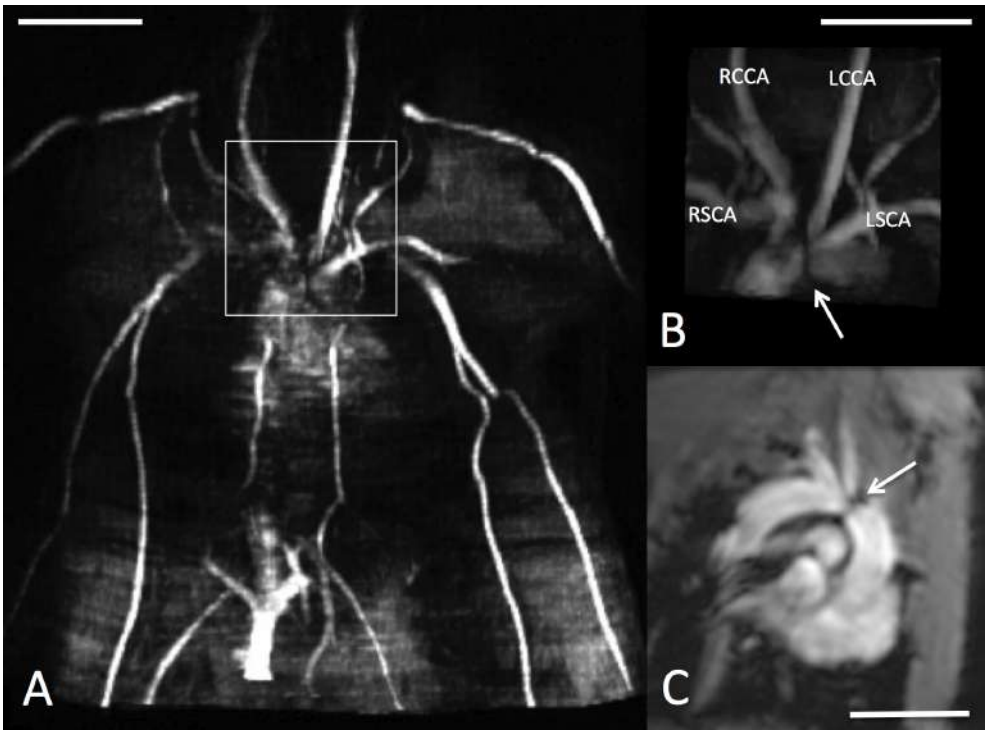

Figure 11. (A) 3D Maximum-intensity projection (MIP) of a TOF angiography of the trunk in a mouse (anterior view). Blurring corresponds to artefacts due to heart motion. Imaging parameters: TE/TR 2.4/12ms; matrix 256x256x120, slice thickness 0.4m, flip angle 80°. (B) Detail of the aortic arch and the supra-aortic vasculature, showing the transverse aortic stenosis due to surgical banding (arrow). LCCA = left common carotid artery, RCCA = right common carotid artery, LSCA = left subclavian artery, RSCA right subclavian artery. (C) Sagittal view of the aorta with FLASH sequence, in the same animal. The arrow indicates the transverse aortic constriction. Scale bars represent 500μm.

1.2.3. Phase contrast velocity mapping

A PC-MRA sequence was applied to our mouse model of aortic banding, in order to obtain flow and (subsequently) stenosis diameter and normalize ventricular hypertrophy data to the pressure gradient induced by the surgical intervention. Proper acquisition of PC images was performed as shown in figure 12, but, unfortunately, automated extraction of flow data in the region of interest was not directly possible with classical softwares (Segment, Osirix and Paravision). Further perspectives would include the use of a pixel-by-pixel method in order to measure the flow velocity from phase-contrast images using the following formula : $v = PCSI/MSI \times 1/\pi \times Venc \times \alpha$ were PCSI = signal intensity of phase image, MSI = signal intensity of magnitude image and α = fitting constant for the physically measured velocity, as described by Kim and colleagues (Kim, Seo et al. 2010). This implies to perform preliminary experiments using a flow phantom in order to accurately determine the value of α for our 11.7T machine.

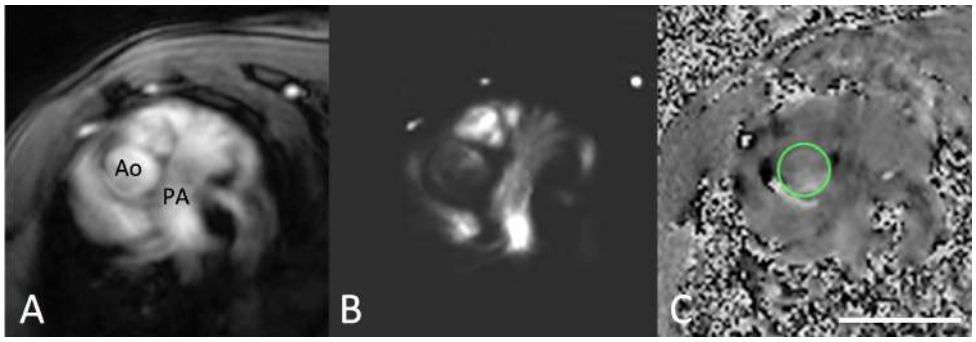

Figure 12. Transverse FLASH view of the mouse ascending aorta (A) and corresponding phase contrast magnitude (B) and phase images (C). The region of interest is indicated in green on the phase image. Ao = aorta, PA = pulmonary artery. Imaging parameters: TE/TR 2.3/8.7ms, spatial resolution 0.138mm/pixel, slice thickness 1mm, VENC 250cm//s. Scale bar represents 500μm.

2. Study of a murine model of ischaemic cardiomyopathy induced by surgical ligature of the left anterior descending artery

This work was included in a paper published in JCI Insight (De Pauw, Andre et al. 2017).

2.1. Description of the experimental model: Dnmt3a-mediated extinction of Wnt/beta-catenin

Ischaemic cardiomyopathy represents a worlwide public health issue with increasing incidence and mortality (Writing Group, Mozaffarian et al. 2016). Duration of ischaemia resulting from blood supply deprivation is recognized as a critical factor, leading to cardiomyocyte apoptosis and inflammatory processes with, in fine, scar formation and reduction of ventricular function. Up to now, therapies have not adressed the cardiomyocyte loss and only aimed to alleviate symptoms and differ progression to heart failure. In recent years, stem cell regenerative therapy has emerged as a promising approach to deal with this issue leading to an explosion of pre-clinical and clinical studies evaluating various cell types and delivery protocols (Faiella and Atoui 2016).

We worked in collaboration with the team of Professor Jean-Luc Balligand in order to evaluate ventricular function and local remodelling in a mouse model of myocardial infarction (MI) upon treatment with cardiac stem cells (CSC) epigenetically reprogrammed to promote differentiation in cardiomyocyte (De Pauw, Sekkali et al. 2014). We assessed the reparative potential of Dnmt3-silenced CSC in infarcted C57Bl6J mice *vs.* control CSC cells (transfected with scramble siRNA or vehicle (PBS)), injected in the site of infarction soon after LAD ligature. 40 mice were scanned one day and one month after the MI surgery, for a total of 76 MRI examinations due to mortality. All MRI examinations were performed in blinded manner, and 3 readouts were provided: conventional systolic function assessment, quantification of the number of dyskinetic segments and assessment of the LV wall thickness at the site of infarction.

In parallel to the above study, we also investigated the feasibility of other sequences such as tagging and late gadolinium enhancement on a mouse model of myocardial infarction at 11.7T.

2.2. Application of UHF MRI techniques

2.2.1. Left ventricular systolic function assessment

Severe systolic dysfunction was found in mice with MI. Figure 13 shows significant impairment of EF and EDV in infarcted mice one day and 28 days after the surgical procedure, with progressive dilation of LV over time, compared to representative unoperated control mice of the same age and strain (EF : 39.4±3.6% after one day and 37.7±4.8% after 28 days vs 61.2±2.1% in control animals ; EDV : 77.2±4.4µl after one day and 89.4±7.3µl after 28 days vs 59.6±3.1µl).

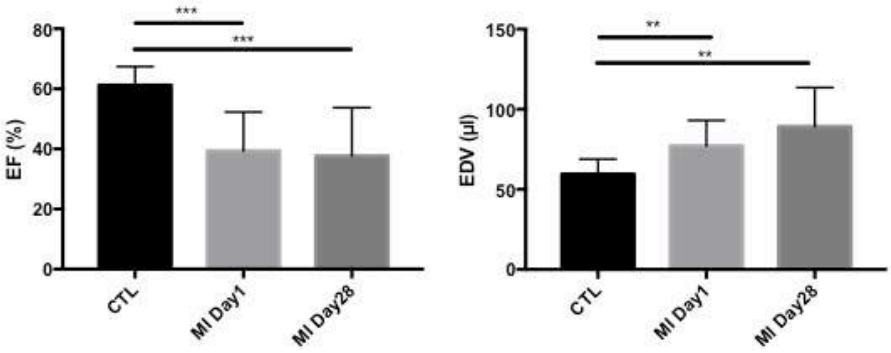

Figure 13. Left ventricular ejection fraction (left) and end-diastolic volume (right) in mice having undergone a LAD ligation procedure, 1 day and 28 days after the surgery compared to representative unoperated control mice (CTL) of the same age and strain. **P≤.0.01; ***P≤.0.001 vs control mice.

Figure 14 shows 2-chambers and 4-chambers views in an infarcted mouse 28 days after the LAD ligation, with obvious LV dilation and LV wall thinning. A large akinetic zone and a turbulent blood flow are visible on cine images from the same animal.

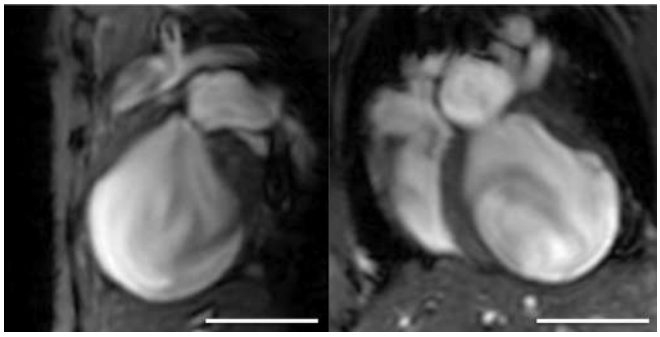

Figure 14. Representative 2-chambers (left) and 4-chambers (right) FLASH images in a mouse model of myocardial infarction, 28 days after the LAD ligation, with obvious LV dilation and LV wall thinning. Scale bars represent 500μm.

The asymmetric nature of this kind of ischaemic lesions highlights the interest of the full volume acquisition of MRI compared to techniques using geometrical assumptions to extrapolate function, particularly echocardiography.

Interestingly, we were able to show better recovery of ventricular function (i.e., stroke volume) after 28 days of MI in mice treated with CSC transfected with Dnmt3 siRNA compared to mice treated with CSC transfected with scramble siRNA (Si-Scramble group: SV after one day: 23.4±1.9μl and SV after 28 days: 30.8±3.2μl, ns; Si-RNA group: SV after one day: 24.2±2.4μl and SV after 28 days :35.1±2.8μl, p=0,010, Fig.15.

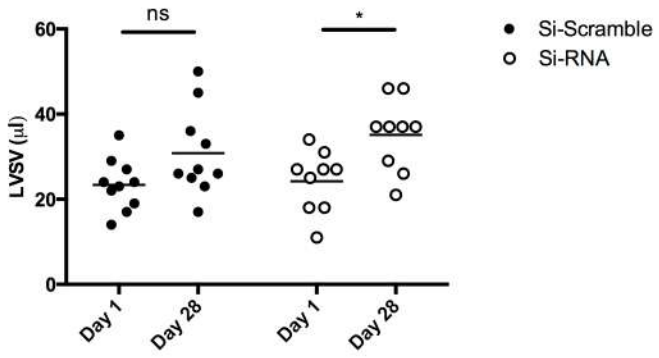

Figure 15. Stroke volume data in infarcted mice treated with si-Scramble and si-RNA transfected cells, one day and 28 days after LAD ligation and cell treatment, showing

a better recovery of stroke volume 28 days after myocardial infarction in mice treated with Dnmt3 si-RNA transfected cells compared to control (Si-Scramble transfected) cells. *P≤.0.01.

A semi-automated technique was also used for the determination of the ventricular thickening at the level of the free wall, the septum and in the infarcted area. Importantly, we showed that mice treated with CSC transfected with Dnmt3 SiRNA maintained a better wall thickening in the infarcted area *vs.* mice receiving control cells (Si-Scramble group: %LVWT after one day: 6.9±2.1% and %LVWT after 28 days: 0.8±0.6%, p=0,015; Si-RNA group: %LVWT after one day: 3.5±1.8% and %LVWT after 28 days: 6.2±3.0%, ns, Figure 16).

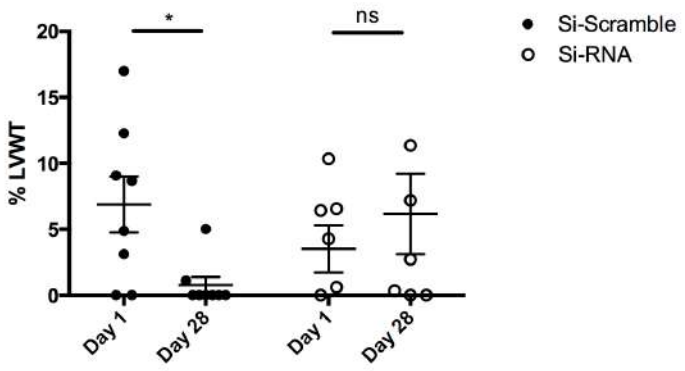

Figure 16. Left ventricular wall thickening (LVWT) in systole (expressed as % of diastolic thickness) in the infarcted area in mice treated with si-Scramble and si-Dnmt3a transfected cells, one day and 28 days after LAD ligation and cell treatment. Mice injected with CSC after downregulation of Dnmt3a (si-RNA) show better preservation of systolic LVWT compared with control CSC (si-Scramble) at day 28. *P≤.0.05.

2.2.2. Intramyocardial function and strain measurement

a) Quantification of regional contractile performance with vector-based methods

In models of cardiovascular diseases characterized by inhomogenous dyskinetic regions in the myocardium, detailed quantification of the regional contractile

performance of the heart may bring additional information to functional and volumetric indices. In our team, we were able to produce tagged images in different models of cardiomyopathies. Analysis of vectors with the HARP software has not been routinely used by our team as a good alternative approach for the investigation of regional dysfunction was obtained in the MI model with semi-automated quantification of dyskinetic segments on cine short axis. However, as shown in Figure 17, the use of HARP is possible on tagged images obtained from mice, and the technique could be further developped, especially in models with more subtle changes in regional contractile performance.

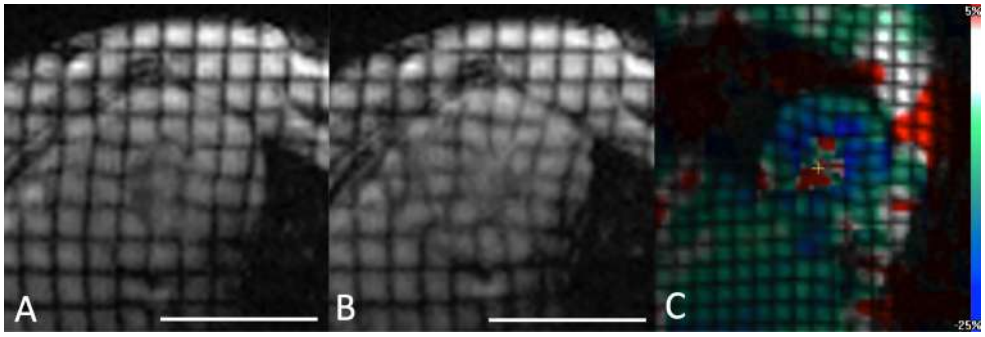

Figure 17. (A, B) SPAMM tagged images in a normal mouse. Compared to the reference image in end-diastole (A), the tag lines show clear contraction and twist of myocardium in end-systole (B). Imaging parameters: TE/TR 1.8ms/12ms; tag distance 0.3mm, tag thickness 1mm. Scale bars represent 500μm.

(C) Representative short-axis strain map obtained with HARP software (Diagnosoft, Inc., Baltimore, MD, USA). Blue zones correspond to the highest deformation. Figure C was kindly provided by Pr B. Gerber.

b) Manual quantification of dyskinetic segments on cine sequence

Regional analysis of left ventricular function is of prime interest in experimental models of MI. In particular, it is important to rationalize data with the initial damage created by the LAD ligation, which may vary because of anatomical variations of coronary territories. Recovery of function in ischaemic segments is also an interesting

evolutionary marker for the longer-term evaluation of therapeutic interventions in experimental models. Therefore, we assessed the number of dyskinetic segments at the beginning of our study and after one month of follow-up, according to previously published standardized segmentation (Cerqueira, Weissman et al. 2002), showing that there was no statistically significant difference in the recovery of dyskinetic segments over time between the different groups studied (Figure 18).

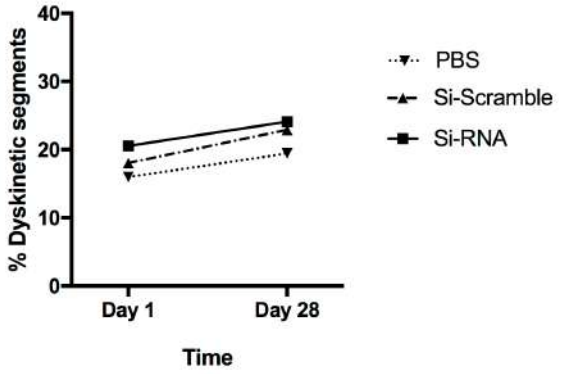

Figure 18. Mean percentage of dyskinetic segments in mice treated with PBS, si-Scramble or si-Dnmt3a transfected cells, one day and 28 days after LAD ligation and cell treatment. N=9 in PBS group, 10 in Si-Scramble group and 8 in Si-RNA group. No significant difference of recovery of dyskinetic segment over time was found between the groups (one-way ANOVA, p=0.38).

2.2.3. Late gadolinium enhancement and myocardial viability

We applied the late gadolinium enhancement technique to our mouse model of LAD ligation in order to study myocardial viability one month after the surgical procedure. Using a FISP sequence with inversion recovery, 10 minutes after intraperitoneal administration of a bolus of gadolinium DTPA, we could highlight the infarction area (Figure 19).

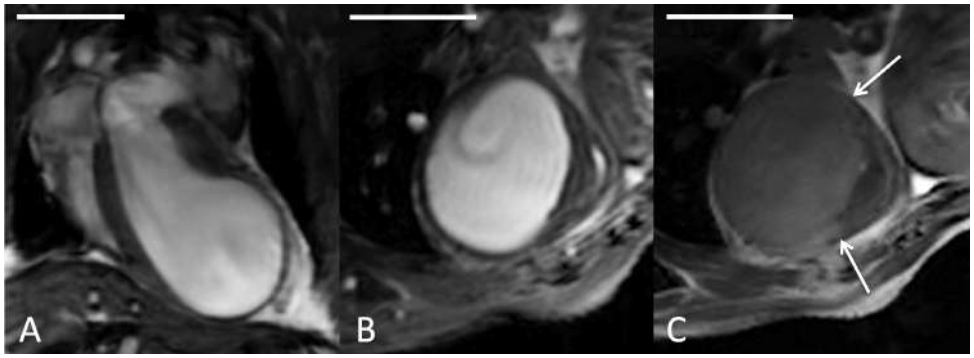

Figure 19. 4-chambers (A) and short-axis FLASH (B) and inversion-recovery T1-weighted MR images (C) in a mouse with LAD ligation, 20 minutes after peritoneal injection of a 0.5mmol /kg bolus of gadolinium DTPA. Limits between the non-viable infarcted myocardium (hyperenhanced zone), and the healthy myocardium (dark zone) are well visible (arrows). Imaging parameters: TE/TR 2.2ms/4.5ms, inversion time 350ms. Scale bars represent 500μm.

3. Study of a murine model of dilated cardiomyopathy induced by auto-antibodies directed against the β1-adrenoceptor

This work was published in Scientific Reports (Vanhoutte, Guilbaud et al. 2017).

3.1. Description of the experimental model of dilated cardiomyopathy induced by auto-antibodies directed against the β1-adrenoceptor

Dilated cardiomyopathy (DCM) is a heart muscle disease characterized by LV enlargement and LV systolic dysfunction in the absence of abnormal loading conditions (hypertension, valve disease) or coronary artery disease (Elliott, Andersson et al. 2008), with normal LV wall thickness (Maron, Towbin et al. 2006). Besides many "idiopathic DCM", a broad range of causes has been identified, including genetic, toxic, metabolic or infectious diseases. DCM is a common and largely irreversible form of heart muscle disease with an estimated prevalence of 1:2500; it is the third most frequent cause of heart failure and heart transplantation (Maron, Towbin et al. 2006). It is also the most common form of cardiomyopathy among children, with an annual incidence of DCM in children <18 years of age of 0.57 per 100 000 overall, with a majority (66%) of idiopathic diseases (Go, Mozaffarian et al. 2014). Hence, much remains to be done to explain these pathological conditions. Over the past 2 decades, the detrimental role played by autoantibodies targeting the β1-adrenergic receptor (β1-aabs) has been established.

Clinical studies have shown that the presence of β1-autoantibodies (β1-aabs) is associated with dilated cardiomyopathy (30-90%) (Limas, Goldenberg et al. 1992, Magnusson, Wallukat et al. 1994, Wallukat, Wollenberger et al. 1995), ischaemic cardiomyopathy (10%) (Jahns, Boivin et al. 1999) and Chagas' disease (30%) (Elies, Ferrari et al. 1996), with, overall, greater occurrence of poor LV function (Jahns, Boivin et al. 1999), ventricular arrhythmias (Bohl, Lygate et al. 2009), sudden cardiac death (Iwata, Yoshikawa et al. 2001, Bohl, Lygate et al. 2009) and mortality (Stork, Boivin et al. 2006). On the contrary, their prevalence seemed to be low in healthy

individuals and in patients with heart failure due to valvular or hypertensive disease (Jahns, Boivin et al. 1999). However, wide range of β1-aabs prevalence has been reported. It seems conceivable that the definition of antibody positivity and the screening modalities account for these discrepancies, as it has become clear now that only functionally activating β1-aabs were responsible for clinical consequences (Nikolaev, Boivin et al. 2007). These gross statistics require further clarification in order to better understand the prevalence and progression of this large panel of cardiac diseases triggered by this autoimmune deregulation. A multicentric prospective and retrospective study is currently conducted in patients suffering from myocarditis, ischaemic and hypertensive heart disease (Deubner, Berliner et al. 2010), using a specific screening method in order to detect only functionally active β1-aabs (Nikolaev, Boivin et al. 2007).

Evidence form different animal studies confirmed the direct pathogenicity of aabs directed against the β1-adrenoreceptor. A highly antigenic fragment containing B and T cell epitopes has first been identified on the second extracellular loop (β1-EC_{II}) of this seven-membrane-spanning receptor (Magnusson, Hoyer et al. 1989, Tate, Magnusson et al. 1994, Mobini, Magnusson et al. 1999) (figure 20). Then studies on animal models have established the development of a cardiomyopathy after active immunization against this antigen (indirect evidence) (Matsui, Fu et al. 1997, Iwata, Yoshikawa et al. 2001, Buvall, Bollano et al. 2006) and assessed the possibility of generating cardiac impairment after transfer of homologous pathogenic antibodies to healthy animals (direct evidence) (Jahns, Boivin et al. 2004). The two main hypotheses evoked to explain the development of such antibodies include homologies between the receptor and microbial determinants or the exposition of potentially antigenic components from injured cardiomyocytes because of various insults (Jahns, Boivin et al. 2006).

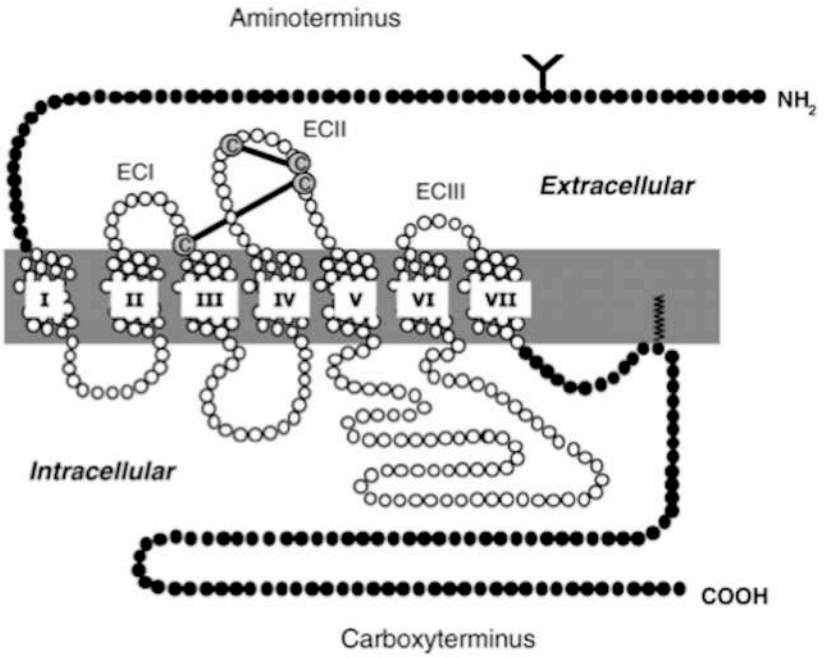

Figure 20. Scheme depicting the predicted secondary structure of the β1-adrenoreceptor. The receptor consists of seven transmembrane α-helices (I-VII) forming a hydrophobic pocket which spans the membrane lipid bilayer (dark grey). The transmembrane domains are linked together by three extracellular (ECI-III) and three intracellular loops. The N-terminus is located in the extracellular, and the C-terminus in the intracellular space. In addition, the presumed disulfide-bonds (S-S) between cysteines of the first and second extracellular loop are depicted. Reproduced from Jahns et al. (Jahns, Boivin et al. 2006).

The functional effects of β1-aabs at the cellular and molecular levels are incompletely understood. Preliminary results suggest that they act as allosteric agonists (Jahns, Boivin et al. 2006), enabling dimerization and stabilization of β1-AR in its active conformation (Gouldson, Higgs et al. 2000), subsequently promoting sustained downstream signalling in a manner distinct from the natural ligand (Hebert 2007, Tutor, Penela et al. 2007). This leads to cardiomyocyte apoptosis (Staudt, Mobini et al. 2003), enhanced contractility and prolonged action potential duration (Christ, Wettwer et al. 2001). During progression of β1-aabs-induced cardiomyopathy, increased levels of GRK2 have been documented in several rodent studies (Buvall, Bollano et al. 2006, Buvall, Tang et al. 2007, Ma, Premaratne et al. 2012), suggesting desensitization and

down-regulation of β1-AR. Some therapies, including the use of apheresis (Matsui, Larsson et al. 2006), aptamers (Haberland, Wallukat et al. 2011), peptides competing with the receptor epitope (Munch, Boivin-Jahns et al. 2012, Boivin, Beyersdorf et al. 2015) and conventional beta-blockers (Miao, Liu et al. 2006, Boivin, Beyersdorf et al. 2015) have proven to be useful in order to prevent the development of cardiac dysfunction due to β1-aabs. However, their cost-effectiveness and accessibility differ.

The β3-adrenoreceptor (β3AR) has recently emerged has a potential therapeutic target in the presence of an excessive β-adrenergic stimulation on the heart, as it mediates a countervailing influence to β1 and β2-AR (Niu, Watts et al. 2012) and is resistant to homologous desensitization (Liggett, Freedman et al. 1993). Moreover β3-ARs are upregulated in various conditions of adrenergic overstimulation (Dincer, Bidasee et al. 2001, Moniotte, Kobzik et al. 2001, Moniotte, Belge et al. 2007), arguing in favor of a potential influence of these receptors on chronic remodelling. Our team has recently demonstrated that transgenic mice with cardiac-specific overexpression of β3-AR were protected from hypertrophic and fibrotic remodelling due to neurohormonal stimulation (Belge, Hammond et al. 2014). Whether β3 stimulation may prevent or correct autoimmune DCM is however unknown.

Up to now, the anatomical characterization of the cardiomyopathy induced by β1-aabs has mostly been obtained by echocardiography. However, cardiac dysfunction appears slowly and frequently starts with subtle diastolic dysfunction and elevated filling pressures. With the limited accuracy and reproducibility of echocardiography, prolonged protocols with numerous animals are needed before identifying early modifications in immunized individuals.

In our work, we studied the evolution of systolic and diastolic LV function of mice submitted to β1-AR immunization with the 11.7T MRI in order to see if this technique could allow theearlier detection of remodelling induced by aabs. We also aimed to study whether β3-AR overexpressing mice were protected from cardiac remodelling induced by chronic stimulation with β1-aabs, as pharmacological agonists of the β3-AR are readily available.

3.2. Characterization of aabs-induced cardiomyopathy in C57BL/6J mice

We actively immunized 10 C57Bl/6J mice against the β1-AR through monthly subcutaneous injections of a peptide corresponding to the second extracellular loop of the receptor, for a total of 28 weeks. In parallel, 10 control animals were s.c. administered the vehicle solution.

3.2.1. Immunization

As shown in Figure 21, immunized mice showed a gradual increase of circulating antibodies directed against β1AR-EC_{II}, reaching a peak after 2 booster doses, whereas β1-aabs remained undetectable in control mice. 3 mice died in the immunized group within the first 12 weeks of protocol. All deaths occurred soon after booster injections, in animals presenting the most rapid increase in antibody titers, possibly due to occurrence of aabs-induced lethal arrhythmias (Lee, Huang et al. 2011, Zuo, Du et al. 2015) or to hemodynamic instability related to inflammatory boost. No correlation was found between the absolute antibody titer and their pathophysiological effects. All control mice survived the procedure.

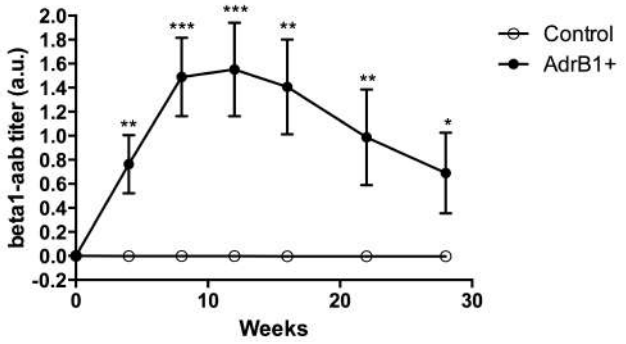

Figure 21. Titer of antibodies against β1AR-EC_{II} determined by ELISA throughout the study period, in sera of control and immunized mice. Data are represented as mean +/- SEM, and normalized to basal optical density obtained before injection. *P≤.0.05; **P≤.0.01; ***P≤.0.001 vs control.

3.2.2. Morphometric measurements

Ex vivo morphometric measurements performed at 28 weeks of follow-up after sacrifice of the animals showed a statistically significant increase in the LV/TL ratio of mice immunized against the β1AR-EC_{II} compared to control mice (5.6±0.1 vs 5.0±0.1 mg/mm; p<0,05) (Figure 22).

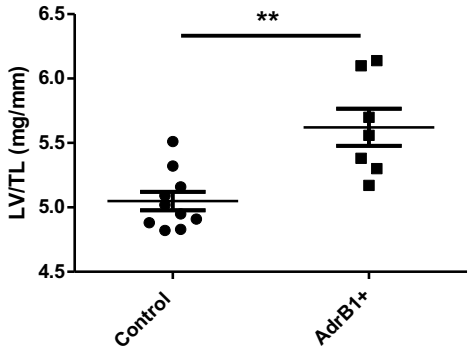

Figure 22. Morphometric LV/TL ratio at 28 weeks in C57Bl6J mice immunized against β1AR-ECII (AdrB1+) and their controls receiving the vehicle. **P≤.0.01

3.2.3. Histology

Histomorphometric analysis of cardiomyocytes transverse areas confirmed significantly larger myocytes with increased vascular density in β1-immunized mice (p<0.05). No differences in collagen (Sirius red labeling) or inflammatory infiltration (CD45/CD11b staining) were observed between the two groups (Figure 23).

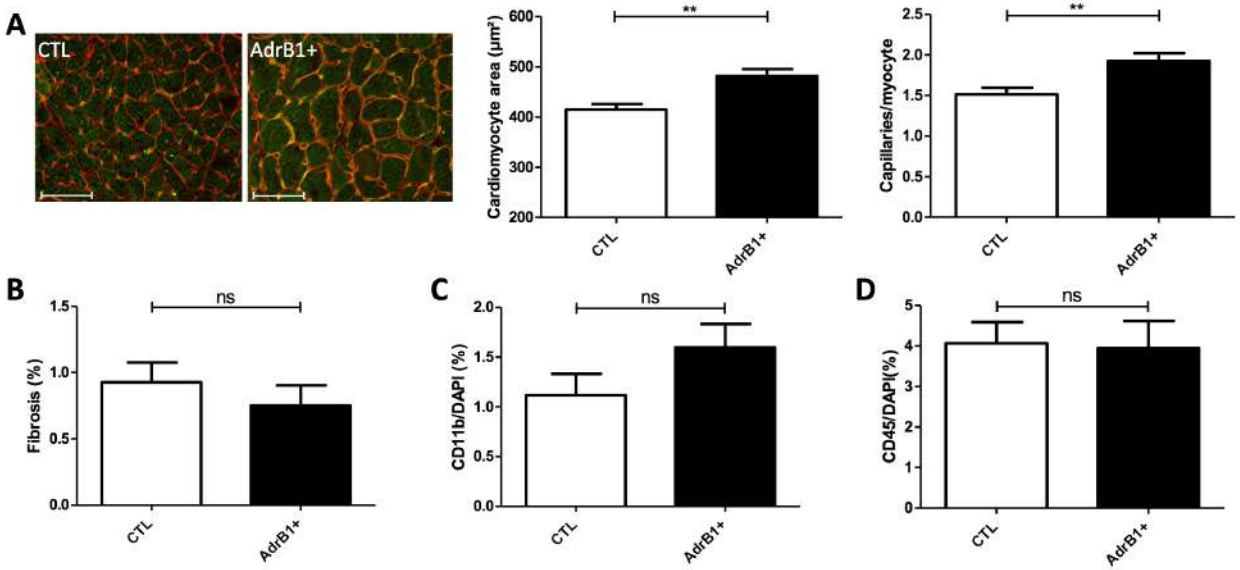

Figure 23. Histology of mouse hearts. (A) Left panel: representative cross-sections of hearts from control (CTL) and treated (AdrB1+) mice stained with isolectin B4 and wheat germ agglutinin. Scale bar, 50μm. Right panel: columns indicate the respective myocyte area and capillary density from same sections in each group, showing cardiomyocytes hypertrophy compensated by higher capillary density in hearts from immunized mice. (B) Quantification of collagen infiltration with sirius red staining. (C, D) Quantification of inflammatory infiltration with CD11b and CD45 stainings. *P≤.0.05; **P≤.0.01 vs control.

3.2.4. Cardiac transcript expression

We also performed qPCR analyses to identify changes in mRNA expression from corresponding cardiac tissues (Table 4). mRNA expression of βAR-1 and -2 (ADRB1-2) remained unchanged between control and immunized group while a two-fold increase in βAR-3 gene expression (ADRB3) was observed in the immunized group (although not reaching statistical significance, Table 4). No re-expression of the fetal gene program was found based on the levels of myosin heavy chains (MYH6 and MYH7 coding for the alpha and beta isoform, respectively) and natriuretic peptides (ANP and BNP for atrial and brain forms, respectively), a trend toward an increase in the BNP gene expression was however obeserved in β1-immunized mice (p=0.07, Table 4).

Table 4. mRNA expressions in heart lysates after 28 weeks of treatment

Gene	Control	Immunized mice	p-value
Adrb1	0.85 ± 0.06	0.83 ± 0.08	0.87 (ns)
Adrb2	0.87 ± 0.06	0.81 ± 0.06	0.60 (ns)
Adrb3	0.36 ± 0.11	0.73 ± 0.14	0.11(ns)
Myh6	0.79 ± 0.27	1.24 ± 0.46	0.39(ns)
Myh7	1.98 ± 0.61	1.27 ± 0.52	0.4(ns)
Nppa	1.04 ± 0.20	1.19 ± 0.25	0.65(ns)
Nppb	0.36 ± 0.04	0.66 ± 0.17	0.07(ns)

Data are represented as mean±SEM, mRNA expressions in β1-immunized mice (n=7) are normalized to expression measured in control mice (n=10).

3.3. Characterization of aabs-induced cardiomyopathy in β3TG mice

19 heterozygote male mice overexpressing the human β3-AR (β3TG) and 21 wild-type littermate controls (β3WT) of identical age and sex were then studied. 12 mice of each group were monthly immunized under light anaesthesia with isoflurane. No retroorbital- blood was taken at the same time, in order to avoid excessive stress in the animals. 16 mice receiving the vehicle were used as controls only.

5 mice died in each group with active immunization against β1AR-ECII, with 7 remaining animals in both groups at the end of the protocol. One mouse died in the control group.

Ex vivo measurements at 28 weeks showed statistically significant difference between the two immunized groups, with a clear decrease in LV/TL ratio in transgenic immunized mice compared to wild-type animals (5.1±0.99 vs 4.4±0.5 mg/mm; $p<0,05$; see Fig 26 below).

No differences in myocyte transverse section and collagen infiltration were observed between the groups.

3.4. Application of UHF MRI techniques

3.4.1. Left ventricular systolic function assessment

a) C57Bl6JL/ mice

In our study with C57BL/6J mice, we were able to show with UHF MRI the first cardiomyopathic changes as soon as 10 weeks after immunization against the β1-AR, whereas previous studies using echocardiography documented the first anatomical changes at 25 weeks (Buvall, Tang et al. 2007). Furthermore, LV hypertrophy (increase in LV/TL ratio) was detected before transition to the complete phenotype of DCM (Iwata, Yoshikawa et al. 2001) (Figure 24 and 25, Table 5).

Table 5. *In vivo* MRI parameters in mice at 10, 18 and 27 weeks and *ex vivo* data for LV mass and LV/TL after sacrifice at 28 weeks.

	10 weeks		18 weeks		27 weeks	
	CTL	AdrB1+	CTL	AdrB1+	CTL	AdrB1+
n	10	9	10	7	10	7
EDV (µl)	56,4 ± 1,6	64,2 ± 3,8	59,6 ± 1,5	69,1 ± 4,3*	57,2 ± 1,2	67,3 ± 2,5**
ESV (µl)	24,0 ± 2,5	22,9 ± 2,0	27,0 ± 13,8	32,0 ± 14,0	22,0 ± 1,5	29,0 ± 4**
SV (µl)	32,6 ± 2,3	41,4 ± 3,2*	29,0 ± 16,3	41,0 ± 21,0	35,3 ± 1,0	39,6 ± 2,6
EF (%)	57,7 ± 4,0	64,1 ± 2,7	51,0 ± 15,5	59 ± 7,0	61,8 ± 1,1	58,7 ± 2,4
LV mass MRI (mg)	74,1 ± 1,7	81,1 ± 2,1*	74,8 ± 1,4	83,9 ± 3,6*	75,9 ± 1,1	88,0 ± 2,0****
LV/TL MRI (mg/mm)	3,8 ± 0,1	4,2 ± 0,1*	3,9 ± 0,1	4,4 ± 0,2**	3,9 ± 0,07	4,6 ± 0,1***
ES septum thickness (mm)	1,5 ± 0,1	1,3 ± 0,1	1,2 ± 0,1	1,4 ± 0,1	1,4 ± 0,1	1,4 ± 0,1
LV mass ex vivo (mg)					97,9 ± 1,9	107,5 ± 2,7**
LV/TL ex vivo (mg/mm)					5,0 ± 0,1	5,6 ± 0,1**

n represents the number of animals in each group.
SV=stroke volume; EF=ejection fraction; LV=left ventricle; TL= tibial length; ES=end-systolic.
***P≤.0.05; **P≤.0.01; ***P≤.0.001; ****P≤0.0001 vs control.**

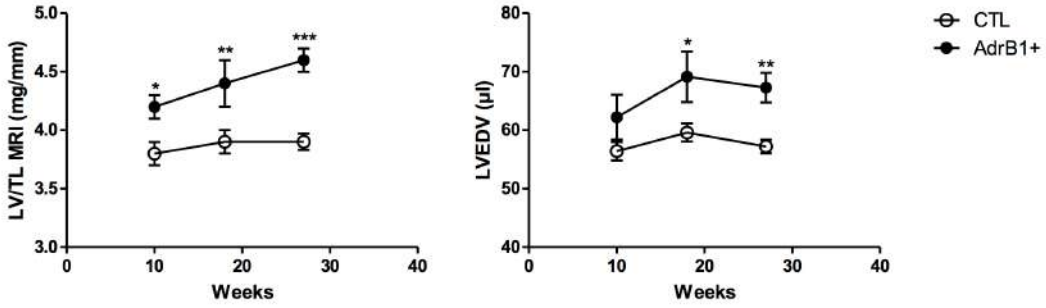

Figure 24. MRI follow-up of LV mass/tibial length ratio (LV/TL), end-diastolic volume (EDV) in immunized and control mice. Error bars indicate plus or minus SEM. *P≤.0.05; **P≤.0.01; ***P≤.0.001 vs control.

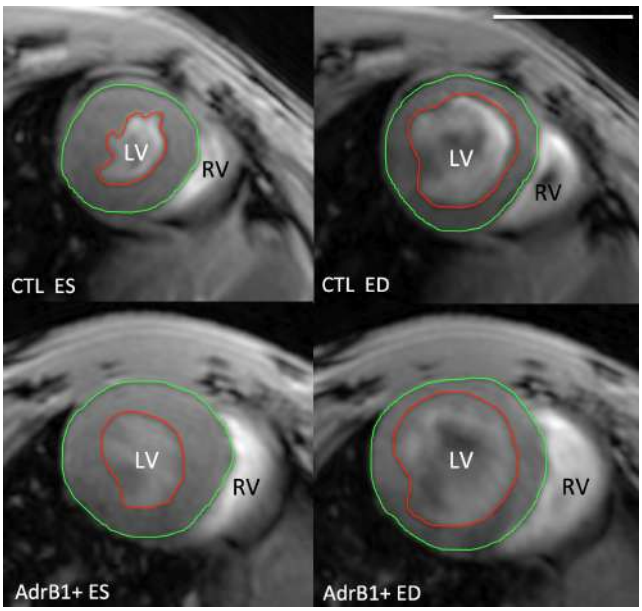

Figure 25. Representative MRI short-axis views of mouse hearts after 27 weeks of evolution in end-diastolic (ED) and end-systolic (ES) phases, with endocardial (red) and epicardial (green) contours, showing left ventricular dilation in β1-immunized mice (AdrB1) vs control (CTL). LV = left ventricle, RV = right ventricle. Scale bar represents 500µm.

b) β3TG mice

MRI measurements after 27 weeks showed statistically significant difference between the two immunized groups: LV/TL ratio remained unaltered in immunized β3-overexpressing mice compared to immunized wild-type animals, reaching values of 3.5±0.2 vs 4.3±0.2 mm/mg ($p<0.05$), respectively (Figure 26, left panel). These data were confirmed by *ex vivo* LV/TL measurements after sacrifice of the animal (right panel). Other sytolic function parameters were not modified compared to control group after 27 weeks of follow-up.

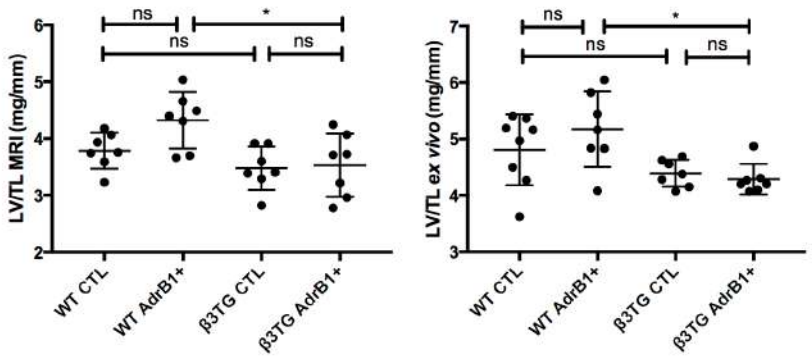

Figure 26. (A) MRI LV/TL ratio at 27 weeks in transgenic mice overexpressing the beta3 adrenergic receptor and immunized (TG AdrB1+) or not (TG CTL) against AdrB1-ECII, and their wild-type littermates with (WT AdrB1+) or without (WT CTL) immunization. (B) *Ex vivo* LV/TL ratio obtained at 28 weeks after sacrifice in the same animals. *P≤.0.05.

3.4.2. Left ventricular diastolic function assessment

Diastolic dysfunction is defined as a condition in which abnormalities in mechanical function are present during diastole. These abnormalities can occur in the presence or absence of a clinical syndrome of heart failure and with preserved systolic function or not (Zile and Brutsaert 2002). Whatever its severity, it is associated with marked increase in all-causes mortality, independent of age, sex and EF (Redfield, Jacobsen et al. 2003). The increase in the reported prevalence and incidence of diastolic

dysfunction, and its significant impact on morbidity and mortality, underscore the necessity of screening and understanding this condition using imaging techniques.

Contrary to systolic function evaluation, diastolic function assessment by CMR in rodents remains challenging. Clinical CMR techniques include determination of time-volume or time-area curves from the classical functional sequences, measurements of mitral and pulmonary valve inflow velocities or myocardial tagging in order to assess diastolic "untwisting" (Daneshvar, Wei et al. 2010). If some of these methods are difficult to transfer to small animals, time-area curves based techniques are easily accessible. Here, we aimed to test the feasibility of this approach in our mouse models of cardiomyopathies.

We applied the method described by Drelicharz et al. (Drelicharz, Wozniak et al. 2009) to our different models of cardiomyopathies in order to extract systolic and diastolic functional index from time-area curves with 25 phases per cardiac cycles, showing that we could obtain consistent results (Figure 27).

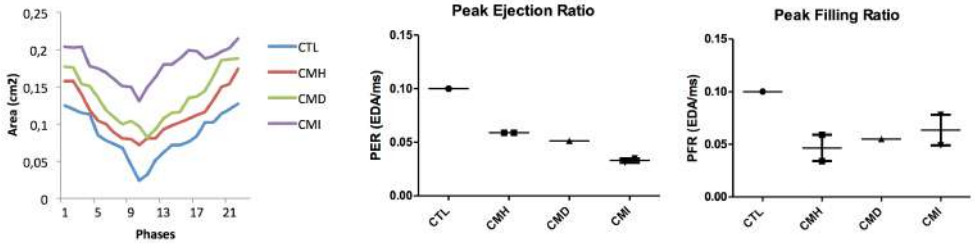

Figure 27. LV function parameters calculated from time-area curves. The curve was obtained by plotting the LV midventricular slice area against the time after R-wave (left). LV area was normalized against the individual end-diastolic area (EDA). Peak ejection ratio (PER) and peak filling ratio (PFR) were estimated as slopes from the systolic and diastolic limb and expressed in EDA/ms. Curves are obviously blunted in mice with cardiomyopathies, with attenuation of the systolo-diastolic inflection. Highest volumes (and dilation) are obtained in DCM and ICM. PER was impaired (middle), which correlated well with systolic dysfunction assessed by classical analysis. Impaired PFR (right) is a reflection of poor lusitropic response. CTL=control mice; DCM= dilated cardiomyopathy; HCM= hypertrophic cardiomyopathy; ICM= ischaemic cardiomyopathy.

As the time-area curves method remains time-consuming, we preferred to use the other simplified approach based on measurements of systolic and diastolic indexes. After internal validation on various models of cardiomyopathies, the method was applied to the C57Bl6JL/ mice immunized against the β1-AR and the control animals. We were able to show progressive development of diastolic dysfunction in immunized mice, with an impaired diastolic index compared to control mice at 27 weeks of follow-up (51.4±1.1% vs 63.1±4.3%; $p<0.05$) whereas systolic function, assessed both by EF and systolic indexes remained within normal values in the immunized group (Figure 28).

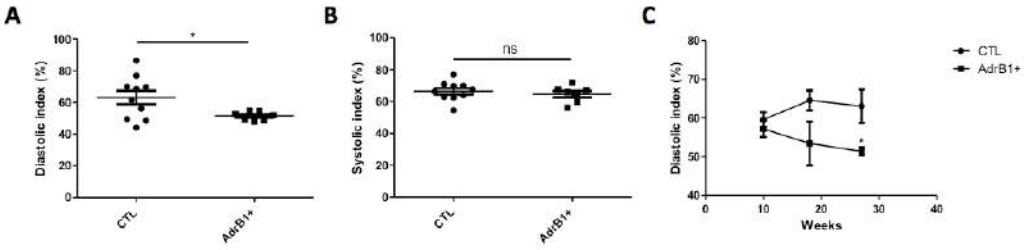

Figure 28. MRI diastolic (A) and systolic indexes (B) in mice immunized against the β1-adrenoreceptor (AdrB1+) and in control animals (CTL), after 27 weeks of follow-up. Time-course of diastolic index is shown in C, highlighting progressive impairment of diastolic function in immunized animals. Error bars indicate plus or minus SEM. *P≤.0.05 vs control.

Interestingly, diastolic indexes measurements reinforced first cardiac function data obtained in immunized mice overexpressing the human β3TG mice and their controls. First, significant differences between the two immunized groups were observed as soon as 18 weeks. Second, while LV/TL ratio measurements only revealed a trend towards an increase in control littermates of transgenic animals, diastolic indexes revealed a significant reduction after 27 weeks, confirming the earliness of diastolic dysfunction detection (Fig.29).

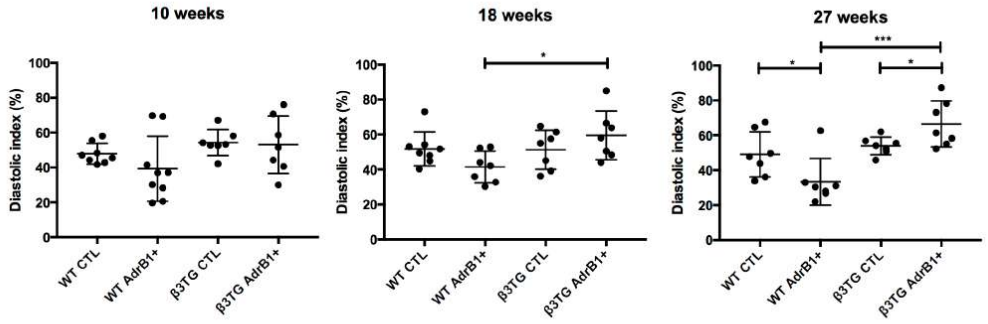

Fig 29. Diastolic indexes determined at 10, 18 and 27 weeks in transgenic mice overexpressing the β3- adrenergic receptor and immunized (β3TG AdrB1+) or not (β3TG CTL) against β1-ECII, and their wild-type littermates with (WT AdrB1+) or without (WT CTL) immunization. *P≤.0.05 ; ***P≤.0.001.

Chapter V - CONCLUSIONS

We demonstrated the feasibility and interest of UHF MRI techniques for cardiovascular investigation in mouse models of cardiomyopathies of various origins.

1. Left ventricular function data obtained with UHF MRI are accurate and reproducible

Up to now, high-frequency echocardiography remained the most widely used technique to characterize the cardiac phenotype of rodents. Although few data are available in the literature on its reproducibility [22-25], it is generally accepted that its intra and interobserver variability is low for most ventricular measurements (<20%, [26]). However, it is also known that this method is less efficient in the presence of abnormal ventricular geometry and heterogeneous regional myocardial function [26-28] which is often the case in animal models of cardiovascular diseases. Approaches such as echocardiography using geometrical assumptions to evaluate left ventricular function are not as accurate as data coming from a full volume acquisition, as it is the gold standard in CMR imaging [15]. In a rat model of myocardial infarction, Stuckey et al. showed that 2D-echo was indeed less reproducible than 11.7 Tesla MRI [13], in a vertical bore magnet acquiring 28-40 frames per heart cycle.
Studies comparing measurement obtained with echocardiography and MRI in a model are scarce [13,28], but overall they suggest that end-diastolic dimensions and LV wall thickness are poorly correlated. This could be at least in part explained by the better delineation of cardiac trabeculations in CMR imaging, and better temporal resolution [27]. Similarly, studies comparing the evaluation of left ventricular function in mice by MRI or conductance microcatheter (Millar) have shown a striking underestimation of absolute volumetric values with the catheter method [29,30], influenced by the calibration technique used [30]. These pitfalls further suggest that it is not wise to

compare LV measurements obtained with different techniques in various experimental groups.

Development of ultra high field MRI systems (≥7.0 Tesla) over the past decade has brought new perspectives in small animals imaging. As there is a direct relationship between the main field strength (B_0) and the signal to noise ratio (S/N), higher field provides better imaging quality and improve spatial and temporal resolution or acquisition speed. Hence, most pioneering CMR laboratories currently work on 7 or 9 Tesla systems [9], and they are likely to transition to even higher fields in the near future. If some reproducibility data on CMR in rodents are available, they mainly report very small numbers of animals (n<10) [10-12], including rats [12-13], field strengths ≤ 7 Tesla [14] or vertical bores [11-13], the latter representing a less physiological environment. Overall, this does not really reflect the current use of ultra high field MRI for the characterization of experimental models in cardiovascular research. Moreover, interexperiment variability is not reported in most studies, including that of Heijman et al [14], which reported the most sizable number of mice (n=22), at 6.3T. Therefore, we believe that our reproducibility data obtained with an horizontal bore at 11.7 Tesla on a group of more than 20 mice brings additional material for the validation of the technique.

Indeed, in our study, including healthy mice and a model of hypertrophic cardiomyopathy, intraobserver, interobserver and interexperiment reproducibility was good for LV mass, LV/TL and EDV (CoV between 5,4 and 11,8%). These results are consistent with the few data available in the experimental field [10-15], although different statistical tests do not allow a thorough comparison, but coefficients of variability remain higher than those obtained in humans [31]. If the reproducibility of ESV, SV and EF is less satisfactory, various factors may account for these differences. First, differences of contour tracings in the basal and apical sections were often seen at the time of postprocessing because myocardial limits are less clearly visible at these levels. Secondly, at least when studying interexperiment variability, an additional potential source of error in the determination of volumes could have been introduced by the partial volume effect due to a finite slice thickness. Finally, and above all, there

was an important scale effect: any tiny variation in measurements had enormous repercussions on the reproducibility of the data, as it related to very small volumes (µl). This explains why the smallest volumes, especially the SV, suffered the most variability. This highlights the need to develop stronger sequences to adequately measure SV and cardiac output in mice. In particular, a phase-contrast angiography sequence applied on the ascending aorta could be more appropriate for direct measurement of the SV and, subsequently, the EF [32].

When morphometric and CMR imaging LV measurements were compared, both showed a strong correlation and were able to demonstrate similar differences in LV mass or LV/TL between our experimental groups. However, LV mass estimated by CMR was consistently smaller in absolute values than those obtained *ex vivo*. The one week delay between MRI examination and sacrifice for morphometric evaluation could in part account for this discrepancy. But this is also very likely related to the great accuracy of CMR post-processing, allowing to exclude from the analysis intraventricular blood and tissues not belonging to the LV, whereas those may have been mistakenly included in the morphometric measurements.

In conclusion, our work showed that the mouse LV systolic function can be assessed on an 11.7T MRI scanner, with an excellent reproducibility of LV mass and end-diastolic volumes analysis, allowing longitudinal phenotypic evaluation of animals with healthy or hypertrophic myocardium. Furthermore, *in vivo* LV mass MRI measurements were constantly in line with *ex vivo* morphometric data, bringing evidence that high-field CMR imaging is not only reproducible but also accurate. Importantly, we highlighted the need to interpret CMR data by taking into account their shortcomings, focusing on LV mass and LV EDV as parameters that are not only the most reproducible but also the most relevant in various pathophysiological conditions such as cardiac remodelling and hypertrophy.

2. UHF MRI allows to detect subtle recovery signs in a mouse model of ischaemic cardiomyopathy treated with modified cardiac stem cells

Myocardial infarction remains a major public health issue. Healing of the infarcted myocardium proceeds through remodelling of the remaining tissue and, to a limited extent, regeneration of lost cardiac muscle. Both processes involve activation of endogenous cardiac progenitor cells in cardiac niches that, upon specific stimuli, undergo proliferation and differentiation toward vascular or muscle lineages and release paracrine factors acting on neighboring cells to modulate tissue repair (Sanganalmath and Bolli 2013). Hence, over years, stem cell therapy has emerged as new perspective of treatment and studies concerning the healing effect of modified cardiac progenitor cells on experimental models of myocardial infarction have exploded. Unfortunatelly, regarding poor stem cell regenerative capacity and their modest ability to improve cardiac function, perspectives of achievement in humans remain modest up to now, even if significant progress continues to be made (Nguyen, Rhee et al. 2016). As MRI techniques provide direct characterization of the cardiac phenotype in 3D, and novel sequences allow specific functional investigations, they may bring aditional information in such experimental models characterized by abnormal ventricular geometry, compared to conventional techniques such as echocardiography.

In a collaborative work, we examined with UHF MRI the effects of the injection of epigenetically modified CSC on the function of infarcted hearts. After rationnalizing data to the number of dyskinetic segments caused by LAD ligation, we showed that there was no difference in the recovery of dyskinetics segments between treated and control mice. Besides, we highlighted that CSC-treated mice regained better stroke volume one month after the intervention and retained a better LV wall thickness in the infarcted zone. These results are in line with other biological findings, showing potential therapeutic interest for cardiac repair. One can assume that such subtle changes could have been ignored by the usual techniques such as echocardiography.

3. UHF MRI allows better characterization of a mouse model of dilated cardiomyopathy induced by β1-aabs

The major findings of this study are related to the application of UHF MRI technology to study the early development of β1aabs-driven autoimmune cardiac dysfunction and to the identification of β3-counterbalancing pathway preventing the occurrence of DCM in this model.

3.1. UHF MRI allows early characterization of aabs-induced structural modifications

Previous studies using echocardiography have reported the first anatomical changes at rest in β1-immunized BalbC (Buvall, Tang et al. 2007) and C57BL/6J mice (Ma, Premaratne et al. 2012) at 25 weeks. In our study using UHF MRI, we were able to show first aabs-induced cardiomyopathic changes in β1-AR-immunized C57BL/6J mice after 10 weeks. In accordance with the preliminary observation of Iwata et al, LV hypertrophy (increase in LV/TL ratio) was detected before transition to the complete phenotype of DCM (Iwata, Yoshikawa et al. 2001).

3.2. UHF MRI allows early assessment of aabs-induced functional modifications

We applied a recently described method based on the concepts of echocardiographic color kinesis (Okayama, Nakano et al. 2013, Buonincontri, Hu et al. 2014) in order to derive systolic and diastolic indexes in our animals. We found that diastolic dysfunction was detectable before systolic dysfunction. These results open new perspectives for clinical investigations in patients carrying β1-aabs. Indeed, several methods (i.e. echographic speckle tracking and MR tagging (Daneshvar, Wei et al. 2010)) are available now besides the classical echocardiographic E/A measurements in order to thoroughly investigate diastolic function in patients. If these data are confirmed by further clinical studies, appearance of diastolic dysfunction in β1-aabs-positive patients could be used as an early marker of evolution to heart failure, resulting in an intensification of treatments.

3.3. Overexpression of β3-AR protects from cardiac remodelling induced by β1-aabs

Besides the above technological benefits of UHF MRI applied to autoimmune DCM, we showed that transgenic mice harboring a cardiac-specific human β3-AR transgene were protected from myocardial dysfunction induced by β1-aabs. Of note, although only a trend to cardiac dilation (ie, increased LV/TL ratio) was detectable in the immunized WT group (vs non-immunized mice) at the end of our study (unlike in C57Bl/6J mice), a significant reduction in the diastolic index confirmed the development of autoimmune cardiac alterations in these mice. Different genetic backgrounds are likely to account for this discrepancy but this observation also emphasises the earliness of the diastolic dysfunction in autoimmune DCM. In β3-overexpressing mice, the diastolic index was not decreased in response to immunization (and was even slightly increased). Altogether, these data indicate a significant protective effect of β3-AR against the development of heart damages induced by β1-aabs (vs immunized WT mice) and thereby open new therapeutic perspectives in the treatment of autoimmune DCM.

As β3-AR have functionally opposite effects to β1-AR and β2-AR on cardiac muscle and are more resistant than β1-AR and β2-AR to homologous desensitization (Liggett, Freedman et al. 1993) they represent attractive candidates for efficient pharmacological modulation in the diseased heart (Balligand 2009). Recent data published by our lab have already shown that β3TG mice were protected against cardiomyopathic changes induced by neurohormone infusion (i.e. angiotensin II or isoproterenol) (Belge, Hammond et al. 2014). The present study confirms the beneficial effects of β3-adrenergic stimulation to prevent the development of DCM. In addition to attenuating β1-β2-adrenergic inotropic responses, NO production due to β3-AR stimulation may benefit left ventricular diastolic function at early stages of cardiac dysfunction, by improving diastolic relaxation, thereby exerting a beneficial hemodynamic effect through maintenance of the Frank-Starling response (Heymes, Vanderheyden et al. 1999). The latter property seems even more relevant for the treatment of β1-aabs-

induced cardiomyopathy in light of early diastolic dysfunction reported in our C57Bl6L/J mice immunized against β1-ECII.

A limitation in our study is the use of transgenic β3-AR-overexpressing mice which per se means that this pathway is continuously influencing the cardiac phenotype of these animals and may thus prevent a dysfunction by acting from the earliest stages of its development. Still, these results pave the way for the evaluation of *bona fide* β3-AR agonists or the preferred use of β-blockers endowed with such β3-AR stimulatory activity in the treatment of autoimmune β1-aabs-induced DCM. Nebivolol represents a third generation selective β1-AR antagonist with ancillary metabolic effects involving a β3-AR stimulation. Nebivolol could thus bring an increment of efficacy *vs.* conventional beta-blockers (i.e. bisoprolol) whose usefulness has already been demonstrated in the context of β1-aabs-induced DCM (with however a lower efficiency than therapies neutralizing peptides) (Boivin, Beyersdorf et al. 2015). The team of Chantal Dessy previously showed that nebivolol treatment of coronary microvessels led to NO-dependant vasorelaxation (Dessy, Saliez et al. 2005) while others documented a further protection of nebivolol administration against endothelial dysfunction through a net reduction of oxidative stress (Mason, Kalinowski et al. 2005). Altogether, these studies suggest that the dual β1/ β3-AR modulation, already demonstrated in previous studies for heart failure and myocardial infarction with Nebivolol (vs metoprolol) (Sorrentino, Doerries et al. 2011), could thus be extended to patients with β1-aabs-induced DCM.

Chapter VI – PERSPECTIVES

1. Further development of UHF MRI sequences at 11.7T for the characterization of murine models of cardiomyopathy

In comparison to the available and "ready-to-use" echocardiography, UHF MRI remains a cumbersome technique, which requires bulky and expensive equipment, and a significant expertise for the development and analysis of sequences. Although it struggles to be used in all cardiovascular research platforms, the technique is not unaffordable and may certainly benefit from a multidisciplinary approach. Imaging platforms bringing the expertise of scientists from various fields is certainly an asset in this context.

In our case, it seems worthwhile to finalize the development of the phase-contrast MR sequence in order to allow flow measurements in all dimensions. This implies a preliminary study using a flow fantom in order to determine a specific constant for the 11.7T machine and to use a pixel-by-pixel method as described by Kim and colleagues (Kim, Seo et al. 2010) to measure the flow velocity from phase-contrast images. Measurements could then be automated with dedicated software. The accuracy of myocardial tagging in mouse could also be studied as far as the HARP software is available, as tagged images can be easily produced.

Despite the many challenges encountered when moving to higher field strength and small animal imaging, UHF MRI has undoubtedly become an essential technique in cardiovascular research, as evidenced by the extensive literature on the subject in recent years. We may anticipate that because of the huge ongoing development in the field, further refinement of the technique will allow even wider opportunities to track the pathophysiological phenotypes of experimental animals.

2. Investigating the β1-aabs-induced cardiomyopathy

If there is no longer any doubt about the cardio-pathogenic role of β1-aabs, their real prevalence and exact clinical significance remains to be assessed by large-scale clinical studies. The ETiCS study (Deubner, Berliner et al. 2010) is currently addressing this issue in patients suffering from different heart diseases by means of a previously validated highly sensitive fluorescence-based functional assay in order to detect only functionally active β1-aabs. The trial, conducted is several european center, is designed as followed: a prospective part will enrol 200 patients with acute myocarditis and 200 patients with acute myocardial infarction, in order to test the hypotheses that agonist-like-β1-aabs may arise following a first acute inflammatory or ischaemic event and that these aabs may have an impact on cardiac function and patient outcome. Meanwhile, a retrospective part will determine the prevalence and titre-course of β1-aabs in 900 well-characterized patients with ichaemic (n=300) or dilated cardiomyopathy (n=400) and hypertensive heart disease (n=200), enrolled in different trials of the German Competence Network. During their one-year follow-up, beside screening of β1-aabs, all patients will undergo regular evaluation including quality of life questionnaire SF36, patient health questionnaire PHQ-9, clinical examination, ECG, Holter-ECG, echocardiography and cardiac MRI.

In the present work, we showed that β1-aabs accounted for left ventricular diastolic dysfunction before the onset of systolic dysfunction. Investigating the diastolic function of patients harboring these antibodies with available echocardiographic (E/A ratio or speckle-tracking) or MRI techniques (vector-based methods) would certainly make sense as it has not been reported up to now and may have a significant impact on the follow-up and treatment.

Moreover, we showed that stimulation of the β3-adrenoreceptor blunted the development of β1-aabs-induced DCM, making it an attractive therapeutic target. Therefore, beta-blockers with β3-agonist activity such as nebivolol or specific pharmacological β3-agonists such as mirabegron should be considered in further pre-clinical and clinical studies.

3. Clinical perspectives in the Pediatric Cardiology Department

In clinical facilities, standardized MRI protocols are often used, with restrained access to parameters. Learning experimental MRI helps to better understand principles underlying image acquisitions and to refine and customize protocols in order to improve image quality, scan time and resolution for specific applications. It also opens to new opportunities of sequence development. Hence, several clinical applications may emerge from this work.

Particularly, little is known about right ventricular and diastolic function in patients with congenital heart diseases. Yet recent data suggest that it could bring new insights into our clinical care (Leong, De Pasquale et al. 2010, Tadic 2015, Panesar and Burch 2017). In the UCL Pediatric Cardiology Department, we plan to determine diastolic index using the technique described in this work in specific groups of CHD patients, as sequential MR short axis functional sequences are already available in our clinical database. We also intend to develop tagging or other strain measurement technique in the near future.

REFERENCES

Arbustini, E., N. Narula, L. Tavazzi, A. Serio, M. Grasso, V. Favalli, R. Bellazzi, J. A. Tajik, R. O. Bonow, V. Fuster and J. Narula (2014). "The MOGE(S) classification of cardiomyopathy for clinicians." J Am Coll Cardiol **64**(3): 304-318.

Balligand, J. L. (2009). "beta(3)-Adrenoceptor stimulation on top of beta(1)-adrenoceptor blockade "Stop or Encore?"." J Am Coll Cardiol **53**(17): 1539-1542.

Belge, C., J. Hammond, E. Dubois-Deruy, B. Manoury, J. Hamelet, C. Beauloye, A. Markl, A. C. Pouleur, L. Bertrand, H. Esfahani, K. Jnaoui, K. R. Gotz, V. O. Nikolaev, A. Vanderper, P. Herijgers, I. Lobysheva, G. Iaccarino, D. Hilfiker-Kleiner, G. Tavernier, D. Langin, C. Dessy and J. L. Balligand (2014). "Enhanced expression of beta3-adrenoceptors in cardiac myocytes attenuates neurohormone-induced hypertrophic remodeling through nitric oxide synthase." Circulation **129**(4): 451-462.

Bland, J. M. and D. G. Altman (1986). "Statistical methods for assessing agreement between two methods of clinical measurement." Lancet **1**(8476): 307-310.

Bohl, S., C. A. Lygate, H. Barnes, D. Medway, L. A. Stork, J. Schulz-Menger, S. Neubauer and J. E. Schneider (2009). "Advanced methods for quantification of infarct size in mice using three-dimensional high-field late gadolinium enhancement MRI." Am J Physiol Heart Circ Physiol **296**(4): H1200-1208.

Boivin, V., N. Beyersdorf, D. Palm, V. O. Nikolaev, A. Schlipp, J. Muller, D. Schmidt, V. Kocoski, T. Kerkau, T. Hunig, G. Ertl, M. J. Lohse and R. Jahns (2015). "Novel receptor-derived cyclopeptides to treat heart failure caused by anti-beta1-adrenoceptor antibodies in a human-analogous rat model." PLoS One **10**(2): e0117589.

Buonincontri, G., C.-H. Hu, S. Sawiak and T. Krieg (2014). P516Diastolic dysfunction in diabetic mice revealed by MRI.

Buvall, L., E. Bollano, J. Chen, W. Shultze and M. Fu (2006). "Phenotype of early cardiomyopathic changes induced by active immunization of rats with a synthetic peptide corresponding to the second extracellular loop of the human beta-adrenergic receptor." Clin Exp Immunol **143**(2): 209-215.

Buvall, L., M. S. Tang, A. Isic, B. Andersson and M. Fu (2007). "Antibodies against the beta1-adrenergic receptor induce progressive development of cardiomyopathy." J Mol Cell Cardiol **42**(5): 1001-1007.

Cerqueira, M. D., N. J. Weissman, V. Dilsizian, A. K. Jacobs, S. Kaul, W. K. Laskey, D. J. Pennell, J. A. Rumberger, T. Ryan, M. S. Verani, S. American Heart Association Writing Group on Myocardial and I. Registration for Cardiac (2002). "Standardized myocardial segmentation and nomenclature for tomographic imaging of the heart. A statement for healthcare professionals from the Cardiac Imaging Committee of the Council on Clinical Cardiology of the American Heart Association." Circulation **105**(4): 539-542.

Christ, T., E. Wettwer, D. Dobrev, E. Adolph, M. Knaut, G. Wallukat and U. Ravens (2001). "Autoantibodies against the beta1 adrenoceptor from patients with dilated cardiomyopathy prolong action potential duration and enhance contractility in isolated cardiomyocytes." J Mol Cell Cardiol **33**(8): 1515-1525.

Daneshvar, D., J. Wei, K. Tolstrup, L. E. Thomson, C. Shufelt and C. N. Merz (2010). "Diastolic dysfunction: improved understanding using emerging imaging techniques." Am Heart J **160**(3): 394-404.

De Pauw, A., E. Andre, B. Sekkali, C. Bouzin, H. Esfahani, N. Barbier, A. Loriot, C. De Smet, L. Vanhoutte, S. Moniotte, B. Gerber, V. di Mauro, D. Catalucci, O. Feron, D. Hilfiker-Kleiner and J. L. Balligand (2017). "Dnmt3a-mediated inhibition of Wnt in cardiac progenitor cells improves differentiation and remote remodeling after infarction." JCI Insight **2**(12).

De Pauw, A., B. Sekkali, A. Loriot, C. De Smet, D. Catalucci, D. Hilfiker-Kleiner and J.-L. Balligand (2014). P587MiR-29a controls cardiac stem cells differentiation through Dnmt3a-mediated extinction of Wnt/beta-catenin.

Dessy, C., J. Saliez, P. Ghisdal, G. Daneau, Lobysheva, II, F. Frerart, C. Belge, K. Jnaoui, P. Noirhomme, O. Feron and J. L. Balligand (2005). "Endothelial beta3-adrenoreceptors mediate nitric oxide-dependent vasorelaxation of coronary microvessels in response to the third-generation beta-blocker nebivolol." Circulation **112**(8): 1198-1205.

Deubner, N., D. Berliner, A. Schlipp, G. Gelbrich, A. L. Caforio, S. B. Felix, M. Fu, H. Katus, C. E. Angermann, M. J. Lohse, G. Ertl, S. Stork, R. Jahns, T.-C. Etiology and G. Survival-Study (2010). "Cardiac beta1-adrenoceptor autoantibodies in human heart disease: rationale and design of the Etiology, Titre-Course, and Survival (ETiCS) Study." Eur J Heart Fail **12**(7): 753-762.

Dincer, U. D., K. R. Bidasee, S. Guner, A. Tay, A. T. Ozcelikay and V. M. Altan (2001). "The effect of diabetes on expression of beta1-, beta2-, and beta3-adrenoreceptors in rat hearts." Diabetes **50**(2): 455-461.

Drelicharz, L., M. Wozniak, T. Skorka, U. Tyrankiewicz, S. Heinze-Paluchowska, M. Jablonska, A. Gebska and S. Chlopicki (2009). "Application of magnetic resonance imaging in vivo for the assessment of the progression of systolic and diastolic dysfunction in a mouse model of dilated cardiomyopathy." Kardiol Pol **67**(4): 386-395.

Elies, R., I. Ferrari, G. Wallukat, D. Lebesgue, P. Chiale, M. Elizari, M. Rosenbaum, J. Hoebeke and M. J. Levin (1996). "Structural and functional analysis of the B cell epitopes recognized by anti-receptor autoantibodies in patients with Chagas' disease." J Immunol **157**(9): 4203-4211.

Elliott, P., B. Andersson, E. Arbustini, Z. Bilinska, F. Cecchi, P. Charron, O. Dubourg, U. Kuhl, B. Maisch, W. J. McKenna, L. Monserrat, S. Pankuweit, C. Rapezzi, P. Seferovic, L. Tavazzi and A. Keren (2008). "Classification of the cardiomyopathies: a position statement from the European Society Of Cardiology Working Group on Myocardial and Pericardial Diseases." Eur Heart J **29**(2): 270-276.

Faiella, W. and R. Atoui (2016). "Therapeutic use of stem cells for cardiovascular disease." Clin Transl Med **5**(1): 34.

Go, A. S., D. Mozaffarian, V. L. Roger, E. J. Benjamin, J. D. Berry, M. J. Blaha, S. Dai, E. S. Ford, C. S. Fox, S. Franco, H. J. Fullerton, C. Gillespie, S. M. Hailpern, J. A. Heit, V. J. Howard, M. D. Huffman, S. E. Judd, B. M. Kissela, S. J. Kittner, D. T. Lackland, J. H. Lichtman, L. D. Lisabeth, R. H. Mackey, D. J. Magid, G. M. Marcus, A. Marelli, D. B. Matchar, D. K. McGuire, E. R. Mohler, 3rd, C. S. Moy, M. E. Mussolino, R. W. Neumar, G. Nichol, D. K. Pandey, N. P. Paynter, M. J. Reeves, P. D. Sorlie, J. Stein, A. Towfighi, T. N. Turan, S. S. Virani, N. D. Wong, D. Woo, M. B. Turner, C. American Heart Association Statistics and S. Stroke Statistics (2014). "Heart disease and stroke statistics--2014 update: a report from the American Heart Association." Circulation **129**(3): e28-e292.

Gouldson, P. R., C. Higgs, R. E. Smith, M. K. Dean, G. V. Gkoutos and C. A. Reynolds (2000). "Dimerization and domain swapping in G-protein-coupled receptors: a computational study." Neuropsychopharmacology **23**(4 Suppl): S60-77.

Haberland, A., G. Wallukat, C. Dahmen, A. Kage and I. Schimke (2011). "Aptamer neutralization of beta1-adrenoceptor autoantibodies isolated from patients with cardiomyopathies." Circ Res **109**(9): 986-992.

Hebert, T. E. (2007). "Anti-beta1AR antibodies in dilated cardiomyopathy: are these a new class of receptor agonists?" Cardiovasc Res **76**(1): 5-7.

Heijman, E., J. P. Aben, C. Penners, P. Niessen, R. Guillaume, G. van Eys, K. Nicolay and G. J. Strijkers (2008). "Evaluation of manual and automatic segmentation of the mouse heart from CINE MR images." J Magn Reson Imaging **27**(1): 86-93.

Heymes, C., M. Vanderheyden, J. G. Bronzwaer, A. M. Shah and W. J. Paulus (1999). "Endomyocardial nitric oxide synthase and left ventricular preload reserve in dilated cardiomyopathy." Circulation **99**(23): 3009-3016.

Hu, P., D. Zhang, L. Swenson, G. Chakrabarti, E. D. Abel and S. E. Litwin (2003). "Minimally invasive aortic banding in mice: effects of altered cardiomyocyte insulin signaling during pressure overload." Am J Physiol Heart Circ Physiol **285**(3): H1261-1269.

Iwata, M., T. Yoshikawa, A. Baba, T. Anzai, H. Mitamura and S. Ogawa (2001). "Autoantibodies against the second extracellular loop of beta1-adrenergic receptors predict ventricular tachycardia and sudden death in patients with idiopathic dilated cardiomyopathy." J Am Coll Cardiol **37**(2): 418-424.

Iwata, M., T. Yoshikawa, A. Baba, T. Anzai, I. Nakamura, Y. Wainai, T. Takahashi and S. Ogawa (2001). "Autoimmunity against the second extracellular loop of beta(1)-adrenergic receptors induces beta-adrenergic receptor desensitization and myocardial hypertrophy in vivo." Circ Res **88**(6): 578-586.

Jahns, R., V. Boivin, L. Hein, S. Triebel, C. E. Angermann, G. Ertl and M. J. Lohse (2004). "Direct evidence for a beta 1-adrenergic receptor-directed autoimmune attack as a cause of idiopathic dilated cardiomyopathy." J Clin Invest **113**(10): 1419-1429.

Jahns, R., V. Boivin and M. J. Lohse (2006). "Beta 1-adrenergic receptor-directed autoimmunity as a cause of dilated cardiomyopathy in rats." Int J Cardiol **112**(1): 7-14.

Jahns, R., V. Boivin and M. J. Lohse (2006). "beta(1)-Adrenergic receptor function, autoimmunity, and pathogenesis of dilated cardiomyopathy." Trends Cardiovasc Med **16**(1): 20-24.

Jahns, R., V. Boivin, C. Siegmund, F. Boege, M. J. Lohse and G. Inselmann (1999). "Activating beta-1-adrenoceptor antibodies are not associated with cardiomyopathies secondary to valvular or hypertensive heart disease." J Am Coll Cardiol **34**(5): 1545-1551.

Jahns, R., V. Boivin, C. Siegmund, G. Inselmann, M. J. Lohse and F. Boege (1999). "Autoantibodies activating human beta1-adrenergic receptors are associated with reduced cardiac function in chronic heart failure." Circulation **99**(5): 649-654.

Kim, T., J. H. Seo, S. S. Bang, H. W. Choi, Y. Chang and J. Lee (2010). "Optimization of MR phase-contrast-based flow velocimetry and shear stress measurements." Int J Cardiovasc Imaging **26 Suppl 1**: 133-142.

Kober, F., I. Iltis, P. J. Cozzone and M. Bernard (2004). "Cine-MRI assessment of cardiac function in mice anesthetized with ketamine/xylazine and isoflurane." MAGMA **17**(3-6): 157-161.

Lee, H. C., K. T. Huang, X. L. Wang and W. K. Shen (2011). "Autoantibodies and cardiac arrhythmias." Heart Rhythm **8**(11): 1788-1795.

Leong, D. P., C. G. De Pasquale and J. B. Selvanayagam (2010). "Heart failure with normal ejection fraction: the complementary roles of echocardiography and CMR imaging." JACC Cardiovasc Imaging **3**(4): 409-420.

Liggett, S. B., N. J. Freedman, D. A. Schwinn and R. J. Lefkowitz (1993). "Structural basis for receptor subtype-specific regulation revealed by a chimeric beta 3/beta 2-adrenergic receptor." Proc Natl Acad Sci U S A **90**(8): 3665-3669.

Limas, C. J., I. F. Goldenberg and C. Limas (1992). "Assessment of immune modulation of beta-adrenergic pathways in human dilated cardiomyopathy: influence of methodologic factors." Am Heart J **123**(4 Pt 1): 967-970.

Ma, L. P., G. Premaratne, E. Bollano, C. Lindholm and M. Fu (2012). "Interleukin-6-deficient mice resist development of experimental autoimmune cardiomyopathy induced by immunization of beta1-adrenergic receptor." Int J Cardiol **155**(1): 20-25.

Magnusson, Y., S. Hoyer, R. Lengagne, M. P. Chapot, J. G. Guillet, A. Hjalmarson, A. D. Strosberg and J. Hoebeke (1989). "Antigenic analysis of the second extra-cellular loop of the human beta-adrenergic receptors." Clin Exp Immunol **78**(1): 42-48.

Magnusson, Y., G. Wallukat, F. Waagstein, A. Hjalmarson and J. Hoebeke (1994). "Autoimmunity in idiopathic dilated cardiomyopathy. Characterization of antibodies against the beta 1-adrenoceptor with positive chronotropic effect." Circulation **89**(6): 2760-2767.

Maron, B. J., J. A. Towbin, G. Thiene, C. Antzelevitch, D. Corrado, D. Arnett, A. J. Moss, C. E. Seidman, J. B. Young, A. American Heart, H. F. Council on Clinical Cardiology, C. Transplantation, C. Quality of, R. Outcomes, G. Functional, G. Translational Biology Interdisciplinary Working, E. Council on and Prevention (2006). "Contemporary definitions and classification of the cardiomyopathies: an American Heart Association Scientific Statement from the Council on Clinical Cardiology, Heart Failure and Transplantation Committee; Quality of Care and Outcomes Research and Functional Genomics and Translational Biology Interdisciplinary Working Groups; and Council on Epidemiology and Prevention." Circulation **113**(14): 1807-1816.

Mason, R. P., L. Kalinowski, R. F. Jacob, A. M. Jacoby and T. Malinski (2005). "Nebivolol reduces nitroxidative stress and restores nitric oxide bioavailability in endothelium of black Americans." Circulation **112**(24): 3795-3801.

Matsui, S., M. L. Fu, S. Katsuda, M. Hayase, N. Yamaguchi, K. Teraoka, T. Kurihara, N. Takekoshi, E. Murakami, J. Hoebeke and A. Hjalmarson (1997). "Peptides derived from cardiovascular G-protein-coupled receptors induce morphological cardiomyopathic changes in immunized rabbits." J Mol Cell Cardiol **29**(2): 641-655.

Matsui, S., L. Larsson, M. Hayase, S. Katsuda, K. Teraoka, T. Kurihara, H. Murano, K. Nishikawa and M. Fu (2006). "Specific removal of beta1-adrenoceptor autoantibodies by immunoabsorption in rabbits with autoimmune cardiomyopathy improved cardiac structure and function." J Mol Cell Cardiol **41**(1): 78-85.

Miao, G. B., J. C. Liu, M. B. Liu, J. L. Wu, G. Zhang, J. Chang and L. Zhang (2006). "Autoantibody against beta1-adrenergic receptor and left ventricular remodeling changes in response to metoprolol treatment." Eur J Clin Invest **36**(9): 614-620.

Mobini, R., Y. Magnusson, G. Wallukat, M. Viguier, A. Hjalmarson and J. Hoebeke (1999). "Probing the immunological properties of the extracellular domains of the human beta(1)-adrenoceptor." J Autoimmun **13**(2): 179-186.

Moniotte, S., C. Belge, B. Sekkali, P. B. Massion, B. Rozec, C. Dessy and J. L. Balligand (2007). "Sepsis is associated with an upregulation of functional beta3 adrenoceptors in the myocardium." Eur J Heart Fail **9**(12): 1163-1171.

Moniotte, S., L. Kobzik, O. Feron, J. N. Trochu, C. Gauthier and J. L. Balligand (2001). "Upregulation of beta(3)-adrenoceptors and altered contractile response to inotropic amines in human failing myocardium." Circulation **103**(12): 1649-1655.

Mortality, G. B. D. and C. Causes of Death (2015). "Global, regional, and national age-sex specific all-cause and cause-specific mortality for 240 causes of death, 1990-2013: a systematic analysis for the Global Burden of Disease Study 2013." Lancet **385**(9963): 117-171.

Munch, G., V. Boivin-Jahns, H. P. Holthoff, K. Adler, M. Lappo, S. Truol, H. Degen, N. Steiger, M. J. Lohse, R. Jahns and M. Ungerer (2012). "Administration of the cyclic peptide COR-1 in humans (phase I study): ex vivo measurements of anti-beta1-adrenergic receptor antibody neutralization and of immune parameters." Eur J Heart Fail **14**(11): 1230-1239.

Nguyen, P. K., J. W. Rhee and J. C. Wu (2016). "Adult Stem Cell Therapy and Heart Failure, 2000 to 2016: A Systematic Review." JAMA Cardiol **1**(7): 831-841.

Nichols, M., N. Townsend, P. Scarborough and M. Rayner (2014). "Cardiovascular disease in Europe 2014: epidemiological update." Eur Heart J **35**(42): 2950-2959.

Nikolaev, V. O., V. Boivin, S. Stork, C. E. Angermann, G. Ertl, M. J. Lohse and R. Jahns (2007). "A novel fluorescence method for the rapid detection of functional beta1-adrenergic receptor autoantibodies in heart failure." J Am Coll Cardiol **50**(5): 423-431.

Niu, X., V. L. Watts, O. H. Cingolani, V. Sivakumaran, J. S. Leyton-Mange, C. L. Ellis, K. L. Miller, K. Vandegaer, D. Bedja, K. L. Gabrielson, N. Paolocci, D. A. Kass and L. A. Barouch (2012). "Cardioprotective effect of beta-3 adrenergic receptor agonism: role of neuronal nitric oxide synthase." J Am Coll Cardiol **59**(22): 1979-1987.

Okayama, S., T. Nakano, S. Uemura, S. Fujimoto, S. Somekawa, M. Watanabe, T. Nakajima and Y. Saito (2013). "Evaluation of left ventricular diastolic function by fractional area change using cine cardiovascular magnetic resonance: a feasibility study." J Cardiovasc Magn Reson **15**: 87.

Panesar, D. K. and M. Burch (2017). "Assessment of Diastolic Function in Congenital Heart Disease." Front Cardiovasc Med **4**: 5.

Redfield, M. M., S. J. Jacobsen, J. C. Burnett, Jr., D. W. Mahoney, K. R. Bailey and R. J. Rodeheffer (2003). "Burden of systolic and diastolic ventricular dysfunction in the community: appreciating the scope of the heart failure epidemic." JAMA **289**(2): 194-202.

Richardson, P., W. McKenna, M. Bristow, B. Maisch, B. Mautner, J. O'Connell, E. Olsen, G. Thiene, J. Goodwin, I. Gyarfas, I. Martin and P. Nordet (1996). "Report of the 1995 World Health Organization/International Society and Federation of Cardiology Task Force on the Definition and Classification of cardiomyopathies." Circulation **93**(5): 841-842.

Rockman, H. A., R. S. Ross, A. N. Harris, K. U. Knowlton, M. E. Steinhelper, L. J. Field, J. Ross, Jr. and K. R. Chien (1991). "Segregation of atrial-specific and inducible expression of an atrial natriuretic factor transgene in an in vivo murine model of cardiac hypertrophy." Proc Natl Acad Sci U S A **88**(18): 8277-8281.

Ruff, J., F. Wiesmann, K. H. Hiller, S. Voll, M. von Kienlin, W. R. Bauer, E. Rommel, S. Neubauer and A. Haase (1998). "Magnetic resonance microimaging for noninvasive quantification of myocardial function and mass in the mouse." Magn Reson Med **40**(1): 43-48.

Sanganalmath, S. K. and R. Bolli (2013). "Cell therapy for heart failure: a comprehensive overview of experimental and clinical studies, current challenges, and future directions." Circ Res **113**(6): 810-834.

Schneider, J. E., P. J. Cassidy, C. Lygate, D. J. Tyler, F. Wiesmann, S. M. Grieve, K. Hulbert, K. Clarke and S. Neubauer (2003). "Fast, high-resolution in vivo cine magnetic resonance imaging in normal and failing mouse hearts on a vertical 11.7 T system." J Magn Reson Imaging **18**(6): 691-701.

Sorrentino, S. A., C. Doerries, C. Manes, T. Speer, C. Dessy, I. Lobysheva, W. Mohmand, R. Akbar, F. Bahlmann, C. Besler, A. Schaefer, D. Hilfiker-Kleiner, T. F. Luscher, J. L. Balligand, H. Drexler and U. Landmesser (2011). "Nebivolol exerts beneficial effects on endothelial function, early endothelial progenitor cells, myocardial neovascularization, and left ventricular dysfunction early after myocardial infarction beyond conventional beta1-blockade." J Am Coll Cardiol **57**(5): 601-611.

Staudt, Y., R. Mobini, M. Fu, S. B. Felix, J. P. Kuhn and A. Staudt (2003). "Beta1-adrenoceptor antibodies induce apoptosis in adult isolated cardiomyocytes." Eur J Pharmacol **466**(1-2): 1-6.

Stork, S., V. Boivin, R. Horf, L. Hein, M. J. Lohse, C. E. Angermann and R. Jahns (2006). "Stimulating autoantibodies directed against the cardiac beta1-adrenergic receptor predict increased mortality in idiopathic cardiomyopathy." Am Heart J **152**(4): 697-704.

Stuckey, D. J., C. A. Carr, D. J. Tyler and K. Clarke (2008). "Cine-MRI versus two-dimensional echocardiography to measure in vivo left ventricular function in rat heart." NMR Biomed **21**(7): 765-772.

Tadic, M. (2015). "Multimodality Evaluation of the Right Ventricle: An Updated Review." Clin Cardiol **38**(12): 770-776.

Tate, K., Y. Magnusson, M. Viguier, R. Lengagne, A. Hjalmarson, J. G. Guillet and J. Hoebeke (1994). "Epitope analysis of T- and B-cell response against the human beta 1-adrenoceptor." Biochimie **76**(2): 159-164.

Tavernier, G., G. Toumaniantz, M. Erfanian, M. F. Heymann, K. Laurent, D. Langin and C. Gauthier (2003). "beta3-Adrenergic stimulation produces a decrease of cardiac contractility ex vivo in mice overexpressing the human beta3-adrenergic receptor." Cardiovasc Res **59**(2): 288-296.

Tutor, A. S., P. Penela and F. Mayor, Jr. (2007). "Anti-beta1-adrenergic receptor autoantibodies are potent stimulators of the ERK1/2 pathway in cardiac cells." Cardiovasc Res **76**(1): 51-60.

Tyler, D. J., C. A. Lygate, J. E. Schneider, P. J. Cassidy, S. Neubauer and K. Clarke (2006). "CINE-MR imaging of the normal and infarcted rat heart using an 11.7 T vertical bore MR system." J Cardiovasc Magn Reson **8**(2): 327-333.

van de Weijer, T., P. A. van Ewijk, H. R. Zandbergen, J. M. Slenter, A. G. Kessels, J. E. Wildberger, M. K. Hesselink, P. Schrauwen, V. B. Schrauwen-Hinderling and M. E. Kooi (2012). "Geometrical models for cardiac MRI in rodents: comparison of quantification of left ventricular volumes and function by various geometrical models with a full-volume MRI data set in rodents." Am J Physiol Heart Circ Physiol **302**(3): H709-715.

Vanhoutte, L., B. Gallez, O. Feron, J. L. Balligand, H. Esfahani, W. d'Hoore and S. Moniotte (2015). "Variability of Mouse Left Ventricular Function Assessment by 11.7 Tesla MRI." J Cardiovasc Transl Res.

Vanhoutte, L., B. L. Gerber, B. Gallez, C. Po, J. Magat, B. Jean-Luc, O. Feron and S. Moniotte (2016). "High field magnetic resonance imaging of rodents in cardiovascular research." Basic Res Cardiol **111**(4): 46.

Vanhoutte, L., C. Guilbaud, R. Martherus, C. Bouzin, B. Gallez, C. Dessy, J. L. Balligand, S. Moniotte and O. Feron (2017). "MRI Assessment of Cardiomyopathy Induced by beta1-Adrenoreceptor Autoantibodies and Protection Through beta3-Adrenoreceptor Overexpression." Sci Rep **7**: 43951.

Vetter, V. L., T. M. Covington, N. P. Dugan, D. M. Haley, H. Dykstra, M. Overpeck, V. R. Iyer and J. Shults (2015). "Cardiovascular deaths in children: general overview from the National Center for the Review and Prevention of Child Deaths." Am Heart J **169**(3): 426-437 e423.

Wallukat, G., A. Wollenberger, R. Morwinski and H. F. Pitschner (1995). "Anti-beta 1-adrenoceptor autoantibodies with chronotropic activity from the serum of patients with dilated cardiomyopathy: mapping of epitopes in the first and second extracellular loops." J Mol Cell Cardiol **27**(1): 397-406.

Wiesmann, F., J. Ruff, S. Engelhardt, L. Hein, C. Dienesch, A. Leupold, R. Illinger, A. Frydrychowicz, K. H. Hiller, E. Rommel, A. Haase, M. J. Lohse and S. Neubauer (2001). "Dobutamine-stress magnetic resonance microimaging in mice : acute changes of cardiac geometry and function in normal and failing murine hearts." Circ Res **88**(6): 563-569.

Wiesmann, F., S. Ruff J Fau - Engelhardt, L. Engelhardt S Fau - Hein, C. Hein L Fau - Dienesch, A. Dienesch C Fau - Leupold, R. Leupold A Fau - Illinger, A. Illinger R Fau - Frydrychowicz, K. H. Frydrychowicz A Fau - Hiller, E. Hiller Kh Fau - Rommel, A. Rommel E Fau - Haase, M. J. Haase A Fau - Lohse, S. Lohse Mj Fau - Neubauer and

S. Neubauer (2001). "Dobutamine-stress magnetic resonance microimaging in mice : acute changes of cardiac geometry and function in normal and failing murine hearts." (1524-4571 (Electronic)).

Writing Group, M., D. Mozaffarian, E. J. Benjamin, A. S. Go, D. K. Arnett, M. J. Blaha, M. Cushman, S. R. Das, S. de Ferranti, J. P. Despres, H. J. Fullerton, V. J. Howard, M. D. Huffman, C. R. Isasi, M. C. Jimenez, S. E. Judd, B. M. Kissela, J. H. Lichtman, L. D. Lisabeth, S. Liu, R. H. Mackey, D. J. Magid, D. K. McGuire, E. R. Mohler, 3rd, C. S. Moy, P. Muntner, M. E. Mussolino, K. Nasir, R. W. Neumar, G. Nichol, L. Palaniappan, D. K. Pandey, M. J. Reeves, C. J. Rodriguez, W. Rosamond, P. D. Sorlie, J. Stein, A. Towfighi, T. N. Turan, S. S. Virani, D. Woo, R. W. Yeh, M. B. Turner, C. American Heart Association Statistics and S. Stroke Statistics (2016). "Heart Disease and Stroke Statistics-2016 Update: A Report From the American Heart Association." Circulation **133**(4): e38-360.

Zile, M. R. and D. L. Brutsaert (2002). "New concepts in diastolic dysfunction and diastolic heart failure: Part I: diagnosis, prognosis, and measurements of diastolic function." Circulation **105**(11): 1387-1393.

Zuo, L., Y. Du, J. Ma, K. Wang, Y. Zhao, F. Bai, B. Wu, X. Ma and H. Liu (2015). "Pro-arrhythmic action of autoantibodies against the second extracellular loop of beta1-adrenoceptor and its underlying molecular mechanisms." Int J Cardiol **198**: 251-258.

J. of Cardiovasc. Trans. Res. (2015) 8:362–371
DOI 10.1007/s12265-015-9638-0

Variability of Mouse Left Ventricular Function Assessment by 11.7 Tesla MRI

Laetitia Vanhoutte[1,2,3] · Bernard Gallez[2] · Olivier Feron[3] · Jean-Luc Balligand[3] · Hrag Esfahani[3] · William d'Hoore[4] · Stéphane Moniotte[1]

Received: 9 April 2015 / Accepted: 2 June 2015 / Published online: 13 June 2015

Abstract We studied intraobserver (n=24), interobserver (n=24) and interexperiment (n=12) reproducibility of left ventricular (LV) mass and volume measurements in mice using an 11.7 T MRI system. The LV systolic function was assessed with a short-axis FLASH-cine sequence in 29 mice, including animals having undergone transverse aortic constriction. Bland-Altman and regression analysis were used to compare the different data sets. Reproducibility was excellent for the LV mass and end-diastolic volume (coefficient of variability (CoV) between 5.4 and 11.8 %), good for end-systolic volume (CoV 15.2–19.4 %) and moderate for stroke volume and ejection fraction (CoV 14.7–20.9 %). We found an excellent correlation between LV mass determined by MRI and ex vivo morphometric data (r=0.92). In conclusion, LV systolic function can be assessed on an 11.7 T MRI scanner with high reproducibility for most parameters, as needed in longitudinal studies. However, data should be interpreted taking into account the moderate reproducibility of small volumes.

Keywords Mice · Ultra-high-field MRI · Systolic function · Reproducibility · Cardiac hypertrophy

Editor-in-Chief Jennifer L. Hall oversaw the review of this article

✉ Laetitia Vanhoutte
laetitia.vanhoutte@uclouvain.be

Bernard Gallez
bernard.gallez@uclouvain.be

Olivier Feron
olivier.feron@uclouvain.be

Jean-Luc Balligand
jl.balligand@uclouvain.be

Hrag Esfahani
hrag.esfahani@uclouvain.be

William d'Hoore
william.dhoore@uclouvain.be

Stéphane Moniotte
stephane.moniotte@uclouvain.be

[1] Division of Paediatric Cardiology, Department of Paediatrics, Cliniques Universitaires St. Luc, Université Catholique de Louvain (UCL), Avenue Hippocrate 10/1380, B-1200 Brussels, Belgium

[2] Biomedical Magnetic Resonance Unit (REMA), Louvain Drug Research Institute (LDRI), UCL, Brussels, Belgium

[3] Pole of Pharmacology and Therapeutics (FATH), Institute of Experimental and Clinical Research (IREC), UCL, Brussels, Belgium

[4] Institute for Health and Society (IRSS), UCL, Brussels, Belgium

Abbreviations

CMR	Cardiovascular magnetic resonance
CoV	Coefficient of variability
EDV	End-diastolic volume
EF	Ejection fraction
ESV	End-systolic volume
FLASH	Fast low angle shot
LV	Left ventricle
SV	Stroke volume
TL	Tibial length

Introduction

With heart diseases as the leading cause of morbidity and mortality in Western countries, cardiovascular research remains the prime importance in the field of scientific research [1]. In this context, recent developments in genetic, surgical and pharmacological modalities have led to a wider selection of animal models, especially small rodents, allowing us to better understand the underlying mechanisms of

cardiovascular diseases and to study new therapeutic interventions. However, characterization of the mouse cardiac phenotype remains challenging because of a small heart size—myocardial mass is 2000-fold smaller than human [2]—and rapid heart rate (400–600 beats/min).

The development of high-field MRI offers a valuable alternative to high-frequency echocardiography because of its potential higher reproducibility, the numerous imaging sequences available allowing specific investigations (biventricular function, fibrosis and viability, wall motion abnormalities) as well as the relatively non-invasive aspect of the technique, making it ideal for longitudinal monitoring of small animals [2–8]. Over time, the progression of the magnetic field strength of MRI scanners, from 3 to 11.7 T, has led to a better signal-to-noise ratio and an improvement of the spatial and temporal resolution. There are currently more than 40 MR systems installed worldwide operating at 7 T or higher [9].

Even if regularly used to study experimental models of cardiovascular diseases, data related to the reproducibility of left ventricular systolic function assessment in mice with these high-field magnets are limited. To our best knowledge, studies existing either used very small groups of animals ($n<10$) [10–12], only rats [12, 13], field strength under 7 T [14] or vertical bores [11–13]. They further only focused on the intra- and interobserver reproducibility or compared segmentation techniques [14, 15]; only one study by Stuckey et al. reported interexperimental reproducibility data on a group of 12 rats [13].

Such data are crucial to establish whether this technique is routinely applicable to mouse models, especially in dynamic studies using repeated acquisitions [16], and to determine how it compares to high-frequency echocardiographic analysis. In this study, our goals were to evaluate the intraobserver, interobserver and interexperiment variability of left ventricular (LV) mass and volumes in mice with an 11.7 T horizontal bore MR system and to compare these MRI data with ex vivo morphometric measurements.

Methods

Animals

29 C57Bl/6J male mice (Janvier, Paris) aged 10–28 weeks were studied. Mice were housed under standard conditions with ad libitum access to water and chow.

Surgical Procedures

Eleven mice have undergone minimally invasive transverse aortic constriction (TAC) to produce various degrees of cardiac hypertrophy [17, 18] in order to study the experimental variability of the technique in a wider range of physiopathological conditions (namely, with a wider spectrum of LV hypertrophy).

Mice were anaesthetized with an intraperitoneal injection of a mixture of ketamine (150 mg/kg) and xylazine (10 mg/kg) and placed in supine position. Under a microscope, an incision was performed on the right side of the sternum in order to avoid injury to the mammary artery. The thymus was pushed aside, and a constrictive band was placed and tightened around the aorta and a 27-G blunted needle, which was then removed. The ligature was not tightened in sham-operated mice. Chest was closed with a polypropylene suture. Thirteen mice were used as sham animals, and another 5 were control mice, for a total of 29 animals studied.

CMR Image Acquisition

Experiments were performed on an 11.7 T MRI system dedicated to small animal applications (Biospec, Bruker, Ettlingen, Germany). A quadrature ^{1}H resonator was used for radiofrequency transmission (inner diameter=72 mm, length=6.6 cm) in conjunction with a surface receive-only coil array (length=10.7 cm). All animals underwent at least one MRI examination. In the previously operated mice, the imaging took place 8 weeks after the surgical procedure. In 12 animals, the procedure was repeated twice, with a maximum interval of 24 h.

The animals were anaesthetized in an induction chamber by exposure to isoflurane 3 %. The isoflurane was then maintained between 0.5 and 3 % during the entire procedure in order to get a steady cardiac frequency around 500 beats/min [19]. Mice were placed in prone position and monitored for electrocardiogram and respiration with neonatal electrodes wrapped around the paws and a specific pillow placed under the animal. Examinations were performed in a temperature-controlled setting, with a rectal probe and a dedicated heating blanket.

Cardiac scout images were obtained in the conventional planes with a tripilot sequence. An intragate 2D cine Fast Low Angle Shot (FLASH) sequence was applied to acquire a set of seven to eight 1-mm-thick contiguous short-axis images covering the entire ventricles, perpendicular to the LV long axis. The following parameters were set: repetition time, 5.83 ms; echo time, 1.45 ms; flip angle, 25°; field of view, 30.0×30.0 mm; and matrix size, 256×256, resulting in an in-plane resolution of 0.12×0.12 mm^2, with an acquisition time of approximately 9 min, and 10 frames per cardiac cycle.

CMR Image Analysis

The LV systolic function was assessed from the stack of short-axis images by tracing epicardial and endocardial borders, including papillary muscles, on the Segment software (Medviso®v1.8, Lund, Sweden) [20]. End-diastolic (EDV), end-systolic (ESV) and stroke volume (SV) were determined

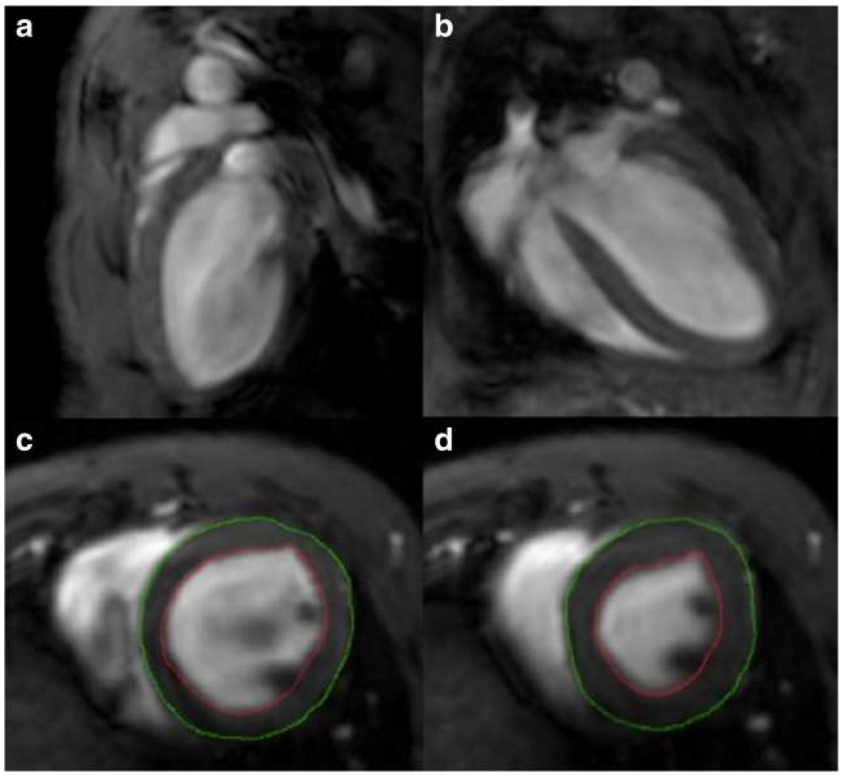

Fig. 1 Representative vertical long axis (**a**), horizontal long axis (**b**), and end-diastolic (**c**) and end-systolic (**d**) short-axis images in mice, with endocardial (*red*) and epicardial (*green*) outlines

(μl). LV ejection fraction (EF, in %) and LV mass (mg) were subsequently deduced. Twenty-four stacks of images were read twice by the same observer and once by an independent observer. The 24 series of images resulting from repeated acquisitions on the same animals were read by the first observer. The average time for image post-processing was about 15 min per animal. All analyses were performed on a blinded basis.

Morphometric Measurements

One week after the MRI procedure, mice were sacrificed. Their body weight, heart weight, left ventricular mass and tibial length (TL) were measured.

Statistical Analysis

Since most data were treated retrospectively, the 29 animals studied have not all been included in the various analysis groups. For intra- and interobserver variability, the same 24 mice were studied, including 13 sham and 11 TAC animals. For interexperiment variability, 12 animals were studied, including 3 sham, 4 TAC (also included in the intra- and interobserver analysis) and 5 control animals.

For intraobserver variability, the same stack of images was read twice by the same observer (data sets 1 and 1′). For interobserver variability, the same stack of images was read blindly by two independent observers (data sets 1 and 2). For interexperiment variability, two different stacks of images

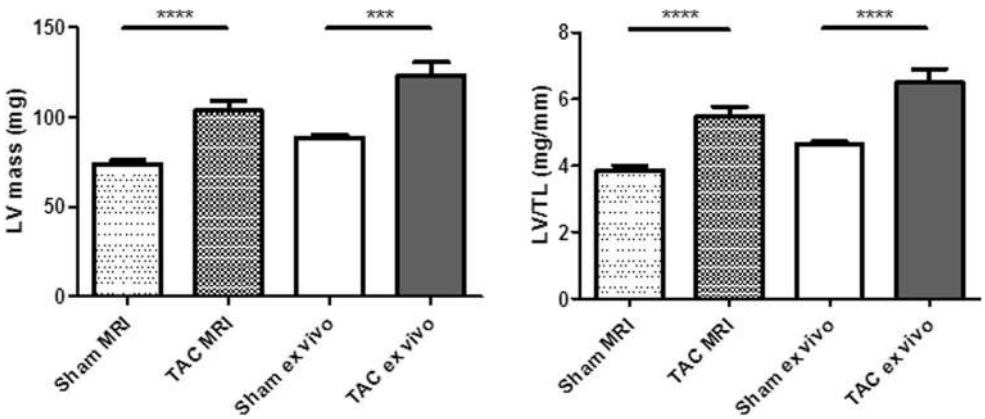

Fig. 2 Mass (mg) and LV/TL ratio (mg/mm) in sham and TAC mice assessed by MRI or ex vivo morphometric measurements. MRI data are issued from the first reading (data set 1). ***$P \leq 0.001$; ****$P \leq 0.0001$ vs sham

Table 1 Cardiac function and LV mass of sham and TAC mice. MRI data are issued from the first reading (data set 1)

	Sham	TAC
n	13	11
Body weight (g)	28.2±0.3	27.8±0.5
LV mass ex vivo (mg)	88.7±1.6	122.8±7.7***
LV/TL ex vivo (mg/mm)	4.7±0.1	6.5±0.4****
LV mass MRI (mg)	73.5±2.4	103.6±5.7****
LV/TL MRI (mg/mm)	3.9±0.1	5.5±0.3****
Heart rate (bpm)	496.6±11.1	509.5±11.3
EDV (μl)	60.1±2.4	76.1±5.4**
ESV (μl)	23.2±1.6	45.8±5.5***
SV (μl)	36.5±1.9	30.4±1.8*
EF (%)	61.2±2.0	41.6±3.7****
CO (ml/min)	18.1±0.9	15.4±0.8*

n represents the number of animals in each group. *EDV* end-diastolic volume, *ESV* end-systolic volume, *SV* stroke volume, *EF* ejection fraction, *CO* cardiac output

*$P \leq .0.05$; **$P \leq .0.01$; ***$P \leq .0.001$; ****$P \leq 0.0001$ vs sham

acquired in the same animal were read by the first observer (data sets 3 and 3′).

The mean and standard deviation of each parameter were computed in each group. Agreement between intraobserver, interobserver and interexperiment measurements was assessed by means of the Bland and Altman test [21] that plots the difference between the two measurements against the average of the two methods. The bias corresponds to the mean difference. The limits of agreement were estimated using the mean bias between the two readings plus or minus twice the standard deviation of the differences (SDD). The difference between the two measurements will be within these limits for 95 % of observations. The coefficient of variability (CoV) corresponds to the SDD divided by the mean of the measurements and multiplied by 100 %. It represents the percentage of dispersion of the measurements.

Unpaired Student's *t* test was used for intergroup comparison, including a comparative analysis of morphological and functional data (MRI data set 1) obtained for sham ($n=13$) and TAC mice ($n=11$). Paired *t* test was used to compare intraobserver, interobserver and interexperiment results for each parameter.

Table 2 Intraobserver, interexperiment and interobserver variability for LV mass (mg), LV/TL ratio (mg/mm), EDV (μl), ESV (μl), SV (μl) and EF (%). The table lists the mean±SD values and the Bland-Altman analysis results. Numbering of the data is organized as follows: 1 and 3 correspond to the first readings, 1′ is the reading of the same stack of images by the same observer (intraobserver), 2 is the reading of the same stack of images by an independent observer (interobserver) and 3′ corresponds to the reading of a second stack of images acquired on the same animal by the first observer (interexperiment)

Intraobserver variability ($n=24$)	LV mass	LV/TL	EDV	ESV	SV	EF
Mean±SD data #1	87.3±4.2	4.6±0.2	67.4±3.2	33.6±3.5	33.7±1.4	52.2±2.8
Mean±SD data #1	86.2±4.1	4.5±0.2	68.2±3.3	34.7±3.7	33.4±1.8	50.9±3.2
Bias	−1.1	−0.1	0.8	1.1	−0.3	−1.3
Limits of agreement	−10.4 to 8.1	−0.6 to 0.4	−6.4 to 7.9	−9.1 to 11.3	−10.4 to 9.7	−16.8 to 14.1
SDD	4.7	0.2	3.6	5.2	5.1	7.9
Coefficient of variability	5.4 %	5.4 %	5.4 %	15.2 %	15.3 %	15.3 %
Intraobserver variability ($n=24$)	LV mass	LV/TL	EDV	ESV	SV	EF
Mean±SD data #1	87.3±4.2	4.6±0.2	67.4±3.2	33.6±3.5	33.7±1.4	52.2±2.8
Mean±SD data #2	91.5±4.4	4.8±0.2	61.8±3.0	29.1±2.9	32.8±1.0	55.0±2.4
Bias	4.1	0.2	−5.6	−4.5	−0.9	2.8
Limits of agreement	−6.0 to 14.2	−0.3 to 0.8	−17.3 to 6.1	−16.4 to 7.4	−12.7 to 10.9	−12.7 to 18.3
SDD	5.1	0.3	6.0	6.1	6.0	7.9
Coefficient of variability	5.8 %	5.9 %	9.2 %	19.4 %	18.1 %	14.7 %
Interexperiment variability ($n=12$)	LV mass	LV/TL	EDV	ESV	SV	EF
Mean±SD data #3	83.5±5.8	4.3±0.4	72.6±4.2	35.4±5.5	37.1±2.3	53.4±4.5
Mean±SD data #3	87.3±5.7	4.5±0.4	70.2±4.6	34.2±6.0	35.8±2.7	53.9±5.0
Bias	3.8	0.2	−2.4	−1.3	−1.3	0.5
Limits of agreement	−9.3 to 16.8	−0.5 to 0.9	−18.9 to 14.1	−12.7 to 10.2	−16.2 to 13.7	−13.9 to 14.9
SDD	6.6	0.4	8.4	5.8	7.6	7.4
Coefficient of variability	7.8 %	8.3 %	11.8 %	16.8 %	20.9 %	15.5 %

n represents the number of animals studied

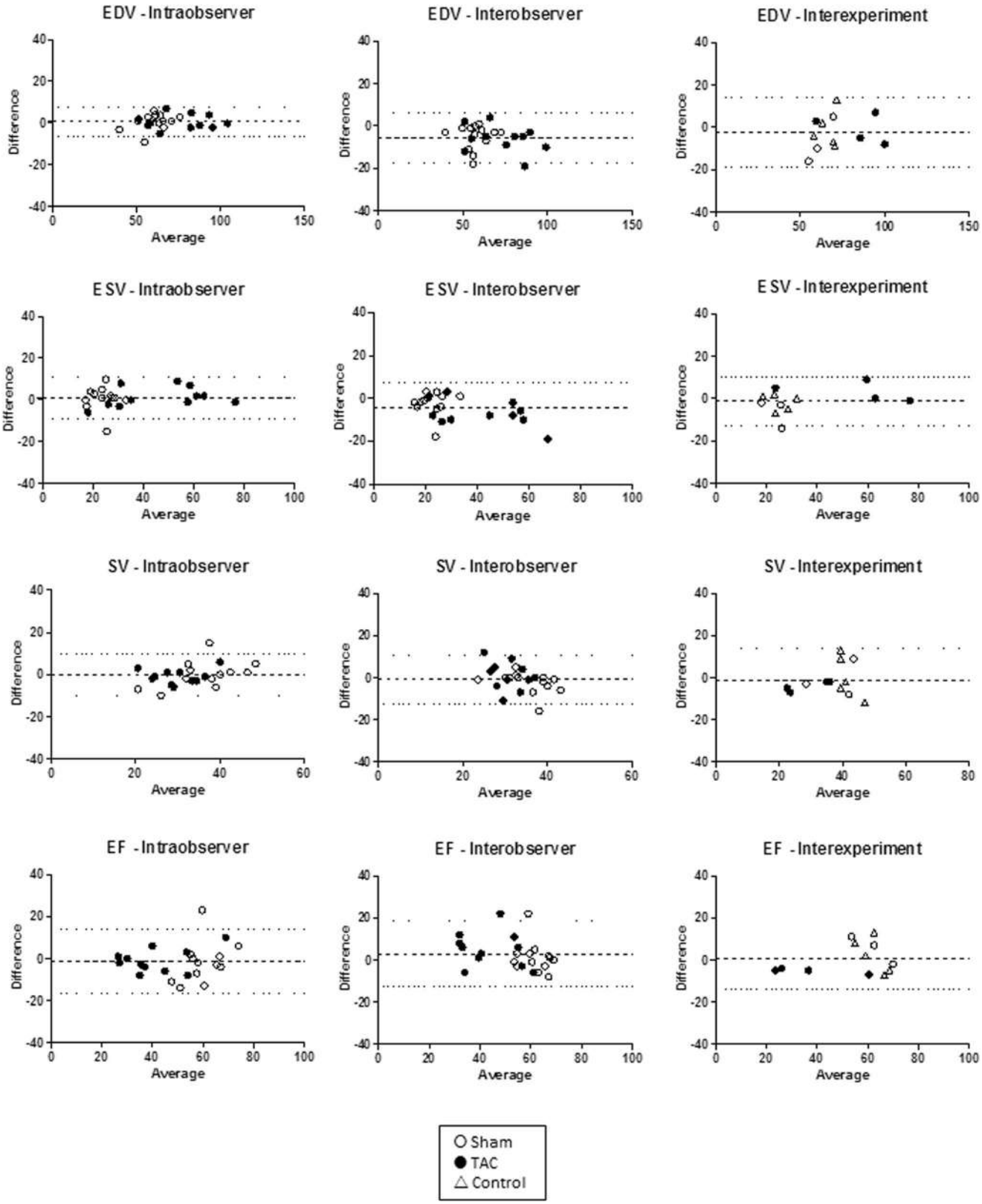

Fig. 3 Bland-Altman plots for EDV, ESV, SV and EF, assessing the agreement between the readings (interobserver, intraobserver and interexperiment). The relative variability is defined as the difference between observations divided by their mean. The *dashed lines* indicate the mean difference, while *dotted lines* indicate 95 % limits of agreement. All measurements showed a rather similar agreement of these main four parameters, not only in intra- or interobserver experiments (*left and central column*) but also in interexperiment analyses (*right column*)

A Pearson correlation was calculated in order to compare in vivo MRI data (data set 2) and ex vivo morphometric measurements of the LV mass and LV/TL ratio for the 13 sham and 11 TAC animals. A p value of <0.05 was considered statistically significant. Statistical analyses were performed with GraphPad Prism 5 (San Diego, USA).

Results

Using the CMR imaging protocol described above, high-grade quality images were obtained in all animals (Fig. 1).

Baseline Characteristics

Quantitative data were in line with previously published results [10, 11, 14–16, 19]. As expected, LV mass was significantly higher in the 11 animals with transverse aortic constriction and hypertrophic cardiomyopathy than in the 13 sham animals. When using the LV mass/tibial length ratio (LV/TL), which normalizes the LV mass to the body size, sham mice showed a ratio of 4.7±0.1 and 3.8±0.1 mg/mm for morphometric and MRI measurements, respectively, and TAC mice showed a ratio of 6.5±0.4 and 5.4±0.3, respectively, demonstrating a clearly different cardiac phenotype between both groups (p<0.05, Fig. 2). Detailed cardiac functional parameters and LV mass measurements for the sham and TAC groups are summarized in Table 1.

Intraobserver, Interobserver and Interexperiment Variability of MRI Data

The mean±SD values of all morphometric data as well as the Bland-Altman analysis were obtained for the 29 animals studied. Detailed results are displayed in Table 2 and Fig. 3. We did not find statistically significant differences between the mean values of LV mass, LV/TL ratio, LV EDV, LV ESV, LV SV and LV EF when comparing the various sets of data (p>0.05).

As expected, the SDD, and hence the limits of agreement, were smaller for all parameters in the intraobserver study, whereas the least clustered data were found in the interexperiment study, with similar to larger confidence interval compared to the interobserver study.

Using the Bland and Altman analysis, high reproducibility was found for LV mass, LV/TL and EDV, with a notably low intraobserver CoV of 5.4 % for all these parameters and CoV <12 % in the interexperiment study, suggesting that these can effectively be used in longitudinal studies. Good agreement was found for EF, with a CoV between 14.7 % in the interobserver study and 15.5 % in the interexperiment study. The small volumes suffered the most variability, with intermodality CoV between 15.2 and 20.9 % for ESV and SV, which implies that they are more difficult to quantify accurately and could be of limited value when measured during repeated acquisitions.

Fig. 4 *Scatterplots* showing the intraobserver, interobserver and interexperiment correlations between two readings for LV/TL, EDV, ESV, SV and EF. Our linear regression analysis shows an excellent correlation for all intraobserver data, but moderate correlation in SV and EF for interobserver data and in SV for interexperiment data. The regression line is given with a 95 % confidence interval (*dotted lines*). R-squares and p values are reported in the *left upper corner* of each graph

Linear Regression Analysis

Linear regression analysis for all mice revealed an adequate intraobserver, interobserver and interexperiment correlation for LV/TL, EDV, ESV and EF with R-square ranging between 0.67 and 0.95. Correlation for SV was the weakest of all parameters, with R-square between 0.30 (interobserver study) and 0.67 (intraobserver study). The line of best fit intercepted the origin for most measurements, and when not, the correlation remained significant, with a b_0 significantly different from zero. The scatter plots with individual regression line, 95 % confidence interval, R-squares and corresponding p-values are provided in Fig. 4.

Correlation Between In Vivo MRI and Ex Vivo Morphometric LV Mass Measurements

We demonstrated a strong correlation between LV mass measurements by LV mass weighing or high-field CMR imaging (data set 2), with a Pearson correlation (r) of 0.92 for both LV mass and LV/TL ratio (p<0.05, Fig. 5). Of note, MRI data in absolute values were always smaller than morphometric data.

Discussion

In cardiovascular imaging, variations within and between observers and between different acquisitions remain an important issue when evaluating in vivo data. This is particularly relevant when experimental groups are studied longitudinally to test a new hypothesis.

Up to now, high-frequency echocardiography remained the most widely used technique to characterize the cardiac phenotype of rodents. Although few data are available in the literature on its reproducibility [22–25], it is generally accepted that its intra- and interobserver variability is low for most ventricular measurements (<20 %, [26]). However, it is also known that this method is less efficient in the presence of abnormal ventricular geometry and heterogeneous regional myocardial function [26–28] as it is often the case in animal models of cardiovascular diseases.

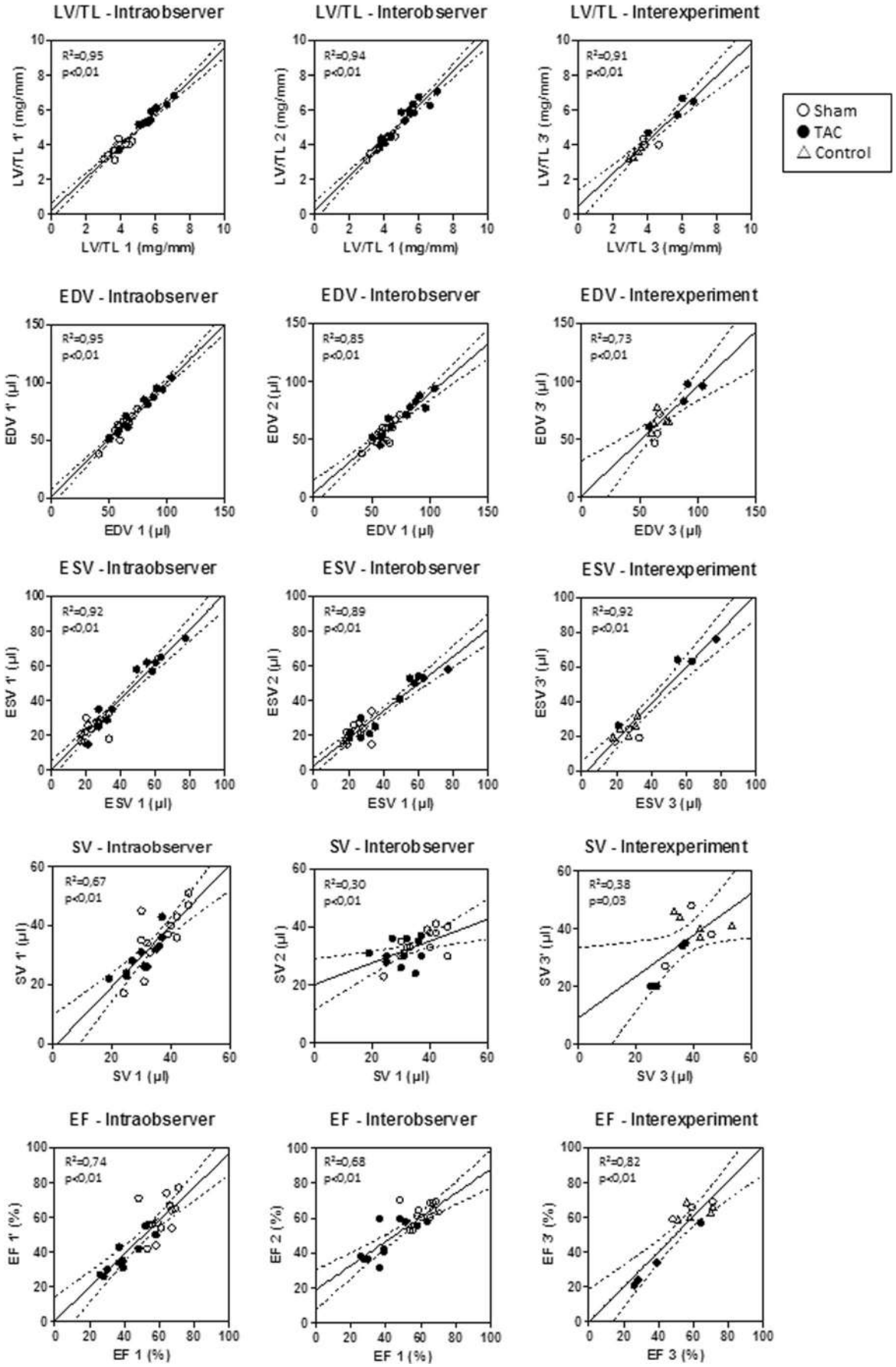
LV/TL - Intraobserver
R²=0,95
p<0,01
LV/TL 1' (mg/mm)
LV/TL 1 (mg/mm)
LV/TL - Interobserver
R²=0,94
p<0,01
LV/TL 2 (mg/mm)
LV/TL 1 (mg/mm)
LV/TL - Interexperiment
R²=0,91
p<0,01
LV/TL 3' (mg/mm)
LV/TL 3 (mg/mm)
Sham
TAC
Control
EDV - Intraobserver
R²=0,95
p<0,01
EDV 1' (µl)
EDV 1 (µl)
EDV - Interobserver
R²=0,85
p<0,01
EDV 2 (µl)
EDV 1 (µl)
EDV - Interexperiment
R²=0,73
p<0,01
EDV 3' (µl)
EDV 3 (µl)
ESV - Intraobserver
R²=0,92
p<0,01
ESV 1' (µl)
ESV 1 (µl)
ESV - Interobserver
R²=0,89
p<0,01
ESV 2 (µl)
ESV 1 (µl)
ESV - Interexperiment
R²=0,92
p<0,01
ESV 3' (µl)
ESV 3 (µl)
SV - Intraobserver
R²=0,67
p<0,01
SV 1' (µl)
SV 1 (µl)
SV - Interobserver
R²=0,30
p<0,01
SV 2 (µl)
SV 1 (µl)
SV - Interexperiment
R²=0,38
p=0,03
SV 3' (µl)
SV 3 (µl)
EF - Intraobserver
R²=0,74
p<0,01
EF 1' (%)
EF 1 (%)
EF - Interobserver
R²=0,68
p<0,01
EF 2 (%)
EF 1 (%)
EF - Interexperiment
R²=0,82
p<0,01
EF 3' (%)
EF 3 (%)

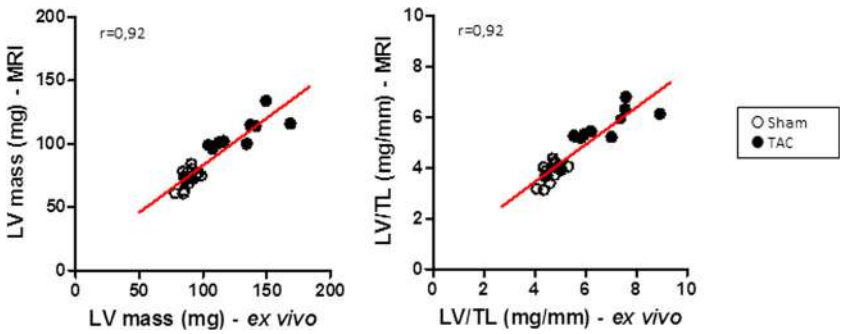

Fig. 5 Correlation between in vivo MRI data and ex vivo morphometric data in terms of LV mass and LV/TL ratio. MRI data are issued from data set 1′

Approaches such as echocardiography using geometrical assumptions to evaluate left ventricular function are not as accurate as data coming from a full volume acquisition, as it is the gold standard in CMR imaging [15]. In a rat model of myocardial infarction, Stuckey et al. showed that 2D echo was indeed less reproducible than 11.7 T MRI [13] in a vertical bore magnet acquiring 28–40 frames per heart cycle.

Studies comparing measurements obtained by echocardiography and MRI in a model are scarce [13, 28], but overall, they suggest that end-diastolic dimensions and LV wall thickness are poorly correlated. This could be at least in part explained by the better delineation of cardiac trabeculations in CMR imaging and better temporal resolution [27]. Similarly, studies comparing left ventricular function in mice by MRI or conductance microcatheter (Millar) have shown a striking underestimation of absolute volumetric values with the catheter method [29, 30] influenced by the calibration technique used [30]. These pitfalls further suggest that it is not wise to compare LV measurements obtained with different techniques in various experimental groups.

Development of ultra-high-field MRI systems (≥7.0 T) over the past decade has brought new perspectives in small animal imaging. As there is a direct relationship between the main field strength (B_0) and the signal-to-noise ratio (S/N), higher field provides better imaging quality and improves spatial and temporal resolution or acquisition speed. Hence, most pioneering CMR laboratories currently work on 7 or 9 T systems [9], and they are likely to transition to even higher fields in the near future. If some reproducibility data on CMR in rodents are available, they mainly report very small numbers of animals ($n<10$) [10–12], including rats [12, 13], field strengths ≤7 T [14] or vertical bores [11–13], the latter representing a less physiological environment. Overall, this does not really reflect the current use of ultra-high-field MRI for the characterization of experimental models in cardiovascular research. Moreover, interexperiment variability is usually not evaluated in most studies, including the work of Heijman et al. [14] reporting the most sizable number of mice ($n=22$) at 6.3 T. Therefore, we believe that our reproducibility data obtained with a horizontal bore at 11.7 T on a group of more than 25 mice bring additional material for the validation of the technique.

In our study, purposedly including healthy mice and a model of hypertrophic cardiomyopathy, intraobserver, interobserver and interexperiment reproducibility was good for LV mass, LV/TL and EDV (CoV between 5.4 and 11.8 %). These results are consistent with the few data available in the experimental field [10–15], although the use of different statistical tests does not allow a thorough comparison. Coefficients of variability remain higher than those obtained in humans [31]. If the reproducibility of ESV, SV and EF is less satisfactory, various factors may account for these differences. First, contour tracings in the basal and apical sections of the heart are often subject to interpretation at the time of post-processing because myocardial limits are less clearly visible at these levels. Secondly, at least when studying interexperiment variability, an additional potential source of error in the determination of volumes could have been introduced by the partial volume effect due to a finite slice thickness. Finally, and above all, there was an important scale effect: any tiny variation in measurements had enormous repercussions on the reproducibility of the data, as it related to very small volumes (μl). This explains why the smallest volumes, especially the SV, suffered the most variability. This highlights the need to develop stronger sequences to adequately measure SV and cardiac output in mice. In particular, a phase-contrast angiography sequence applied on the ascending aorta could be more appropriate for direct measurement of the SV and, subsequently, the EF [32].

When morphometric and CMR imaging LV measurements were compared, both showed a strong correlation and were able to demonstrate similar differences in LV mass or LV/TL between our experimental groups. However, LV mass estimated by CMR was consistently smaller in absolute values than those obtained ex vivo. The 1-week delay between MRI examination and sacrifice for morphometric evaluation could in part account for this discrepancy. However, this is also very likely related to the great accuracy of CMR post-processing, allowing to exclude intraventricular blood and tissues not belonging to the LV from the analysis, whereas those may have been mistakenly included in the morphometric measurements.

Conclusions

This study showed that the mouse LV systolic function can be assessed on an 11.7 T MRI scanner, with an excellent reproducibility of LV mass and end-diastolic volumes analysis, allowing longitudinal phenotypic evaluation of animals with healthy or hypertrophic myocardium. Furthermore, in vivo LV mass MRI measurements were constantly in line with ex vivo morphometric data, bringing evidence that high-field CMR imaging is not only reproducible but also accurate.

Development of new CMR imaging sequences remains a great challenge for the future, as it will allow more detailed non-invasive characterizations of animal models. Here, we highlight the need to interpret CMR data by taking into account their shortcomings, focusing on LV mass and LV EDV as parameters that are not only the most reproducible but also the most relevant in various pathophysiological conditions such as cardiac remodeling and hypertrophy.

Acknowledgments We thank Julie Magat and Hassan Jassar for their assistance during the MRI manipulations. This work was supported by grants from the Fonds de la Recherche Scientifique FRS-FNRS, the Foundation Saint-Luc and the Belgian National Foundation for Research in Pediatric Cardiology.

Conflict of Interest No potential conflicts of interest were disclosed.

Animal Studies All institutional and national guidelines for the care and use of laboratory animals were followed and approved by the appropriate institutional committees. No human studies were carried out by the authors for this article.

References

1. Mozaffarian, D., Benjamin, E. J., Go, A. S., Arnett, D. K., Blaha, M. J., Cushman, M., de Ferranti, S., Després, J., Fullerton, H. J., Howard, V. J., Huffman, M. D., Judd, S. E., Kissela, B. M., Lackland, D. T., Lichtman, J. H., Lisabeth, L. D., Liu, S., Mackey, R. H., Matchar, D. B., McGuire, D. K., Mohler, E. R., 3rd, Moy, C. S., Muntner, P., Mussolino, M. E., Nasir, K., Neumar, R. W., Nichol, G., Palaniappan, L., Pandey, D. K., Reeves, M. J., Rodriguez, C. J., Sorlie, P. D., Stein, J., Towfighi, A., Turan, T. N., Virani, S. S., Willey, J. Z., Woo, D., Yeh, R. W., & Turner, M. B. (2015). Heart disease and stroke statistics—2015 update: a report from the American Heart Association. *Circulation, 131*(4), e29–e322.
2. Schneider, J. E., Wiesmann, F., Lygate, C. A., & Neubauer, S. (2006). How to perform an accurate assessment of cardiac function in mice using high-resolution magnetic resonance imaging. *Journal of Cardiovascular Magnetic Resonance, 8*, 693–701.
3. Vallée, J. P., Ivancevic, M. K., Nguyen, D., Morel, D. R., & Jaconi, M. (2004). Current status of cardiac MRI in small animals. *Magnetic Resonance Materials in Physics, Biology and Medicine, 17*(3–6), 149–156.
4. Epstein, F. H. (2007). MR in mouse models of cardiac disease. *NMR in Biomedicine, 20*(3), 238–255.
5. Price, A. N., Cheung, K. K., Cleary, J. O., Campbell, A. E., Riegler, J., & Lythgoe, M. F. (2010). Cardiovascular magnetic resonance imaging in experimental models. *The Open Cardiovascular Medicine Journal, 4*, 278–292.
6. Vandsburger, M. H., & Epstein, F. H. (2011). Emerging MRI methods in translational cardiovascular research. *Journal of Cardiovascular Translational Research, 4*(4), 477–492.
7. Akki, A., Gupta, A., & Weiss, R. G. (2013). Magnetic resonance imaging and spectroscopy of the murine cardiovascular system. *American Journal of Physiology Heart and Circulation Physiology, 304*(5), H633–H648.
8. Meßner, N. M., Zöllner, F. G., Kalayciyan, R., & Schad, L. R. (2014). Pre-clinical functional magnetic resonance imaging part II: the heart. *Zeitschrift für Medizinische Physik, 24*(4), 307–322.
9. Kraff, O., Fischer, A., Nagel, A. M., Mönninghoff, C., & Ladd, M. E. (2015). MRI at 7 tesla and above: demonstrated and potential capabilities. *Journal of Magnetic Resonance Imaging, 41*(1), 13–33.
10. Ruff, J., Wiesmann, F., Hiller, K. H., Voll, S., von Kienlin, M., Bauer, W. R., Rommel, E., Neubauer, S., & Haase, A. (1998). Magnetic resonance microimaging for noninvasive quantification of myocardial function and mass in the mouse. *Magnetic Resonance in Medicine, 40*, 43–48.
11. Schneider, J. E., Cassidy, P. J., Lygate, C., Tyler, D. J., Wiesmann, F., Grieve, S. M., Hulbert, K., Clarke, K., & Neubauer, S. (2003). Fast, high-resolution in vivo cine magnetic resonance imaging in normal and failing mouse hearts on a vertical 11.7 T system. *Journal of Magnetic Resonance Imaging, 18*, 691–701.
12. Tyler, D. J., Lygate, C. A., Schneider, J. E., Cassidy, P. J., Neubauer, S., & Clarke, K. (2006). CINE-MR imaging of the normal and infarcted rat heart using an 11.7 T vertical bore MR system. *Journal of Cardiovascular Magnetic Resonance, 8*, 327–333.
13. Stuckey, D. J., Carr, C. A., Tyler, D. J., & Clarke, K. (2008). Cine-MRI versus two-dimensional echocardiography to measure in vivo left ventricular function in rat heart. *NMR in Biomedicine, 21*(7), 765–772.
14. Heijman, E., Aben, J. P., Penners, C., Niessen, P., Guillaume, R., van Eys, G., Nicolay, K., & Strijkers, G. J. (2008). Evaluation of manual and automatic segmentation of the mouse heart from CINE MR images. *Journal of Magnetic Resonance Imaging, 27*(1), 86–93.
15. van de Weijer, T., van Ewijk, P. A., Zandbergen, H. R., Slenter, J. M., Kessels, A. G., Wildberger, J. E., Hesselink, M. K., Schrauwen, P., Schrauwen-Hinderling, V. B., & Kooi, M. E. (2012). Geometrical models for cardiac MRI in rodents: comparison of quantification of left ventricular volumes and function by various geometrical models with a full-volume MRI data set in rodents. *American Journal of Physiology Heart and Circulation Physiology, 302*(3), H709–H715.
16. Wiesmann, F., Ruff, J., Engelhardt, S., Hein, L., Dienesch, C., Leupold, A., Illinger, R., Frydrychowicz, A., Hiller, K. H., Rommel, E., Haase, A., Lohse, M. J., & Neubauer, S. (2001). Dobutamine-stress magnetic resonance microimaging in mice: acute changes of cardiac geometry and function in normal and failing murine hearts. *Circulation Research, 88*, 563–569.
17. Rockman, H. A., Ross, R. S., Harris, A. N., Knowlton, K. U., Steinhelper, M. E., Field, L., Ross, J., & Chien, K. R. (1991). Segregation of atrial specific and inducible expression of an ANF transgene in an in vivo murine model of cardiac hypertrophy. *Proceedings of the National Academy of Sciences of the United States of America, 88*, 8277–8281.
18. Hu, P., Zhang, D., Swenson, L., Chakrabarti, G., Abel, E. D., & Litwin, S. E. (2003). Minimally invasive aortic banding in mice: effects of altered cardiomyocyte insulin signaling during pressure overload. *American Journal of Physiology Heart and Circulation Physiology, 285*(3), H1261–H1269.
19. Kober, F., Iltis, I., Cozzone, P. J., & Bernard, M. (2004). Cine-MRI assessment of cardiac function in mice anesthetized with ketamine/

xylazine and isoflurane. *Magnetic Resonance Materials in Physics, Biology and Medicine, 17*(3–6), 157–161.
20. Heiberg, E., Sjögren, J., Ugander, M., Carlsson, M., Engblom, H., & Arheden, H. (2010). Design and validation of segment-freely available software for cardiovascular image analysis. *BMC Medical Imaging, 10*, 1.
21. Bland, J. M., & Altman, D. G. (1986). Statistical methods for assessing agreement between two methods of clinical measurement. *Lancet, 1*, 307–310.
22. Hoit, B. D., Khoury, S. F., Kranias, E. G., Ball, N., & Walsh, R. A. (1995). In vivo echocardiographic detection of enhanced left ventricular function in gene-targeted mice with phospholamban deficiency. *Circulation Research, 77*(3), 632–637.
23. Tanaka, N., Dalton, N., Mao, L., Rockman, H. A., Peterson, K. L., Gottshall, K. R., Hunter, J. J., Chien, K. R., & Ross, J., Jr. (1996). Transthoracic echocardiography in models of cardiac disease in the mouse. *Circulation, 94*(5), 1109–1117.
24. Yang, X. P., Liu, Y. H., Rhaleb, N. E., Kurihara, N., Kim, H. E., & Carretero, O. A. (1999). Echocardiographic assessment of cardiac function in conscious and anesthetized mice. *American Journal of Physiology Heart and Circulation Physiology, 277*, H1967–H1974.
25. Collins, K. A., Korcarz, C. E., Shroff, S. G., Bednarz, J. E., Fentzke, R. C., Lin, H., Leiden, J. M., & Lang, R. M. (2001). Accuracy of echocardiographic estimates of left ventricular mass in mice. *American Journal of Physiology Heart and Circulation Physiology, 280*(5), H1954–H1962.
26. Ram, R., Mickelsen, D. M., Theodoropoulos, C., & Blaxall, B. C. (2011). New approaches in small animal echocardiography: imaging the sounds of silence. *American Journal of Physiology Heart and Circulation Physiology, 301*(5), H1765–H1780.
27. Ghanem, A., Roll, W., Hashemi, T., Dewald, O., Djoufack, P. C., Fink, K. B., Schrickel, J., Lewalter, T., Luderitz, B., & Tiemann, K. (2006). Echocardiographic assessment of left ventricular mass in neonatal and adult mice: accuracy of different echocardiographic methods. *Echocardiography, 23*, 900–907.
28. Amundsen, B. H., Ericsson, M., Seland, J. G., Pavlin, T., Ellingsen, Ø., & Brekken, C. (2011). A comparison of retrospectively self-gated magnetic resonance imaging and high-frequency echocardiography for characterization of left ventricular function in mice. *Laboratory Animal, 45*(1), 31–37.
29. Jacoby, C., Molojavyi, A., Flögel, U., Merx, M. W., Ding, Z., & Schrader, J. (2006). Direct comparison of magnetic resonance imaging and conductance microcatheter in the evaluation of left ventricular function in mice. *Basic Research in Cardiology, 101*(1), 87–95.
30. Nielsen, J. M., Kristiansen, S. B., Ringgaard, S., Nielsen, T. T., Flyvbjerg, A., Redington, A. N., & Bøtker, H. E. (2007). Left ventricular volume measurement in mice by conductance catheter: evaluation and optimization of calibration. *American Journal of Physiology Heart and Circulation Physiology, 293*(1), H534–H540.
31. Luijnenburg, S. E., Robbers-Visser, D., Moelker, A., Vliegen, H. W., Mulder, B. J., & Helbing, W. A. (2010). Intra-observer and interobserver variability of biventricular function, volumes and mass in patients with congenital heart disease measured by CMR imaging. *International Journal of Cardiovascular Imaging, 26*(1), 57–64.
32. Janiczek, R. L., Blackman, B. R., Roy, R. J., Meyer, C. H., Acton, S. T., & Epstein, F. H. (2011). Three-dimensional phase contrast angiography of the mouse aortic arch using spiral MRI. *Magnetic Resonance in Medicine, 66*, 1382–1390.

SCIENTIFIC REPORTS

OPEN

Received: 26 October 2016
Accepted: 01 February 2017
Published: 09 March 2017

MRI Assessment of Cardiomyopathy Induced by β1-Adrenoreceptor Autoantibodies and Protection Through β3-Adrenoreceptor Overexpression

Laetitia Vanhoutte[1,2], Céline Guilbaud[1], Ruben Martherus[1], Caroline Bouzin[1], Bernard Gallez[3], Chantal Dessy[1], Jean-Luc Balligand[1], Stéphane Moniotte[2] & Olivier Feron[1]

The cardiopathogenic role of autoantibodies (aabs) directed against β1-adrenoreceptors (β1-AR) is well established. In mouse models, they cause progressive dilated cardiomyopathy (DCM) whose characterization with echocardiography requires prolonged protocols with numerous animals, complicating the evaluation of new treatments. Here, we report on the characterization of β1-aabs-induced DCM in mice using 11.7T MRI. C57BL/6J mice (n = 10 per group) were immunized against the β1-AR and left ventricular (LV) systolic function was assessed at 10, 18 and 27 weeks. Increase in LV mass/tibial length ratio was detected as the first modification at 10 weeks together with dilation of cavities, thereby outperforming echocardiography. Significant impairment in diastolic index was also observed in immunized animals before the onset of systolic dysfunction. Morphometric and histological measurements confirmed these observations. The same protocol performed on β3-AR-overexpressing mice and wild-type littermates (n = 8–12 per group) showed that transgenic animals were protected with reduced LV/TL ratio compared to wild-type animals and maintenance of the diastolic index. This study demonstrates that MRI allows a precocious detection of the subtle myocardial dysfunction induced by β1-aabs and that β3-AR stimulation blunts the development of β1-aabs-induced DCM, thereby paving the way for the use of β3AR-stimulating drugs to treat this autoimmune cardiomyopathy.

Because of its high prevalence, morbidity and mortality, heart failure remains a major health problem. Among the mechanisms leading to this condition, the detrimental role played by autoantibodies targeting the β1-adrenergic receptor (β1-aabs) has been established in the last two decades. Clinical studies have shown that the prevalence of β1-aabs is associated with dilated cardiomyopathy (DCM)[1–3], ischemic cardiomyopathy[4] and Chagas' disease[5], with – overall – a more frequent occurrence of poor LV function[4], ventricular arrhythmias[6], sudden cardiac death[6,7] and mortality[8]. By contrast, prevalence is apparently lower in patients with heart failure due to valvular or hypertensive diseases[9]. These gross statistics require further clarification in order to better understand the time course of appearance and exact roles of these antibodies in patients suffering from cardiac diseases of various etiologies. A multicentric prospective and retrospective study is currently conducted in patients suffering from myocarditis, ischemic and hypertensive heart diseases[10].

Evidence has accumulated from animal studies confirming the direct pathogenicity of β1-aabs. A highly antigenic fragment containing B and T cell epitopes has been identified on the second extracellular loop (β1-EC_{II}) of the β1-adrenoreceptor (β1-AR)[11–13]. Studies on animal models have established the development of cardiac

[1]Pole of Pharmacology and Therapeutics (FATH), Institut de Recherche Expérimentale et Clinique (IREC), Université catholique de Louvain, Brussels, Belgium. [2]Department of Paediatric Cardiology, Cliniques universitaires St Luc, Université catholique de Louvain, Brussels, Belgium. [3]Biomedical Magnetic Resonance Unit (REMA), Louvain Drug Research Institute (LDRI), Université catholique de Louvain, Brussels, Belgium. Correspondence and requests for materials should be addressed to O.F. (email: olivier.feron@uclouvain.be) or L.V. (email: laetitia.vanhoutte@uclouvain.be)

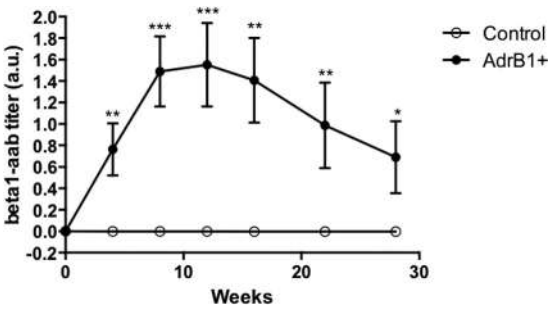

Figure 1. Titer of antibodies against β1AR-ECII determined by ELISA throughout the study period, in sera of control (CTL, n = 10) and β1-immunized (AdrB1+, n = 7–10) mice. Data are represented as mean+/−SEM, and normalized to basal optical density obtained before injection, *P ≤ 0.0.05; **P ≤ 0.0.01; ***P ≤ 0.0.001*vs* control.

dysfunction after the active immunization against this antigen (indirect evidence)[14–16] and assessed the possibility of generating cardiac impairment after transfer of homologous pathogenic antibodies to healthy animals (direct evidence)[17]. The two main hypotheses raised to explain the development of such antibodies include homologies between the receptor and microbial determinants or the exposition of potentially antigenic components of the cardiomyocytes following cardiac damages[18].

The functional effects of β1-aabs at the cellular and molecular levels are incompletely understood. Preliminary results suggest that they act as allosteric agonists[19], enabling dimerization and stabilization of β1-AR in its active conformation[20], subsequently promoting sustained downstream signaling in a manner distinct from the natural ligand[21,22]. This leads to cardiomyocyte apoptosis[23], enhanced contractility and prolonged action potential duration[24]. During progression of aabs-induced cardiomyopathy, increased levels of GRK2 have also been documented in several rodent studies[16,25,26], suggesting desensitization and down-regulation of β1-AR. Some therapies, including the use of apheresis[27], aptamers[28], peptides competing with the receptor epitope[29,30] and conventional beta-blockers[30,31] have proven to be useful in order to partially prevent the development of cardiac dysfunction due to β1-aabs.

The β3-adrenoreceptor (β3-AR) has recently emerged has a potential therapeutic target in the presence of an excessive β-adrenergic stimulation on the heart, as it mediates a countervailing influence to β1 and β2-AR activation[32] and is resistant to homologous desensitization[33]. Moreover β3-ARs are upregulated under various conditions of adrenergic overstimulation[34–36], arguing in favor of a potential influence of these receptors on chronic remodeling. Our group has recently demonstrated that transgenic mice with cardiac-specific overexpression of β 3-AR were protected from hypertrophic and fibrotic remodeling due to neurohormonal stimulation[37]. Whether β3 stimulation may prevent or correct autoimmune DCM is however unknown.

Up to now, the anatomical characterization of the cardiomyopathy induced by β1-aabs in animals has mostly been performed using echocardiography. However, cardiac dysfunction appears slowly and frequently starts with subtle diastolic dysfunction and elevated filling pressures. With the limited accuracy and reproducibility of echocardiography, prolonged protocols with numerous animals are needed before identifying early modifications in immunized individuals. The recent development of ultra-high field MRI (UHF MRI) has brought new perspectives in cardiovascular imaging of small animal models, due to its higher accuracy and reproducibility[38] and the numerous sequences available. Here, we studied the evolution of systolic and diastolic LV function of mice submitted to β1-AR immunization with an 11.7T MRI scanner to evaluate whether this technique could permit earlier detection of remodeling induced by aabs. We also aimed to study whether β3-AR overexpressing mice could be protected from cardiac remodeling induced by chronic exposure to β1-aabs.

Results

Mouse model of β1AR aabs-induced cardiomyopathy. We actively immunized C57Bl/6J mice against the β1-AR through monthly subcutaneous injections of a peptide corresponding to the second extracellular loop of the receptor, for a total of 28 weeks. In parallel, control animals were s.c. administered the vehicle solution. Immunized mice showed a gradual increase of circulating antibodies directed against β_1AR-EC_{II}, reaching a peak after 2 booster doses, whereas β_1-aabs remained undetectable in control mice (Fig. 1). 3 mice died in the immunized group within the first 12 weeks of protocol. Deaths occurred in animals presenting the most rapid increase in antibody titers, suggesting the occurrence of aabs-induced lethal arrhythmias[39,40]. No alterations in body weight, food intake and behavior were observed in surviving mice.

MRI cardiac function evaluation upon induction of β1AR aabs. After 10 weeks of follow-up, mice immunized against the β_1AR-EC_{II} already showed a statistically significant increase in the LV/TL ratio compared to control mice (4.2 ± 0.1 *vs* 3.8 ± 0.1 mg/mm, $p < 0.05$) (Fig. 2, left panel and Table 1). Over time, a continuous increase of this parameter was observed in the β_1-immunized group, accompanied by signs of progressive dilation of LV (Fig. 2, left panel and Table 1). These MRI data for LV mass and LV/TL were confirmed by *ex vivo* measurements at 28 weeks (Table 1).

A statistically significant difference for EDV was noticeable after 18 weeks between treated and control mice (69.1 ± 4.3 *vs* 59.6 ± 1.5 μl, $p < 0.05$) (Fig. 2, middle panel and Table 1), and after 27 weeks for ESV (29.0 ± 4.0

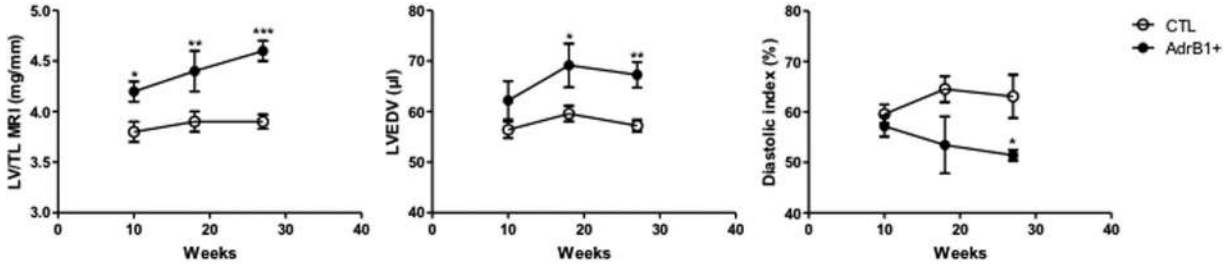

Figure 2. MRI follow-up in β1-immunized (n = 7–9) and control mice (n = 10). The panels depict the time course of the following parameters: LV mass/tibial length ratio (LV/TL), end-diastolic volume (EDV) and diastolic index. Error bars indicate SEM. *P ≤ 0.0.05; **P ≤ 0.0.01; ***P ≤ 0.0.001; ****P ≤ 0.0.0001 *vs* control.

	10 weeks		18 weeks		27 weeks	
	CTL	AdrB1+	CTL	AdrB1+	CTL	AdrB1+
n	10	9	10	7	10	7
EDV (µl)	56,4 ± 1,6	64,2 ± 3,8	59,6 ± 1,5	69,1 ± 4,3*	57,2 ± 1,2	67,3 ± 2,5**
ESV (µl)	24,0 ± 2,5	22,9 ± 2,0	27,0 ± 13,8	32,0 ± 14,0	22,0 ± 1,5	29,0 ± 4**
SV (µl)	32,6 ± 2,3	41,4 ± 3,2*	29,0 ± 16,3	41,0 ± 21,0	35,3 ± 1,0	39,6 ± 2,6
EF (%)	57,7 ± 4,0	64,1 ± 2,7	51,0 ± 15,5	59 ± 7,0	61,8 ± 1,1	58,7 ± 2,4
LV mass MRI (mg)	74,1 ± 1,7	81,1 ± 2,1*	74,8 ± 1,4	83,9 ± 3,6*	75,9 ± 1,1	88,0 ± 2,0****
LV/TL MRI (mg/mm)	3,8 ± 0,1	4,2 ± 0,1*	3,9 ± 0,1	4,4 ± 0,2**	3,9 ± 0,07	4,6 ± 0,1***
ES septum thickness (mm)	1,5 ± 0,1	1,3 ± 0,1	1,2 ± 0,1	1,4 ± 0,1	1,4 ± 0,1	1,4 ± 0,1
Systolic index (%)	66,8 ± 1,5	67,8 ± 2,5	66,8 ± 1,9	63,2 ± 3,0	66,5 ± 1,9	64,8 ± 2,0
Diastolic index (%)	59,6 ± 1,9	57,2 ± 2,1	64,5 ± 2,6	53,5 ± 5,6	63,1 ± 4,3	51,4 ± 1,1*
LV mass *ex vivo* (mg)					97,9 ± 1,9	107,5 ± 2,7**
LV/TL *ex vivo* (mg/mm)					5,0 ± 0,1	5,6 ± 0,1**

Table 1. *In vivo* MRI parameters in mice at 10, 18 and 27 weeks and *ex vivo* data for LV mass and LV/TL after sacrifice at 28 weeks. n represents the number of animals in each group. EDV = end-diastolic volume; ESV = end-systolic volume; SV = stroke volume; EF = ejection fraction; LV = left ventricle; TL = tibial length; ES = end-systolic.*P ≤ 0.0.05; **P ≤ 0.0.01; ***P ≤ 0.0.001; ****P ≤ 0.0001 *vs* control.

vs 22.0 ± 1.5 µl, $p < 0.05$) (Table 1). No difference was observed between the two groups for end-systolic septum thickness. Figure 3 shows representative short-axis images in β_1-immunized and control mice at the end of the protocol.

Analysis of the diastolic index showed an impaired diastolic function in the treated group from 18 weeks that become significantly altered at 27 weeks (51.4 ± 1.1 *vs* 63.1 ± 4.3%, $P < 0.05$) (Fig. 2, right panel and Table 1). By contrast, systolic function assessed both by EF and systolic index remained within normal values in the immunized group (Table 1).

Cardiac histology and gene expression upon induction of β1AR aabs. Histomorphometric analysis of cardiomyocyte transverse area confirmed significantly larger myocytes with increased vascular density in β_1-immunized mice ($p < 0.05$) (Fig. 4A). No differences in collagen (Sirius red labeling) (Fig. 4B) or inflammatory infiltration (CD45/CD11b staining) (Fig. 4C and D) were observed between the two groups.

We also performed qPCR analyses to identify changes in mRNA expression from corresponding cardiac tissues (Table 2). mRNA expression of βAR-1 and -2 (ADRB 1–2) remained unchanged between control and β_1-immunized group while a two-fold increase in βAR-3 gene expression (ADRB3) was observed in the immunized group (although not reaching statistical significance, Table 2). No re-expression of the fetal gene program was found based on the levels of myosin heavy chains (MYH6 and MYH7 coding for the alpha and beta isoform, respectively) and natriuretic peptides (ANP and BNP for atrial and brain forms, respectively); a trend toward an increase in the BNP gene expression was however observed in β_1-immunized mice ($p = 0.07$, Table 2).

β3TG mice are protected from β1AR aabs-induced cardiomyopathy. We tested whether the overexpression of the β3-AR could protect from developing β1-aabs-induced DCM by applying the protocol of immunization previously described to 12 transgenic (heterozygous) mice overexpressing the β3-AR (TG) and 12 wild-type littermates (WT). 5 mice died in each group upon active immunization against β_1AR-EC_{II} before the end of the protocol.

Cardiac MRI measurements after 27 weeks showed statistically significant differences between the two immunized groups: LV/TL ratio remained unaltered in immunized β_3-overexpressing mice, with a value of

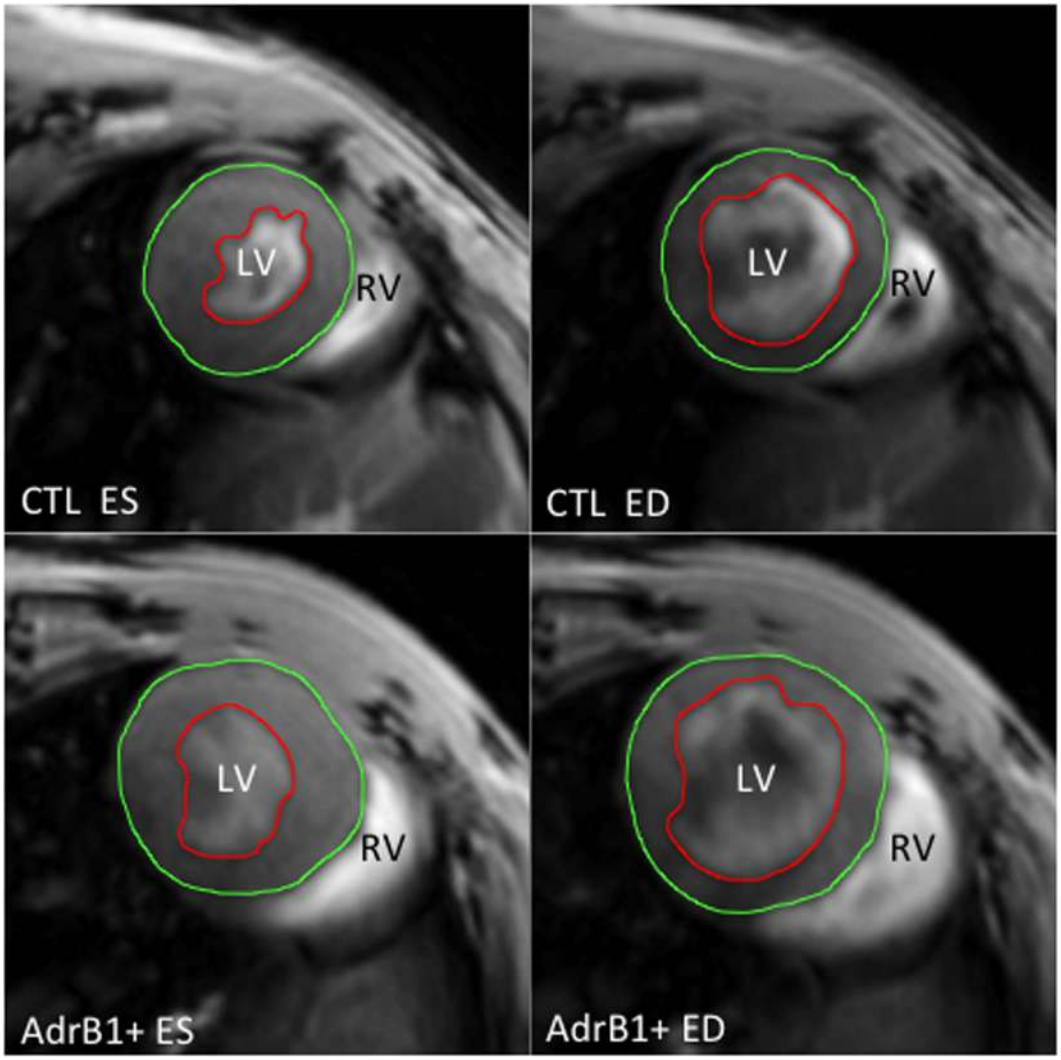

Figure 3. Representative MRI short-axis views of mouse hearts after 27 weeks of evolution in end-diastolic (ED) and end-systolic (ES) phases, with endocardial (red) and epicardial (green) contours, showing left ventricular dilation in β1-immunized (AdrB1+) vs control mice. LV = left ventricle, RV = right ventricle.

3.5 ± 0.2 mm/mg (*vs.* 4.3 ± 0.2 mm/mg in immunized wild-type animals, $p < 0.05$) (Fig. 5A, left panel). These data were confirmed by *ex vivo* LV/TL measurements after sacrifice of the animals (Fig. 5A, right panel). Interestingly, while determination of systolic indexes did not reveal any difference between mouse groups (Fig. 5B), evaluation of diastolic indexes reinforced the concept of β3-AR-mediated protection. First, significant differences between the two immunized groups were observed as soon as 18 weeks (Fig. 5C). Second, while LV/TL ratio measurements only revealed a trend towards an increase in control littermates of transgenic animals (see two first sets of points in Fig. 5A graphs), diastolic indexes revealed a statistically significant reduction after 27 weeks, confirming the earliness of diastolic dysfunction in this DCM model (Fig. 5C). Other MRI measurements were not altered when compared to control groups after 27 weeks of follow-up (not shown).

Discussion

The major findings of this study are related to the application of UHF MRI technology to study the early development of β1aabs-driven autoimmune cardiac dysfunction and to the identification of β3-AR as key actor of a counterbalancing pathway preventing the occurrence of DCM in this model.

Previous studies using echocardiography have reported the first anatomical changes at rest in β_1-immunized BalbC[25] and C57BL/6J mice[26] at 25 weeks. In our study with C57BL/6J mice immunized against the β1-AR, using UHF MRI, we were able to show early aabs-induced cardiomyopathic changes after only 10 weeks. LV hypertrophy (increase in LV/TL ratio) was detected before transition to the complete phenotype of DCM. Furthermore, we applied to our UHF MRI study a recently described method based on the concepts of echocardiographic color kinesis[41,42] in order to derive systolic and diastolic indexes in our animals. This led us to document that diastolic dysfunction was detectable before the occurrence of systolic dysfunction. These results open new perspectives for clinical investigations in patients carrying β1-aabs. Indeed, several methods (i.e. echographic speckle tracking and MR tagging ref. 43) are now available besides the classical echocardiographic mitral inflow color Doppler

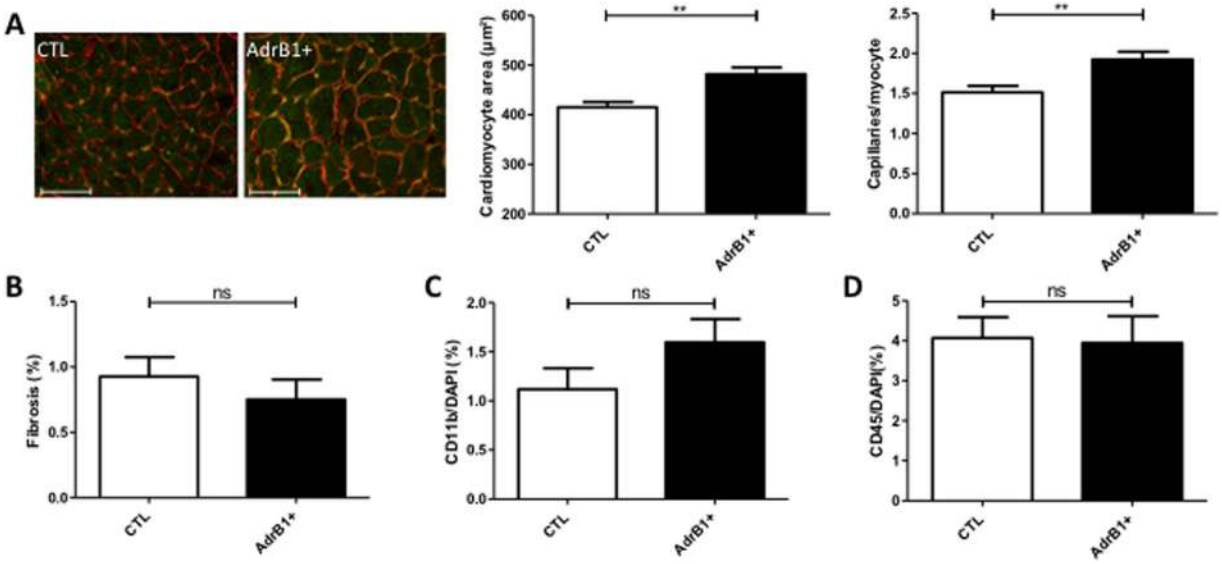

Figure 4. Histology of mouse hearts. (**A**) Left panel: representative cross-sections of hearts from control and β1-immunized (AdrB1+) mice stained with isolectin B4 (green) and wheat germ agglutinin (red). Scale bar, 50 μm. Right panel: columns indicate the respective myocyte area and capillary density from same sections in each group, showing cardiomyocyte hypertrophy compensated by higher capillary density in hearts from immunized mice. (**B**) Quantification of collagen infiltration with sirius red staining. (**C,D**) Quantification of inflammatory infiltration with CD11b and CD45 stainings. *P ≤ 0.0.05; **P ≤ 0.0.01 *vs* control. n = 7–10 mice per group.

Gene	Control mice	Immunized mice	p-value
ADRB1	1.00 ± 0.07	0.98 ± 0.10	0,87 (ns)
ADRB2	1.00 ± 0.07	0.94 ± 0.07	0,60 (ns)
ADRB3	1.00 ± 0.30	2.02 ± 0.39	0,11 (ns)
MYH6	1.00 ± 0.34	1.56 ± 0,58	0,39 (ns)
MYH7	1.00 ± 0.31	0.64 ± 0,26	0,40 (ns)
ANP	1.00 ± 0.19	1.14 ± 0.24	0,65 (ns)
BNP	1.00 ± 0.11	1.83 ± 0.46	0,07 (ns)

Table 2. mRNA expressions in heart lysates after 28 weeks of treatment. Data are presented as mean ± SEM, mRNA expressions in β1-immunized mice (n = 7) are normalized to expression measured in control mice (n = 10).

(E/A) measurements in order to thoroughly investigate diastolic function in patients. If these data are confirmed by further clinical studies, appearance of diastolic dysfunction in β1-aabs-positive patients could be used as an early marker of evolution to heart failure, requiring an intensification of treatments.

Besides the above technological benefits of UHF MRI applied to autoimmune DCM, we showed that transgenic mice harboring a cardiac-specific human β3-AR transgene were protected from myocardial dysfunction induced by β1-aabs. Although, unlike in C57BL/6J mice, only a trend to a cardiac dilation (ie, increased LV/TL ratio) was detectable in the immunized WT group (*vs.* non-immunized mice) at the end of our study, a significant reduction in the diastolic index confirmed the development of β1aabs-mediated cardiac alterations in these mice. Different genetic backgrounds are likely to account for the LV/TL ratio discrepancy but this observation also emphasize the earliness of the diastolic dysfunction in this model of autoimmune DCM. Importantly, in β3-AR overexpressing mice, the diastolic index was not decreased in response to immunization and was actually even slightly increased. Altogether, these data indicate a significant protective effect of β3-AR overexpression against the development of heart damage induced by β1-aabs (*vs.* immunized WT mice) and thereby open new therapeutic perspectives in the treatment of autoimmune DCM.

As β3-AR have functionally opposite effects to β1-AR and β2-AR on cardiac muscle and are more resistant than β1-AR and β2-AR to homologous desensitization[33], they represent attractive candidates for efficient pharmacological modulation in the diseased heart[44]. Recent data published by our team have already shown that β3TG mice were protected against early cardiac dysfunction induced by neurohormone infusion (i.e. angiotensin II or isoproterenol)[37]. The present study confirms the potential beneficial effects of β3-adrenergic stimulation to also prevent the development of autoimmune DCM. In addition to the attenuation of β1-adrenergic inotropic responses, the nitric oxide production consecutive to a β3-AR stimulation of microvascular endothelial cells[45] and cardiac myocytes[37] may help to maintain a normal left ventricular diastolic function during the early stages

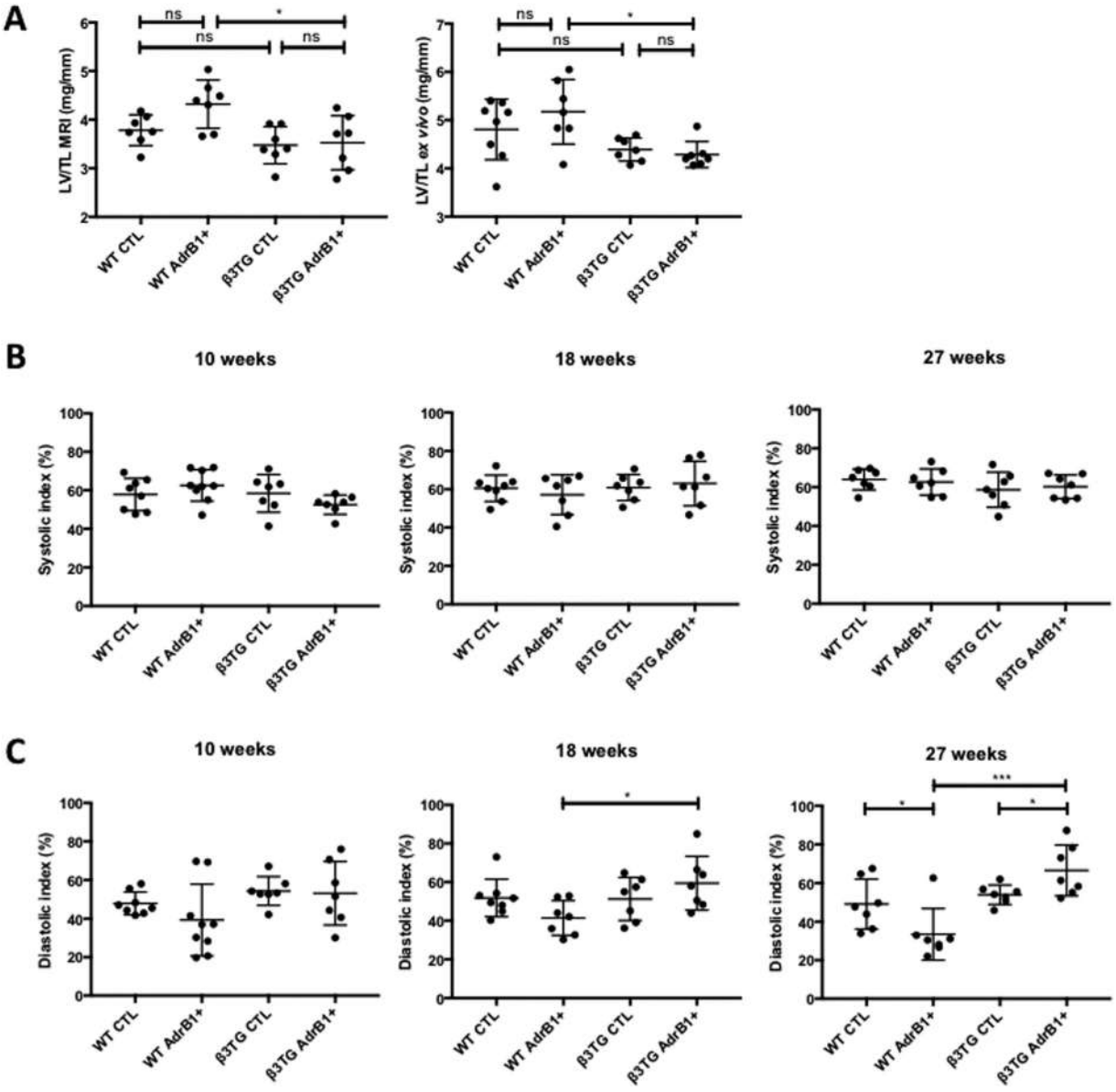

Figure 5. (**A**) MRI LV/TL (left) and *ex vivo* LV/TL (right) ratios at 27 and 28 weeks, respectively, in transgenic mice overexpressing the beta3 adrenergic receptor and immunized (TG AdrB1+) or not (TG CTL) against AdrB1-ECII, and their wild-type littermates with (WT AdrB1+) or without (WT CTL) immunization. Systolic **(B)** and diastolic **(C)** indexes determined in the same animals after 10, 18 and 27 weeks, $*P \leq 0.0.05$; $**P \leq 0.0.01$ as indicated.

of cardiac dysfunction; improving diastolic relaxation can indeed exert a beneficial hemodynamic effect through the maintenance of the Frank-Starling response[46]. The latter property seems even more relevant for the treatment of β1-aabs-induced cardiomyopathy, in the light of the early diastolic dysfunction reported in mice immunized against $\beta1\text{-}EC_{II}$.

A limitation in our study is the use of transgenic β3 AR-overexpressing mice which *per se* means that this pathway is continuously influencing the cardiac phenotype of these animals and may thus prevent dysfunction from the earliest stages of its development. Still, these results pave the way for the evaluation of *bona fide* β3-AR agonists or the preferred use of β-blockers endowed with such β3-AR stimulatory activity in the treatment of autoimmune β1-aabs-induced DCM. Nebivolol represents a third generation selective β1-AR antagonist with ancillary metabolic effects involving a β3-AR stimulation. Nebivolol could thus bring an increment of efficacy *vs.* conventional beta-blockers whose usefulness has already been demonstrated in the context of β1-aabs-induced DCM (with however a lower efficiency than therapies using neutralizing peptides)[30]. We previously showed that nebivolol treatment of coronary microvessels led to NO-dependent vasorelaxation[47] while others documented a further protection of nebivolol administration against endothelial dysfunction though a net reduction in oxidative stress[48]. Altogether these studies suggest that the dual β1/β3-AR modulation, already demonstrated in

previous studies for heart failure and myocardial infarction with Nebivolol[49], could be extended to patients with β_1-aabs-induced DCM.

In conclusion, we showed that UHF MRI allows the precocious detection of mouse myocardial remodeling induced by β1-aabs, at earlier time-points than anticipated based on previous reports using echocardiography. Importantly, this technology allowed us to identify a diastolic dysfunction occurring before the onset of systolic dysfunction in this autoimmune cardiac disease and to provide evidence supporting the therapeutic potential of drugs endowed with beta-3 AR agonistic activity for the treatment of β1-aabs-induced DCM.

Methods

Animals and immunization. All the experiments involving mice received the approval of the "Comité d'Ethique pour l'Expérimentation Animale de l'Université catholique de Louvain" (approval reference #2012/UCL/MD005) and were carried out according to national animal care regulations. This study conforms to the Guide for the Care and Use of Laboratory Animals published by the US National Institutes of Health (NIH Publication No. 85–23, revised 1996). Mice were housed under standard conditions with *ad libitum* access to water and chow.

C57BL/6J mice. A group of ten 8-weeks C57BL/6J male mice (Janvier, Paris, France) were monthly immunized with 200 μg of a synthetic peptide (Eurogentec, Seraing, Belgium) corresponding to the human and mouse β_1AR-EC_{II} (residues 197–222: H-W-W-R-A-E-S-D-E-A-R-R-C-Y-N-D-P-K-C-C-D-F-V-T-N-R) through subcutaneous injection. The peptide was dissolved in 0.1 M Na_2CO_3/1% β-mercaptoethanol and emulsified in complete Freund's adjuvant for the first injection and incomplete adjuvant for the followings in order to avoid excessive inflammatory response. Another group of 10 C57BL/6J male mice received only the vehicle and were used as controls. Mice were anaesthetized (150 mg/kg ketamine, 10 mg/kg xylazine, i.p.) prior each injection, allowing simultaneous collection of retro-orbital blood samples.

β3TG mice. Male mice harboring an α-myosin heavy chain promoter-driven human β3-AR transgene generated as described previously[50], were used to produce heterozygous β3TG mice and wild-type littermate controls (n = 40); the original β3TG mouse line had been selected to exhibit a moderate overexpression of the transgene (matching the *ex vivo* myocardial response to a β3-AR agonist). Mice from β3TG and wild-type groups were randomly distributed in two subgroups and immunized according to the protocol described above, except that subcutaneous injections were performed under light anaesthesia with isoflurane 2–3% in oxygen for 3 minutes, and that no retro-orbital blood sample was taken at the same time to minimize animal stress. 12 mice per group were immunized with the peptide while 8 mice per group receive the vehicle and were used as controls.

Morphometric measurements. At the end of the study, after a follow-up of 28 weeks, animals were euthanized by cervical disclocation and their left ventricular weight and tibial length were measured. Hearts and sera were collected for analysis and stored at −80 °C.

Autoantibody detection. To detect β1AR autoantibodies in mouse sera, the β_1AR-EC_{II} synthetic peptide was used in an enzyme-linked immunosorbent assay (ELISA). Plates (Reacti-Bind, Thermo scientific, Rockford, IL) were coated overnight at room temperature with 1 μg/ml peptide (Eurogentec, Seraing, Belgium). Coating and blocking procedures were carried out using Ultrablock and Neptune buffers form AbD Serotec (Oxford, UK) according to the manufacturer's instructions. Sera (diluted 1/2500) were then incubated overnight at 4 °C. After washing, specific hybridization was measured with a peroxidase-conjugated antimouse IgG antibody (dilution 1/10000) and addition of 3,3′,5,5′-tetramethylbenzidine from Calbiochem (Merck Chemicals, Nottingham, UK). The absorbance was determined at 450 nm in a microplate reader (Victor X4; Perkin Elmer, Waltham, MA).

MRI measurements. *Cardiac MRI (CMR) acquisition.* Each animal was scanned at 10, 18 and 27 weeks of treatment on a 11.7T MRI scanner dedicated to small animal applications (Biospec, Bruker, Ettlingen, Germany). A quadrature ^{1}H resonator was used for radiofrequency transmission (inner diameter = 72 mm, length = 6.6 cm) in conjunction with a surface receive-only coil array (length = 10.7 cm). Anaesthesia was induced with 3% isoflurane in oxygen, and then maintained with 0.5–2% isoflurane during the entire procedure, in order to remain within physiological heart rates (around 500 heartbeats/min). Animals were placed in prone position and monitored for electrocardiogram and respiration with neonatal electrodes wrapped around the paws and a pneumatic sensor placed under the animal. The body temperature was followed by using a rectal probe and regulated with a dedicated heating blanket. Cardiac scout images were obtained in the conventional planes with a tripilot sequence. Then an Intragate 2D cine Fast Low Angle Shot (FLASH) sequence was applied to acquire a stack of seven to eight 1-mm thick contiguous short-axis images covering the entire ventricles, perpendicular to the LV long-axis. Imaging parameters: repetition time: 5.83 ms; echo time: 1.45 ms; flip angle: 25°; field of view: 30.0 × 30.0; and matrix size: 256 × 256; resulting in an in-plane resolution of 0.12 × 0.12 mm^2.

CMR Image analysis. The LV systolic function was assessed from the stack of short axis images by tracing epicardial and endocardial borders on Segment software (Medviso v1.8, Lund, Sweden). End-diastolic (EDV), end-systolic (ESV) and stroke volume (SV) were determined (μl). LV ejection fraction (EF, as %) and LV mass (mg) were subsequently deduced. Systolic and diastolic indexes were determined as previously described[41,42]. Briefly, we visually determined the end-diastolic phase, end-systolic phase and the phase at 30% of diastole, and traced the endocardial contours at the mid-ventricular level on the Osirix imaging software (v4.0; Pixmeo; Geneva, Switzerland). Then we calculated the systolic fractional area change (systolic index, as %) through the following formula: EDA-ESA/EDA, where EDA = end-diastolic area and ESA = end-sytolic area. The fractional

area change during the first 30% of diastole (diastolic index, as %) was also calculated through the following formula: dA-ESA/EDA-ESA, where dA = area at 30% of diastole. All analyses were performed on a blinded basis.

Cardiac histochemistry. At the end of the study hearts were excised and representative pieces of left ventricles were fixed in 4% formaldehyde after rinsing with saline. For analysis of cardiac fibrosis, 5-μm sections of paraffin embedded hearts were stained with picrosirius red. Stained sections were digitalized with a SCN400 slide scanner (Leica Biosystems, Wetzlar, Germany). Quantification was made with Tissue IA software (Leica Biosystems, Dublin, Ireland). Area occupied by interstitial fibrosis was expressed as a percentage of total myocardial area. To quantify transverse cardiomyocyte area and capillary density, cryosections were stained with Wheat germ agglutinin (WGA) as a membrane marker, and with biotinylated-Isolectine B4 as an endothelial marker. Mounted slides were observed with an Axioimager Z1/Apotome microscope equipped with a MRM camera (Zeiss, Germany). The data analysis was performed with Axiovision software (Zeiss, Germany). A minimum of 40 to 100 cells from 9 sections were measured in each heart. Other heart cryosections were incubated with antibodies raised against the monocyte marker CD11b and the lymphocytic marker CD45 (rat anti-CD11b and rat anti-CD45, both from BD Bioscience, San Jose, CA). Slides were scanned with a MIRAX Scanner (Zeiss, Germany) and analyzed with FRIDA software (Johns Hopkins University, Baltimore, MD). All analyses were performed on a blinded basis.

Quantitative Polymerase Chain Reaction (qPCR). Total RNA was isolated from heart tissues using TRI-reagent (Fermentas, Alost, Belgium) according to the manufacturer's instructions. 1 μg total RNA was reverse transcribed with RevertAidTM M-MuLV Reverse Transcriptase (Thermofischer Scientific, Alost, Belgium) using hexamer primers. Resulting cDNA served as template for quantitative real-time PCR analysis using the following primers: *Adrb1* (Forward: 5′-GCTGATCTGGTCATGGGATT-3′, Reverse: 5′-AAGTCCAGAGCTCGCAGAAG-3′), *Adrb2* (Forward: 5′-TTCGAAAACCTATGGGAACG-3′, Reverse: 5′-GGGATCCTCACACAGCAGTT-3′), *Adrb3* (Forward: 5′-ACCAGAAGCCCTCAGCATCCCA-3′, Reverse: 5′-CACCCGCTTGTTTCAGGAGTCAC-3′), *Myh6* (Forward: 5′- GGGACATTGGTGCCAAGAAGA-3′, Reverse: 5′-ATTGTGGATTGGCCACAGCG-3′), *Myh7* (Forward: 5′-ACCAACCTGTCCAAGTTCCG-3′, Reverse: 5′-ACTCCTCATTCAGGCCCTTG-3′), *Nppa* (Forward: 5′TGATAGATGAAGGCAGGAAGCCGC-3′, Reverse: 5′-AGGATTGGAGCCCAGAGTGGACTAGG-3′), *Nppb* (Forward: 5′-GCCAGTCTCCAGAGC AATTC-3′, Reverse: 5′-AGCTGTCTCTGGGCCATTT-3′), *Gapdh* (Forward: 5′-TGCACCACCAACTGCTTAGC-3′, Reverse: 5′-GGATGCAGGGATGATGTTCT-3′). All samples were processed in triplicate reactions using Takyon for SYBR low Rox (Eurogentec, Seraing, Belgium) on the ViiA7 Real-Time PCR System (Applied Biosystems) using a fast cycling protocol. GAPDH was used as a reference endogenous gene to normalize the results. Results are shown as fold expression relative to untreated samples according to the $\Delta\Delta C_T$ method.

Statistical Analysis. Data are expressed as mean ± SEM. Raw data were analyzed for normal distribution using the Shapiro-Wilk test. When normally distributed, unpaired Student *t* test was used to compare differences between two groups and one-way analysis of variance followed by Bonferroni post-hoc test was used to compare 3 or more groups. In the absence of normal distribution, the statistical significance of differences was tested with non-parametric tests (Mann-Whitney or Kruskall-Wallis followed by Dunn's test). $P < 0.05$ was considered statistically significant. Statistical analyses were performed with GraphPad Prism 5.04 (San Diego, CA) and JMP 11.2.0 (SAS Institute, Cary, NC).

References

1. Limas, C. J., Goldenberg, I. F. & Limas, C. Assessment of immune modulation of beta-adrenergic pathways in human dilated cardiomyopathy: influence of methodologic factors. *Am Heart J* **123,** 967–970 (1992).
2. Magnusson, Y., Wallukat, G., Waagstein, F., Hjalmarson, A. & Hoebeke, J. Autoimmunity in idiopathic dilated cardiomyopathy. Characterization of antibodies against the beta 1-adrenoceptor with positive chronotropic effect. *Circulation* **89,** 2760–2767 (1994).
3. Wallukat, G., Wollenberger, A., Morwinski, R. & Pitschner, H. F. Anti-beta 1-adrenoceptor autoantibodies with chronotropic activity from the serum of patients with dilated cardiomyopathy: mapping of epitopes in the first and second extracellular loops. *J Mol Cell Cardiol* **27,** 397–406 (1995).
4. Jahns, R. *et al.* Autoantibodies activating human beta1-adrenergic receptors are associated with reduced cardiac function in chronic heart failure. *Circulation* **99,** 649–654 (1999).
5. Elies, R. *et al.* Structural and functional analysis of the B cell epitopes recognized by anti-receptor autoantibodies in patients with Chagas' disease. *J Immunol* **157,** 4203–4211 (1996).
6. Bohl, S. *et al.* Advanced methods for quantification of infarct size in mice using three-dimensional high-field late gadolinium enhancement MRI. *Am J Physiol Heart Circ Physiol* **296,** H1200–1208 (2009).
7. Iwata, M. *et al.* Autoantibodies against the second extracellular loop of beta1-adrenergic receptors predict ventricular tachycardia and sudden death in patients with idiopathic dilated cardiomyopathy. *J Am Coll Cardiol* **37,** 418–424 (2001).
8. Stork, S. *et al.* Stimulating autoantibodies directed against the cardiac beta1-adrenergic receptor predict increased mortality in idiopathic cardiomyopathy. *Am Heart J* **152,** 697–704 (2006).
9. Jahns, R. *et al.* Activating beta-1-adrenoceptor antibodies are not associated with cardiomyopathies secondary to valvular or hypertensive heart disease. *J Am Coll Cardiol* **34,** 1545–1551 (1999).
10. Deubner, N. *et al.* Cardiac beta1-adrenoceptor autoantibodies in human heart disease: rationale and design of the Etiology, Titre-Course, and Survival (ETiCS) Study. *Eur J Heart Fail* **12,** 753–762 (2010).
11. Magnusson, Y. *et al.* Antigenic analysis of the second extra-cellular loop of the human beta-adrenergic receptors. *Clin Exp Immunol* **78,** 42–48 (1989).
12. Tate, K. *et al.* Epitope analysis of T- and B-cell response against the human beta 1-adrenoceptor. *Biochimie* **76,** 159–164 (1994).
13. Mobini, R. *et al.* Probing the immunological properties of the extracellular domains of the human beta(1)-adrenoceptor. *J Autoimmun* **13,** 179–186 (1999).
14. Matsui, S. *et al.* Peptides derived from cardiovascular G-protein-coupled receptors induce morphological cardiomyopathic changes in immunized rabbits. *J Mol Cell Cardiol* **29,** 641–655 (1997).

15. Iwata, M. *et al.* Autoimmunity against the second extracellular loop of beta(1)-adrenergic receptors induces beta-adrenergic receptor desensitization and myocardial hypertrophy *in vivo*. *Circ Res* **88,** 578–586 (2001).
16. Buvall, L., Bollano, E., Chen, J., Shultze, W. & Fu, M. Phenotype of early cardiomyopathic changes induced by active immunization of rats with a synthetic peptide corresponding to the second extracellular loop of the human beta-adrenergic receptor. *Clin Exp Immunol* **143,** 209–215 (2006).
17. Jahns, R. *et al.* Direct evidence for a beta 1-adrenergic receptor-directed autoimmune attack as a cause of idiopathic dilated cardiomyopathy. *J Clin Invest* **113,** 1419–1429 (2004).
18. Jahns, R., Boivin, V. & Lohse, M. J. beta(1)-Adrenergic receptor function, autoimmunity, and pathogenesis of dilated cardiomyopathy. *Trends Cardiovasc Med* **16,** 20–24 (2006).
19. Jahns, R., Boivin, V. & Lohse, M. J. Beta 1-adrenergic receptor-directed autoimmunity as a cause of dilated cardiomyopathy in rats. *Int J Cardiol* **112,** 7–14 (2006).
20. Gouldson, P. R. *et al.* Dimerization and domain swapping in G-protein-coupled receptors: a computational study. *Neuropsychopharmacology* **23,** S60–77 (2000).
21. Tutor, A. S., Penela, P. & Mayor, F. Jr. Anti-beta1-adrenergic receptor autoantibodies are potent stimulators of the ERK1/2 pathway in cardiac cells. *Cardiovasc Res* **76,** 51–60 (2007).
22. Hebert, T. E. Anti-beta1AR antibodies in dilated cardiomyopathy: are these a new class of receptor agonists? *Cardiovasc Res* **76,** 5–7 (2007).
23. Staudt, Y. *et al.* Beta1-adrenoceptor antibodies induce apoptosis in adult isolated cardiomyocytes. *Eur J Pharmacol* **466,** 1–6 (2003).
24. Christ, T. *et al.* Autoantibodies against the beta1 adrenoceptor from patients with dilated cardiomyopathy prolong action potential duration and enhance contractility in isolated cardiomyocytes. *J Mol Cell Cardiol* **33,** 1515–1525 (2001).
25. Buvall, L., Tang, M. S., Isic, A., Andersson, B. & Fu, M. Antibodies against the beta1-adrenergic receptor induce progressive development of cardiomyopathy. *J Mol Cell Cardiol* **42,** 1001–1007 (2007).
26. Ma, L. P., Premaratne, G., Bollano, E., Lindholm, C. & Fu, M. Interleukin-6-deficient mice resist development of experimental autoimmune cardiomyopathy induced by immunization of beta1-adrenergic receptor. *Int J Cardiol* **155,** 20–25 (2012).
27. Matsui, S. *et al.* Specific removal of beta1-adrenoceptor autoantibodies by immunoabsorption in rabbits with autoimmune cardiomyopathy improved cardiac structure and function. *J Mol Cell Cardiol* **41,** 78–85 (2006).
28. Haberland, A., Wallukat, G., Dahmen, C., Kage, A. & Schimke, I. Aptamer neutralization of beta1-adrenoceptor autoantibodies isolated from patients with cardiomyopathies. *Circ Res* **109,** 986–992 (2011).
29. Munch, G. *et al.* Administration of the cyclic peptide COR-1 in humans (phase I study): *ex vivo* measurements of anti-beta1-adrenergic receptor antibody neutralization and of immune parameters. *Eur J Heart Fail* **14,** 1230–1239 (2012).
30. Boivin, V. *et al.* Novel receptor-derived cyclopeptides to treat heart failure caused by anti-beta1-adrenoceptor antibodies in a human-analogous rat model. *PLoS One* **10,** e0117589 (2015).
31. Miao, G. B. *et al.* Autoantibody against beta1-adrenergic receptor and left ventricular remodeling changes in response to metoprolol treatment. *Eur J Clin Invest* **36,** 614–620 (2006).
32. Niu, X. *et al.* Cardioprotective effect of beta-3 adrenergic receptor agonism: role of neuronal nitric oxide synthase. *J Am Coll Cardiol* **59,** 1979–1987 (2012).
33. Liggett, S. B., Freedman, N. J., Schwinn, D. A. & Lefkowitz, R. J. Structural basis for receptor subtype-specific regulation revealed by a chimeric beta 3/beta 2-adrenergic receptor. *Proc Natl Acad Sci USA* **90,** 3665–3669 (1993).
34. Moniotte, S. *et al.* Upregulation of beta(3)-adrenoceptors and altered contractile response to inotropic amines in human failing myocardium. *Circulation* **103,** 1649–1655 (2001).
35. Dincer, U. D. *et al.* The effect of diabetes on expression of beta1-, beta2-, and beta3-adrenoreceptors in rat hearts. *Diabetes* **50,** 455–461 (2001).
36. Moniotte, S. *et al.* Sepsis is associated with an upregulation of functional beta3 adrenoceptors in the myocardium. *Eur J Heart Fail* **9,** 1163–1171 (2007).
37. Belge, C. *et al.* Enhanced expression of beta3-adrenoceptors in cardiac myocytes attenuates neurohormone-induced hypertrophic remodeling through nitric oxide synthase. *Circulation* **129,** 451–462 (2014).
38. Vanhoutte, L. *et al.* Variability of Mouse Left Ventricular Function Assessment by 11.7 Tesla MRI. *J Cardiovasc Transl Res* (2015).
39. Lee, H. C., Huang, K. T., Wang, X. L. & Shen, W. K. Autoantibodies and cardiac arrhythmias. *Heart Rhythm* **8,** 1788–1795 (2011).
40. Zuo, L. *et al.* Pro-arrhythmic action of autoantibodies against the second extracellular loop of beta1-adrenoceptor and its underlying molecular mechanisms. *Int J Cardiol* **198,** 251–258 (2015).
41. Okayama, S. *et al.* Evaluation of left ventricular diastolic function by fractional area change using cine cardiovascular magnetic resonance: a feasibility study. *J Cardiovasc Magn Reson* **15,** 87 (2013).
42. Buonincontri, G., Hu, C.-H., Sawiak, S. & Krieg, T. *P516Diastolic dysfunction in diabetic mice revealed by MR* (2014).
43. Daneshvar, D. *et al.* Diastolic dysfunction: improved understanding using emerging imaging techniques. *Am Heart J* **160,** 394–404 (2010).
44. Balligand, J. L. beta(3)-Adrenoceptor stimulation on top of beta(1)-adrenoceptor blockade "Stop or Encore?". *J Am Coll Cardiol* **53,** 1539–1542 (2009).
45. Dessy, C. *et al.* Endothelial beta3-adrenoceptors mediate vasorelaxation of human coronary microarteries through nitric oxide and endothelium-dependent hyperpolarization. *Circulation* **110,** 948–954 (2004).
46. Heymes, C., Vanderheyden, M., Bronzwaer, J. G., Shah, A. M. & Paulus, W. J. Endomyocardial nitric oxide synthase and left ventricular preload reserve in dilated cardiomyopathy. *Circulation* **99,** 3009–3016 (1999).
47. Dessy, C. *et al.* Endothelial beta3-adrenoreceptors mediate nitric oxide-dependent vasorelaxation of coronary microvessels in response to the third-generation beta-blocker nebivolol. *Circulation* **112,** 1198–1205 (2005).
48. Mason, R. P., Kalinowski, L., Jacob, R. F., Jacoby, A. M. & Malinski, T. Nebivolol reduces nitroxidative stress and restores nitric oxide bioavailability in endothelium of black Americans. *Circulation* **112,** 3795–3801 (2005).
49. Sorrentino, S. A. *et al.* Nebivolol exerts beneficial effects on endothelial function, early endothelial progenitor cells, myocardial neovascularization, and left ventricular dysfunction early after myocardial infarction beyond conventional beta1-blockade. *J Am Coll Cardiol* **57,** 601–611 (2011).
50. Tavernier, G. *et al.* beta3-Adrenergic stimulation produces a decrease of cardiac contractility *ex vivo* in mice overexpressing the human beta3-adrenergic receptor. *Cardiovasc Res* **59,** 288–296 (2003).

Acknowledgements

The authors wish to thank the Biomedical Magnetic Resonance Unit (REMA) for assistance during MRI manipulations. We thank Chantal Fregimilicka (IREC Imaging Platform - 2IP) for histochemistry experiments and Sabrina El Bachiri (technological platform for Methodology Support and Statistical Calculation - SMCS) for helpful discussions about statistical analysis. This work was supported by grants from the Fonds de la Recherche Scientifique FRS-FNRS, the Foundation Saint-Luc and the National Foundation for Research in Pediatric Cardiology. LV, CD and OF are Research Fellow, Senior Research Associate and honorary Research Director of the FRS-FNRS, respectively.

Author Contributions

O.F. and C.D. conceived and designed the immunization experiments. L.V.H., S.M. and J.L.B. conceived and analysed the cardiac M.R.I. experiments. L.V.H. performed the experiments including all the MRI-related measurements under the supervision of B.G. and S.M., C.G. and L.V.H. handled the animals for blood and tissue collection. R.M. and C.B. supervised qPCR and histological experiments, respectively. L.V.H. and O.F. prepared figures and L.V.H., S.M. and O.F. wrote the manuscript. All authors reviewed the manuscript.

Additional Information

Competing Interests: The authors declare no competing financial interests.

How to cite this article: Vanhoutte, L. *et al.* MRI Assessment of Cardiomyopathy Induced by β1-Adrenoreceptor Autoantibodies and Protection Through β3-Adrenoreceptor Overexpression. *Sci. Rep.* **7**, 43951; doi: 10.1038/srep43951 (2017).

Publisher's note: Springer Nature remains neutral with regard to jurisdictional claims in published maps and institutional affiliations.

JCI insight

RESEARCH ARTICLE

Dnmt3a-mediated inhibition of Wnt in cardiac progenitor cells improves differentiation and remote remodeling after infarction

Aurelia De Pauw,[1] Emilie Andre,[1] Belaid Sekkali,[1] Caroline Bouzin,[1] Hrag Esfahani,[1] Nicolas Barbier,[1] Axelle Loriot,[2] Charles De Smet,[2] Laetitia Vanhoutte,[1,3] Stéphane Moniotte,[3] Bernhard Gerber,[4] Vittoria di Mauro,[5] Daniele Catalucci,[5] Olivier Feron,[1] Denise Hilfiker-Kleiner,[6] and Jean-Luc Balligand[1]

[1]Pole of Pharmacology and Therapeutics (FATH), Institut de Recherche Expérimentale et Clinique, and Department of Medicine, Cliniques Saint-Luc, and [2]Group of Genetics and Epigenetics, de Duve Institute, Université Catholique de Louvain, Brussels, Belgium. [3]Division of Paediatric Cardiology and [4]Pole of Cardiovascular Research, Institut de Recherche Expérimentale et Clinique and Cliniques Saint-Luc, Université Catholique de Louvain, Brussels, Belgium. [5]Humanitas Clinical and Research Center, National Research Council, Institute of Genetic and Biomedical Research, Milan, Italy. [6]Molecular Cardiology, Medizinische Hochschule Hannover, Hanover, Germany.

Adult cardiac progenitor cells (CPCs) display a low capacity to differentiate into cardiomyocytes in injured hearts, strongly limiting the regenerative capacity of the mammalian myocardium. To identify new mechanisms regulating CPC differentiation, we used primary and clonally expanded Sca-1$^+$ CPCs from murine adult hearts in homotypic culture or coculture with cardiomyocytes. Expression kinetics analysis during homotypic culture differentiation showed downregulation of Wnt target genes concomitant with increased expression of the Wnt antagonist, Wnt inhibitory factor 1 (Wif1), which is necessary to stimulate CPC differentiation. We show that the expression of the *Wif1* gene is repressed by DNA methylation and regulated by the de novo DNA methyltransferase Dnmt3a. In addition, miR-29a is upregulated early during CPC differentiation and downregulates Dnmt3a expression, thereby decreasing *Wif1* gene methylation and increasing the efficiency of differentiation of Sca-1$^+$ CPCs in vitro. Extending these findings in vivo, transient silencing of Dnmt3a in CPCs subsequently injected in the border zone of infarcted mouse hearts improved CPC differentiation in situ and remote cardiac remodeling. In conclusion, miR-29a and Dnmt3a epigenetically regulate CPC differentiation through Wnt inhibition. Remote effects on cardiac remodeling support paracrine signaling beyond the local injection site, with potential therapeutic interest for cardiac repair.

Introduction

Healing of the infarcted myocardium proceeds through remodeling of the remaining tissue and, to a limited extent, regeneration of lost cardiac muscle. Both processes involve activation of endogenous cardiac progenitor cells (CPCs) in cardiac niches that, upon specific stimuli, undergo proliferation and differentiation toward vascular or muscle lineages and release paracrine factors acting on neighboring cells to modulate tissue repair (1). A number of progenitor cells have been identified in the adult mouse and/or human heart based on their expression of specific surface markers, e.g., c-kit (2) and Sca-1 (3), or transcription factors, such as homeobox gene islet1 (Isl1) (4), or their ability to efflux Hoechst dye 33342 (identified as side population cells, ref. 5). Although adult CPCs were shown to contribute to cell homeostasis during aging (6), their ability to regenerate cardiac muscle through durable engraftment, survival, and terminal differentiation seems marginal, at least in the adult mammalian heart (7, 8). An improved understanding of the mechanisms driving their proliferation, survival, and terminal differentiation, as well as paracrine signaling, would be highly desirable for their future therapeutic exploitation.

Just as sequential steps drive the specification of pluripotent stem cells to mesodermal and then car-

Conflict of interest: The authors have declared that no conflict of interest exists.

Submitted: November 16, 2016
Accepted: May 15, 2017
Published: June 15, 2017

Reference information:
JCI Insight. 2017;2(12):e91810. https://doi.org/10.1172/jci.insight.91810.

diac lineages during embryogenesis, the terminal differentiation of adult CPCs follows similar signaling events that determine their fate, some of which recapitulate early specification during organogenesis. One of these signals is the bimodal activity (i.e., early activation followed by later extinction) of the canonical Wnt/β-catenin pathway that drives cardiac mesoderm formation in the embryo (9, 10). Recent studies have confirmed the importance of the same signaling sequence in human induced pluripotent stem cells (iPSCs) (11) and embryonic stem cells (ESCs) (12), in which early activation of BMP and Wnt, followed by Wnt inhibition, progressively removes repressive roadblocks in the path toward cardiac myocyte differentiation. We and others (13) have confirmed similar paradigms in adult CPCs (that have constitutive Wnt activity, ref. 14), in which secondary extinction of Wnt/β-catenin using genetic invalidation (15) or paracrine NO signaling (14) promotes the expression of late cardiac differentiation markers in CPCs in vitro and in vivo. Accordingly, small-molecule inhibitors of canonical Wnt similarly promote cardiac myocyte formation from mammalian (including human) ESCs or iPSCs in differentiation protocols in vitro (16).

However, transposition of the paradigm using pharmacologic Wnt blockade in vivo would be impractical due to expected adverse effects from indiscriminate Wnt inhibition in other cell types (17, 18). This calls for a better understanding of the dynamic regulation of Wnt signaling in the cardiac tissue, especially the mechanisms driving Wnt extinction in CPCs that promotes their progression toward cardiac myocyte differentiation.

We used a well-characterized model of adult mouse Sca-1$^+$ CPCs (14, 19) to study the kinetics of expression of Wnt regulators and Wnt target genes in the course of in vitro differentiation into cardiomyocytes. We identified Wnt inhibitory factor 1 (Wif1) as a key modulator of their differentiation and found its expression to be epigenetically regulated by DNA methylation. Early expression of miR-29a downregulates the expression of the DNA methyltransferase Dnmt3a to demethylate the Wif1 gene, allowing its expression to promote CPC differentiation. Injection of CPCs with downregulated Dnmt3a in infarcted hearts attenuates adverse remodeling and preserves left ventricular function in vivo.

Results

Downregulation of Wnt/β-catenin commits adult mouse Sca-1$^+$ CPCs to cardiac myocyte differentiation. After two rounds of MACS isolation, the positive fraction of isolated Sca-1$^+$ population cells was purified to nearly 90% after exclusion of dead cells, as previously described (14, 19). Freshly isolated cells scored negative for myocyte (e.g., α-cardiac actinin, and cardiac troponin I and T), endothelial cell (e.g., CD31), and smooth muscle cell (e.g., α-smooth muscle actin) markers. However, transcription factors expressed early in the myocyte lineage (Nkx2.5, GATA-4) were each detected in the freshly isolated Sca-1$^+$ CPCs. We next induced differentiation of CPCs toward the cardiac myocyte lineage using pretreatment with 5-azacytidine (AZA) for 3 days, followed by repetitive pulses of TGF-β, as previously described (20). Efficient early commitment to the myocyte lineage was assessed through the time-dependent expression of early cardiac-specific transcription factors, such as Nkx2.5, together with expression of cardiac structural genes, such as *Tnnt2*, for up to 26 days (Supplemental Figure 1A; supplemental material available online with this article; https://doi.org/10.1172/jci.insight.91810DS1). At this time point, some primitive sarcomeric organization was also observed by immunohistochemistry (Supplemental Figure 1B).

We previously demonstrated that adult mouse CPCs display a constitutive activity of the canonical Wnt/β-catenin pathway (14) and that their differentiation toward cardiomyocytes is enhanced upon genetic deletion of β-catenin in vitro and in vivo (14, 15). We therefore evaluated the dynamic activity of the endogenous Wnt/β-catenin pathway during in vitro differentiation of CPCs. We first monitored the time-dependent expression of Wnt target genes upon differentiation with AZA/TGF-β, as used above. Typical Wnt target genes, such as *Axin2* and *Wnt4*, were downregulated in the course of differentiation, together with a decrease in β-catenin protein level. Moreover, this was paralleled with time-dependent downregulation of the Wnt activators *Lef1* and *Snai2* (Figure 1A); however, upregulation of Wnt repressors *Hbp1* and *Wif1* was evident (Figure 1C). The inhibition of Wnt signaling was further confirmed using the TOPflash reporter assay in HEK cells superfused with conditioned media from CPCs differentiated by AZA/TGF-β (Figure 1B). Altogether, this profile suggests repression of the constitutive Wnt/β-catenin activity in the course of CPC differentiation.

To further assess the causality of Wnt repression in the differentiation process, we tested the effect of the pharmacologic inhibitor of Wnt/β-catenin, namely inhibitor of Wnt signaling response (IWR1) (21), on the differentiation of CPCs. Inhibitor treatment resulted in enhanced differentiation of CPCs, as reflected by the increased number of cardiac troponin T–expressing (cTnT-expressing) cells and by the increased expression of *Nkx2.5* in CPCs treated with IWR1 with or without AZA (Figure 1D).

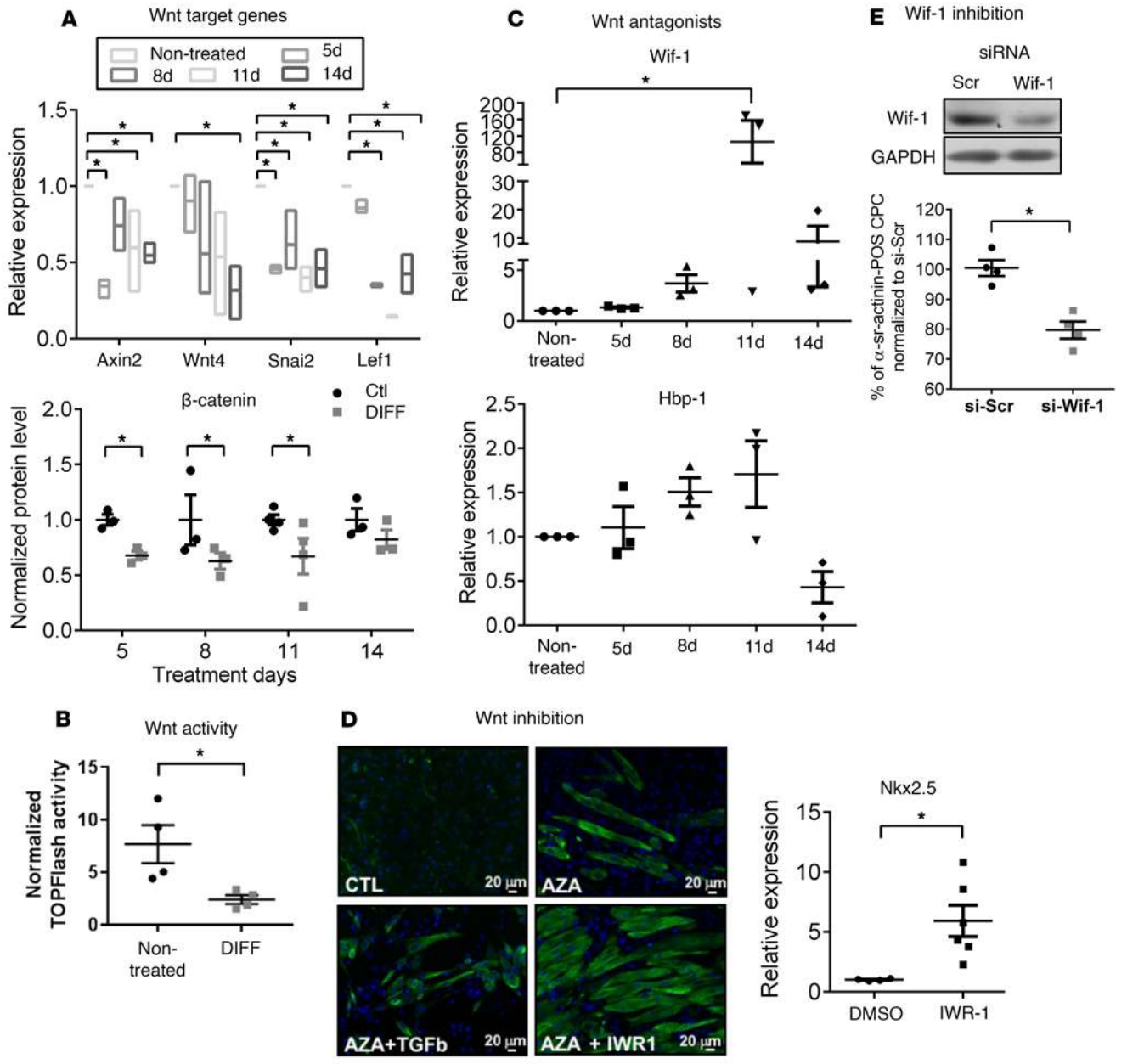

Figure 1. Cardiac progenitor cell differentiation is concomitant with a downregulation of Wnt signaling and upregulation of Wnt inhibitors and is potentiated by inhibition of Wnt/β-catenin. Cultured cardiac progenitor cells (CPCs) were incubated or not (control cells [Ctl]) with 5-azacytidine (AZA) and TGF-β (DIFF) for 5, 8, 11, or 14 days. Gene expression (relative to respective time Ctl) was analyzed using RT-qPCR and normalized to GAPDH. (**A**) Relative expression of Wnt/β-catenin pathway target genes (*Axin2*, *Wnt4*) and Wnt activators (*Lef1* and *Snai2*). Bounds of boxes represent minimum and maximum values, inner line represent means. *$P < 0.05$ vs. CTL; $n = 3$ different preparations; Kruskal-Wallis with Bonferroni correction. Expression of β-catenin protein levels in DIFF, relative to Ctl at each time point. *$P < 0.05$ vs. Ctl; $n \geq 3$ different preparations; Mann-Whitney test. (**B**) CPCs were cultured in Ctl or DIFF medium for 8 days and their supernatant was incubated with HEK cells expressing the TOPflash reporter construct, indicative of Wnt morphogen production by and Wnt activity in donor CPCs. TOPflash signal was normalized for transfection efficiency (cotransfected TKRenilla). *$P <$ 0.05 vs. Ctl; $n = 4$ different cultures; Mann-Whitney. (**C**) Relative (to respective time Ctl) expression of Wnt repressors *Wif1* and *Hbp1*. *$P < 0.05$ vs. Ctl; n = 3 different preparations; Kruskal-Wallis with Bonferroni correction. (**D**) Representative images of CPCs treated or not with AZA and either TGF-β or the pharmacologic inhibitor of Wnt signaling response (IWR1, 10 μM) for 26 days. Immunocytochemistry was performed using an antibody against cardiac troponin T. Relative gene expression of *Nkx2.5* in CPCs treated with IWR1 in absence of AZA for 11 days. *$P < 0.05$, $n \geq 4$ experiments; Mann-Whitney test. Scale bar: 20 μm. (**E**) *Wif1* expression modulates CPC differentiation in coculture. Expression of Wif1 in CPCs transfected with 50 nM siRNA targeting *Wif1* (or siRNA scramble) for 48 hours. CPCs transfected with siRNA-*Wif1* (si-Wif1) or scramble control (si-Scr) were cocultured with cardiomyocytes and their differentiation monitored by expression of α-sr-actinin. Results are reported as relative to differentiation in si-Scr–transfected CPCs (set at 100%). CPC differentiation is significantly decreased upon *Wif1* inhibition. *$P < 0.05$; $n = 4$ different preparations; Mann-Whitney test.

We next investigated the molecular mechanisms underlying Wnt signaling downregulation and particularly the functional significance of sustained upregulation of *Wif1* during the early steps of CPC differentiation. To do this, we first silenced *Wif1* expression in CPCs and tested the effect on their spontaneous (i.e., without pharmacologic treatment) differentiation in a coculture assay with neonatal rat cardiomyocytes (NNCMs), as previously described (14, 15). CPCs were first prelabeled with the permanent cell tracer CM-DiI, transfected with siRNA targeting *Wif1* (or siRNA scramble) for 24 hours, and then mixed with NNCMs in 1:5 ratio and cocultured for 14 days. The efficiency of *Wif1* inhibition on Wif1 expression was verified in parallel in homotypic CPC cultures (Figure 1E; see complete unedited blots in the supplemental material). Cells doubly stained cells for CM-DiI and α-sarcomeric actinin (α-sr-actinin) were considered to be CPCs undergoing cardiac differentiation; CPC differentiation was quantified as the ratio of cells doubly stained for CM-DiI and α-sr-actinin. We have previously excluded cell fusion using FISH and genetic techniques as confounders in the readout of this assay (14). Monocultures of CPCs were evaluated in parallel. No α-sr-actinin staining was observed in any monoculture (data not shown). As illustrated in Figure 1E, downregulation of Wif1 significantly decreased the number of differentiating CPCs cocultured with NNCMs by 21%, suggesting a role for this endogenous Wnt inhibitor in mediating CPC differentiation.

Wif1 gene expression is regulated by Dnmt3a-dependent methylation in CPCs, which regulates their differentiation to the myocyte lineage. Wif1, a secreted antagonist of the Wnt/β-catenin pathway, was shown to be epigenetically regulated by DNA methylation in cancer cells (22–25). De novo DNA methylation is mediated mainly by the DNA methyltransferases Dnmt3a and Dnmt3b. To determine whether Dnmt3a and/or Dnmt3b could be putative regulators of *Wif1* expression in CPCs, we first quantified protein abundance of both isoforms in CPCs during in vitro differentiation (Figure 2A; see complete unedited blots in the supplemental material). We found that the abundance of Dnmt3a, but not Dnmt3b, was strongly reduced early in the differentiation process (–48.77% ± 1.00% compared with the control). To verify the causality of Dnmt3a downregulation in *Wif1* regulation, we treated naive CPCs with siRNA targeting Dnmt3a (Figure 2B; see complete unedited blots in the supplemental material) and measured the relative expression of *Wif1* by quantitative real-time PCR (Figure 2C). Downregulation of Dnmt3a in CPCs triggered an upregulation of *Wif1* expression (by 4-fold compared with the control siRNA scramble), supporting a negative regulatory role of Dnmt3a on *Wif1* expression in CPCs. To verify that Dnmt3a affects *Wif1* gene expression through its de novo methyltransferase activity, we analyzed the DNA methylation pattern of the *Wif1* gene in untreated CPCs after siRNA downregulation of Dnmt3a for 72 hours. DNA methylation patterns were determined by bisulfite sequencing of the –88- to 102-bp region of *Wif1*, which contains a high number of CpG sites. Dnmt3a downregulation produced a significant decrease in the DNA methylation level within the *Wif1* promoter region (–65.8% ± 13%, compared with control siRNA scramble), in particular at two CpG sites located immediately downstream of the transcription start site (Figure 2D). Therefore, downregulation of Dnmt3a, as observed during CPC differentiation, decreases DNA methylation and promotes *Wif1* gene expression.

To further assess the causality of Dnmt3a downregulation in cardiac lineage specification, we analyzed the effect of Dnmt3a inhibition on the efficiency of differentiation of CPCs cocultured with NNCMs. Freshly isolated CPCs were prelabeled with the permanent cell tracer CM-Dil, transfected with siRNA targeting *Dnmt3a* or siRNA scramble constructs, and cocultured with NNCMs as described above (14). Cells doubly stained cells for CM-DiI and cTnT were considered to be CPCs undergoing cardiac differentiation; CPC differentiation was quantified as the ratio of cells doubly stained for CM-DiI and α-sr-actinin. Monocultures of CPCs were evaluated in parallel. No cTnT staining was observed in any monoculture (data not shown). By comparison, approximately 15%–20% of siRNA scramble–treated CPCs were doubly positive for cTnT and CM-DiI, indicative of cardiac differentiation, upon coculture with NNCMs. However, the number of differentiated CPCs was significantly higher when the cells were first transfected with siRNA-*Dnmt3a* (+61.6% ± 12 %, compared with siRNA scramble) (Figure 2E). This indicates that Dnmt3a regulates CPC differentiation to the cardiac lineage.

miR-29a downregulates Dnmt3a, with subsequent upregulation of Wif1 expression and CPC differentiation. In search of epigenetic regulators of myocyte commitment that would coordinately regulate Dnmt3a downregulation and Wif1 upregulation, we performed an in silico bioinformatic search for microRNA putatively targeting *Dnmt3a*. Using 5 different algorithms, we identified the miR-29 family as strong potential candidates, as they were the only ones predicted by all 5 to target *Dnmt3a* 3′UTR (Supplemental Table 2). Therefore, we examined the expression level of miR-29a and miR-29b in the course of CPC differentiation and found an early (5 days) and transient upregulation of mature miR-29a in differentiation medium (+344% ± 50.8 %, compared with control,

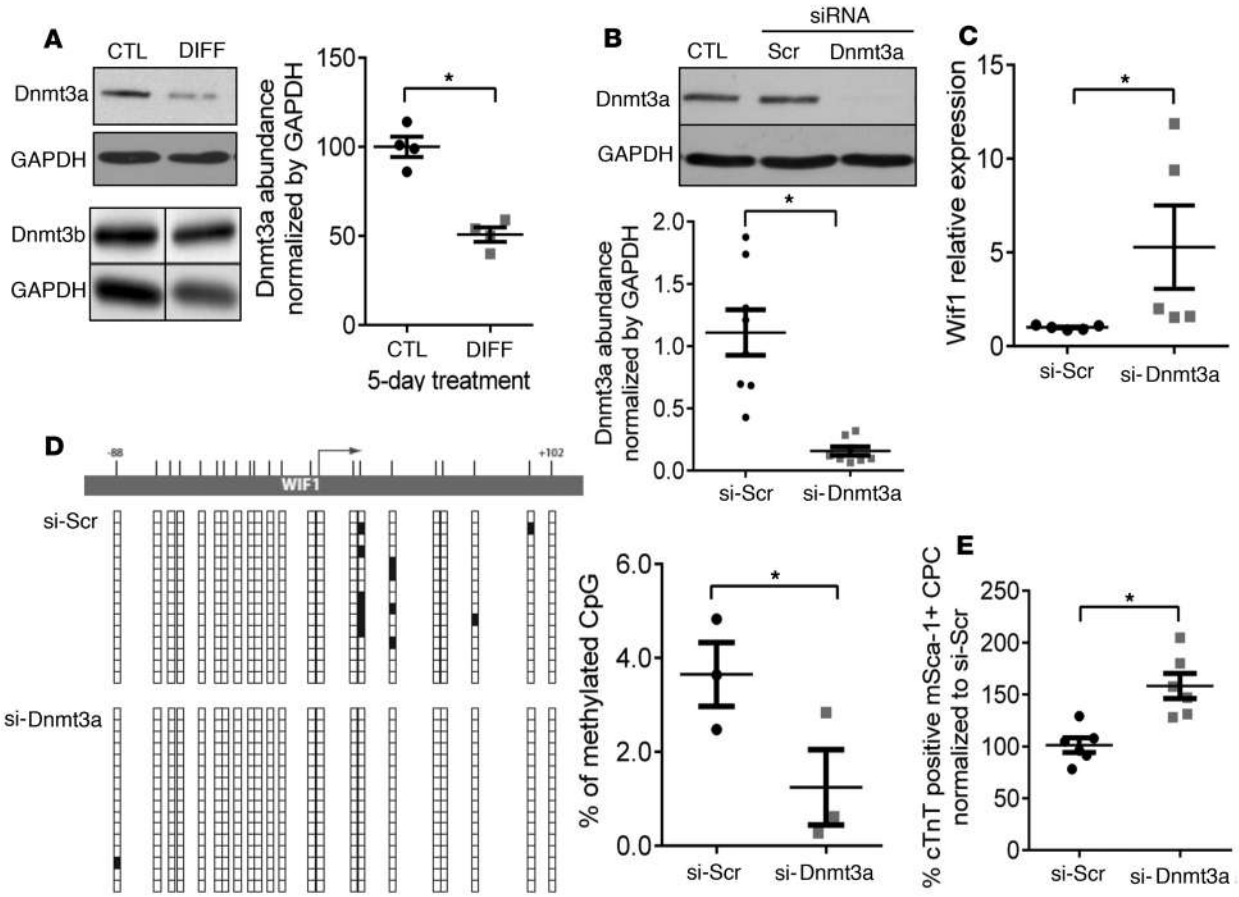

Figure 2. Dnmt3a downregulation upregulates *Wif1* expression in cardiac progenitor cells and promotes their differentiation to the myocyte lineage. (**A**) Cultured cardiac progenitor cells (CPCs) were treated with 5-azacytidine and TGF-β (DIFF medium) for 5 days, and Dnmt3a and Dnmt3b abundance was measured by immunoblotting (corrected for equal protein loading by GAPDH immunodetection). **P* < 0.05 vs. CTL; *n* = 4 experiments; unpaired *t* test. (**B** and **C**) Untreated CPCs were transfected with siRNA targeting *Dnmt3a* for 72 hours, and (**B**) the effect on Dnmt3a protein level was measured by Western Blot and (**C**) the effect on *Wif1* transcripts was measured by qRT-PCR. Results were normalized by GAPDH protein or mRNA abundance, respectively. **P* < 0.05 vs. Si-Scr; *n* = 5–7 experiments; unpaired *t* test. (**D**) Analysis of the methylation pattern of the *Wif1* gene in CPCs transfected with Si-Dnmt3a for 72 hours. CpG methylation in the *Wif1* gene region extending from −88 to +102 bp was assessed by bisulfite sequencing. Representative images of (un)methylated CpG in corresponding *Wif1* region. Vertical bars correspond to the location of CpG sites. Vertical lines of boxes below correspond to multiple clones of the corresponding sequences of *Wif1* (white box: unmethylated; black box: methylated). Percentage of methylated CpGs in the *Wif1* DNA fragments, calculated as a ratio of the number of methylated CpG to the total number of CpG sites from CPCs treated with Si-Dnmt3a (or Si-Scr). **P* < 0.05 vs. Si-Scr; *n* = 3 experiments; unpaired *t* test. (**E**) CM-DiI–stained CPCs were first transfected with si-Dnmt3a (or si-Scramble) and then cocultured with neonatal cardiomyocytes (NNCM) for 14 days. Differentiation was assessed from the percentage of cardiac troponin T–positive (cTnT-positive) CPC. Dnmt3a inhibition increases the efficiency of CPC differentiation in coculture with NNCMs. **P* < 0.05 vs. Si-Scr; *n* > 3 experiments; unpaired *t* test.

Figure 3A). The expression of miR-29b was also upregulated but with more variability among the independent replicates (Supplemental Figure 2). Of note, the upregulation of miR-29a at day 5 of the differentiation process coincided with the initial rise, followed by sustained upregulation of *Wif1* (see Figure 1C). Using anti-miR (LNA-miR-29a) and a mimic construct of miR-29a in naive CPCs, we confirmed that miR-29a reciprocally regulates Dnmt3a protein level as well as Wif1 expression (Figure 3, B and C; see complete unedited blots in the supplemental material). To verify that miR-29a upregulates Wif1 expression through Dnmt3a repression, we treated CPCs with both anti-miR-29a and siRNA-Dnmt3a (and respective control constructs) and measured the relative expression level of *Wif1* by qRT-PCR (Figure 3D). Combined inhibition of miR-29a and its target Dnmt3a abrogated the effect on *Wif1* expression, showing that miR-29a indirectly regulates *Wif1* expression through Dnmt3a downregulation. We further analyzed the methylation pattern of *Wif1* by bisulfite sequencing in CPCs transfected with anti-miR-29a. miR-29a inhibition significantly increased the level of DNA methylation in the *Wif1* gene (Figure 3E) and, in particular, at the two CpG sites that were found to be targeted by Dnmt3a (Figure 2D). These results demonstrate that miR-29a exerts epigenetic regulation of *Wif1* via Dnmt3a.

To confirm the involvement of miR-29a in cardiac differentiation of CPCs, we examined the effect of miR-29a inhibition on CPC differentiation upon coculture with NNCMs (as used above) (Figure 4A). Pretreatment of CPCs with LNA-miR-29a decreased their differentiation rate (63% ± 3.7 % of CPCs treated with the control LNA scramble). To test if miR-29a regulates differentiation through other putative targets (than Dnmt3a), we further cotransfected CPCs with LNA-miR-29a and siRNA-Dnmt3a (and respective control constructs) before coculture with NNCMs. Whereas miR-29a inhibition alone decreased CPC differentiation, as expected (Figure 4B, 3rd tick mark), combined miR-29a inhibition and repression of Dnmt3a abrogated the effect of miR-29a downregulation (Figure 4B, 4th tick mark). These data identified Dnmt3a as a functionally relevant target for miR-29a–mediated CPC differentiation.

Transient inhibition of Dnmt3a in CPCs promotes myocyte differentiation of CPCs in vivo. We next examined the relevance of these epigenetic mechanisms on CPC differentiation in vivo in a mouse infarction model. CPCs were first transfected with siRNA-Dnmt3a (or scramble construct) ex vivo for 18 hours and then were directly injected in 3 distinct sites peripheral to the infarcted left ventricular (LV) area induced by permanent ligature of the left anterior descending (LAD) coronary artery. Efficient Dnmt3a downregulation was verified in parallel in a sample of each batch of cells. After injection, mice were phenotyped by cardiac MRI at 24 hours and then at 28 days after myocardial infarction (MI) before sacrifice. An additional group was sacrificed at day 15 after MI for histological analysis only.

To measure the effect of the transient downregulation of Dnmt3a on CPC differentiation in vivo, we first identified cells doubly stained with Sca-1 and GATA4 markers as progenitor cells with cardiogenic potential (3, 20, 26). Histological analysis of LV sections (at 15 and 30 days) of the infarction border zones revealed the presence of small cells coexpressing GATA4 and Sca-1, albeit in very small proportion compared with the total number of GATA4-expressing cells (approximately 0.04% of $GATA^+$ cells detected per μm^2 tissue (Figure 5A). Among these doubly stained cells, we identified a small number of cells that coexpressed α-sr-actinin, indicating differentiation toward the cardiac lineage (Figure 5B), although the staining remained punctate, indicative of poor sarcomeric organization. No cell with adult-type differentiation was detected at either time point. Nevertheless, the number of Sca-1/GATA4/α-sr-actinin–expressing cells was almost double at 15 days after MI in hearts injected with siRNA-Dnmt3a–treated CPCs compared with controls (siRNA scramble CPCs) and increased by approximately 33% at 30 days after MI, revealing a positive effect of Dnmt3a downregulation on CPC differentiation in vivo (Figure 5C).

Injection of CPCs with downregulated Dnmt3a attenuates adverse cardiac remodeling in infarcted hearts. Interestingly, histological analysis of the remote myocardial areas revealed similar myocyte sizes (transverse areas) (Figure 6A), a transient increase in inflammatory infiltrates (CD45 staining) (Figure 6D), and decreased interstitial fibrosis (Sirius red staining) (Figure 6B) at 15 days as well as a significant increase in capillary densities (CD31 staining) at 30 days after MI (Figure 6C) in hearts injected with siRNA-Dnmt3a–treated CPCs compared with controls, suggesting potential paracrine effects of injected modified cells on cardiac tissue remodeling. We also examined the expression of miR-29a by in situ hybridization in the peri-infarct areas and found a significant increase in miR-29a abundance in hearts injected with siRNA-Dnmt3a–treated CPCs compared with controls both at 15 and 30 days after MI (Figure 7).

Finally, we examined the effect of the injection of epigenetically modified CPCs on the function of infarcted hearts. Infarct sizes (as determined from the number of akinetic/dyskinetic LV wall segments by MRI) were identical between treatment groups. Although the study was not powered for survival analysis, we observed a trend for better survival of mice injected with siRNA-Dnmt3a–treated cells compared with controls (Figure 8A). Likewise, mice in the active treatment group displayed a better recovery in LV functional parameters, such as LV stroke volume (Figure 8B) and a preserved LV wall thickening (Figure 8C), at 30 days after infarction.

Discussion

Using previously characterized adult CPCs and differentiation protocol, we show that the canonical Wnt/β-catenin pathway is downregulated in the early stages of differentiation and that its inhibition is sufficient to promote CPC differentiation to cardiomyocytes in vitro. This is consistent with ours and others' previous data demonstrating the obligatory role of secondary Wnt/β-catenin inhibition for mesoderm specification toward the cardiac lineage as well as for the differentiation of adult $Sca\text{-}1^+$ CPCs in vitro and in vivo (9, 12–15). Recent data in human ESCs have similarly identified the

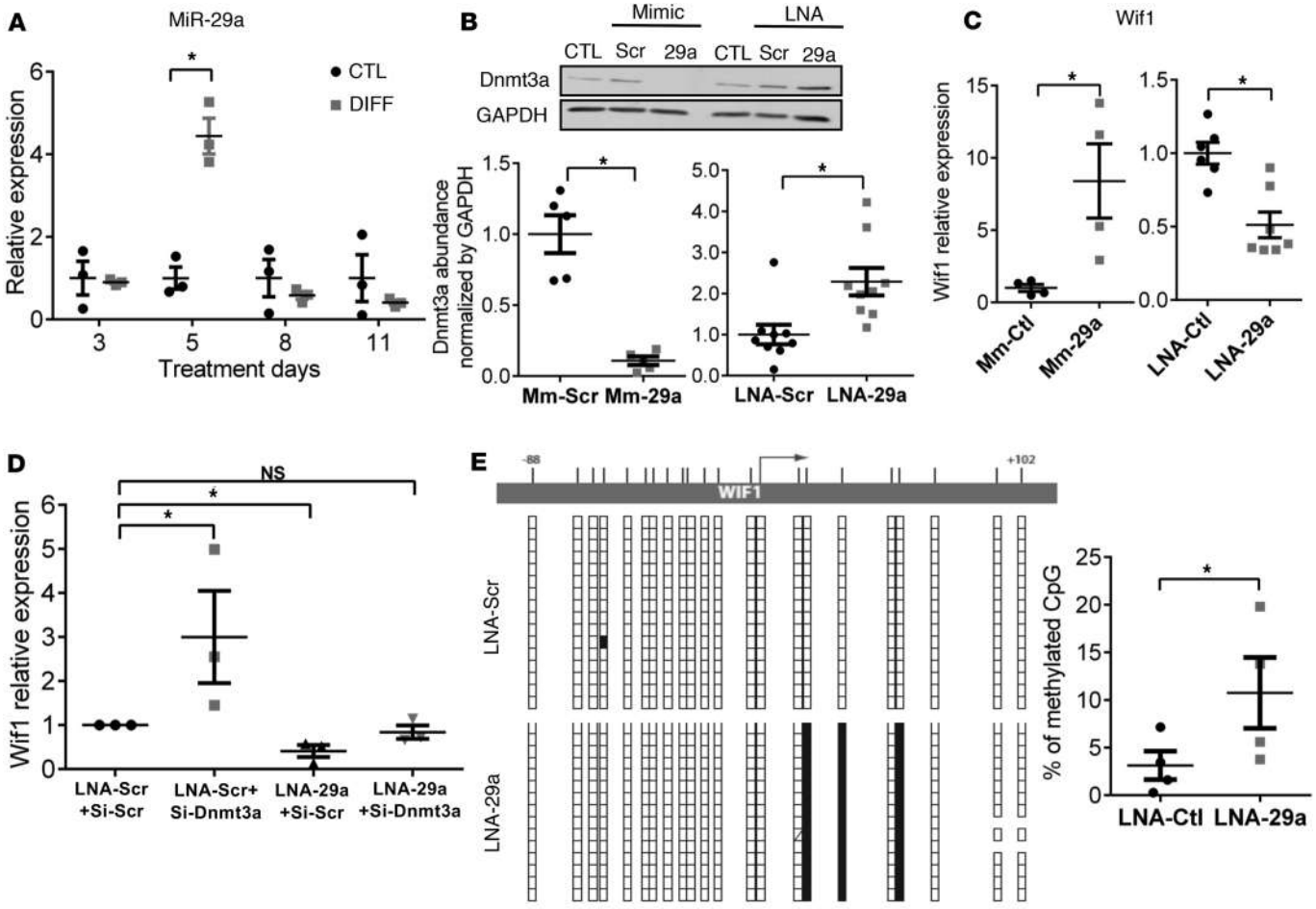

Figure 3. miR-29a increases *Wif1* through repression of Dnmt3a and its de novo methylation of *Wif1* gene. (**A**) Cultured cardiac progenitor cells (CPCs) were treated with 5-azacytidine/TGF-β (DIFF) or control medium (CTL) for 3 to 11 days. Expression of miR-29a was measured by qRT-PCR and normalized to 5S. *$P < 0.05$ vs. CTL at day 5; Mann-Whitney test. miR-29a in DIFF at day 5 is also different from DIFF at days 3, 8, and 11 by Kruskal-Wallis with Bonferroni correction; $n = 3$ experiments. (**B**) Untreated CPCs were transfected with either a miR-29a mimic construct (Mm-29a) or LNA-miR-29a (LNA-29a) or respective scramble constructs (Scr). Dnmt3a proteins (by Western Blot) and (**C**) *Wif1* transcripts (by qRT-PCR), normalized by GAPDH protein or mRNA abundance, are reported as fold changes from CTL (set at 1). *$P < 0.05$ vs. mimic/LNA-scr; $n = 4$–8 experiments; unpaired *t* test. (**D**) Untreated CPCs were cotransfected with si-Dnmt3a and LNA-29a (or Scr controls). Relative expression of *Wif1* mRNA (qRT-PCR, normalized to GAPDH) is expressed as fold change from CTL (transfected with both Scr constructs, set at 1). *$P < 0.05$ vs. LNA-Scr+si-Scr, 1-way ANOVA, Bonferroni's test; $n = 3$ experiments. (**E**) Untreated CPCs were transfected with LNA-29a (or LNA-Scr) for 72 hours, and CpG methylation of the *Wif1* gene region extending from −88 to +102 bp was assessed by bisulfite sequencing. Representative image of (un)methylated CpG in corresponding *Wif1* region. Each vertical line of boxes below corresponds to multiple clones of the corresponding sequence of the *Wif1* gene (white box: unmethylated; black box: methylated). Percentage of methylated CpG in the *Wif1* DNA fragments. *$P < 0.05$ vs. LNA-Scr; $n = 4$ experiments; unpaired *t* test.

sequential role of synergistic activation of Wnt and BMP for initial mesoderm formation, followed by Wnt inhibition required for cardiac differentiation (12). Although this and other studies focused on downstream networks of transcriptional regulators, virtually nothing is known about the mechanism driving this secondary Wnt extinction.

Our expression kinetics and targeted RNA invalidation data point to the Wnt antagonist, Wif1, as a functionally relevant mediator of endogenous Wnt inhibition for CPC differentiation. Indeed, the progressive increase in *Wif1* expression in AZA-treated CPCs coincides with the downregulation of Wnt target genes, and *Wif1* siRNA targeting in naive (i.e., not treated with AZA) CPCs (that exhibit constitutive activity of Wnt signaling, ref. 14) attenuates their differentiation capacity in the coculture model, which is similar to the in vivo situation. The induction of *Wif1* expression following demethylation treatment with AZA is in line with previous reports on the regulation (i.e., inhibition) of *Wif1* gene expression by methylation in cancer cells (22–25). However, its progressive increase (peaking at day 11, i.e., 8 days after AZA was stopped) suggested intermediate epigenetic regulators. Indeed, we found that the de novo DNA methyltransferase Dnmt3a is strongly decreased

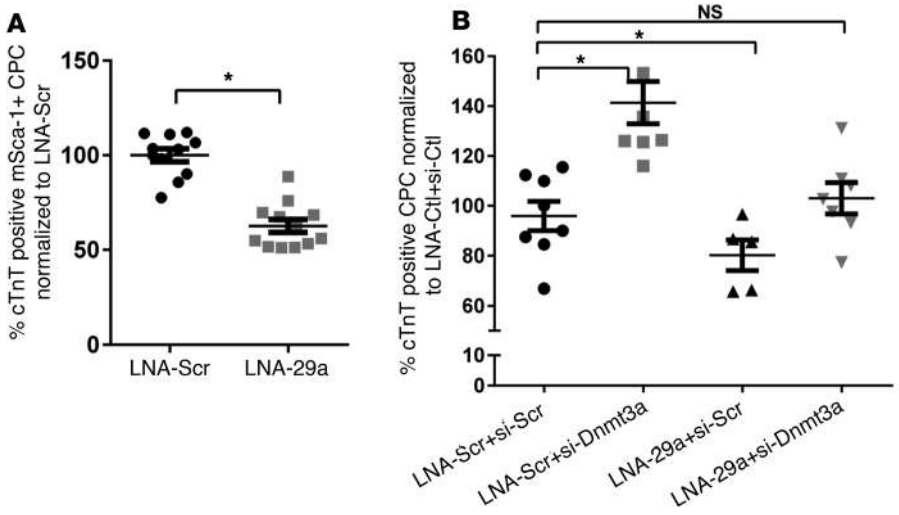

Figure 4. miR-29a promotes cardiac progenitor cell differentiation to cardiomyocytes through Dnmt3a downregulation. CM-DiI–stained cardiac progenitor cells (CPCs) were first transfected with locked nucleic acid targeting miR-29a (LNA-miR-29a) (or LNA-Scr) and/or siRNA-Dnmt3a (or si-Scr) and then cocultured with neonatal cardiomyocytes (NNCMs) for 14 days. The efficiency of CPC differentiation was determined by the percentage of doubly stained cells for CM-DiI and cardiac troponin T (cTnT). (**A**) CPCs transfected with LNA-miR-29a have a lower capacity to differentiate into cardiomyocytes, (**B**) whereas cotransfection of CPCs with both LNA-miR-29a and siRNA-Dnmt3a does not affect their efficiency of differentiation compared with cells cotransfected with respective controls (LNA-Scr+si-Scr). (**A**)*$P < 0.05$ vs. LNA-Scr; $n > 3$ experiments; unpaired *t* test. (**B**) *$P < 0.05$ vs. LNA-Scr+si-Scr; $n > 3$ experiments; 1-way ANOVA, with Bonferroni's test.

early (at day 5, i.e., 2 days after AZA treatment arrest) during cardiac differentiation, concomitant with a strong increase in the expression of miR-29a. In addition, the functional importance of both Dnmt3a and miR-29a for *Wif1* gene methylation and Wif1 expression as well as for CPC differentiation was verified in naive CPCs in monocultures as well as in the coculture model, respectively. Our identification of the miR-29 family based on bioinformatic analysis corroborates previous reports on Dnmt3a regulation by miR-29a in other cell types (27, 28) and is supported by our expression as well as miR-29a mimic and inhibition data. Altogether, we demonstrated that miR-29a indirectly modifies the methylation pattern of the *Wif1* gene, promoting its expression through Dnmt3a downregulation, which is also key for the effect of miR-29a on differentiation. Wnt signaling regulators, such as Wif1, most probably belong to a subset of the methylation-dependent genes sensitive to Dnmt3a downregulation. Other genes coding cardiac-specific proteins, such as *Myh6*, *Myh7*, *Tnni3*, and *Tnnt2*, were reported to be similarly sensitive to DNA methylation (29–31). Likewise, besides its indirect regulation of methylation-sensitive genes through Dnmt3a targeting, miR-29a probably modulates the stability and/or translation of other transcripts regulating cardiogenesis that are not identified here. Notably, although the expression of miR-29a itself may also be methylation sensitive (32), its upregulation did not occur immediately after AZA treatment, suggesting that additional signaling events may support its temporary overexpression at day 5.

Our demonstration of similarly enhanced differentiation of CPCs with downregulated Dnmt3a in infarcted hearts extends our paradigm in vivo. We chose a model of transient decrease of Dnmt3a in injected CPCs because a prolonged downregulation could affect chromatin remodeling in an uncontrolled way and induce adverse effects (33). Likewise, we did not inject miR-29a mimics in the border zones of the injured tissue to avoid uncontrolled effects on multiple cell types and neither did we inject CPCs transfected with miR-29a mimics, as we questioned the concentration- and time-dependent efficiency of target(s) inhibition in vivo.

As observed in our in vitro experiments, transient Dnmt3a inhibition enhanced CPC differentiation in vivo, as revealed by costaining of Sca-1$^+$ CPCs with GATA-4 and α-sr-actinin. Despite expression of some late markers of differentiation, most of the identified cells were still mononucleated and lacked organized sarcomeres even 4 weeks after injection, indicating incomplete maturation to the adult phenotype. Indeed, others have shown that only 50% of cells undergoing differentiation present a binucleation and an organized sarcomeric structure as late as 12 weeks after the injury (26), illustrating the long-term process of cardiac differentiation in vivo. We did not prelabel CPCs before injection, as it was not the purpose of this study to track cell survival/migration in the infarcted heart. Consistent with several previous studies (26, 34, 35), the number of cells differentiating to the cardiac myocyte lineage was minimal but nevertheless significantly increased by 30%–60% in hearts injected with Dnmt3a-targeted CPCs. As the cells were not labeled, part of the differentiating CPCs may include endogenous progenitors sensitive to paracrine signaling from the injected cells.

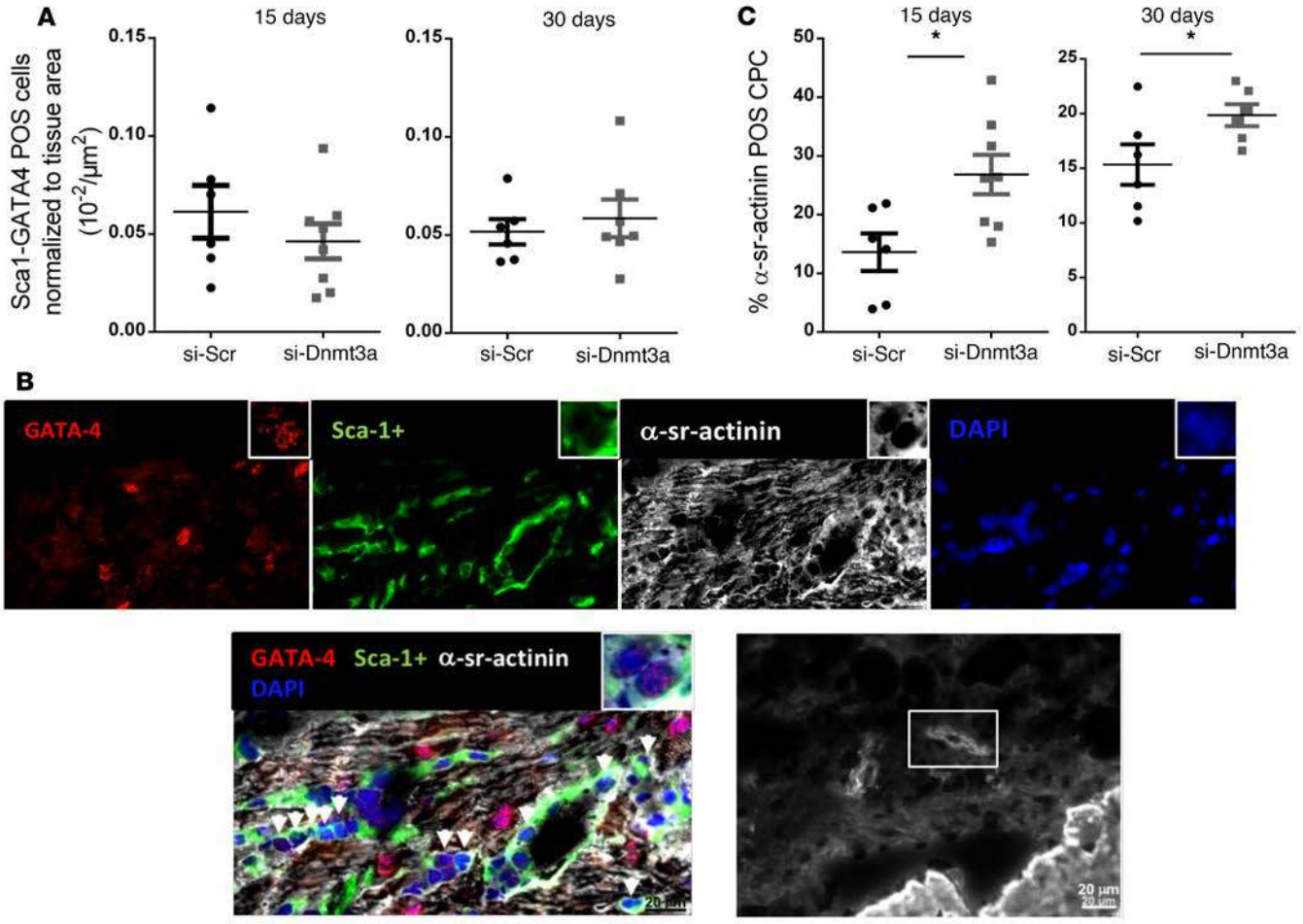

Figure 5. Downregulation of Dnmt3a in cardiac progenitor cells injected in infarcted hearts improves cardiac progenitor cell differentiation in vivo. Cardiac progenitor cells (CPCs) were first transfected with si-Dnmt3a and then injected in the border zone of infarcted mouse hearts after LAD ligature. (**A**) Mice were sacrificed at 15 or 30 days for immunohistochemical analysis of heart sections. Quantification of Sca-1/GATA4^{POS} cells per μm^2 tissue in the border zones of the myocardial infarct (MI). *$P < 0.05$ compared with respective si-Scr; n = 6–8 mice; Mann-Whitney test. (**B**) Representative section of mouse peri-infarct region stained for GATA4, Sca-1$^+$, α-sr-actinin, and DAPI. Arrows indicate multiple small cells positive for Sca-1 and GATA4. Few of these doubly positive cells also express α-sr-actinin, although without visible sarcomeric organization. Representative cell with the beginning of a sarcomeric organization. Scale bar: 20 μm; original magnification, ×40 (inset). (**C**) Quantification of CPC differentiation in vivo 15 and 30 days after MI. Results are expressed as ratios of CPCs triple positive for GATA4/Sca-1/α-sr-actinin, as index of their differentiation, to the total number of GATA4/Sca-1$^+$ CPCs. The percentage of CPCs expressing the cardiac sarcomeric protein is higher in hearts injected with CPCs with downregulated Dnmt3a at both time points. *$P < 0.05$ compared with respective si-Scr; n = 6–8 mice; Mann-Whitney test.

Such paracrine signals may also account for the preservation of cardiac function and prevention of wound expansion in mice injected with modified CPCs, with a significantly higher LV stroke volume and LV wall thickening at day 28 after acute MI (at similar initial MI sizes). Indeed, it is unlikely that the small number of differentiating CPCs, mostly at an immature state, were sufficient to restore contracting muscle. We also observed a trend toward higher survival rate in mice that received modified CPCs, suggestive of distal signaling to neighboring cells affecting broader aspects of cardiac function (36–39).

Our histomorphometric analysis of infarcted hearts suggests a modified secretome in siRNA-Dnmt3a–treated CPCs. Collagen measurements revealed a significant decrease in interstitial fibrosis as soon as 2 weeks after MI, possibly through differential expression of secreted antifibrotic factors. Interestingly, miR-29a is a well-known antifibrotic microRNA targeting various collagens and other extracellular matrix proteins as well as profibrotic Smad3 signaling (40, 41). Its expression was shown to be strongly decreased in the region of the fibrotic scar after MI, while its downregulation participates in the increased cardiac fibrosis in the injured heart (40). In lung cancer cells, Tan et al. have shown that miR-29a expression is methylation sensitive and that Dnmt3a/b downregulation regulates its expression in a positive feedback loop (32). An upregulation and

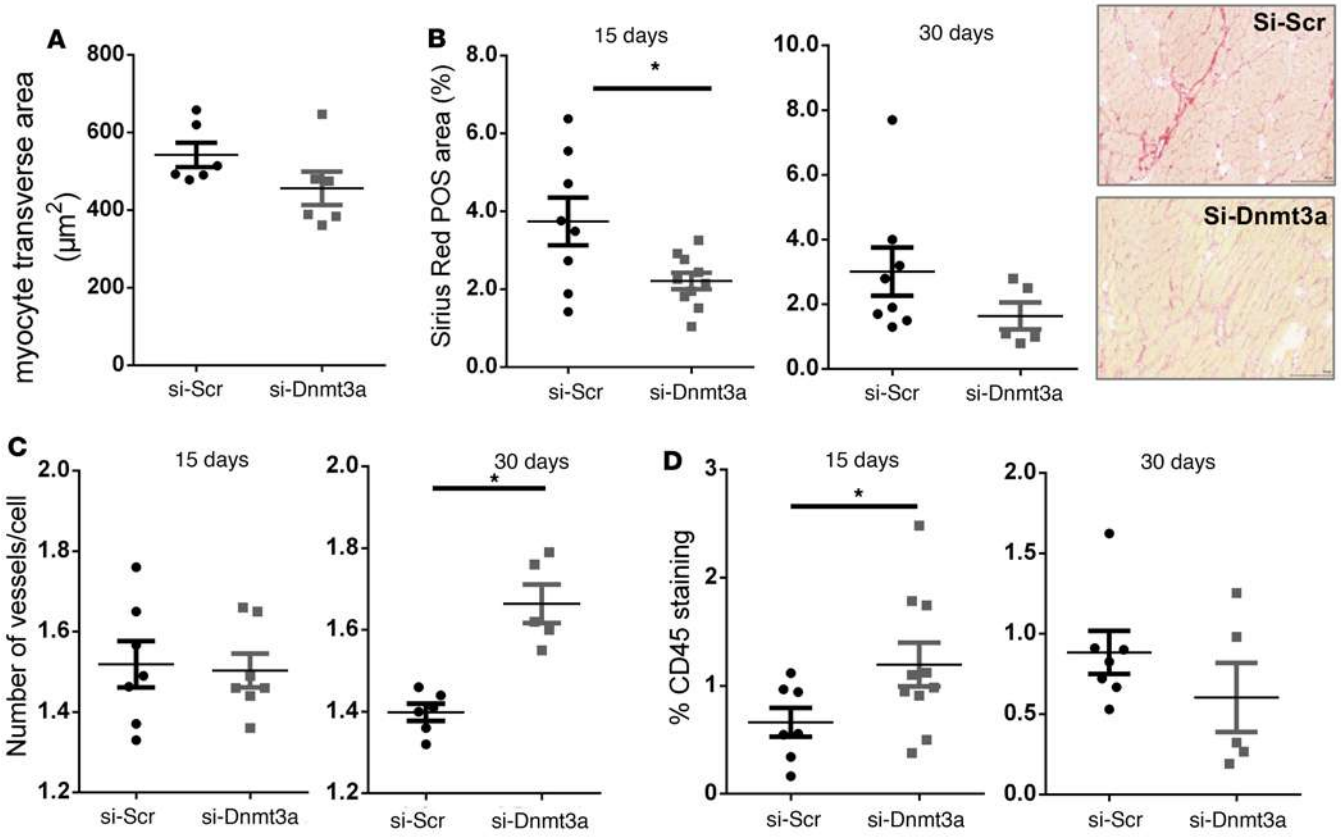

Figure 6. Injection of cardiac progenitor cells with downregulated Dnmt3a attenuates myocardial remodeling in areas remote from the infarcted region. Cardiac progenitor cells (CPCs) were first transfected with si-Dnmt3a and then injected in the border zone of infarcted mouse hearts after LAD ligature. Mice were sacrificed at 15 or 30 days for immunohistochemical analysis of remote heart sections. (**A**) Myocyte transverse area (μm²) at 30 days. Remote myocardial transverse sections were stained with rhodamine wheat germ agglutinin (WGA) and quantified in 400 cells per heart in 6 hearts per group. (**B**) Interstitial fibrosis measured by Picrosirius red staining at 15 and 30 days. Areas of collagen fibers are identified in red (original magnification, ×20) were normalized to tissue area. Average of interstitial fibrosis was quantified in 3–6 sections per heart. *n* = 8–10 hearts at 15 days; *n* = 5–8 hearts at 30 days. **P* < 0.05 compared with control; Mann-Whitney test. (**C**) Cardiac capillary density measured by isolectin staining and normalized to myocyte cell number at 15 and 30 days after surgery. Average capillary density was quantified in 3 sections /heart. *n* = 7 hearts at 15 days; *n* = 5–6 hearts at 30 days. **P* < 0.05 compared with control; Mann-Whitney test. (**D**) Inflammatory cell infiltrate measured by immunostaining of CD45 15 and 30 days after surgery. *n* = 7–10 hearts at day 15; *n* = 5–7 hearts at day 30. **P* < 0.05; Mann-Whitney test.

increased secretion of miR-29a, as a secondary effect of Dnmt3a inhibition in modified CPCs, may participate to the beneficial antifibrotic effect we observed in vivo. Moreover, in human cardiac tissue, profibrotic changes induced by prolonged hypoxia during MI are associated with a global DNA hypermethylation and increased expression of Dnmt1 and Dnmt3b enzymes (42). Indeed, Dnmt3-induced hypermethylation of antifibrotic genes, such as *THY-1* (43) or *RASSF1A* (44), was shown to contribute to fibroblast activation and fibrogenesis. Therefore, miR-29a overexpression, as observed in this study, could also affect cardiac fibrosis by targeting Dnmt3a/b, propagating Dnmt3 downregulation in surrounding cells.

Our histological analysis also revealed an increased capillary density in the remote myocardial area 4 weeks after MI, suggestive of increased neoangiogenesis in hearts injected with modified CPCs. Emerging evidence supports the role of epigenetic DNA methylation in endothelial cell differentiation and homeostasis. Knockdown of Dnmt1 and Dnmt3a promotes the angiogenesis of human mesenchymal stem cells, leading to arterial specific differentiation (45). In HUVECS and mouse carotid arteries endothelium, mechanosensitive genes, such as *HoxA5*, *Klf3*, and *Klf4*, are hypermethylated upon disturbed blood flow, as found in atherosclerotic vessels, while AZA treatment restores their methylation pattern (46–48). Again, the increased capillary density in hearts injected with modified CPCs may have been induced by modified paracrine factors and/or the overexpression of miR-29a in cardiac tissue, subsequently targeting Dnmt3a/b expression in neighboring endothelial cells. Altogether these data indicate propagation of differential cell signaling by modified CPCs beyond the injection site in the injured area.

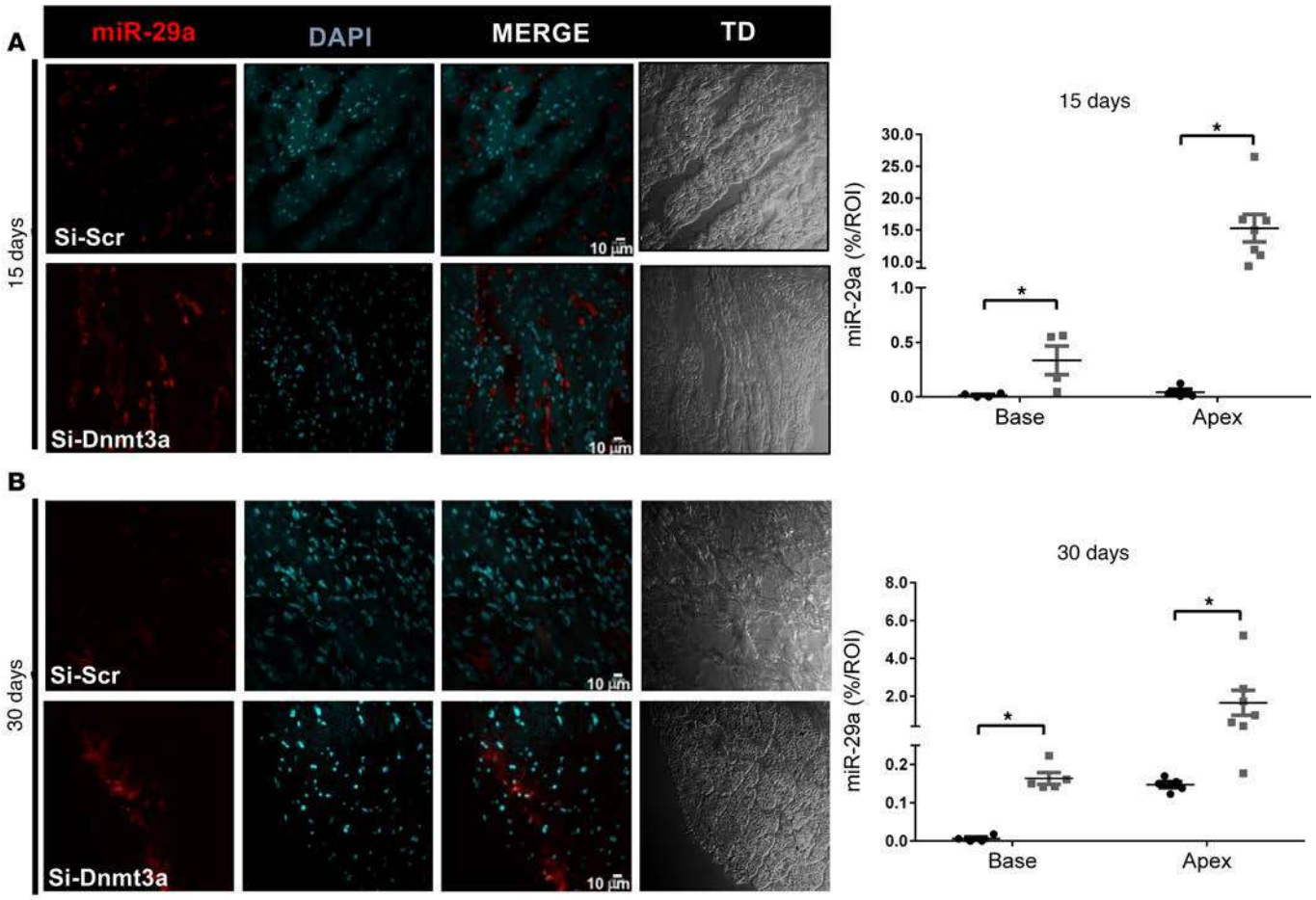

Figure 7. In situ hybridization of miR-29a in infarcted hearts with siRNA-Dnmt3a–injected cardiac progenitor cells. Cardiac progenitor cells (CPCs) were first transfected with si-Dnmt3a and then injected in the border zone of infarcted mouse hearts after LAD ligature. Mice were sacrificed at 15 or 30 days for in situ hybridization analysis of remote heart sections. (**A** and **B**) Hybridization signals in remote myocardial areas at (**A**) 15 days or (**B**) 30 days after MI in hearts injected with si-Scr–treated CPCs or si-Dnmt3a–treated CPCs. Quantification of miR-29a is shown. Signals in hearts injected with Si-Scr CPCs are represented by black dots, and signals in hearts injected with siDnmt3a CPCs are represented by gray dots. *$P < 0.05$ compared with respective controls; n = 4–7 hearts; Mann-Whitney test.

The potential benefit of miR-29a overexpression in infarcted myocardium, as outlined above, could be used as a therapeutic opportunity, provided it is delivered at appropriate dose and targeted to specific cell types. However, circulating miR-29a levels were also shown to correlate with hypertrophy and fibrosis in patients with hypertrophic cardiomyopathy (49). Other studies have also suggested adverse effects of miR-29a in the diabetic heart (50) or on vascular integrity in advanced age (51), raising some caution when considering systemic delivery of miR-29a as a therapeutic option. This also reinforces the advantage of our targeted approach with cell-specific regulation of endogenous expression rather than nonspecific supply of exogenous miR-29a mimics.

Methods

Cardiac progenitors and cardiomyocytes isolation. Isolation of Sca-1$^+$ CPCs was performed using hearts of 8- to 10-week-old male C57Bl/6 mice based on the protocol described previously (3, 15) with some modifications, as in ref. 14. In brief, harvested hearts were enzymatically and mechanically digested and then the resulting suspension was filtered twice and red blood cells were removed by osmotic shock. Enrichment of Sca-1$^+$ cells was achieved by sorting the cells using the anti-Sca-1 MicroBead kit (FITC) (Miltenyi Biotec; 130-092-529) and the Magnetic Cell Sorting system (MACS MS column; Miltenyi Biotec; 130-042-201), as described in ref. 14. The quality of the Sca-1$^+$ enrichment fraction was verified by flow cytometry. Cells were seeded on precoated gelatin plates in Ham's F-12K Medium (Thermo Fisher Scientific; 21127022) with 20% FBS (Sig-

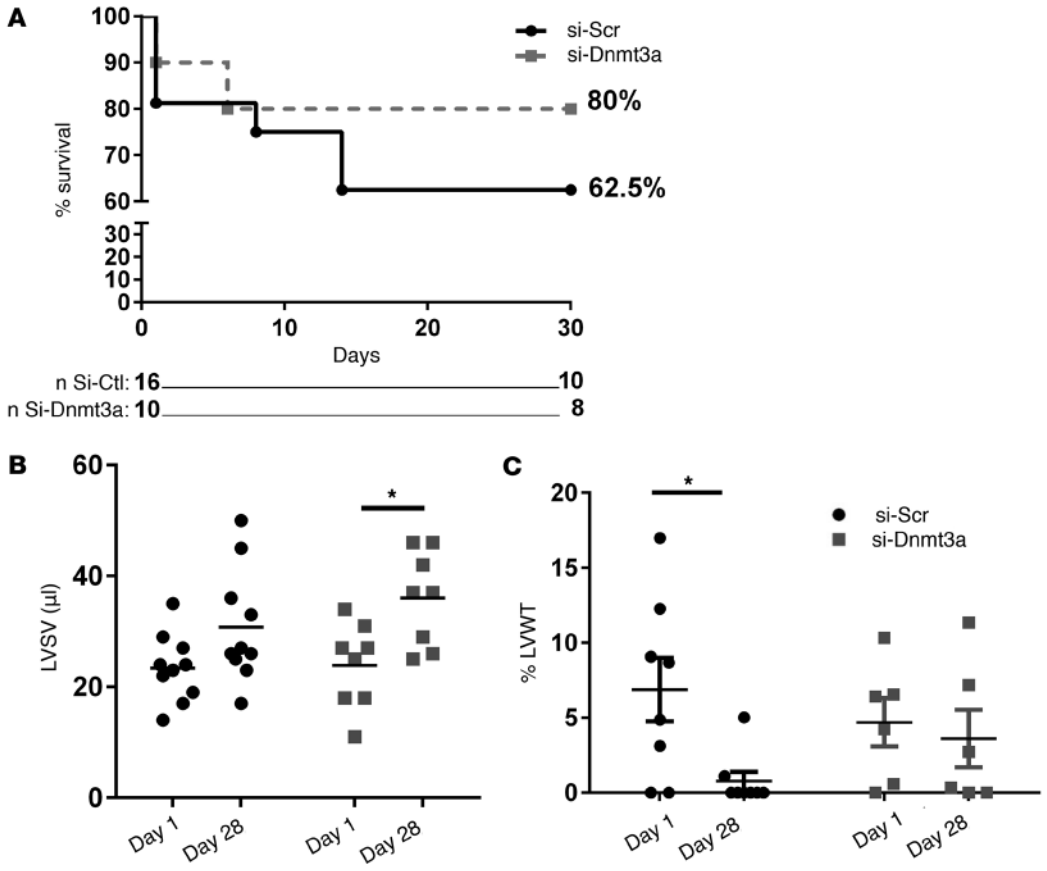

Figure 8. Improved functional recovery of infarcted hearts after injection of cardiac progenitor cells with downregulated Dnmt3a. Cardiac progenitor cells (CPCs) were first transfected with siRNA-targeting Dnmt3a (si-Dnmt3a) and then injected in the border zone of infarcted mouse hearts after LAD ligature. (**A**) Survival curves of mice injected with CPCs pretransfected with si-Dnmt3a (or scramble control). (**B** and **C**) Mice were phenotyped by cardiac magnetic resonance imaging (cMRI) at day 1 and 28 after surgery. (**B**) Left ventricular stroke volume (LVSV) at day 1 and 28 after myocardial infarction. Mice injected with CPCs after downregulation of Dnmt3a (si-Dnmt3a) show better recovery of LVSV compared with control CPCs (si-Scr) at day 28. (**C**) Increase in left ventricular wall thickening (LVWT) in systole (expressed as a percentage of diastolic thickness) in the same mice as in **B**. Mice injected with CPCs after downregulation of Dnmt3a (si-Dnmt3a) show better preservation of systolic LVWT compared with control CPCs (si-Scr) at day 28. *$P < 0.05$ compared with respective values at day 1; n = 8–10 mice; 2-way ANOVA, Sidak's test.

ma-Aldrich; F7524), rhFGF basic (10 ng/ml; R&D Systems; 233-FB), LIF (10^3 unit/ml; Merck Millipore; ESG1107), and 1% penicillin/streptomycin (Thermo Fisher Scientific; 10378016) for 3 to 4 days and then subsequently switched and amplified in Sca-1$^+$ expansion medium, composed of DMEM/F12 GlutaMAX (Thermo Fisher Scientific; 31331028) supplemented with ITS (10 µg/ml insulin, 5 µg/ml transferrin, 5 ng/ml medium sodium selenite; Thermo Fisher Scientific; 41400045), rhFGF basic (10 ng/ml), epidermal growth factor (20 ng/ml; PeproTech; 315-09), LIF (10^3 unit/ml), B27 serum-free supplement (×50 diluted; Thermo Fisher Scientific; 17504044), HEPES (5 mM; Thermo Fisher Scientific; 15630080), and 1% penicillin/streptomycin. CPCs were further clonally expanded by dilution cloning, as reported previously (14, 19).

NNCMs were isolated from 0- to 3-day-old rat pups (Wistar) by consecutive digestions of heart pieces with collagenase type II (Thermo Fisher Scientific; 17101-015) and pancreatin (Sigma-Aldrich; P3292) according to a previously described protocol (20). Cells were separated by using two successive Percoll gradient centrifugations and selective attachment of fibroblasts. Neonatal myocytes were cultured in DMEM/M199 (4:1) (Thermo Fisher Scientific; 11965092 and 41150020) supplemented with 100 mM BrdU (Sigma-Aldrich; B5002) and 1% penicillin/streptomycin.

Differentiation assay of Sca-1$^+$ CPCs in monoculture or in coculture with NNCMs. Differentiation of Sca-1$^+$ CPCs toward the cardiac myocyte lineage was induced with AZA (Sigma-Aldrich; A2385) pretreatment

for 3 days, followed by TGF-β (PeproTech; 240-B-002), as previously described (20). In some experiments, cells were treated with the Wnt pharmacological inhibitor IWR1 (Sigma-Aldrich; I0161) alone or following AZA treatment. The molecule was renewed every day.

For the coculture experiments, isolated Sca-1$^+$ CPCs were first labeled with the permanent cell tracer CM-Dil (Molecular Probes; Thermo Fisher Scientific; C-7000) and then transfected or not with siRNA/anti-miR or mimic for 24 hours. NNCMs were added on top of labeled CPCs in a ratio 1:5 (Sca-1$^+$ CPCs/NNCMs), in DMEM (low glucose) supplemented with 10% FBS. Cocultures were maintained for 14 days before proceeding to immunohistochemical analysis.

Superfusion and TOP-Flash reporter assays. Sca-1$^+$ CPCs were differentiated in monocultures as described above or cultured in control medium. After refreshing media 48 hours before, conditioned media were harvested at day 8 of differentiation and centrifuged in Amicon Ultra-10K columns (Millipore, UFC901024) at 3,200 *g* for 15 minutes at 4°C to concentrate samples to a volume of 1 ml/P100. Concentrated media were used freshly for superfusion on HEK293T reporter cells.

One day before transfection, HEK293T cells were seeded at 320,000 cells/well in a 12-well-plate format in DMEM (Thermo Fisher Scientific, 61965-026) containing 10% fetal calf serum. Cells were transfected with 0.5 μg TOPFlash reporter construct (Addgene, 12456) and 0.05 μg TK-Renilla luciferase plasmid (as control for transfection efficiency, Promega, E2241) using Lipofectamine 2000 Transfection Reagent (Thermo Fisher Scientific; 11668027) in a DNA/Lipofectamine ratio of 1:3. Four hours after transfection, cell media were removed and transfected cells were superfused with conditioned media from differentiated or control Sca-1$^+$ CPCs for 24 hours, using concentrated medium from 1 P100/well. The activity of TOP-Flash and TK-Renilla were measured using the Dual-Luciferase Reporter Assay System (Promega; E1910).

Sca-1$^+$ CPC transfection with siRNA, anti-miR, or mimic. CPCs were seeded at 50% confluency the day before transfection. Cells were transfected with 25 nM siRNA targeting mouse Dnmt3a (Dharmacon; L-065433-01-0005), mouse Wif1 (Dharmacon; L-046832-00-0005), or siRNA-negative control (Dharmacon; D-001810-10-05) using jetPRIME transfection reagent according to the manufacturer's recommendations (Polyplus transfection; 114-07). To mimic miR-29a activity, CPCs were transfected with 25 nM miR-29a mimic (Dharmacon; C-310521-07-0005) or mimic negative control (Dharmacon; CN-001000-01-05) using jetPRIME transfection reagent as well. To inhibit miR-29a activity, CPCs were transfected with 75 nM anti-miR–targeting miR-29a (LNA-29a, Exiqon; 427005-00) or anti-miR negative control (LNA-Scr, Exiqon; 199020-00) using Lipofectamine RNAiMAX Transfection Reagent (Thermo Fisher Scientific; 13778075). Four hours after transfection, medium was changed for complete Sca-1$^+$ expansion medium. Depending on experiments, cells were harvested 24 or 72 hours after transfection. In coculture experiments, CM-Dil–stained CPCs were first transfected with siRNA/mimic/LNA for 4 hours and then washed twice with PBS; NNCMs were added on top of CPCs in a 1:5 ratio (Sca-1$^+$ CPCs/NNCM) as previously described.

Western blot. Protein levels of β-catenin, Wif1, Dnmt3a, and Dnmt3b were assessed in CPCs treated either with AZA and TGF-β or siRNA/mimic/anti-miR. For protein extraction, cells were solubilized in RIPA buffer containing proteinases inhibitors. Specific mouse monoclonal antibody against β-catenin (Thermo Fisher Scientific; 13-8400), rabbit polyclonal antibody against Wif1 (Abcam; ab33281), rabbit monoclonal antibody against Dnmt3a (Cell Signaling, 3598), and rabbit polyclonal antibody against Dnmt3b (Abcam; ab16049) were incubated at dilutions of 1:1,000, 1:500, and 1:1,000, respectively, for both Dnmt3a and Dnmt3b for 1 hour at room temperature. The blots were reprobed with a rabbit monoclonal anti-GAPDH antibody (Cell Signaling, 2118) as a loading control. After chemiluminescence revelation of proteins subjected to immunoblotting, signals were analyzed using digital image processing program (ImageJ, Wayne Rasband, NIH). The data are expressed as relative to GAPDH expression (in arbitrary units).

Immunohistochemical and histomorphometric analysis. For immunocytochemical analysis of in vitro treatment, cells were fixed with 4% formaldehyde, permeabilized in 0.1% Triton/PBS buffer, and then incubated with primary antibody against cTnT (Abcam; ab10214) at 1:200 overnight and Alexa fluor 488 goat anti-mouse antibody (Thermo Fisher Scientific; A-11029) at 1:500 for 1 hour. To evaluate the number of differentiating cells in coculture assays, the ratio of doubly stained CPCs for CM-Dil and cTnT, normalized to the total number of CM-Dil$^+$ CPCs, was used as an index of differentiation. A minimum of 200 cells per well were counted; each condition was performed in 4 replicates (4 wells), and a minimum of 3 independent experiments were performed. Therefore, approximately 800 cells/condition/experiment were counted.

For in vivo experiments, hearts were harvested at 15 or 30 days after surgery, cut in 3 pieces (base, median, and apex), and immediately cryopreserved. To proceed to histological analysis, myocardial samples were serially cut into 5-mm-thick sections and fixed in acetone.

To evaluate the amount of differentiating CPCs in the border zone of the MI, tissue was successively stained with rabbit anti-GATA4 antibody (Thermo Fisher Scientific; PA1-102) at 1:500 overnight, mouse anti-α-sr-actinin (Sigma-Aldrich; A7811) at 1:150 for 30 minutes, and rat FITC-anti-Sca-1 (Miltenyi Biotec; 130-102-297) at 1:10 for 1 hour. GATA-4 and α-sr-actinin stainings were revealed with Alexa Fluor 568 and Alexa Fluor 647 conjugates, respectively (Thermo Fisher Scientific; A11036 and A21247). Nuclei were counterstained with DAPI (Sigma-Aldrich; D9542). To reduce autofluorescence background and remove nonspecific signal from mouse Ig staining, tissues were preincubated with the Avidin/Biotin Blocking kit (Vector Laboratories; SP-2001) and the Mouse on Mouse kit (M.O.M., Vector Laboratories; BMK-2202). The number of CPCs localized in the border zone of the infarction was determined as the doubly stained cells for GATA-4 and Sca-1 per tissue area (in μm^2). A minimum of 5 images (at ×40 magnification) per myocardial section were analyzed on 2 to 6 sections per heart. The number of differentiating cells was calculated as the ratio between triple-stained cells (GATA-4–, Sca-1–, and α-sr-actinin–positive cells) and doubly positive cells for GATA-4 and Sca-1.

To assess cardiac capillary density, tissue was costained with rhodamine-conjugated wheat germ agglutinin (plasma membrane staining, Vector Laboratories; RL-1022) and biotinylated isolectin B4 (GS-IB4, endothelial staining; Vector Laboratories; B-1205) and revealed with Fluorescein Avidin (Vector Laboratories; A-2001). Data from 200 to 400 cells were determined per slide using AxioVision software 4.8.2.0 (Zeiss).

Fluorescent stainings described above were imaged with an AxioImager.z1 microscope equipped with an ApoTome module for structured illumination and AxioVision 4.8.2.0 software (Zeiss).

To evaluate interstitial myocardial fibrosis and inflammatory cell infiltrate, sections were stained either with collagen-specific Picrosirius red (Sirius red in aqueous picric acid; 365548; Sigma-Aldrich) or with rat anti-CD45 (BD Biosciences; 550539) and revealed with biotinylated anti-rat immunoglobulins (Vector Laboratories; BA4001) followed by peroxidase-coupled streptavidin (BD Biosciences; 554066) and DAKO liquid DAB (Agilent; K346811). Sirius red– and CD45-stained sections were then digitalized with a SCN400 slide scanner (Leica Biosystems). The fraction of myocardial tissue occupied by collagen fibers or by CD45 staining was determined as a percentage by quantitative morphometry using TissueIA software (Leica Biosystems).

All histological quantifications were performed in a blinded manner.

FISH. Double-DIG labeled miRCURY LNA detection probes (Exiqon) were used for miR-29a staining, and scrambled probes were used as negative control. In brief, the cryosections were thawed, fixed using fresh 4% (wt/vol) paraformaldehyde, and permeabilized with 0.5% PBS Triton X-100 for 5 minutes on ice. Slides were then incubated overnight with 2 pmoles of probes in a moist chamber at the hybridization temperature suggested by manufacturer's instructions. The next day slides were stringently washed with ×0.1 SSC buffer (3 M NaCl, 0.3 M sodium citrate) (3 times for 10 minutes) at 4°C above the hybridization temperature and washed once for 5 minutes in ×2 SSC at room temperature. Following an incubation with a blocking solution for 30 minutes at room temperature, slides were treated with 1:50 Anti-Digoxigenin-POD, Fab fragments from sheep (Roche; 11207733910) for 2 hours at room temperature. Following 2 washes with 0.1% Tween PBS (PBS-T) and 1 wash in PBS for 5 minutes each, miRNA signal was detected with the TSA Alexa fluor-647 (Thermo Fisher Scientific; T20951). After a final wash with PBS-T and PBS, nuclei were counterstained with DAPI for 5 minutes at room temperature. Fluorescent images were taken with a laser scanning confocal microscope (Olympus, FV1000/SIMS). Quantification of miR-29a was performed using Fiji Imagej software, and values are expressed as the percentage of positive signal relative to background signal.

RNA analysis. Total RNA from cultured cells was isolated using TRIzol (Thermo Fisher Scientific; 15596026). Isolated RNA was subjected to DNase treatment to eliminate genomic DNA contamination. SYBR Green I real-time reverse transcription–PCR (RT–PCR) was carried out with an RT step at 50°C for 30 minutes and an enzyme activation step at 95°C for 15 minutes, followed by 40 cycles of denaturation (95°C for 2 seconds), annealing (59°C for 5 seconds), and extension (72°C for 15 seconds). Analyses were performed on the Bio-Rad iQ5 software 2.0. Results were expressed as relative gene expression using DDCt method.

To detect the level of miRNA, 40 ng total RNA was reverse transcribed using the miRCURY LNATM Universal RT microRNA PCR polyadenylation and cDNA synthesis kit (Exiqon; 203301). qRT-PCR for miR-29a and U6 detection was then performed with microRNA LNATM PCR primers (Exiqon) using the GoTaq qPCR Master Mix (Promega). Relative expression was determined using the DDCt method. See Supplemental Table 1 for oligonucleotide sequences of forward and reverse primers.

Bisulfite sequencing. Analysis of Wif1 promoter methylation was performed in CPCs transfected with siRNA or anti-miR for 72 hours. Genomic DNA was extracted using the chloroform/isoamyl technique, and 5 μg genomic DNA was submitted to sodium bisulfite treatment as previously described (52) and resuspended in 100 μl of DNase-free water. Methylated CpG content determination of Wif1 promoter was performed by PCR amplification and sequencing of bisulfite-treated DNA. For PCR amplification of bisulfite-converted Wif1 sequences, the following nested primers were used: BiWif1 S 5′-GGGTGGGTTGGTTATGTGTTTTT-3′; BiWif1 AS 5′-AGAATTTTATAAGTAGTATAGGTTGGG-3′; nBiWif1 S 5′-GTAGGAGGTTTGAGTGATGATTTAGAAGT-3′; nBiWif1 AS 5′-TGTTGGTATTGTTAGTTTTGTTAGTATCGTGTTTTTG-3′. Nested qPCR product was cloned in PCR4-TOPO plasmid (Invitrogen; P/N 46-0080) and transformed bacterial clones were used for sequencing (Macrogen Inc.).

Surgical procedures. In vivo experiments were performed on 12-week-old C57Bl6/J male mice. Sca-1$^+$ CPCs were transfected ex vivo with 25 nM siRNA targeting Dnmt3a (or siRNA-Scr) for 18 hours and then harvested, counted, and resuspended in 1,000,000 cells/75 μl PBS. Cells were directly injected in 3 distinct sites peripheral to the infarcted LV area (1,000,000 cells/heart) induced by permanent ligature of the LAD. Permanent ligation of the LAD was induced upon anesthesia (2,2,2-TriBromoEthanol, 310 mg/kg, i.p.) with a 8–0 prolene suture (Ethicon). After surgery, a pain relief drug was administered (buprenorphine, 0.1 mg/kg) for 24 hours. Mice were killed 15 or 30 days after surgery, and the hearts were removed for further examination.

Cardiac MRI measurements and image analysis. 29 animals were included in the experiment. Three mice died during follow-up. Mice were scanned on day 1 and day 28 after MI induction on an 11.7 T MRI scanner dedicated to small-animal applications (Biospec, Bruker). A quadrature 1H resonator was used for radiofrequency transmission (inner diameter = 72 mm, length = 6.6 cm) in conjunction with a surface receive-only coil array (length = 10.7 cm). Anesthesia was induced with 3% isoflurane in oxygen and then maintained with 0.5 to 2% isoflurane during the entire procedure. Mice were placed in prone position and monitored for electrocardiogram and respiration with neonatal electrodes wrapped around the paws and a pneumatic sensor placed under the animal. Body temperature was followed by using a rectal probe and regulated with a dedicated heating blanket. Cardiac scout images were obtained in the conventional planes with a tripilot sequence. Then, an Intragate 2D cine Fast Low Angle Shot (FLASH) sequence was applied to acquire a stack of seven to eight 1-mm-thick contiguous short-axis images covering the entire ventricles, perpendicular to the LV long axis. Imaging parameters were as follows: repetition time: 5.83 ms; echo time: 1.45 ms; flip angle: 25°; field of view: 30.0 × 30.0 mm; and matrix size: 256 × 256, resulting in an in-plane resolution of 0.12 × 0.12 mm^2.

All analyses were performed on a blinded basis using Segment imaging software (Medviso v1.8). The LV systolic function was assessed in the stack of short-axis images by tracing epicardial and endocardial borders. End-diastolic, end- systolic, and stroke volume were determined (μl). The number of dyskinetic segments was visually evaluated on short-axis cine sections, according to previously published standardized segmentation distinguishing 6 basal segments, 6 midcavity segments, and 4 apical segments (53).The 17th segment, corresponding to the apex, was not evaluated, as no cine image was acquired in 2- or 4-chamber view. A semiautomated technique was used for the determination of the ventricular thickness at the level of the MI. The "report per slice" tool from Segment Software (Medviso v1.8) was manually placed on a region covering the entire MI zone, and mean end-diastolic and end-systolic wall thickness were then reported.

Statistics. Cell culture experiments were conducted on at least 3 independent cell culture isolates obtained on different days. Statistical analysis was performed using unpaired 2-tailed Student's *t* test, nonparametric tests, or ANOVA followed by Bonferroni post-hoc test, when appropriate after verifying normal values distribution. Statistical tests were performed using GraphPad Prism (GraphPad Software Inc.). Results are reported as mean ± SEM, and *P* values of less than 0.05 were considered significant.

Animal care. All animal procedures conformed to the *Guide for the Care and Use of Laboratory Animals* (National Academies Press, 2011) and were approved by the Institutional Animal Care and Research Advisory Committee of the Université Catholique de Louvain.

Author contributions

ADP, EA, BS, CB, HE, NB, AL, LV, BG, and VDM acquired and analyzed data; CDS, SM, DC, OF, and DHK analyzed data and provided critical scientific input; ADP and JLB planned the experiments, analyzed data, and wrote the manuscript.

Acknowledgments

This work was supported by grants from the Fonds National de la Recherche Scientifique (FNRS, PDR 1.B089.14 and 3.4643.10), the European Commission (UE LSHM-CT-05-018833), and the Federation Wallonie-Bruxelles (ARC 11/16-035) to JLB. ADP was Chargée de Recherche of the FNRS. We thank Delphine Demulder, Adrien Strapart, and Roxane Verdoy for excellent technical work.

Address correspondence to: Jean-Luc Balligand, FATH/UCL, B1.53.09, 52 ave Mounier, 1200 Brussels, Belgium. Phone: 32.2.764.52.60; Email: jl.balligand@uclouvain.be.

BS's present address is: Federal Agency for Medicines and Health Products, Brussels, Belgium

1. Sanganalmath SK, Bolli R. Cell therapy for heart failure: a comprehensive overview of experimental and clinical studies, current challenges, and future directions. *Circ Res*. 2013;113(6):810–834.
2. Smith AJ, et al. Isolation and characterization of resident endogenous c-Kit+ cardiac stem cells from the adult mouse and rat heart. *Nat Protoc*. 2014;9(7):1662–1681.
3. Oh H, et al. Cardiac progenitor cells from adult myocardium: homing, differentiation, and fusion after infarction. *Proc Natl Acad Sci U S A*. 2003;100(21):12313–12318.
4. Laugwitz KL, et al. Postnatal isl1+ cardioblasts enter fully differentiated cardiomyocyte lineages. *Nature*. 2005;433(7026):647–653.
5. Oh H, et al. Cardiac muscle plasticity in adult and embryo by heart-derived progenitor cells. *Ann N Y Acad Sci*. 2004;1015:182–189.
6. Laflamme MA, Murry CE. Heart regeneration. *Nature*. 2011;473(7347):326–335.
7. van Berlo JH, et al. c-kit+ cells minimally contribute cardiomyocytes to the heart. *Nature*. 2014;509(7500):337–341.
8. Zaruba MM, Soonpaa M, Reuter S, Field LJ. Cardiomyogenic potential of C-kit(+)-expressing cells derived from neonatal and adult mouse hearts. *Circulation*. 2010;121(18):1992–2000.
9. Naito AT, et al. Developmental stage-specific biphasic roles of Wnt/beta-catenin signaling in cardiomyogenesis and hematopoiesis. *Proc Natl Acad Sci U S A*. 2006;103(52):19812–19817.
10. Clevers H, Loh KM, Nusse R. Stem cell signaling. An integral program for tissue renewal and regeneration: Wnt signaling and stem cell control. *Science*. 2014;346(6205):1248012.
11. Kattman SJ, et al. Stage-specific optimization of activin/nodal and BMP signaling promotes cardiac differentiation of mouse and human pluripotent stem cell lines. *Cell Stem Cell*. 2011;8(2):228–240.
12. Rao J, et al. Stepwise clearance of repressive roadblocks drives cardiac induction in human ESCs. *Cell Stem Cell*. 2016;18(3):341–353.
13. Qyang Y, et al. The renewal and differentiation of Isl1+ cardiovascular progenitors are controlled by a Wnt/beta-catenin pathway. *Cell Stem Cell*. 2007;1(2):165–179.
14. De Pauw A, et al. Paracrine nitric oxide induces expression of cardiac sarcomeric proteins in adult progenitor cells through soluble guanylyl cyclase/cyclic-guanosine monophosphate and Wnt/β-catenin inhibition. *Cardiovasc Res*. 2016;112(1):478–490.
15. Zelarayán LC, et al. Beta-Catenin downregulation attenuates ischemic cardiac remodeling through enhanced resident precursor cell differentiation. *Proc Natl Acad Sci U S A*. 2008;105(50):19762–19767.
16. Willems E, et al. Small-molecule inhibitors of the Wnt pathway potently promote cardiomyocytes from human embryonic stem cell-derived mesoderm. *Circ Res*. 2011;109(4):360–364.
17. Duan J, et al. Wnt1/βcatenin injury response activates the epicardium and cardiac fibroblasts to promote cardiac repair. *EMBO J*. 2012;31(2):429–442.
18. Oerlemans MI, Goumans MJ, van Middelaar B, Clevers H, Doevendans PA, Sluijter JP. Active Wnt signaling in response to cardiac injury. *Basic Res Cardiol*. 2010;105(5):631–641.
19. Hoch M, et al. Erythropoietin preserves the endothelial differentiation capacity of cardiac progenitor cells and reduces heart failure during anticancer therapies. *Cell Stem Cell*. 2011;9(2):131–143.
20. Smits AM, et al. Human cardiomyocyte progenitor cells differentiate into functional mature cardiomyocytes: an in vitro model for studying human cardiac physiology and pathophysiology. *Nat Protoc*. 2009;4(2):232–243.
21. Chen B, et al. Small molecule-mediated disruption of Wnt-dependent signaling in tissue regeneration and cancer. *Nat Chem Biol*. 2009;5(2):100–107.
22. Urakami S, et al. Epigenetic inactivation of Wnt inhibitory factor-1 plays an important role in bladder cancer through aberrant canonical Wnt/beta-catenin signaling pathway. *Clin Cancer Res*. 2006;12(2):383–391.
23. Fendri A, et al. Epigenetic alteration of the Wnt inhibitory factor-1 promoter is common and occurs in advanced stage of Tunisian nasopharyngeal carcinoma. *Cancer Invest*. 2010;28(9):896–903.
24. Liu YL, Yang HP, Zhou XD, Gong L, Tang CL, Wang HJ. The hypomethylation agent bisdemethoxycurcumin acts on the WIF-1 promoter, inhibits the canonical Wnt pathway and induces apoptosis in human non-small-cell lung cancer. *Curr Cancer Drug Targets*. 2011;11(9):1098–1110.
25. Hou HA, et al. Distinct association between aberrant methylation of Wnt inhibitors and genetic alterations in acute myeloid leukaemia. *Br J Cancer*. 2011;105(12):1927–1933.
26. Noseda M, et al. PDGFRα demarcates the cardiogenic clonogenic Sca1+ stem/progenitor cell in adult murine myocardium. *Nat Commun*. 2015;6:6930.
27. Fabbri M, et al. MicroRNA-29 family reverts aberrant methylation in lung cancer by targeting DNA methyltransferases 3A and 3B. *Proc Natl Acad Sci U S A*. 2007;104(40):15805–15810.
28. Hu W, et al. miR-29a maintains mouse hematopoietic stem cell self-renewal by regulating Dnmt3a. *Blood*. 2015;125(14):2206–2216.
29. Abbey D, Seshagiri PB. Aza-induced cardiomyocyte differentiation of P19 EC-cells by epigenetic co-regulation and ERK signal-

ing. *Gene*. 2013;526(2):364–373.
30. Tompkins JD, et al. Mapping human pluripotent-to-cardiomyocyte differentiation: methylomes, transcriptomes, and exon DNA methylation "memories". *EBioMedicine*. 2016;4:74–85.
31. Fang X, et al. Knockdown of DNA methyltransferase 3a alters gene expression and inhibits function of embryonic cardiomyocytes. *FASEB J*. 2016;30(9):3238–3255.
32. Tan M, Wu J, Cai Y. Suppression of Wnt signaling by the miR-29 family is mediated by demethylation of WIF-1 in non-small-cell lung cancer. *Biochem Biophys Res Commun*. 2013;438(4):673–679.
33. Klutstein M, Nejman D, Greenfield R, Cedar H. DNA methylation in cancer and aging. *Cancer Res*. 2016;76(12):3446–3450.
34. Hsieh PC, et al. Evidence from a genetic fate-mapping study that stem cells refresh adult mammalian cardiomyocytes after injury. *Nat Med*. 2007;13(8):970–974.
35. Uchida S, et al. Sca1-derived cells are a source of myocardial renewal in the murine adult heart. *Stem Cell Reports*. 2013;1(5):397–410.
36. Huang C, Gu H, Yu Q, Manukyan MC, Poynter JA, Wang M. Sca-1+ cardiac stem cells mediate acute cardioprotection via paracrine factor SDF-1 following myocardial ischemia/reperfusion. *PLoS One*. 2011;6(12):e29246.
37. Li TS, et al. Direct comparison of different stem cell types and subpopulations reveals superior paracrine potency and myocardial repair efficacy with cardiosphere-derived cells. *J Am Coll Cardiol*. 2012;59(10):942–953.
38. Hong KU, et al. c-kit+ Cardiac stem cells alleviate post-myocardial infarction left ventricular dysfunction despite poor engraftment and negligible retention in the recipient heart. *PLoS One*. 2014;9(5):e96725.
39. Liu ML, et al. Anti-inflammatory peptides from cardiac progenitors ameliorate dysfunction after myocardial infarction. *J Am Heart Assoc*. 2014;3(6):e001101.
40. van Rooij E, et al. Dysregulation of microRNAs after myocardial infarction reveals a role of miR-29 in cardiac fibrosis. *Proc Natl Acad Sci U S A*. 2008;105(35):13027–13032.
41. Xiao J, et al. miR-29 inhibits bleomycin-induced pulmonary fibrosis in mice. *Mol Ther*. 2012;20(6):1251–1260.
42. Watson CJ, et al. Hypoxia-induced epigenetic modifications are associated with cardiac tissue fibrosis and the development of a myofibroblast-like phenotype. *Hum Mol Genet*. 2014;23(8):2176–2188.
43. Neveu WA, Mills ST, Staitieh BS, Sueblinvong V. TGF-β1 epigenetically modifies Thy-1 expression in primary lung fibroblasts. *Am J Physiol, Cell Physiol*. 2015;309(9):C616–C626.
44. Tao H, et al. DNMT3A silencing RASSF1A promotes cardiac fibrosis through upregulation of ERK1/2. *Toxicology*. 2014;323:42–50.
45. Zhang R, et al. Knockdown of DNMT1 and DNMT3a promotes the angiogenesis of human mesenchymal stem cells leading to arterial specific differentiation. *Stem Cells*. 2016;34(5):1273–1283.
46. Jiang YZ, Jiménez JM, Ou K, McCormick ME, Zhang LD, Davies PF. Hemodynamic disturbed flow induces differential DNA methylation of endothelial Kruppel-Like Factor 4 promoter in vitro and in vivo. *Circ Res*. 2014;115(1):32–43.
47. Dunn J, et al. Flow-dependent epigenetic DNA methylation regulates endothelial gene expression and atherosclerosis. *J Clin Invest*. 2014;124(7):3187–3199.
48. Dunn J, Thabet S, Jo H. Flow-dependent epigenetic DNA methylation in endothelial gene expression and atherosclerosis. *Arterioscler Thromb Vasc Biol*. 2015;35(7):1562–1569.
49. Roncarati R, et al. Circulating miR-29a, among other up-regulated microRNAs, is the only biomarker for both hypertrophy and fibrosis in patients with hypertrophic cardiomyopathy. *J Am Coll Cardiol*. 2014;63(9):920–927.
50. Arnold N, Koppula PR, Gul R, Luck C, Pulakat L. Regulation of cardiac expression of the diabetic marker microRNA miR-29. *PLoS One*. 2014;9(7):e103284.
51. Boon RA, et al. MicroRNA-29 in aortic dilation: implications for aneurysm formation. *Circ Res*. 2011;109(10):1115–1119.
52. Loriot A, De Plaen E, Boon T, De Smet C. Transient down-regulation of DNMT1 methyltransferase leads to activation and stable hypomethylation of MAGE-A1 in melanoma cells. *J Biol Chem*. 2006;281(15):10118–10126.
53. Cerqueira MD, et al. Standardized myocardial segmentation and nomenclature for tomographic imaging of the heart. A statement for healthcare professionals from the Cardiac Imaging Committee of the Council on Clinical Cardiology of the American Heart Association. *Int J Cardiovasc Imaging*. 2002;18(1):539–542.